Water Vapour in the Tropical Upper Troposphere and Lower Stratosphere Measured by the Microwave Limb Sounder on UARS

Hannah Clark

Doctor of Philosophy
The University of Edinburgh
1999

Declaration

This thesis has been composed by myself, and all work reported herein is my own except where otherwise stated.

Hannah Clark

Acknowledgements

First and foremost, thanks go to my supervisor, Bob for his support and enthusiasm throughout. Thanks also to Hugh, especially for the data, to past and present members of the MLS team and to Phil for many useful discussions. Acknowledgements are due to the terminal room folk for much help with stubborn computer programs and for continual encouragement.

This work was supported financially by the Natural Environment Research Council.

Abstract

This thesis exploits two water vapour products from the Microwave Limb Sounder (MLS), an instrument on the Upper Atmosphere Research Satellite, to investigate the spatial distribution and temporal variation of water vapour in the tropical region of the upper troposphere and lower stratosphere. Measurements are centred on 215 hPa in the upper troposphere and at 68 hPa and 100 hPa in the lower stratosphere. MLS provides almost global measurements with good vertical resolution, and offers many advantages over other measurement techniques.

Focusing on the tropical region, time-series analysis techniques have been employed to investigate the variability of upper tropospheric water vapour on different timescales. The construction of longitude-time sections has allowed the annual cycle to be investigated in more detail than previously. The amplitude is found to vary greatly with longitude and to be most pronounced over the landmasses of South America and Africa. The oceans are found to have a moderating effect on the annual cycle but secondary maxima occur in regions influenced by the Asian monsoon, and over Indonesia and the central Pacific.

An intraseasonal cycle with a period of 30–85 days is evident over the western Pacific at latitudes from 10°N to 20°S. This is associated with eastward moving moist features apparent in longitude-time sections. Through comparison with meteorological fields from the European Centre for Medium Range Weather Forecasting's re-analysis project, the intraseasonal cycle in water vapour is identified with the convective anomalies associated with the Madden-Julian Oscillation.

Seasonal averages of water vapour at 68 hPa show an expected zonal structure, but some departures from zonal symmetry are observed. In December-February, dry areas are found in the region of the 'stratospheric fountain'. Enhanced moisture is noted in the Asian monsoon region in June-August. The effects of the monsoon and the stratospheric fountain reach higher in the stratosphere than has previously been observed with MLS. Sequences of water vapour fields show that the stratospheric fountain region is the place where the dry phase of the annual cycle first begins.

Contents

List of Acronyms

CISK Conditional Instability of the Second Kind

ECMWF European Centre for Medium Range Weather Forecasts

EEOF Extended Empirical Orthogonal Function

ENSO El Niño and Southern Oscillation

EOF Empirical Orthogonal Function

GLA Goddard Laboratory for Atmospheres

HALOE HALogen Occultation Experiment

ISCCP International Satellite Cloud Climatology Project

ITCZ Intertropical Convergence Zone

LCL Lifting Condensation Level

LIMS Limb Infrared Monitor of the Stratosphere

MJO Madden-Julian Oscillation

MLS Microwave Limb Sounder

MSU Microwave Sounding Unit

NASA National Aeronautics and Space Administration

NCAR National Center for Atmospheric Research

NMC National Meteorological Center

NVAP NASA Water Vapour data set

ppmv parts per million by volume

PV Potential Vorticity

SAGE Stratospheric Aerosol and Gas Experiment

SAMS Stratospheric and Mesospheric Sounder

SPCZ South Pacific Convergence Zone

SSM/I Special Sensor Microwave Imager

SST Sea Surface Temperature

STEP Stratosphere-Troposphere Exchange Project Tropical Experiment

TOVS Television Infrared Observation Satellite, Operational Vertical Sounder

TPW Total Precipitable Water

UARS Upper Atmosphere Research Satellite

UKMO United Kingdom Meteorological Office

UTH Upper Tropospheric Humidity

WISHE Wind-Induced Surface Heat Exchange

WMO World Meteorological Organization

Chapter 1

Introduction

Water vapour in the upper troposphere is of major importance to global climate due to its radiative properties. It is also a useful tracer in stratosphere-troposphere exchange. Historically, measurements of water vapour in the upper troposphere have been difficult to obtain. In situ methods such as radiosondes are limited in their global coverage and in their accuracy. Satellites provide much better temporal and spatial coverage. The Microwave Limb Sounder, an instrument on the Upper Atmosphere Research Satellite, is capable of measuring water vapour in the upper troposphere and lower stratosphere. It provides almost global measurements with better vertical resolution than many other satellites.

The aim of this thesis is to use the MLS water vapour products to provide new information about the water vapour field in the upper troposphere and lower stratosphere. The thesis focuses on the tropical region which, barring instrument failures, is observed daily by MLS. The daily observing pattern of MLS in the tropical region gives it an advantage over other satellite instruments and this is exploited through the construction of time series to investigate temporal variability in this region. In particular, it will be established that water vapour in the upper troposphere varies on both annual and intraseasonal timescales and that the intraseasonal variability is related to the convective anomalies of the Madden-Julian oscillation.

Data is also available on two new levels in the stratosphere, 68 hPa and 100 hPa. Prior to this, 46 hPa was the lowest available level in the stratosphere where the retrieval was considered to be reliable. As an extension to the study of the upper troposphere, these new measurements of water vapour in the lower stratosphere

are examined. Although predominantly zonal in structure, the seasonal water vapour fields at 68 hPa show some departures from zonal symmetry. Importantly, moistening is associated with the Asian monsoon and dry areas in the stratospheric fountain region can be observed at this height, higher in the stratosphere than previously observed. The new data reveals that the transfer of air from troposphere to stratosphere takes place initially in the Asian monsoon and stratospheric fountain regions and is followed by transfer of air in other locations. The use of both the stratospheric and tropospheric measurements offers the opportunity to relate water vapour variability in the upper troposphere to that in the lower stratosphere.

The thesis begins by demonstrating the importance of water vapour in the upper troposphere, and with a brief description of aspects of the tropical atmosphere upon which this thesis focuses. Chapter 2 reviews the advantages and disadvantages of the various methods used in making water vapour measurements in the upper troposphere. The MLS instrument and the other data sets used throughout the thesis are described. Chapter 3 introduces the water vapour field, describing how the MLS field compares with existing data, and assesses the validity of the MLS measurements through comparison with the NASA water vapour dataset. Temporal variability in the tropics forms the subject of chapter 4 with a focus upon annual and intraseasonal timescales. This is placed within a physical framework in chapter 5 when the water vapour field is compared with dynamical quantities from the European Centre for Medium Range Weather Forecasting's reanalysis project. Chapter 6 extends the study of upper tropospheric water vapour to the lower stratosphere and examines aspects related to stratosphere-troposphere exchange.

1.1 The Importance of Water Vapour

Water vapour is the main gas responsible for absorbing infrared radiation and hence is the most important greenhouse gas, playing a dominant role in the earth's energy balance (Houghton *et al.* (1990) and Jones and Mitchell (1991)). The response of the climate to increases in anthropogenic greenhouse gases depends critically on the water vapour feedback and so knowledge of its current distribu-

tion and its interactions in the atmosphere is central to the understanding and prediction of climate change. The key role of water vapour will be demonstrated here with a focus upon its radiative role in the upper troposphere and its use as a tracer for stratosphere-troposphere exchange.

1.1.1 The Role of Water Vapour

The earth-atmosphere system absorbs shortwave radiation from the sun and longwave radiation from the earth. The atmosphere absorbs about seventy percent of the longwave, infrared radiation and, according to Kirchoff's law, also emits it at the same wavelength. Radiation is emitted in all directions, some of which is absorbed by the earth. The amount of radiation emitted upwards from the earth and absorbed by the atmosphere is more than the amount of radiation emitted downwards by the atmosphere, resulting in the earth being about 33^oC warmer than it would otherwise be. This is the earth's natural greenhouse effect.

The main gases responsible for the absorption are water vapour, carbon dioxide and ozone. Saturation vapour pressure for water vapour has an exponential relationship to 1/temperature as described by the Clausius Clapeyron equation,

$$e_s(T) = e_{so} \exp\left\{\frac{L}{R_v}\left[\frac{1}{T_0} - \frac{1}{T}\right]\right\} \tag{1.1}$$

where T is temperature, e_s is the saturation vapour pressure, L is the latent heat of vaporisation, R_v is the gas constant for water vapour ($R_v = 461.53\ J\ kg^{-1}\ K^{-1}$) and e_{so} is the saturation vapour pressure at standard pressure (1000 hPa) ($e_{so} = 611Pa$). Water vapour mixing ratios decrease with height from values of about 800 ppmv at altitudes of 6 km to around 200 ppmv at 10 km. The saturation mixing ratio is given by

$$r_s = \frac{e_s}{p - e_s} \tag{1.2}$$

The emission of radiation by the atmosphere is a function of the water vapour profile and so perturbations to the water vapour profile affect the temperature at the earth's surface and the temperature of the earth is related to the water vapour profile.

If global temperatures rise in response to increases in anthropogenic greenhouse gases, it is thought that the amount of water vapour in the atmosphere will increase since it has an exponential dependence on temperature through the

Clausius Clapeyron equation above. As temperature increases, saturation vapour pressure increases and there is a resulting increase in evaporation. Such increase in water vapour with sea surface temperature has been demonstrated by Raval and Ramanathan (1989) and by Stephens (1990).

1.1.2 The Importance of Water Vapour in the Upper Troposphere

The level in the atmosphere at which water vapour occurs is important in determining its effect on the temperature of the surface. Arking (1990) showed that water vapour above 6 km is more important than water vapour near the surface in determining surface temperature. Whether the increase in water vapour will enhance or diminish global warming is a contentious issue. It is generally believed that increases in water vapour will lead to further enhancement of the greenhouse effect through an increase in the absorption of infrared radiation. It is possible that a small decrease at upper levels could lead to a negative feedback and offset a larger increase at lower levels. Here, the response of water vapour in the upper troposphere will be shown to be central to this debate.

There has been suggestion by Lindzen (1990a) that increased warming and water vapour will lead to increased moist convection and to a drying of the upper troposphere by subsidence. The idea put forward by Lindzen is that warming causes deeper cumulus convection. As the air rises and cools, the water vapour condenses out and when the convective towers reach altitudes of about 16 km they are relatively dry. Compensating subsidence dries the atmosphere above 3-5 km. Since the air is drier and contains fewer infrared absorbers than previously, radiation absorption is reduced and so the increased water vapour emission arising from higher temperatures constitutes a negative feedback. In addition, warming leads to the elevation of the height at which the latent heat is deposited and this again is a negative feedback. Evaporated moisture that ends up in convective clouds, condenses out and therefore adds heat to altitudes greater than 5 km. The atmosphere must balance this heat input through radiative cooling and hence it is the distribution of infrared absorbers, primarily water vapour, above this height that has the most significant effect on the temperature of the surface. The idea of Lindzen's (1990 a,b, and 1991) is contested by Betts (1990) and Hansen and

Lacis (1991).

Hansen and Lacis say that if increased convection really does dry the upper troposphere, then it should be drier in summer than in winter and that this should be observable in radiosonde data. Radiosonde data indicate a moistening in summer but since radiosondes are notoriously inaccurate this is dismissed by Lindzen. More precise profiles of water vapour from satellite data also indicate a summertime moistening of the upper troposphere and measurements of the earth's radiation budget show that the greenhouse warming is largest in regions of moist convection in contradiction to Lindzen's theory. Rind *et al.* (1991) and Raval and Ramanathan (1989) both find evidence for the positive feedback role of water vapour and in a later paper on the distribution of tropical tropospheric water vapour, Sun and Lindzen (1993) state that the idea of tropospheric drying by convection is unsupported by observations of humidity distributions. The necessity of accurate measurements of water vapour in the upper troposphere is crucial to resolve the issue.

Soden and Fu (1995) found that on both local and regional scales within the tropics, convection leads to greater upper tropospheric moisture. This would be in contradiction to Lindzen's (1990a) theory that subsidence dries the upper troposphere. However, they find that poleward of 30° latitude, the positive relationship between deep convection and upper tropospheric humidity breaks down and that outside the tropics, variation in convective activity does not have a systematic influence on upper tropospheric humidity. This suggests that other processes in addition to convection are important in determining upper tropospheric moisture outside the tropics which is in agreement with Kelly *et al.*, (1991) and Del Genio *et al.* (1994). Del Genio *et al.* state that the most important source of extra-tropical upper tropospheric humidity is large scale eddies and that the most important sink is cloud formation. They thus conclude that moistening at all latitudes should be expected as climate warms because subtropical drying by subsidence is counteracted by eddies.

Shine and Sinha (1991), using a radiative-convective model, demonstrate that the sensitivity of climate to increases in water vapour depends upon the height at which the increases occur. If the water vapour concentration is increased by a constant absolute amount at all heights, Shine and Sinha found that upper

tropospheric water vapour above 500 hPa alters the radiation budget of the earth most significantly, in agreement with Lindzen (1990a). In contrast to this, if the water vapour is increased by a constant *fractional* amount, changes to the earth's radiation budget are dominated by the lower troposphere, at heights around 800 hPa. Since increases of moisture at low levels in the atmosphere may be offset by decreases at high levels, this idea is important in determining the effects on climate of the water vapour increase that may occur with global warming (Betts, 1990).

Using a model with the same radiation scheme as that used by Shine and Sinha (1991), Sinha and Allen (1995) also show that the vertical profile of radiative sensitivity (defined as the ratio between the level's contribution to the tropopause irradiance change and the percentage change in *absolute* humidity at that level) is peaked in the lower troposphere below 800 hPa and in the upper troposphere around 300 hPa. Similarly, Spencer and Braswell (1997) used a similar method to Shine and Sinha (1991) and measured the sensitivity of clear-sky OLR (OLR_{CLR}) to increases of 3% to the relative humidity of tropical profiles of the Air Force Geophysical Laboratory model. When 3% RH was added to each layer in turn, the upper troposphere was most sensitive and when a constant relative amount of 3% was added to all layers at once, the lower troposphere at about 800 hPa was most sensitive as Shine and Sinha found. Spencer and Braswell conclude that OLR_{CLR} is more sensitive to humidity changes in the free troposphere ($p <$ 700 hPa) than in the boundary layer below.

1.1.3 Water Vapour and Clouds

Since clouds form as a result of water vapour condensation, the two are inherently linked. The radiative role of clouds in the climate has not been satisfactorily determined and changes associated with global warming cannot, at present, be predicted with accuracy by general circulation models because of the lack of global water vapour data. The effective parameterisation of clouds in general circulation models is required to enable understanding of the current climate state and to improve the predictive capability of the models.

Clouds cool the earth by reflecting incoming shortwave radiation but also contribute to warming by absorbing the infrared. In the shortwave region the effect

of cloud cover depends on optical thickness, particle size and phase. In the long-wave region it depends upon cloud top temperature, which is a function of height and on cloud emissivity which is related to optical thickness. How the climate responds to changes in cloudiness depends on the type, height and composition of the clouds. Cloud tops which reach a greater altitude are colder and therefore emit less radiation to space, constituting a positive feedback. A negative feedback may also result from upper tropospheric drying by subsidence as Lindzen (1990a) suggested. Ramanathan and Collins (1991) suggest that as the oceans warm, the clear sky greenhouse effect will enhance warming until the clouds become sufficiently thick to reflect more solar radiation and prevent further warming. There is a negative feedback from the increased reflectivity of upper tropospheric cirrus anvils that helps to control the maximum value of sea surface temperatures.

Overall, investigations so far suggest that clouds have a cooling effect on the climate but that the response of clouds to changes of other variables in the climate system is not completely understood (Arking, 1991). Cess *et al* (1990) compared cloud feedback processes in 19 general circulation models and found that it varied considerably among them, ranging from a modest negative to a strongly positive response. Arking (1991) concluded that clouds may have a strong influence on climate change but that the magnitude or sign of the influence is a long way from being determined.

1.1.4 Water Vapour as a Tracer

Quantities used to 'label' air parcels so that the motion of the air parcel can be followed are known as tracers. To be useful as a tracer, the quantity must be approximately conserved following the motion of the air parcel. Water vapour is an important chemical tracer for atmospheric motion in the stratosphere, having a long lifetime and significant spatial variability. In the stratosphere, an air parcel retains its water vapour mixing ratio for several days.

The troposphere cannot be considered in complete isolation from the stratosphere above it. Air parcels may be exchanged between the upper troposphere and the stratosphere. The role of the stratosphere in maintaining the water vapour budget of the upper troposphere, and the role of the troposphere in maintaining the water vapour budget of the lower stratosphere is an important area of inves-

tigation. Water vapour mixing ratios are much higher in the troposphere than in the stratosphere and much more variable both spatially and temporally. Water vapour can be used to study stratosphere- troposphere exchange and knowledge of moisture distribution may help to confirm the mechanism for the exchange.

1.1.5 Water Vapour and Chemistry

Water vapour plays an important role in atmospheric chemistry because it is the source of the hydroxyl radical and the hydrogen peroxide molecule. The hydroxyl radical is central to gas phase chemistry and the hydrogen peroxide molecule is an oxidising agent. In the stratosphere, these products are catalysts in ozone destruction. An accurate representation of water vapour is useful for modelling the chemistry of the upper troposphere and lower stratosphere.

1.2 The Tropical Atmosphere

MLS data will be exploited to look at water vapour in tropical regions of the upper troposphere and lower stratosphere in more detail than previously possible. This section presents a review of some of the tropical motion systems which can be expected to influence the observed patterns.

The tropics are an important focus for climate studies as it is here that cumulonimbus convection and detrainment take place which are central to debate about the drying of the upper troposphere (Lindzen, 1990). The response of the upper troposphere to the warming during El Niño is often used as a indicator for how the atmosphere will respond to global warming.

Much of the tropical circulation is driven by the interaction between cumulus convection and the large- or meso- scale circulation. Latent heat release is the main energy source and occurs in association with convective cloud systems. Localised diabatic heating which is strongly influenced by sea surface temperature (SST), may excite equatorial waves which can induce a remote response in the circulation (Holton, 1992).

1.2.1 Convection

To examine the process of convection in the humid tropics, it is necessary first to consider the thermodynamics of a dry atmosphere. Potential temperature θ is the temperature that a parcel of dry air at pressure p and temperature T would have if it was adiabatically expanded or compressed to standard pressure p_o.

$$\theta = T\left[\frac{p_o}{p}\right]^{R/c_p} \tag{1.3}$$

where R is the gas constant for dry air (R=287 $J\ kg^{-1}\ K^{-1}$) and c_p is the specific heat at constant pressure ($c_p = 1004\ J\ kg^{-1}\ K^{-1}$).

For dry adiabatic motion, the potential temperature of an air parcel is conserved. Its potential temperature is related to its entropy by the equation

$$S = c_p ln\theta + constant.$$

Parcels which move adiabatically, move along surfaces of constant entropy known as isentropic surfaces. For an atmosphere in which the potential temperature is constant with height, the lapse rate is known as the adiabatic lapse rate Γ_d and described by:

$$\Gamma_d = -\frac{\partial T}{\partial z} = \frac{g}{c_p}$$

The stability of an air parcel can be defined with respect to the adiabatic lapse rate. A dry atmosphere is stable if $\frac{\partial \theta}{\partial z} > 0$ i.e. the actual lapse rate Γ is less than the adiabatic lapse rate Γ_d. If a moist air parcel is forced to rise, it cools until it becomes saturated at the lifting condensation level (LCL). Further lifting results in condensation which releases heat into the air, giving it extra buoyancy and helping it to rise further. The parcel then cools at the saturated adiabatic rate.

For moist air, the equivalent potential temperature θ_e is defined as the potential temperature that the parcel of air would have if all its moisture condensed out and the resulting latent heat was used to warm the parcel. The condensed water is assumed to fall out, taking some heat with it so the process is pseudo-adiabatic. The lapse rate for pseudo-adiabatic ascent is given the symbol Γ_s. If the lapse rate lies between the dry adiabatic and pseudo-adiabatic values ($\Gamma_s < \Gamma < \Gamma_d$) then the parcel is stable with respect to dry adiabatic displacements and unstable

with respect to pseudo-adiabatic displacements. This is known as conditional instability.

The equivalent potential temperature of a hypothetical saturated atmosphere with the same thermal structure as the actual atmosphere is given the symbol θ_e^*. For a saturated parcel $\frac{\partial \theta_e^*}{\partial z} < 0$ to be conditionally unstable. A typical profile for the equator is shown in figure 1.1. From this it can be seen that the lower troposphere is conditionally unstable, $\frac{\partial \theta_e^*}{\partial z}$ is negative.

It is necessary for the parcel to reach the LCL so that it is saturated at the environmental temperature where convection begins. Therefore a forced ascent to LCL is required to produce saturation before instability results. Only surface air has sufficiently high values of θ_e to become buoyant when raised and so low-level convergence is required to initiate convection over the oceans.

The low pressure that forms in the region below the cumulus cloud encourages more convergence which enhances convection by providing more moist air. In this way, the cumulus clouds provide the large-scale heat source that drives the circulation which in turn is responsible for low level convergence through boundary layer or Ekman pumping (Gill, 1982 pp 326). When low level convergence occurs through boundary layer or Ekman layer pumping the above process is referred to as conditional instability of the second kind (CISK). It is possible for a wave to provide the necessary potential vorticity required to produce convergence in the boundary layer. The term for this is wave-CISK.

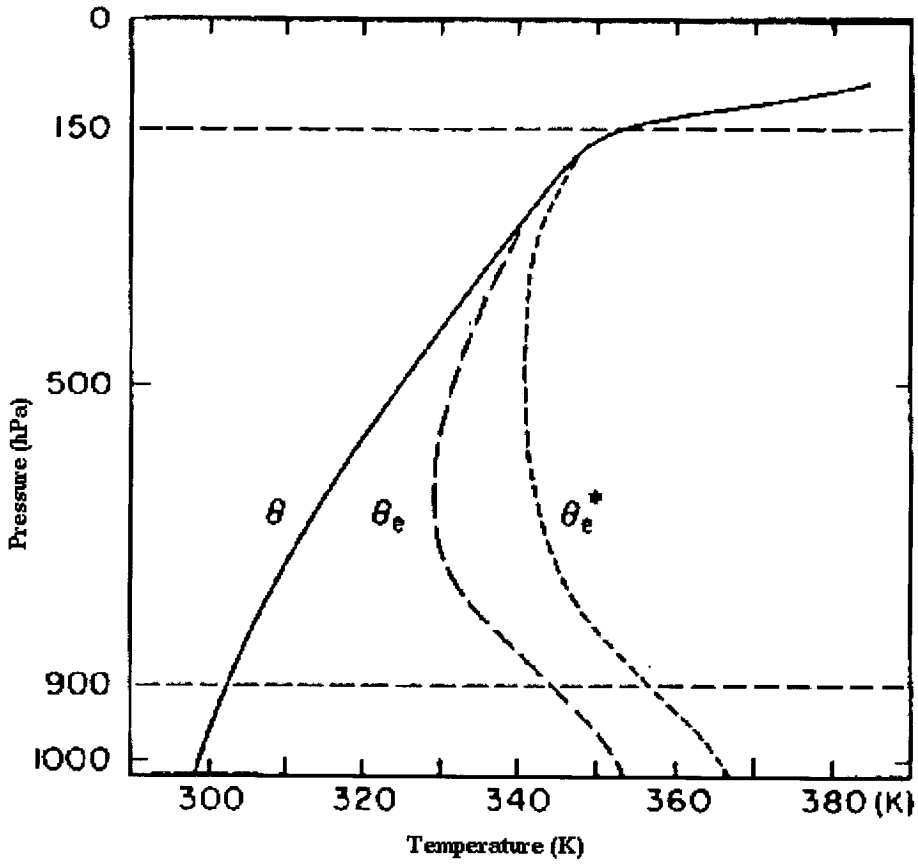

Figure 1.1: Typical vertical profile of potential temperature θ, equivalent potential temperature θ_e, and equivalent potential temperature θ_e^* of a hypothetically saturated atmosphere with the same temperature profile as the unsaturated atmosphere (from Philander, 1990)

1.2.2 Divergence and Vorticity

Vorticity and divergence are both quantities which can help to identify regions where deep convection is taking place. Used in later chapters, they are for reference, defined here.

Divergence (D) is defined as

$$D = \frac{\partial u}{\partial x} + \frac{\partial v}{\partial y} \tag{1.4}$$

where u is the x component of velocity (eastward) and v is the y component of velocity (northward). In spherical polar coordinates it is written as,

$$D = \frac{1}{rcos\phi}\left[\frac{\partial u}{\partial \lambda} + \frac{\partial (vcos\phi)}{\partial \phi}\right] \tag{1.5}$$

where λ is longitude, ϕ is latitude and r is the radial distance i.e. the radius of the earth. In areas of convection, convergence would be expected to take place at lower levels, bringing in water vapour and feeding convection. Divergence would take place above this at the outflow of convection.

Relative vorticity of an air parcel is defined as the curl of its velocity relative to the earth. Generally only the vertical component of relative vorticity ζ is considered and this is expressed in Cartesian coordinates as,

$$\zeta = \frac{\partial v}{\partial x} - \frac{\partial u}{\partial y} \tag{1.6}$$

In spherical polar coordinates this equation becomes,

$$\zeta = \frac{1}{rcos\phi}\left[\frac{\partial v}{\partial \lambda} - \frac{\partial (ucos\phi)}{\partial \phi}\right] \tag{1.7}$$

As air diverges, vorticity decreases to conserve angular momentum. When air converges, vorticity increases. Regions of positive vorticity can therefore be expected to occur at the base of convection, coincident with areas of divergence (negative convergence) at the outflow of the convection aloft.

Potential vorticity is defined as,

$$PV = [\zeta_\theta + f]\left[-g\frac{\partial\theta}{\partial p}\right] \tag{1.8}$$

where p is pressure, g is acceleration due to gravity, and θ is potential temperature as defined in the previous section. ζ_θ is the vertical component of relative vorticity (see equation 1.6) on an isentropic surface and $f = 2\Omega sin\phi$ is the Coriolis parameter. Units of PV are $K\ kg^{-1}m^2\ s^{-1}$.

1.2.3 Equatorial Waves

The equatorial zone can act as a waveguide; disturbances decay away from the equator and are known as 'equatorially trapped'. Both Kelvin waves and Rossby waves can propagate along the equatorial waveguide. For Kelvin waves, the zonal flow is in geostrophic balance with the meridional pressure gradient force causing them to have no meridional velocity and to propagate eastwards. The coriolis force is zero at the equator and this acts as a boundary in a similar way to a coastline (Gill, 1982 pp 437). Rossby waves are due to the variation of Coriolis parameter with latitude. The wave oscillates back and forth about the equilibrium latitude and the restoring force is the meridional gradient of absolute vorticity which is conserved in the motion (Holton, 1992 pp 216). The phase propagation of a Rossby wave is always westward relative to the mean zonal flow. If the mean zonal flow is eastwards with greater velocity than the Rossby wave (as is often the case with mid-latitude westerlies) then the Rossby wave will move eastwards. Usually in the tropics, where zonal winds are easterly, Rossby waves propagate equatorial disturbances westwards.

1.2.4 Walker Circulation, ENSO and Monsoons

The Walker circulation is an atmospheric circulation in the tropical pacific caused by the ocean surface temperatures being about 8°C colder in the eastern Pacific than in the western Pacific. This results in a circulation involving rising motion in the west, eastward flow in the upper troposphere, subsiding motion in the east off the coast of South America and westward flow at ground level. The easterly trade winds pile up warm surface water in the west Pacific and cause the sea

surface to be about half a metre higher than in the east. An upwelling of cold water occurs off the coast of South America. Warm sea surface temperatures in the west lead to convection and a moist upper troposphere, subsiding regions over the cold ocean in the east lead to a dry upper troposphere. The east-west surface pressure gradient associated with the Walker circulation has interannual variation on 2-5 year time-scales and is known as the Southern Oscillation. The Walker circulation is most intense during cold phases of the southern oscillation (La Niña) when the longitudinal sea surface temperature gradients are maximum. The Southern Oscillation is associated with ocean circulation and temperature changes known as El Niño and the two are coupled together and known as El Niño and Southern Oscillation (ENSO).

During an El Niño, the trade winds relax and the warm surface water shifts eastward from the western Pacific towards South America. Lindzen (1990) suggested that El Niño and non-el Niño periods might be used to study the response of water vapour and clouds to warming. Lau *et al.*,(1996) tested the response of the water vapour greenhouse effect simulated by the Goddard Earth Observing System (GEOS) global climate model to changes in SST brought about by ENSO conditions. They found that about 80% of clear sky water vapour greenhouse sensitivity to SST was due to the transport of water vapour by the large-scale circulation and the rest was due to radiative feedback. Under ENSO conditions the non-uniform changes in SST throughout the tropics alter the large-scale circulation and this effect dominates over local radiative feedback. For global warming, SST's are expected to be more uniform across the tropics, circulation changes will be small and radiative effects dominant. Therefore, Lau *et al.*,(1996) concludes that interannual variability should not be used to infer greenhouse sensitivity unless proper account is taken of the large-scale circulation.

Chou (1994) compared clouds and radiation budgets in April of an El Niño year (1987) with that of a non-el Niño year (1985). The sea surface temperature in the El Niño year was on average 0.3K higher than the non-El Niño year but the warming of the earth-atmosphere system due to water vapour was less by $2.5 \mathrm{Wm}^{-2}$ in the El Niño year. Chou's results support Lindzen's idea that warming in the tropics can be offset by cooling resulting from less water vapour in the upper troposphere. Soden (1997) however, in contrast to Chou's findings, found

an increase in greenhouse forcing of $2Wm^{-2}$ during the El Niño period of 1987 along with a rise in sea surface temperature of about 0.4K.

Fu *et al.*,(1997) compared the response of the NCAR Community Climate Model Version 2 (CCM2) to interannual changes in SST with the observed responses of relative humidity (RH) and assimilated moisture transport for the 1987 El Niño. The satellite measurements of upper tropospheric humidity (UTH) came from TOVS, and the moisture transports were assimilated by GEOS-1. CCM2 was found to reproduce the observed large-scale changes in upper tropospheric relative humidity except for being too dry in the 1987 El Niño. The net vertical moisture transport during the El Niño was greater in the model than in the assimilation from GEOS-1 and TOVS but this did not lead to the rising branch of the meridional circulation being moister in the model. The amount of moistening is limited by saturation. The stronger hydrological cycle resulted in a drying of the sub-tropical upper troposphere and reduced the mean UTH over the entire tropics, in agreement with Lindzen (1990). Fu *et al.*, suggest positive water vapour feedback due to a global increase in SST may be weaker than predicted by the model due to the effects of convective drying.

Newell *et al.*,(1997) have shown that MLS humidity measurements are correlated to sea surface temperatures in the tropics. El Niño associated sea surface temperature anomalies are related to anomalies in upper tropospheric water vapour. Figure 1.2 shows El Niño events as observed by MLS. The figure uses all the available data from the UARS mission. Measurements within 5° of the equator are binned into 20° longitude boxes between 140°E and 80°W. The data have been smoothed over a month and are plotted as an anomaly to the multi-year average at the given date and location. The red and yellow colours indicate a moist upper troposphere associated with El Niño.

Monsoons are another feature of the tropical climate and dominate variability in the Indian Subcontinent. They are driven by the heating contrast between land and ocean. During the summer monsoon the Asian continent is much warmer than the Indian Ocean to the south. Deep convection takes place over the Asian continent leading to divergence at high levels. This in turn enhances the surface low over the continent and creates a low level convergent wind which brings in moisture from the ocean. The low level moisture convergence increases the

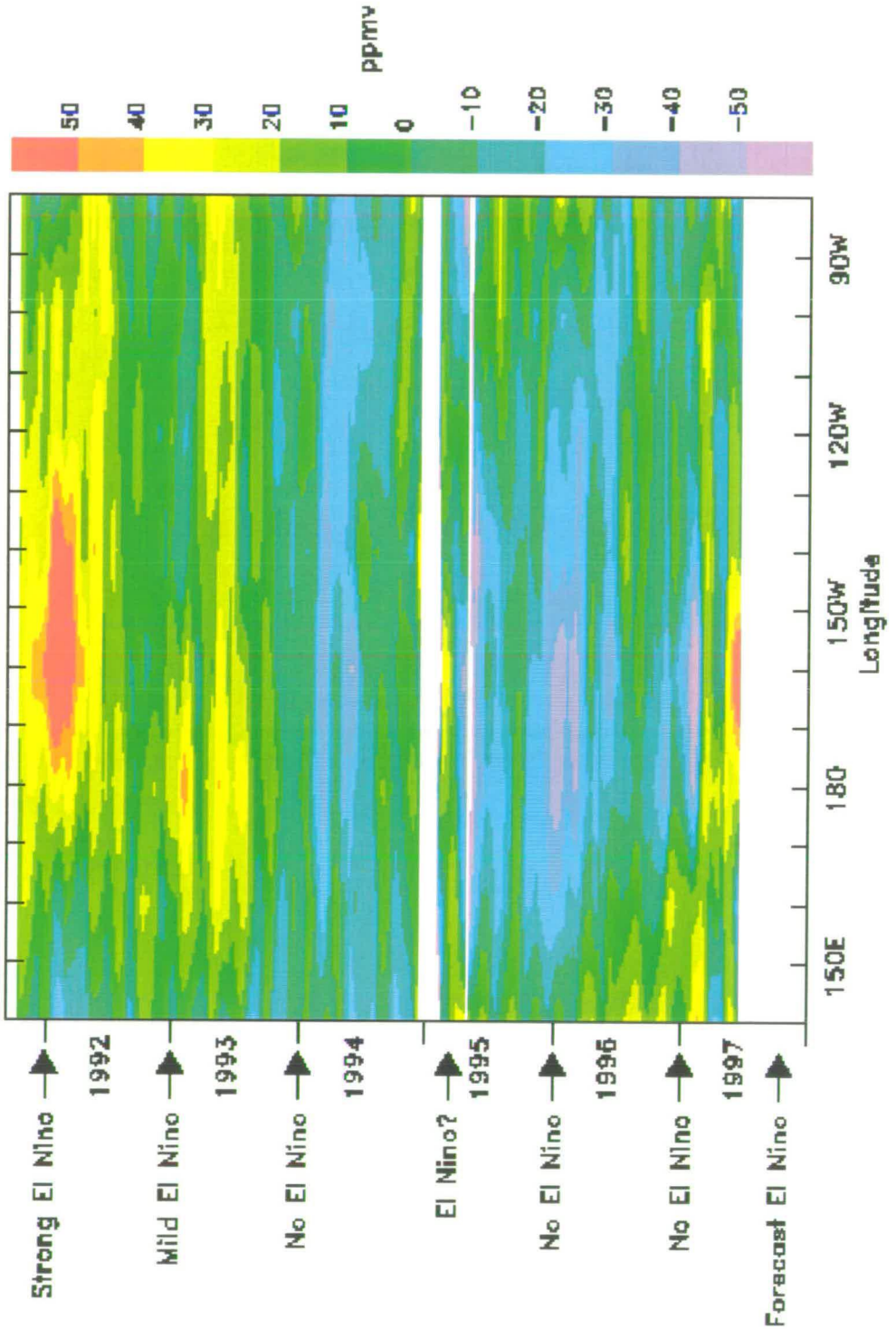

Figure 1.2: Tropical Upper Tropospheric water vapour anomaly from UARS MLS: correlation with El Niño events, figure prepared by Dr. W.G. Read

equivalent potential temperature making the environment more favourable for convection. This leads to warm wet summers. In winter, the situation is reversed with the surface low developing over the Indian ocean leading to cool dry conditions over the continent.

The Indian summer monsoon is influenced by the El Niño. Drought years in India are more common in El Niño years when the SST is higher in the central and Eastern Pacific and wet years are associated with anomalously cold La Niña conditions (e.g. Slingo, 1997). The Indian monsoon is also influenced by intraseasonal oscillations.

1.2.5 The Semi-Annual Oscillation

A semi-annual oscillation of zonal winds and temperature in the tropics and subtropics was noted by van Loon and Jenne (1969, 1970). The oscillation was observed between 100 hPa and 500 hPa and consists of westerly winds from April to June and from October to December, and easterly winds from January to March and from July to September. Their work was based on the analysis of 20 southern hemisphere radiosonde stations spanning 5 years. In a more recent paper, Shea *et al.* (1995) looked for the semi-annual oscillation using data from more radiosonde stations with greater time-spans and data from the European Centre for Medium Range Weather Forecasts (ECMWF). Like Van Loon and Jenne, they found a semi-annual variation in zonal wind and temperature with maxima occurring in April/May, and October/November. Upper tropospheric temperatures oscillate with opposite phase between the tropics and subtropics of the southern hemisphere and it was suggested by van Loon and Jenne (1970) that this is due to the upward branch of the Hadley circulation migrating across the equator.

Chen *et al.* (1996a) used upper-air wind data generated by the Global Data Assimilation System of the National Meteorological Center for 1986-1992 and suggested that the opposite phase relationship between eastern and western hemispheres is a response to the difference in cumulus convection between the Asian-Australian monsoon region (60°E - 120°W) and the extra Asian-Australian monsoon region (120°W - 60 °E) and associated with land-sea contrasts.

1.2.6 The Madden-Julian Oscillation

The Madden-Julian oscillation (MJO) is an intraseasonal oscillation affecting both atmosphere and ocean. It was first observed in 1971 by Madden and Julian (1971) as a quasi-periodic fluctuation in zonal winds over Canton Island (2.8 °S, 171.7 °W). There is now a wide variety of observational evidence in support of the oscillation reviewed by Madden and Julian (1994). The MJO accounts for a great deal of the variability in the tropics and because of its association with convection, it is useful in medium- and long- range weather forecasting in the tropics. Its influences reach beyond the tropics and it can be important for medium- and long- range weather forecasting in the extra-tropics (Ferranti *et al.* 1990; Lau and Chang, 1992). Much more will be said about the Madden-Julian oscillation when it forms the basis of chapters 4 and 5.

1.3 Summary

The response of climate to increases in anthropogenic greenhouse gases depends on the water vapour feedback. Generally this is believed to be positive with increased global temperatures leading to an increase in water vapour and therefore to an increase in warming. Lindzen (1990) suggested that some of this warming may be offset by the upper troposphere becoming drier through increased subsidence. More recent studies (Chou, 1994; Soden, 1997; Spencer and Braswell, 1997) show that some debate still surrounds this issue. Much of the uncertainty is due to the lack of adequate global water vapour measurements in the upper troposphere. The tropics play a central role in this debate as it is here that the deep convection and detrainment takes place. It is in the tropics that water vapour measurements are particularly crucial.

Global water vapour measurements are essential, not only to determine the feedback role of water vapour, but also to improve the ability of general circulation models to predict climate change, to enable the parameterisation of clouds in general circulation models and to help the understanding of upper tropospheric chemistry. In addition it has an important use as a tracer for the study of stratosphere-troposphere exchange.

Phase changes of water also drive the atmospheric circulation in the tropics.

Localised diabatic heating can excite equatorial waves which may induce a remote response in the circulation. Changes in the tropics have an influence beyond the tropics and studies of water vapour in the tropics can aid medium- and long-range weather forecasting in the extratropics.

The reasons for the study of water vapour in the tropical upper troposphere and lower stratosphere have been outlined in this chapter. The next chapter describes the methods available for obtaining the required measurements.

Chapter 2

Measurement of Water Vapour

The requirement for comprehensive and accurate water vapour measurements for understanding the climate system was illustrated in the previous chapter. Here, the attempts to obtain these measurements will be outlined, with particular reference to measurements in the upper troposphere and lower stratosphere and the importance of satellites.

2.1 *In Situ* Measurements

Historically, large scale humidity investigations have relied upon the use of radiosondes, supplemented by aircraft and surface studies. One of the main problems with radiosonde data is that they are not global in coverage. Measurements are made primarily over land and there are large data gaps over the oceans. Although there are long records of radiosonde data available, they are by no means homogeneous due to changes in instrumentation and reporting practices throughout time. Predictions of climate change are therefore based upon an inconsistent set of data. Elliot *et al.* (1990) believe that despite these changes, it is possible to use records of data from the surface to 500mb to detect climatic trends.

Measuring water vapour in the upper troposphere using radiosondes is particularly difficult because performance deteriorates in cold, dry conditions. Elliot and Gaffen (1991) examined and analysed radiosonde precision, instrument changes and reporting practices and concluded that the determination of a water vapour climatology was difficult due to poor sensor response in low temperatures and low accuracy in cold, dry conditions. Further to this they state that data above 500 hPa are not reliable for drawing conclusions about upper tropospheric hu-

midity.

In addition to radiosonde measurements, aircraft studies can be used. The aircraft carry Lyman-α hygrometers, which obtain water vapour mixing ratio data from a fluorescence signal. The hygrometer uses a beam of 121.6nm photons to dissociate water vapour into a hydrogen atom and a hydroxyl free radical in an electronically excited state. The excited free radical will fluoresce at a wavelength of 309nm or collide with and be deactivated by air molecules (Kelly *et al.* 1993). The signal is proportional to the number of water vapour–photon collisions and therefore to the concentration of water vapour. Horizontal profiles are obtained at a constant altitude. The flying altitudes can be chosen so data is more readily available in the upper troposphere than radiosonde data, and since the areas of coverage can be chosen and are not limited to radiosonde stations, data can be obtained in a wider variety of places. Flights are short and infrequent and so data are limited in both a temporal and spatial extent.

2.2 Satellite Measurements

Water vapour has an intense, fundamental vibration-rotation band, centred at $6.3\mu m$. It occurs in a spectral region which is fairly free from contamination by overlapping absorption lines from other molecules. Being close to the peak of terrestrial radiation, it is important in radiative transfer and many satellites make use of this to measure water vapour quantities.

The radiance received at the satellite in the $6.3\mu m$ absorption band can be associated with a 'brightness' temperature derived from the Planck function. Brightness temperature is a measure of the radiance emitted by the atmosphere and therefore by the water vapour so it can be used to indicate the amount of water vapour. Brightness temperature depends upon the temperature of the top few millimetres of precipitable water in the troposphere. If the upper troposphere is dry, radiation can escape from deeper in the atmosphere and this results in a higher brightness temperature. The relationship between $6.3\mu m$ brightness temperature and relative humidity can be seen in fig 2.1. The feasibility of using satellite observations in the $6.3\mu m$ absorption band for calculating upper tropospheric water vapour has been demonstrated for Meteosat by Schmetz and Turpi-

enen (1988), for GOES by Soden and Bretherton (1993) and for the television infrared observation satellite, operational vertical sounder, (TOVS) by Salathé and Chesters (1995).

These three satellites use brightness temperatures to infer relative humidities. The channel on GOES and TOVS is centred at $6.7\mu m$ and is sensitive to water vapour in a layer from 500 to 200mb. Data from TOVS have been archived since 1979 and measurements over the entire earth are made every 12 hours. The Meteosat channel at $6.3\mu m$ is sensitive to a layer between 600 and 300mb. These layers vary according to temperature and moisture profiles and relative satellite viewing angle. The main drawback with these satellites is that the measurements suffer from cloud contamination. A cloud clearance algorithm must be used to remove clouds from the data and this often introduces errors.

The special sensor microwave imager (SSM/I) is a passive remote sensing microwave radiometer and measures upwelling radiation in four spectral channels at 19, 22, 37, and 85 GHz. The microwave emission at 22 GHz increases with precipitable water and the amount of atmospheric water vapour is found by comparing the brightness temperature at 22 GHz with those at 19 and 37 GHz (Soden and Bretherton, 1994). Measurements of total precipitable water are obtained by this method and because of this, values are dominated by water vapour in the lower troposphere and have less relevance to the upper troposphere. Values are strongly linked to sea surface temperature. The measurements have uncertainties of typically 2 to 3 kgm^{-2}. The advantage of microwave instruments is that upwelling radiation is insensitive to scattering by clouds. The disadvantage is that the data are contaminated by land and sea-ice.

The stratospheric aerosol and gas experiment 2 (SAGE II) (Rind *et al.*, 1993) is a solar occultation instrument. Vertical distributions of water vapour are inferred by measuring the extinction of solar radiation. About 30 profiles are obtained daily from heights of 50 km to cloud top. Half the measurements are made at sunrise at one latitude, and half at sunset at another latitude. Measurements are separated by about 24° in longitude.

Advantages of SAGE II are that it has a good vertical resolution of approximately 1 km. It is also self calibrating since all observations are continually compared with solar radiation from outside the atmosphere. The main disad-

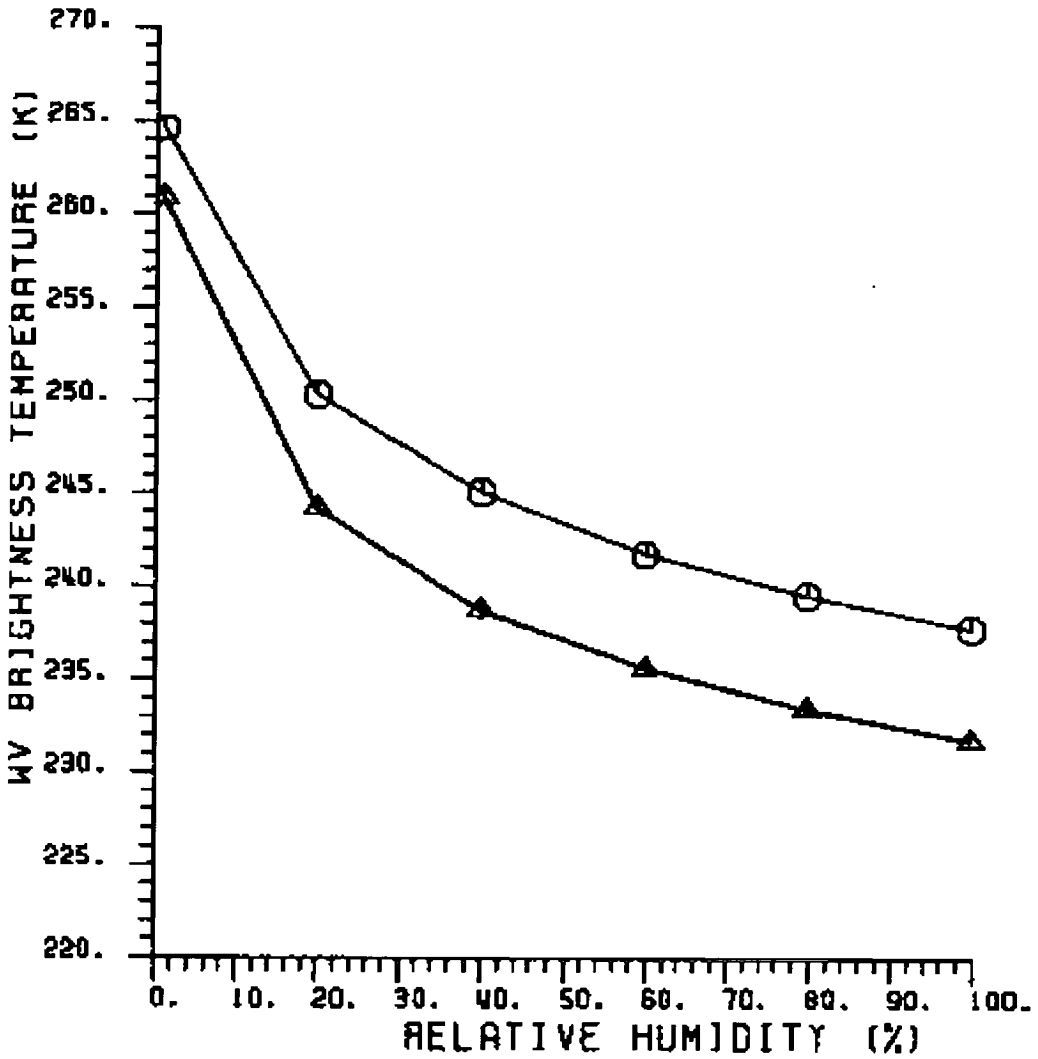

Figure 2.1: Water vapour brightness temperature as a function of relative humidity of the upper troposphere (600 to 300 hPa) for a tropical standard atmosphere and zenith angles of 0^o (octagons) and 62.7^o (triangles), Schmetz and Turpeinen (1988)

.

vantage is that measurements are limited in cloudy regions (Rind *et al.*, 1993) and therefore SAGE II data tends to have a dry bias compared with microwave instruments and radiosondes.

2.3 The Upper Atmosphere Research Satellite (UARS)

The Upper Atmosphere Research Satellite carries ten instruments designed to study chemical and dynamical processes in the upper atmosphere. It was launched on September 12th 1991 and is still operational to the present day. The UARS satellite is in an almost circular orbit at an altitude of 585 km and an inclination of 57^o to the equator. It makes about 14 orbits a day. The UARS mission is described in more detail by Reber, (1993). Among the instruments on UARS, there are 4 which measure water vapour, primarily in the stratosphere; the Improved Stratospheric and Mesospheric Sounder (ISAMS) (Taylor *et al.*, 1993), the Cryogenic Limb Array Etalon Sounder (CLAES) (Roche *et al.*, 1993), the Microwave Limb Sounder (MLS) and the Halogen Occultation Experiment (HALOE). Water vapour measurements from the latter two are used in this thesis and are described in more detail in the two sections which follow.

2.3.1 The Microwave Limb Sounder (MLS)

MLS makes a limb scan perpendicular to the UARS orbit path from a tangent height of 90 km to the surface. Each scan takes 65.5 seconds and consists of a profile of measurements which, in versions 3 and 4, are retrieved onto 3 levels per decade change in pressure i.e. about every 5-6km.

MLS provides a 3 km field of view in the vertical. Latitudinal coverage changes from between 80^oN and 34^oS to 34^oN and 80^oS about every 36 days due to the satellite making a yaw manoeuvre. An example of the ground-track and coverage is shown in figure 2.2 for each yaw direction. The MLS instrument is described in more detail by Barath *et al.*, (1993) and the measurement technique by Waters (1993).

The primary aims of MLS were to measure pressure and temperature over an altitude range of 30-60 km, ozone between 15-80 km, chlorine monoxide over 25-

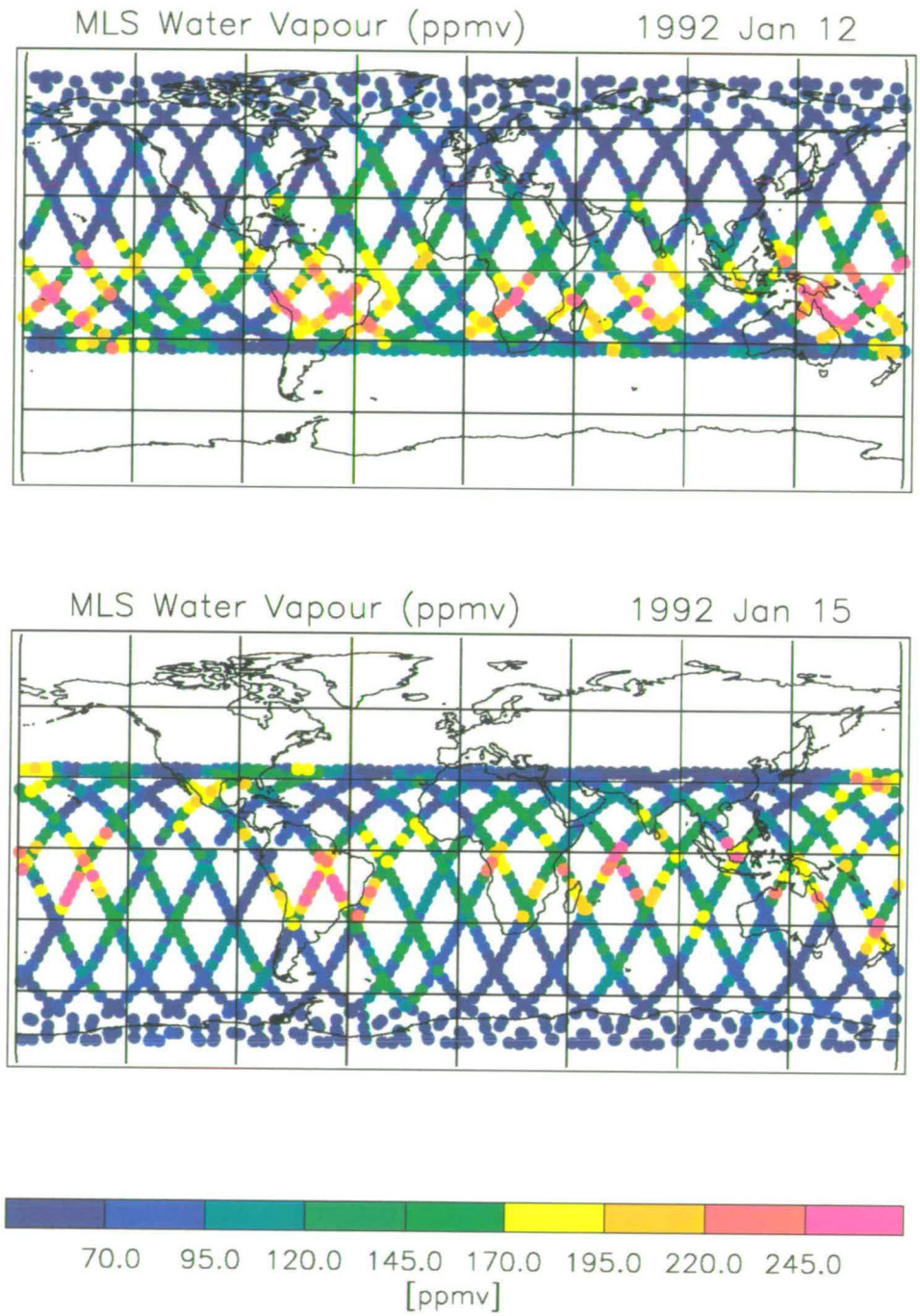

Figure 2.2: MLS footprint positions for north (top) and south (bottom) viewing directions.

45 km and water vapour from 15-85 km. These measurements are made with 3 radiometers sensitive to radiation from the emission lines of the above species. The 63 GHz radiometer captures radiation from the 62.998 and 63.569 GHz emission lines of oxygen. The 205 GHz radiometer measures chlorine monoxide from the emission line at 204.352 GHz and ozone from the emission line at 206.132 GHz and the 183 GHz radiometer measures water vapour and ozone from the transitions at 183.310 and 184.37 8GHz respectively (Barath *et al.*, 1993). Water vapour measurements from MLS have been validated by Lahoz *et al.*, (1996).

The MLS water vapour retrieval is constrained by '*a priori*' information based on a monthly climatology from SAGE II (Pumphrey *et al.*, 1998). The assumed *a priori* uncertainty is set at 2 ppmv throughout the stratosphere. Each MLS measurement has an associated 'error ratio', the ratio of the estimated uncertainty to the *a priori*. When the error ratio exceeds 0.5 the data is flagged as negative, indicating that the climatology contributes more than 25% of the retrieved mixing ratio. This occurs frequently below the 46 hPa level (Lahoz *et al.*, 1996) when the atmosphere becomes optically thick and its opacity exceeds a certain 'opacity criterion'.

Although the section of the limb at the tangent point usually has the greatest optical depth and contributes most to the detected microwave signal, this is not the case when the layers above the tangent point are opaque. The MLS retrieval uses the 'opacity criterion' to determine whether information is retrievable below a certain height (Lahoz *et al.*, 1996). The MLS retrieval algorithm assumes linearity and loses accuracy in regions where the atmosphere is optically thick and the radiative transfer equations become 'non-linear'. This puts a lower altitude limit on the available data. Normally, the opacity criterion is satisfied down to 46 hPa. Below 46 hPa the atmosphere becomes so optically thick that the retrieval fails the opacity criterion and the data is flagged as negative, implying a high dependence on the climatology.

At lower altitudes still, the wings of the 183 GHz emission line become so pressure broadened that no retrievals are possible with the 183 GHz radiometer due to its limited band width. The continuum emission from the wings of the 183 GHz emission line can be picked up by the 205 GHz radiometer. Hence, the upper tropospheric measurements used in this thesis come from the 205 GHz channel

and the lower stratospheric measurements at 68 and 100 hPa come from the 183 GHz channel where the retrieval is non-linear. The two sets of measurements are described in more detail below.

Upper Troposphere

As stated above, the 205 GHz channel on MLS is principally used to measure chlorine monoxide but it is sensitive to water vapour in the upper troposphere (or in the stratosphere when the tropopause is low in polar regions) where concentrations are in the range of 100 to 300 ppmv (Read *et al.*, 1995). The best sensitivity occurs when the water vapour concentration is about 150 ppmv and this most often occurs at the UARS pressure level of 215 hPa. 215 hPa corresponds to a height of about 12 km at low latitudes and about 11 km at high latitudes.

Previous publications relating to MLS water vapour have focused on the 215 hPa level. Some information is also available at 147 hPa and 316 hPa as this thesis will demonstrate in chapter 5. At all three levels (147, 215 and 316 hPa) the estimated uncertainty is 20% corresponding to mixing ratios of 8 ppmv at 147 hPa, 25 ppmv at 215 hPa and 125 ppmv at 316 hPa (Sandor *et al.*, 1998).

Retrievals in the upper troposphere may be affected by thick cirrus clouds. In the tropical region between 6 and 12 km the retrievals are not significantly affected, but at latitudes beyond 40° a significant fraction of the measured radiances may come from scattering by cirrus clouds (Bond, 1996). Ice crystals in cirrus clouds at a concentration of $0.1 \mathrm{gm}^{-3}$ over a horizontal distance of 120 km could contribute up to about 20% of the absorption coefficient at 215 hPa but will usually be less, and at concentrations less than 0.01 g m^{-3} the effect is negligible (Read *et al.*, 1995).

An improved MLS UTH retrieval has been developed which among other features, has a formal error estimation calculation, and has had some preliminary comparisons with the Vaisala thin film capacitive radiosonde measurements. The UTH product produced by this algorithm is now publically available. A nearly linear relationship between the new prototype UTH retrieval (not used in this thesis) and the current analysed product used in this thesis and described by Read *et al.*, (1995) has been found. The comparison was based on 62 representa-

tive days of the new prototype (21 days from June 8th to July 3rd 1994; 32 days from November 25th 1995 to March 1st 1996; and 9 other days between 1991 and 1995). The new prototype retrieval is much drier than the current analysed product, but because a linear relationship exists between the two, results based on relative values remain valid. For example, the 80-90 ppmv values presented by Stone *et al*, (1996) at 40-60°S and 215 hPa are 10-20 ppmv too moist but the wave pattern that they analyse remains valid (Sandor *et al.*, 1998). On a global average, the current analysed product at 215 hPa, used throughout this thesis, is biased high by 50-60 ppmv (everywhere) and has a precision of 5 ppmv (W. G. Read, personal communication, 1997). There is no reported validation of the 147 and 316 hPa data.

Lower Stratosphere

As described above, water vapour from the 183 GHz radiometer measures water vapour in the stratosphere at heights at and above 46 hPa or about 21 km, but below 46 hPa the retrieval becomes non-linear and the data is flagged as bad. A new non-linear retrieval (Pumphrey, 1999) extends measurements to two extra levels, 68 hPa and 100 hPa. Daily measurements (barring instrument failures) are available from 19th September 1991–22 April 1993. Some results of a preliminary version of this retrieval were used by Mote *et al*, (1996) who showed that the data at 100 hPa exhibits seasonal variations consistent with the tape recorder effect.

Comparisons between the present retrieval and profiles from balloon-borne frost-point hygrometers show that the retrieved measurements do make some improvement on the *a priori*. However, data at 100 hPa remain largely based on the *a priori*, a monthly zonal mean climatology from SAGE II (Pumphrey *et al*, 1998) and hence much data is flagged as negative. If however, the profiles were valid at the 46 hPa level and above, the retrievals were retained for the analysis in this thesis.

2.3.2 HALOE

HALOE (Russell *et al.*, 1993; Harries *et al.*, 1996) is a solar occultation instrument and measures water vapour in the lower stratosphere from near the tropopause to about 0.002 hPa with a vertical resolution of about 2 km. HALOE has been

making measurements from 12 October 1991 to the present day, making it a useful dataset for comparison with MLS 205 GHz measurements in the upper troposphere. At the beginning of the UARS mission however, the aerosol from the eruption of Mount Pinatubo prevented HALOE from measuring below 20 hPa. It makes 30 measurements a day, half at one latitude at sunset and half at another latitude at sunrise. Consequently, it is not possible to draw daily maps of HALOE data as it is with MLS, but as the orbit drifts, the observing latitude changes and global coverage builds up over the course of a few weeks. It takes between 8 and 14 days to cover the region 30°S–30°N. The latitude of the measurements is shown in figure 2.3.

2.4 The NVAP Dataset

The NASA water vapour project dataset (NVAP) has been developed by Randel *et al.*, (1996) using a blend of information from a variety of instruments, weighted according to their strengths and weaknesses. The data set is global in coverage and comprises observations from radiosondes, the Special Sensor Microwave Imager (SSM/I) satellite, and the Television InfraRed Observation Satellite, Operational Vertical Sounder (TOVS). It consists of values of total column water vapour, liquid water path and layered water vapour for three atmospheric layers, the three layers being 500 to 300 hPa, 700 to 500 hPa and surface to 700 hPa. Data is daily and available from 1988 to 1992.

Data from radiosondes, SSM/I and TOVS were gridded with a 1^o by 1^o resolution. Radiosonde profiles were considered to be the most accurate and given a weighting of 100%. A 10% weighting was given to TOVS and 90% to SSM/I. Data were spatially interpolated onto any regions with missing data that were smaller than a specified size. Larger areas of missing data were filled with a three day running average.

The data were subject to a quality control in which the performance of each instrument was assessed with respect to certain criteria. Each radiosonde sounding consists of pressure, dew-point depression and temperature measurements. A sounding was only retained if these three measurements at surface, 850 and 700 hPa pressures were present and within acceptable limits. If the sounding

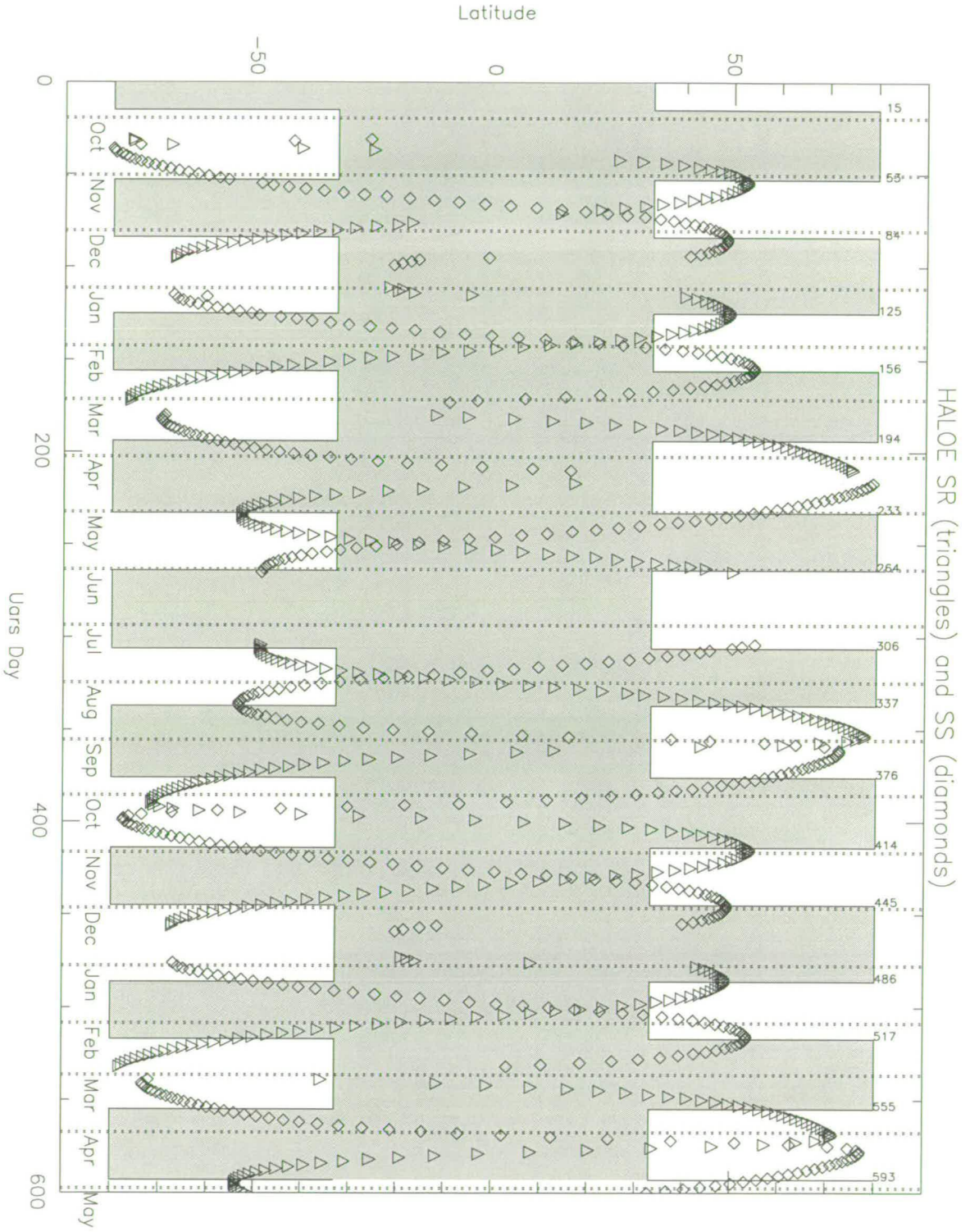

Figure 2.3: The average latitudes of HALOE measurements. Sunrise measurements are indicated by triangles and sunset measurements by diamonds. The shaded region indicates the latitudes covered by MLS measurements over the same periods. (Figure prepared by Dr. H C Pumphrey.)

failed a test at one of the levels, that particular level was ignored but the rest of the sounding retained. The variation in the construction of different radiosondes used globally can cause some biased measurements. Problems with SSM/I data are contamination by land and by sea-ice. High values often occur over small island areas which have not been covered with a land mask. High values resulting from contamination are a problem around polar coastal regions. Areas such as the shorelines of Antarctica, Greenland, Siberia and Japan are particularly prone. The infrared sensor on TOVS cannot measure the moisture in the entire column in cloudy regions. Cloud contaminated points are removed and this introduces a dry bias.

It is total column water vapour that is used in this thesis. This is the depth of water that would occupy a unit of a tube at standard atmospheric temperature and pressure if all the water vapour in a column of air was condensed. In this case, the column of air is between 300 and 500 hPa. Total column water vapour is dominated by the water vapour at the lowest level since temperature decreases with height and saturated vapour pressure decreases exponentially with temperature.

2.5 ECMWF data

Data from the European Centre for Medium Range Weather Forecasts (ECMWF) re-analysis project are used in this thesis. The parameters, temperature, geopotential height, relative humidity, zonal and meridional wind components and vertical velocity are produced on a 2.5^o by 2.5^o grid on 19 pressure levels. The initialised data used here, have had gravity waves suppressed.

2.5.1 ECMWF Humidity Analysis

The input for the humidity analyses is based on surface and radiosonde measurements and from TOVS temperature and precipitable water profiles. Only radiosonde observations from below 250 hPa are used in the assimilation because they are not considered accurate enough at the low temperatures and humidities above this height. TOVS data between 1000 and 300 hPa are also assimilated.

Salathé and Chesters (1995) used TOVS satellite observations to evaluate mois-

ture analyses from ECMWF. It should be noted that the TOVS radiances and the ECMWF analysis are not strictly independent but greater weight is given to the forecast fields than to the satellite data so real data have a limited impact on ECMWF analyses. Upwelling radiances were calculated for the $6.7\mu m$ water vapour band at 300 hPa from the ECMWF model and compared with the corresponding TOVS observations. Monthly mean maps of brightness temperatures were examined for regional patterns and temporal variations. They found that the model reproduced the general locations and the seasonal variations in moisture observed by TOVS. The contrast in brightness temperatures calculated by the model were not as strong as those observed by TOVS suggesting that the ECMWF analysis underestimates the strong moisture contrast between convective and subsidence zones. The contrast was enhanced when an improvement was made to the convective parameterisation of the model. The response of the ECMWF computed brightness temperatures to the changes in convective parameterisation highlighted the sensitivity of upper tropospheric moisture to convection.

Soden and Bretherton (1994) calculated total precipitable water (TPW) from ECMWF which they compared with TPW from SSM/I. Primary features of monthly mean TPW and its seasonal variation were captured well. The ITCZ, Western Pacific maximum and the positions and intensities of moisture over the extratropical oceans also agreed well with observations. The main differences occurred over dry subtropical ridges off the west coasts of continents where the analysis was 1.5-2 times moister than observed.

Soden and Bretherton also calculated the brightness temperatures from the ECMWF model and compared them to the observed brightness temperatures from GOES. Like Salathé and Chesters, they found that the ECMWF model simulated the general features of moisture distribution quite well, but was not very good at representing the strong gradient between the moist convective regions and dry subsiding regions of the Hadley cell, being too dry in the tropics (ascending) and too wet in the subtropics (descending). This suggests that the strength of the Hadley circulation is under-estimated by the model.

Schmetz and van der Berg (1994) compared the monthly mean brightness temperature observations from the water vapour channel on Meteosat (5.7- $7.1\mu m$)

with brightness temperatures calculated by ECMWF. The model was found to simulate large scale features of upper tropospheric moisture well but was too moist in the subtropics and too dry in the convective regions of the ITCZ. In descending branches of the Hadley cell, predicted brightness temperatures are lower than observed by more than 6K i.e. moister than observed by Meteosat. This could be due to the strength of the Hadley cell being under estimated as suggested by Soden and Bretherton (1994).

Vespirini (1998) compared ECMWF operational analyses from August 1992–November 1994 with SSM/I data. In the tropics she found that the analysis depends on model representation of convective processes as did Salathé and Chesters, (1995). The ECMWF model has too strong a meridional circulation bringing down too much dry air in the descending branch. The South Pacific Convergence Zone (SPCZ) tends to remain much more well marked in the ECMWF model than in observations particularly in 1994. This causes a large deficit in moisture of around 40-60% compared with SSM/I. The position of the ITCZ remains around 10°N in the east Pacific and subsidence is either too strong or too close to the core of the ITCZ.

Dry tongues off the western coasts of subtropical continents have too much moisture in the southern hemisphere of the ECMWF model by 30-50%. This is not due to the model itself but to the biased data. Mid-latitudes are too moist by 20-30% and there is a general excess of about 20-30% moisture at large distances from land such as in the mid-Pacific and Atlantic oceans in both northern and southern hemispheres.

Chaboureau *et al.*, (1998) compared total water content from TOVS to SSM/I, NVAP and ECMWF analysis. In maritime stratocumulus cloud (msc) regions which are located off the coasts of California, Mauritania (NH) and Angola (SH), TOVS and ECMWF overestimate TPW compared with SSM/I. This may be because TOVS rejects situations when cloud cover is greater than 60% whereas SSM/I measures all the time. Therefore, long-term trends from TOVS are composed of only a few observations whereas SSM/I uses all the observations. Between 30°N and 30°S, excluding msc regions, there is good agreement between ECMWF and TOVS and SSM/I. At higher latitudes, ECMWF estimates exceed SSM/I by more than 10% and SSM/I exceeds TOVS by 10-20%. Chaboureau

et al., (1998) conclude that the true precipitable water content lies between the estimates given by TOVS and SSM/I.

Chaboureau *et al.* also looked at average water vapour content in various layers. In the 1000-700 hPa layer and msc region, TOVS and ECMWF display values greater than NVAP analyses but in the tropical band, TOVS is smaller than ECMWF and NVAP. In the 700-500 hPa layer in the ITCZ region, TOVS is larger than NVAP or ECMWF. Between 500-300 hPa, ECMWF underestimates precipitable water content compared with the other datasets. ECMWF and NVAP are too dry over the oceans.

Comparisons between ECMWF and measurements taken *in situ* by a frost-point hygrometer during several aircraft flights (Ovarlez and vanVelthofen, 1997), showed that in the upper troposphere, model mixing ratios were generally larger than the measured ones. This is probably a result of the poor performance of hygrometers in the upper troposphere. In regions where the observed mixing ratios were less than 20 ppmv, and throughout the stratosphere, the model generally over-predicted the mixing ratios. Ovarlez and vanVelthofen conclude that despite the quantitative differences, many of the small scale features were well represented by the model.

Overall, it seems that the ECMWF model is able to capture the general distributions of upper tropospheric water vapour as observed by satellites but underestimates the strength of the Hadley circulation, predicting convective regions of the tropics to be too dry and subsidence regions of the subtropics to be too moist.

2.6 Summary

Satellite observations are vital in the accumulation of global water vapour data due to the limited global coverage of radiosondes and their imprecision and inaccuracy in the upper troposphere. Satellites provide a better way to achieve greater spatial and temporal coverage.

The 205 GHz channel on MLS is sensitive to water vapour in the upper troposphere, and the new non-linear retrieval from the 183 GHz channel extends stratospheric measurements to lower levels than were previously available. With a 3 km field of view in the vertical, MLS has greater vertical resolution than that

of infrared instruments such as Meteosat, GOES and TOVS which are sensitive to water vapour in a broad layer of the upper troposphere about 300 hPa thick. The MLS measurement of upper tropospheric humidity (UTH) is relatively insensitive to cirrus clouds, giving it additional advantages over infrared techniques.

MLS provides near global coverage on a daily basis (excepting failures of the instrument). Its coverage is better than that of solar occultation instruments such as SAGE II and HALOE, from which measurements are limited to about 30 per day over a limited latitude range.

The upper tropospheric water vapour product from MLS is relatively new. Comparison with other data is a useful means by which to validate the MLS data. The NVAP dataset described here is one such data-set where there are daily fields coinciding with the first few months of the UARS mission. Although NVAP consists of column integrated precipitable water, it can still serve as a useful indicator of the validity of the MLS measurements. The next chapter describes the water vapour fields from MLS and NVAP and accounts for the differences between them.

Chapter 3

The Water Vapour Field

In the previous chapter a brief outline of the instruments used for accumulating water vapour data was given. This chapter provides an overview of the known water vapour field in the upper troposphere as determined by previous measurements, and assesses the ability of MLS to reproduce the main features of the field. The credibility of the measurements is discussed through a comparison with the NVAP dataset. The success of the ECMWF model in simulating the known features of the water vapour field is also assessed.

3.1 Spatial Distribution

3.1.1 Zonal Patterns

The Hadley circulation involves rising air over the warm tropics and descending motion in the cooler subtropics. Its effects upon upper tropospheric water vapour have been widely noted and can be clearly seen here in upper tropospheric water from MLS and in total precipitable water (500-300 hPa) from NVAP (see figures 3.1 and 3.2 respectively), which show seasonal averages for NH winter, December–February (DJF) and NH summer, June–August (JJA). The zonal structure attributable to the Hadley circulation is evident with mixing ratios and TPW amounts decreasing from their maximum values in the tropics, to minimum values at the poles. Read *et al.*, (1995) and Elson *et al.*, (1995) have previously noted these features in the MLS dataset. Water vapour brightness temperatures from TOVS (Salathé *et al.*, 1995) and from the GOES 6.7μm channel for July 1987 (Soden and Bretherton, 1993), show a similar zonal structure, (see figure

3.3) as do eight years of globally averaged HIRS/2 data (Wu *et al.*, 1993) and Meteosat data for July 1992 (Schmetz and van der Berg, 1994).

The large scale ascent in the Hadley circulation is marked by a narrow band of deep cumulus convection which extends across the tropics, known as the inter-tropical convergence zone (ITCZ). This is well pronounced in figure 3.1 as a band of water vapour mixing ratios of 145–185 ppmv lying just north of the equator in JJA and just south of the equator in DJF. The ITCZ can be seen to be particularly strong in the Indian and Pacific Oceans during DJF whereas in the Atlantic ocean and Eastern Pacific it is less well marked.

The ITCZ is also well pronounced in the NVAP field (fig. 3.2), marked by a narrow band of TPW $\sim$ 2.5mm. In northern winter it is well defined over the Indian and Pacific Oceans but peters out over the Eastern Pacific and Atlantic. In JJA, it stretches almost unbroken around the world. Again, it lies mostly north of the equator in northern summer and mostly south of the equator in northern winter.

A time-series of zonal means is shown for MLS in figure 3.4a. Due to the satellite yaw manoeuvre, latitudes beyond 32° are only observed for about 36 days at a time leading to the periodic gaps in the time-series of about 36 days in duration. The time-series illustrates the annual migration of peak mixing ratios across the equator following the movement of the ITCZ. The highest values are found furthest north in August and furthest south in February.

This displacement of the peak values towards the summer pole is in agreement with observations from HIRS/2 (Wu *et al.*, 1993) and with Elson *et al.*, (1995) who found that peak values follow the sun with a two month lag. Sandor *et al.*, (1998) found this to be the case in the new version of the MLS UTH retrieval. Results from the NVAP dataset for the same time period as MLS and covering the latitude range from 90°N to 90°S are presented in figure 3.4b. The seasonal migration of peak TPW values follows that of UTH, with the peak in the northern hemisphere occurring in August and for the southern hemisphere in February.

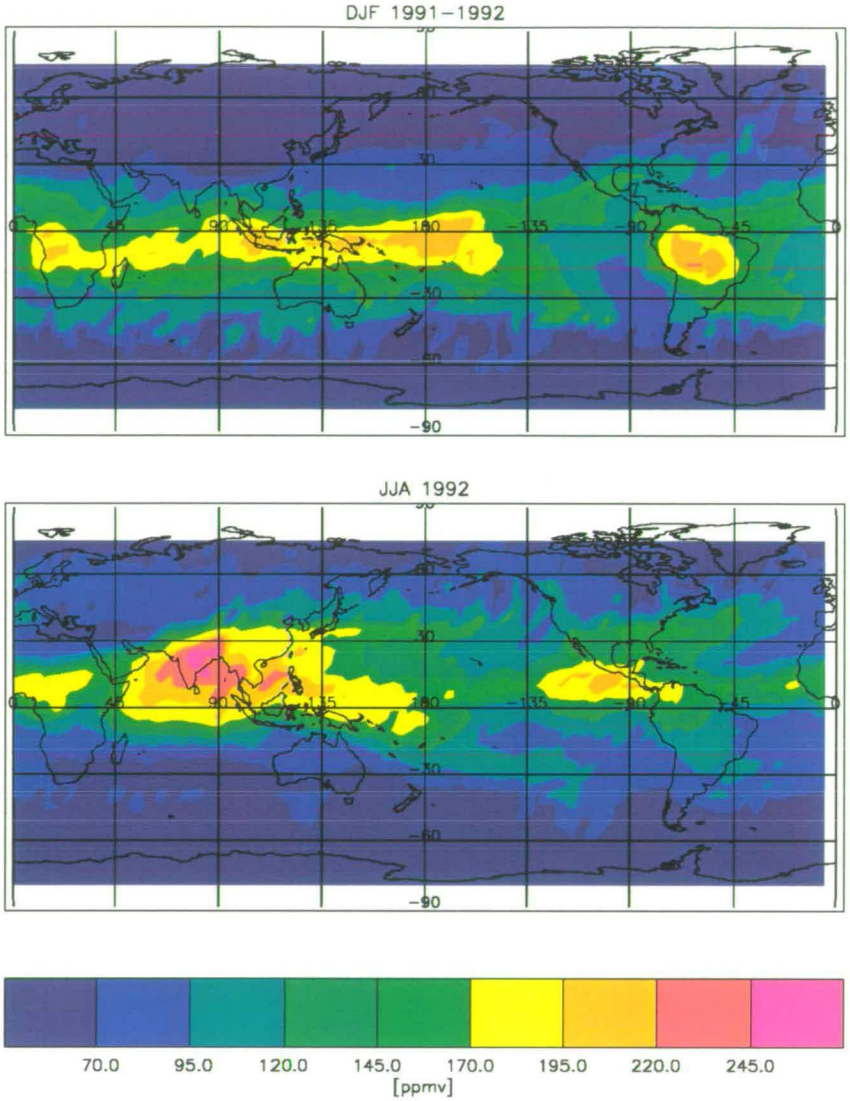

Figure 3.1: Seasonally averaged MLS water vapour (ppmv) at 215 hPa for December–February 1991/2 (DJF) and June–August 1992 (JJA).

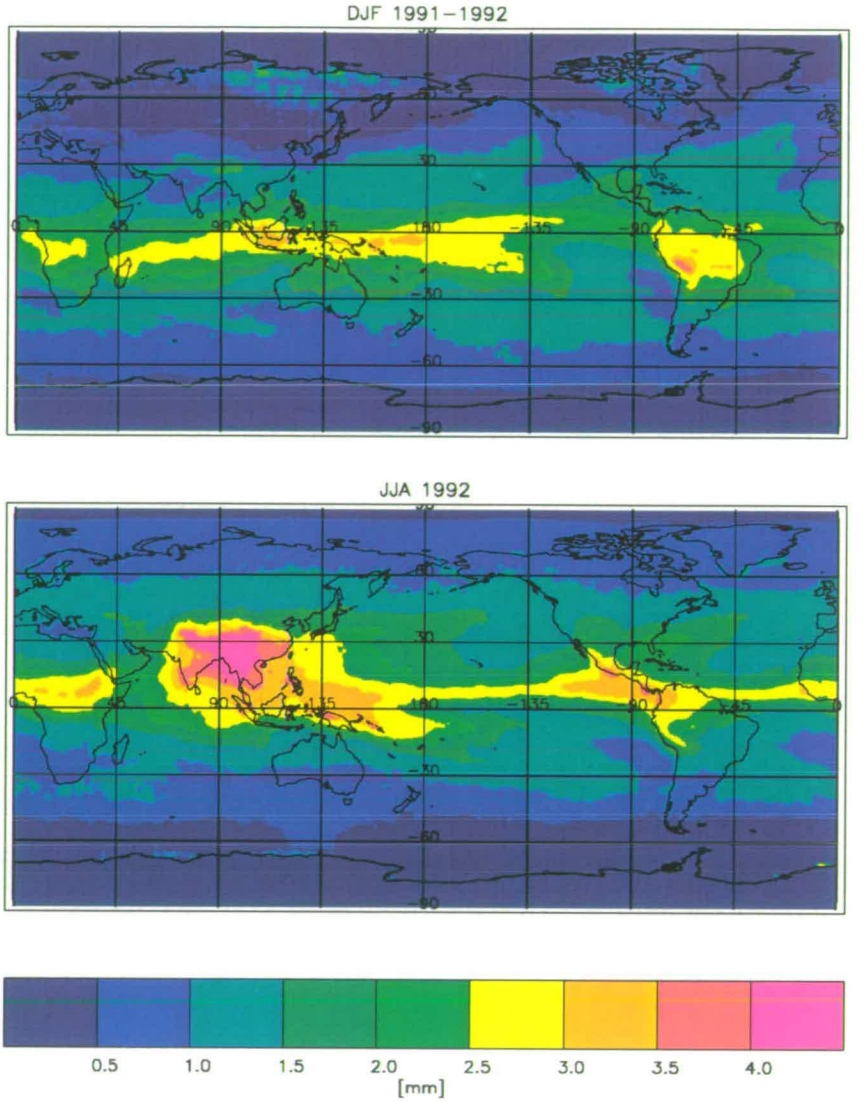

Figure 3.2: Seasonally averaged NVAP total precipitable water (mm) in a column from 500-300 hPa for December–February 1991/2 (DJF) and June–August 1992 (JJA).

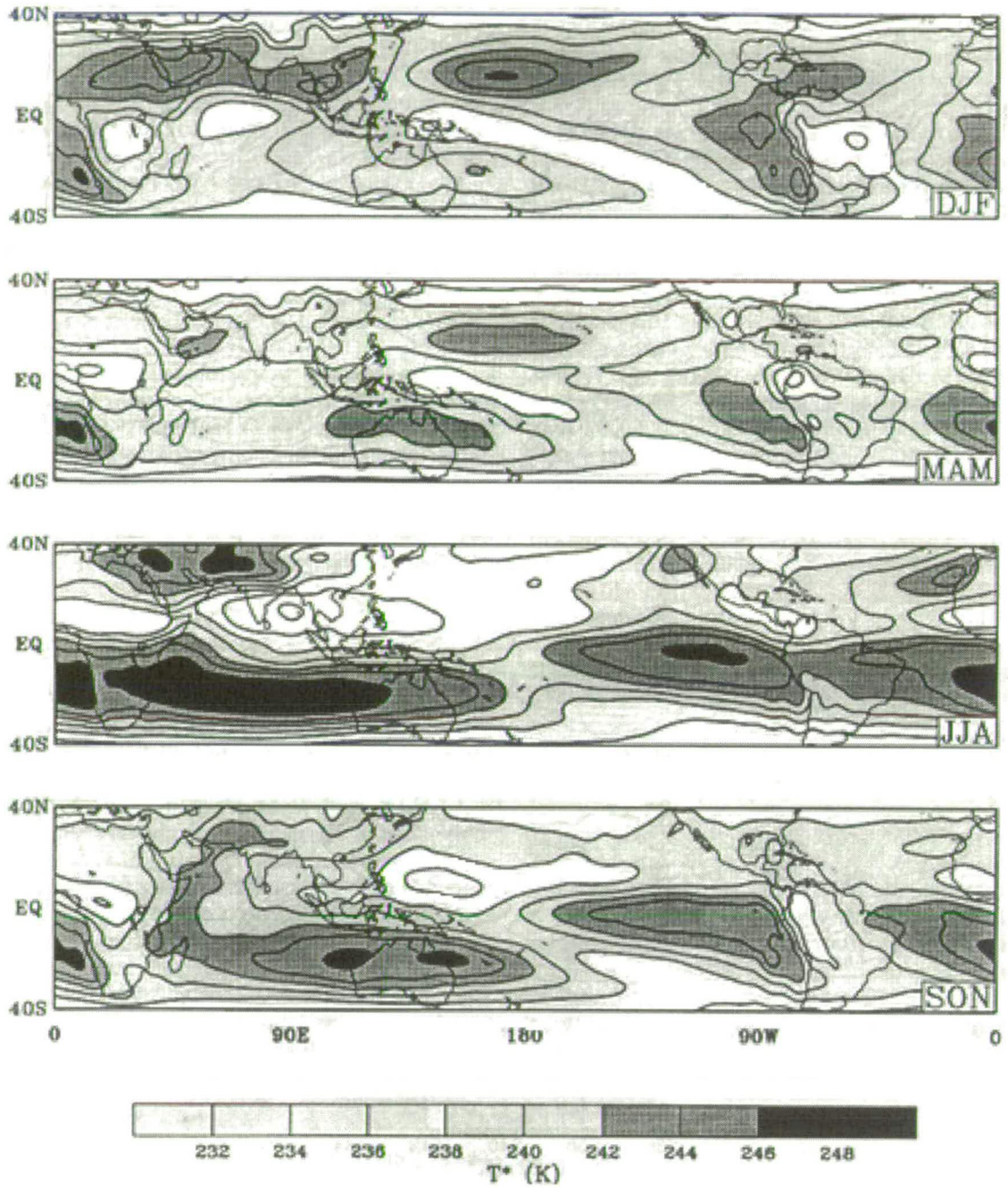

1979-1988 Observed Brightness Temperature

Figure 3.3: The 1979-1988 seasonal average brightness temperatures observed by the TOVS water vapour channels. High values of brightness temperature indicate regions of dry upper troposphere, (Salathé *et al.*, 1995)

.

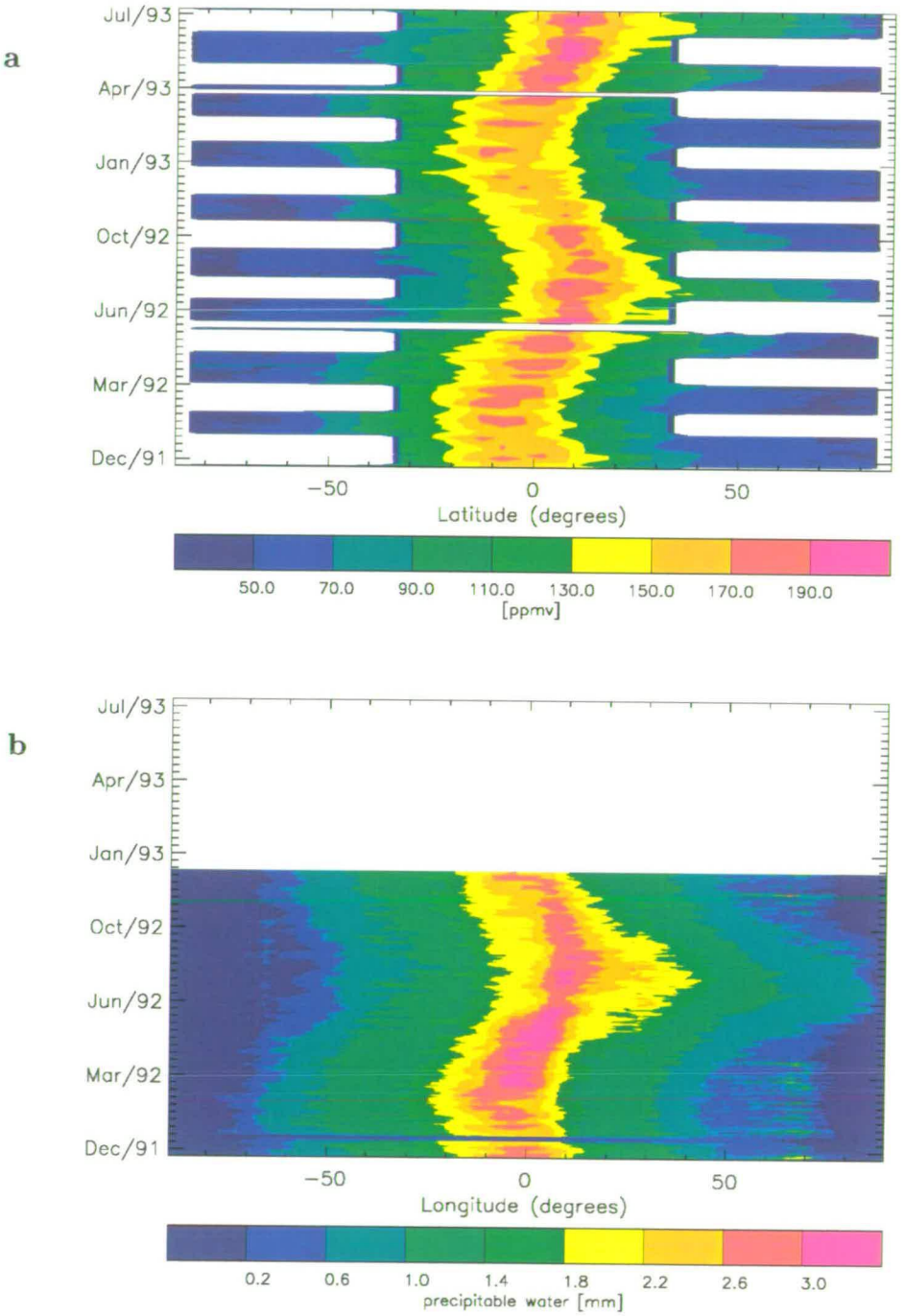

Figure 3.4: Time-series of zonal mean **a)** MLS mixing ratios at 215 hPa (ppmv) and **b)** NVAP total precipitable water 500-300 hPa (mm).

a

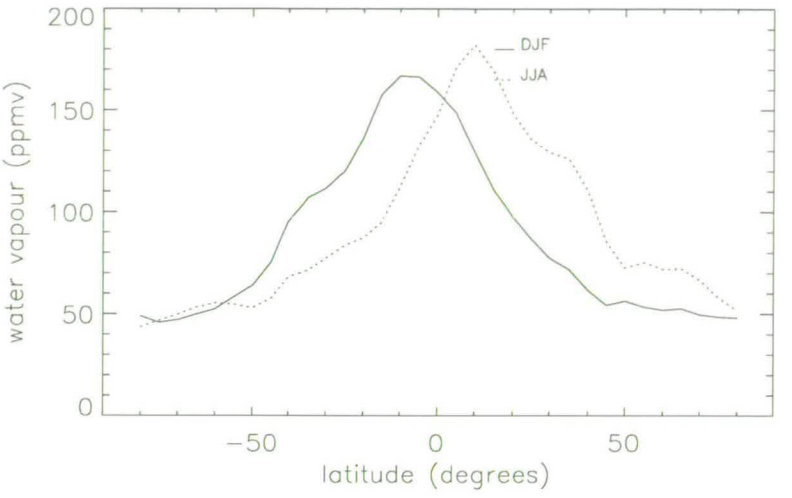

b

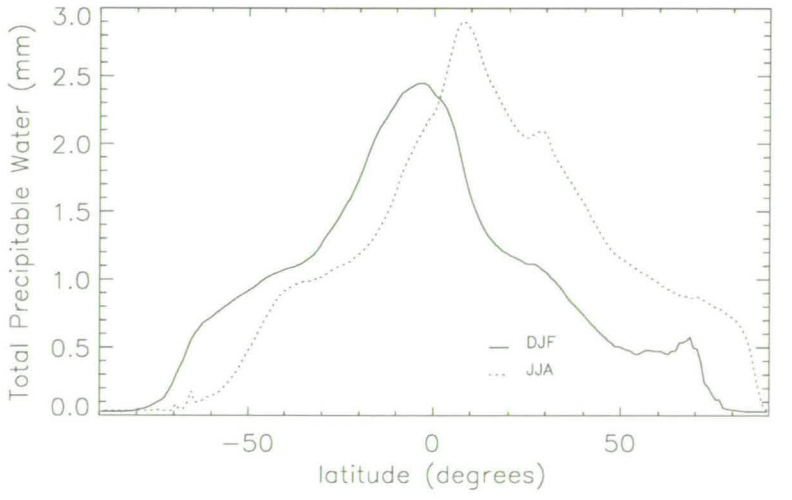

Figure 3.5: Seasonal zonal mean for southern hemisphere summer (DJF) (solid line) and northern hemisphere summer (JJA) (dotted line) for **a)** MLS mixing ratios at 215 hPa (ppmv) and **b)** NVAP total precipitable water 500-300 hPa (mm).

3.1.2 Hemispheric Asymmetries

The summer hemisphere is moister due to the increased convection moistening the summer hemisphere and increased subsidence drying the winter hemisphere. A seasonal comparison of July and January tropospheric moisture from the Stratospheric Aerosol and Gas Experiment (SAGE II) over a five-year period presented in Rind *et al.*, (1991), showed that the specific humidity (mass of water vapour per unit mass of moist air) is higher in both northern and southern hemisphere summers compared to their respective winter values. Soden and Bretherton (1994) point out that the seasonal asymmetry in dryness between northern and southern hemispheres in July and January reflects the increased strength of Hadley cell subsidence over the winter hemisphere. Salathé and Chesters (1995), in agreement with Soden and Bretherton state that the driest regions form in winter under subsiding branches of the circulation.

The seasonal map of NVAP data (figure 3.2) clearly shows that the hemisphere as a whole is moistened in the respective summer. Values of 1–1.5 mm reach 60°N in NH summer but do not reach the equivalent southern latitude in SH summer. This hemispheric moistening is also revealed by the seasonal zonal means for DJF and JJA in figure 3.5. In the MLS zonal mean, the JJA peak mixing ratio is higher than the DJF peak by 10 ppmv and in NVAP by 0.5 mm. As a whole, the hemispheric moistening, indicated by the difference between the solid and dotted lines, is stronger in the northern hemisphere than in the southern and the effect is more noticeable in NVAP (fig. 3.5b) than in MLS (fig. 3.5a). The effect being more noticeable in NVAP data than MLS could be a result of the contribution to the NVAP TPW from 500 hPa and may suggest that these lower altitudes have more seasonal variation than the higher altitudes.

Kelly *et al.* (1991) noticed an asymmetry of upper tropospheric water vapour during winter between the northern and southern hemispheres measured by a Lyman-α hygrometer on board a DC8. Profiles of water vapour were obtained in the upper troposphere above three sites in the northern hemisphere from August to September 1987, and three sites in the southern from December 1988 to February 1989. Figure 3.6 shows a profile for the southern hemisphere and one for the northern; these are the profiles that contained the greatest number of

observations. The profiles showed the troposphere in middle, subpolar and high latitudes to be a factor of 2 to 4 times or 10 ppmv drier in southern hemisphere winter than northern hemisphere winter.

Douglas (1997) used the UK Universities Global Atmospheric Modelling Programme (UGAMP) GCM model to calculate water vapour mixing ratios for each of the three sites. The mixing ratios were calculated at 215 hPa (the central height of Kelly's profiles) and were found to be 46.3 ppmv for the northern and 21.7 ppmv for the southern hemispheres respectively. This seemed to confirm the observations of Kelly *et al.*. Zonal averages of water vapour for the northern hemisphere are between 17 and 145 ppmv and for the southern hemisphere between 7.5 and 105 ppmv, again confirming the interhemispheric difference. The degree of asymmetry between the hemispheres increases with latitude in the model, with the southern hemisphere being one and a half times drier at a latitude of 35^o and being more than twice as dry at 60^o than the corresponding latitudes in the north. Initial MLS data poleward of 40^o suggested that the southern hemisphere is approximately 10 ppmv drier than the northern hemisphere (Read *et al.*, 1995). Both model and MLS data support the idea of an asymmetry.

One suggested reason for the winter-time asymmetry of upper tropospheric water vapour is that the Antarctic is colder than the Arctic because it is a continent and benefits less from heat transported by ocean currents. Air is colder as the poles are approached and the horizontal temperature gradient and vertical wind shear in mid latitudes leads to the generation of mid latitude cyclones. Poleward moving air is dried by sloping convection during cyclogenesis and is a sink mechanism for water vapour reaching the upper troposphere. Since the Antarctic is colder than the Arctic, the drying mechanism is stronger and results in the observed asymmetry (Kelly *et al.*, 1991).

3.1.3 Departures from Zonal Symmetry

In DJF at 215 hPa, there are notable regions of high water vapour, higher than 170 ppmv (figure 3.1), and total precipitable water values greater than 2.5 mm (figure 3.2) which coincide with well known centres of strong convection over South America and Central Africa. These areas of Central and South America and equatorial Africa were observed by Soden and Fu (1995), to have maxima in

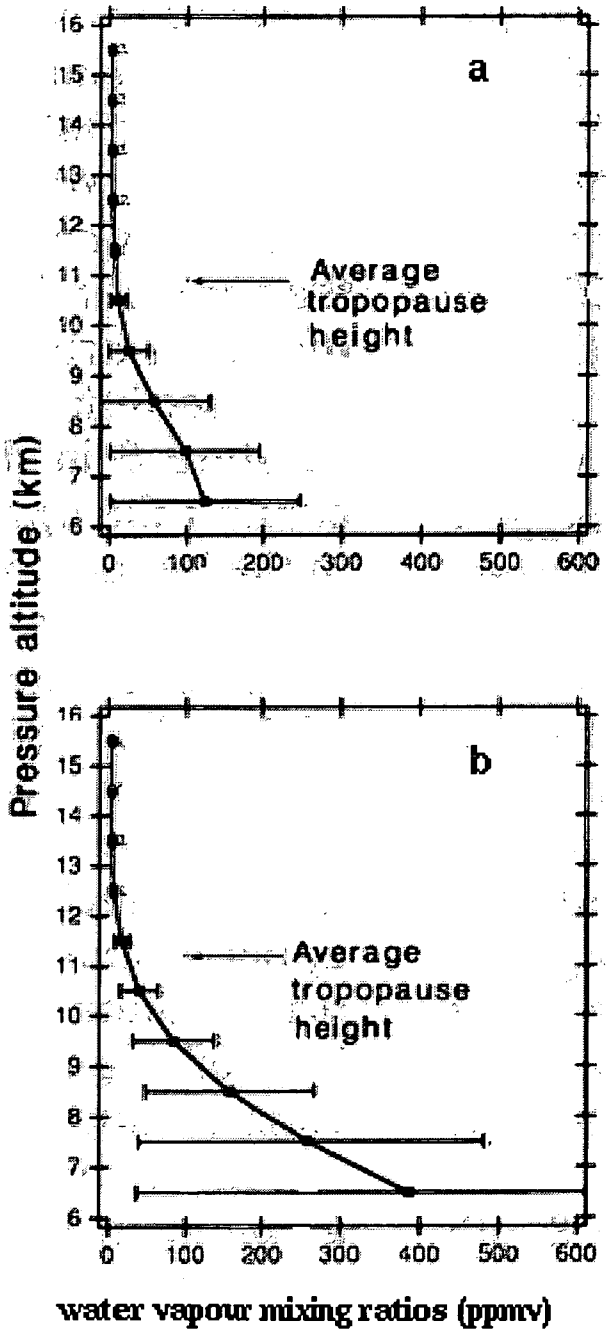

Figure 3.6: The average profiles of total water from a, Punta Arenas (53°S, 71°W) and b, Stavanger (59°N, 6°E). The bars are standard deviations (Kelly *et al.*, 1991).

convection and resulting maxima in upper tropospheric humidity.

In JJA, high mixing ratios and total precipitable water content are found over India and South-East Asia which are related to the monsoon. TOVS data also show enhanced moisture over monsoonal regions of central Africa and northern Brazil coinciding with a high frequency of deep convection (Soden and Fu, 1995).

Salathé and Chesters (1995) (also in TOVS data), find significant dry structures in the seasonal cycle located northwest of the annual monsoon region from June to September (see figure 3.3) and Wu *et al.*, (1993) also mentioned dry regions over the Arabian peninsula particularly in July. Both NVAP data and MLS data show the region of the Arabian peninsula to be dry. Dry structures were also noted across China, India and the Middle East during January and February. A dry region over India is present in the NVAP field for DJF which contains some TOVS data, but it is not evident in MLS data. This may be due to the spatial resolution of MLS being unable to pick out the feature, or it may be an artifact of the cloud clearance algorithm which leads to a dry bias in TOVS data.

Sea Surface Temperature Effects

Heating in equatorial regions has strong departures from zonal symmetry caused by sea surface temperature variations due to the effects of ocean currents. These differences in sea surface temperature produce zonally asymmetric atmospheric circulations which in some regions dominate the Hadley circulation. Both MLS and NVAP fields (figures 3.1 and 3.2) reflect patterns of SST. High mixing ratios and TPW are found over Indonesia and the Western Pacific caused by warm SST. The Eastern Pacific is much drier than the Western Pacific and this contrast results in the Walker circulation. The SPCZ is also evident in both NVAP and MLS data as a band of moisture extending in a SE direction from New Guinea to about 225° E.

In most years, enhanced moisture is evident over the western pacific warm pool and SPCZ though the exact positions of the warm pool and the SPCZ varies depending on El Niño conditions as will be discussed in chapter 4. Moist areas in the western Pacific and along the SPCZ were noted in MLS data (at 215 and 147 hPa) by Newell *et al.*, (1996), and agree with measurements made by a Lyman-α hygrometer on board a DC8 aircraft. TOVS data likewise, show a

maximum in tropospheric humidity over the western Pacific warm pool (Soden and Fu, 1995) and eight years of monthly averages from HIRS/2 show there to be a prominent moist region due to the SPCZ.

The effects of sea surface temperature upon water vapour has been noted in SSM/I data presented in Soden and Bretherton (1994) for July to August 1987 and January to February 1988. SSM/I data form a component of the NVAP data set. Total precipitable water vapour is dominated by water vapour in the lower troposphere due to the exponential increase in water vapour with temperature through the Clausius Clapeyron equation (see equation 1) and the decrease in temperature with height. Maximum values of greater than 50kgm^{-2} signified the presence of the Western Pacific warm pool with values of 10 to 20 kgm^{-2} dominating the middle to high latitude oceans.

Dry tongues resulting from cold oceanic upwelling extend polewards from the tropics off the west coast of North and South America, Africa, and Europe. Dry air extending SW off the coast of California at about 120°W can be seen in DJF and NW from Chile in both DJF and JJA. These intrusions of dry air can also be seen in NVAP and in MLS (figs. 3.2 and 3.1 respectively) as Newell *et al.*, (1996) described.

Moist bands tend to join moist areas together but the eight year monthly average of HIRS/2 data shows the moist zones over the Atlantic and Pacific breaking at the eastern end during boreal winter and the Indian ocean branch breaking along the African coast during September and October. Elson *et al.*, (1995) seem to confirm this, finding that the maximum water vapour concentration in November was weakly split between eastern and western hemispheres.

The Indonesian Fountain

It has been suggested that in the tropics, transport of water vapour from the troposphere up to the stratosphere can occur in convective towers. Convective towers which are tall enough are found over the rising arm of the Walker circulation over Indonesia during Northern hemisphere winter. This is known as the Indonesian (or Stratospheric) fountain, and was proposed by Newell and Gould-Stewart (1981). Data from UARS MLS, at 215 hPa and 147 hPa, for two periods (September 17th to October 22nd 1991 and February 7th to March 14th 1994)

presented by Newell *et al.*, (1996) offer some support to this Indonesian fountain idea.

On the maps of seasonal averages of MLS and NVAP water vapour shown in figures 3.1 and 3.2 respectively, enhanced moisture is seen in the Indonesian region. In DJF, the region of enhanced moisture extends east of the dateline whilst in JJA it remains to the north and west. This region will be the subject of further investigation when stratosphere-troposphere exchange is examined in chapter 6.

Tropospheric Rivers

Newell *et al.*, (1992) noted the existence of 'atmospheric rivers' from water vapour fluxes derived from ECMWF data. Figure 3.7 shows the distribution of water vapour from NVAP for the 3rd January 1992, a day on which Newell's atmospheric rivers were prominent. Filaments of moisture can be seen extending from the equator towards both poles. In the southern hemisphere, there are 3 well pronounced rivers. One beginning in the Indian Ocean, one in the Western Pacific, and one extending off the coast of South America. The positions of these rivers is similar to those shown in Newell *et al.*, (1992). In the northern hemisphere, 2 rivers can be seen, one along the coast of China, and one leading from the Western Pacific up towards the Northwest coast of America. The rivers in the Northern Hemisphere are less well defined than those in the southern hemisphere. Newell *et al.* stated that there are typically five rivers leading to the mid latitudes of the Southern Hemisphere and four or five extending into the Northern Hemisphere.

In the equivalent daily map from MLS (see figure 3.8) the moist filament extending from the Western Pacific to the Northwest coast of America compares well with that in NVAP. The moisture along the coast of SE China is less prevalent in MLS than in NVAP. The southern hemisphere rivers cannot be seen because it was a north looking day. The rivers are less well defined in MLS than in NVAP. This in part is due to the coarser resolution of the MLS measurements and may also be due to the height of the measurements, as according to Newell *et al.*, most of the contribution to the rivers is from the atmosphere below 500 hPa. Since the bottom of the NVAP column is at 500 hPa, and since the vertical integral of the column will be dominated by water vapour at the lower level, it is not surprising

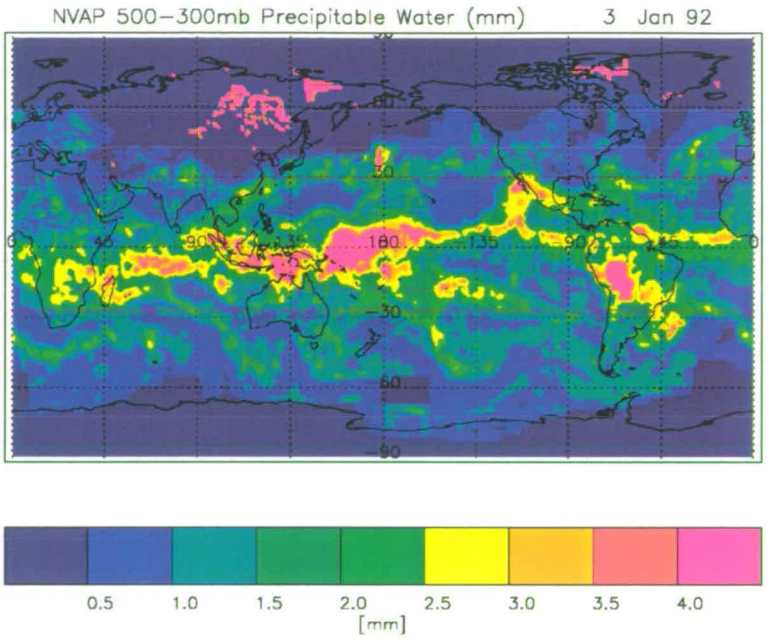

Figure 3.7: NVAP total precipitable water (mm) for the 3rd January 1992

that the rivers can be seen on the NVAP map but not the 215 hPa MLS map.

3.1.4 Differences between MLS and NVAP

NVAP data within a 5° box around each MLS footprint have been averaged and correlated with the MLS water vapour mixing ratio. Some NVAP grid points have been removed from the correlation. They are those points over Siberia and Greenland where total precipitable water vapour quantities are unrealistically high, being greater than 7.2mm in regions where the surrounding TPW is less than 0.5mm. Randel *et al.*, (1996) noted these areas to be a problem and to be due to contamination by sea ice in coastal areas and to the difficulties in removing land effects.

The average correlation between MLS and NVAP calculated for 1st December 1991-31st December 1992 is 0.74. Figure 3.9a shows the relationship between MLS mixing ratios and NVAP total precipitable water for 3rd January 1992. The correlation between the two fields on this day is 0.74. There is a wider distribution of points above the line than below. The crosses in bold type are the

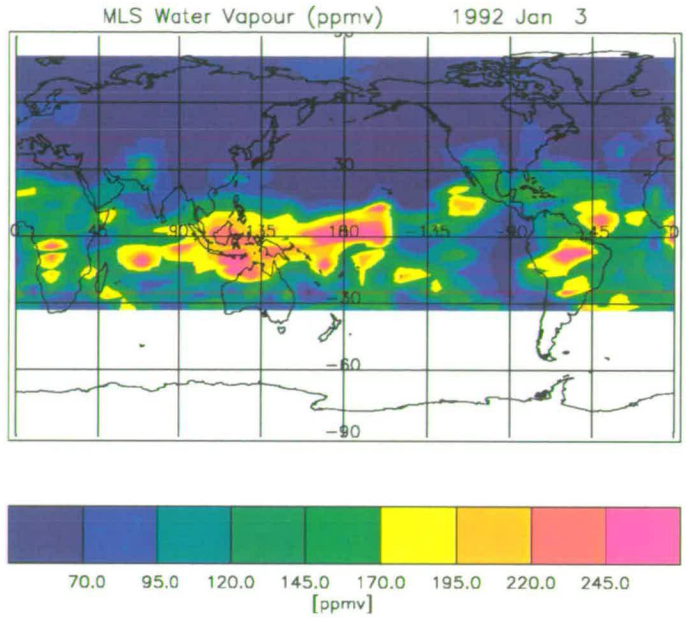

Figure 3.8: MLS water vapour mixing ratios (ppmv) for the 3rd January 1992

30 points furthest above and 30 points furthest below the line of best fit. Their geographical location is plotted in figure 3.9b. Diamonds indicate the position of the 30 points above the line of best fit, and triangles indicate the 30 points below the line of best fit in the scatter plot. The majority of points fall over the oceans where there is a lack of radiosonde measurements that can be incorporated into the NVAP dataset. A moist bias is often introduced by radiosondes and SSM/I, and a dry bias by TOVS (Randel *et al.*, 1996). NVAP may also be expected to be moister than MLS due to it being a column integral and containing water vapour at much lower levels than MLS.

The diamonds show points where MLS indicates a much more moist region than NVAP (see figure 3.9b). They correspond to the 30 highlighted crosses above the line of best fit in figure 3.9a. The geographical location of these points are in those regions of the tropics where deep convection might be expected, such as the Indonesian region and central Africa. This may be due to the dry bias introduced into the NVAP dataset by TOVS data which cannot make measurements in cloudy conditions.

The locations of the 30 points furthest below the line of best fit are marked as triangles in figure 3.9b. These triangles represent places where the MLS measurement is much drier than the NVAP measurement. Since radiosonde data are sparse over the oceans, the likely cause of the cluster of triangles in the central Pacific ocean in the vicinity of the dateline and 30°N, is a moist biasing introduced by SSM/I.

The cluster of triangles in the region of 90°W lie in an area known as the equatorial dry zone, which was investigated by Blackwell and McGuirk, (1996). They found that although this area was reported dry by radiosondes and indicated dry by OLR, it was reported as much moister by TOVS data. Small amounts of precipitable water in the layer 100-300 hPa contaminated the brightness temperature of TOVS, causing it to overestimate the moisture content of the layer below. The inclusion of this data in the NVAP total precipitable water column from 500-300 hPa would account for the NVAP field being too moist compared with MLS.

Correlations like that in figure 3.9a have been made for each day throughout 1992, and it is found that the correlation coefficient varies between 0.67 and 0.85. Since the number of good points used in the correlation is different for each day, a better method of assessing the similarity between the two data sets is to examine the rms difference between the two sets of measurements for each day.

In a similar way to Jackson and Stephens (1995) the rms difference (R) between the MLS measured mixing ratio xm and an NVAP equivalent mixing ratio xn was calculated as;

$$R = \left[\frac{\sum_i^N (xm_i - xn_i)^2}{N}\right]^{0.5}$$

where N is the number of good data points. The NVAP equivalent mixing ratio was calculated from the best-fit line of a scatter plot (like that in figure 3.9) for each day when the NVAP and MLS datasets overlapped. The rms difference is thus, a measure of the spread of points in the correlation plot.

The yearly average of the rms difference is 38 ppmv. It is important to note that there is no seasonal trend to the rms difference. The best-fit line is as good in northern hemisphere summer when convection in the Asian monsoon region is

a

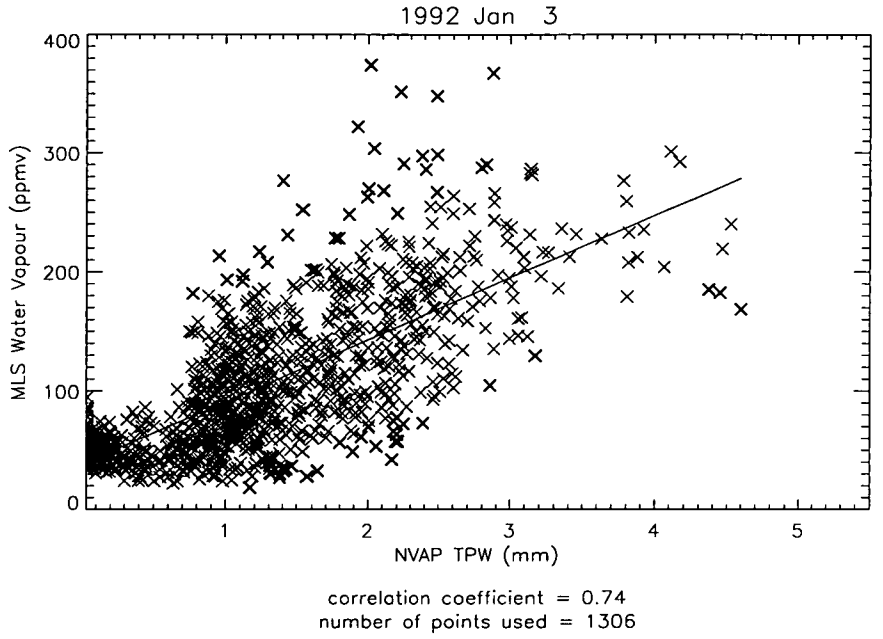

b

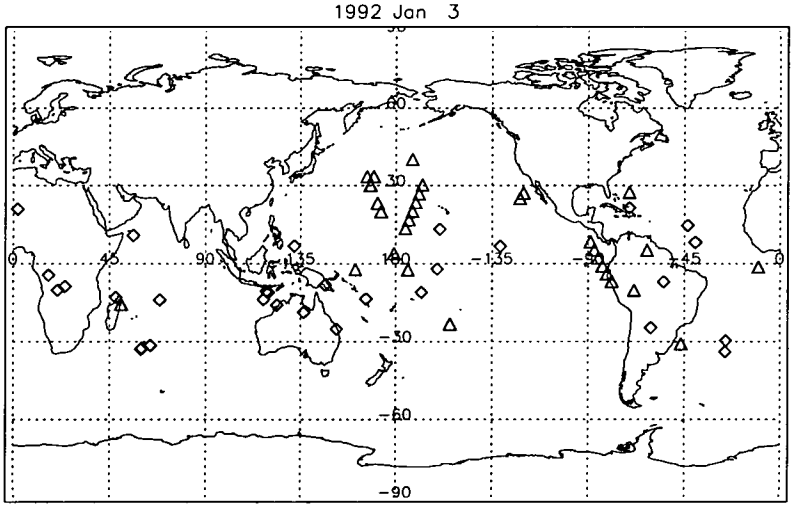

Figure 3.9: **a)** Scatter plot showing the relationship between MLS mixing ratio (ppmv) and NVAP total precipitable water (mm) for 3rd January 1992. **b)** Map showing the position of the furthest outliers in the scatter plot. Diamonds correspond to outliers above the best fit line, and triangles to outliers below the best fit line.

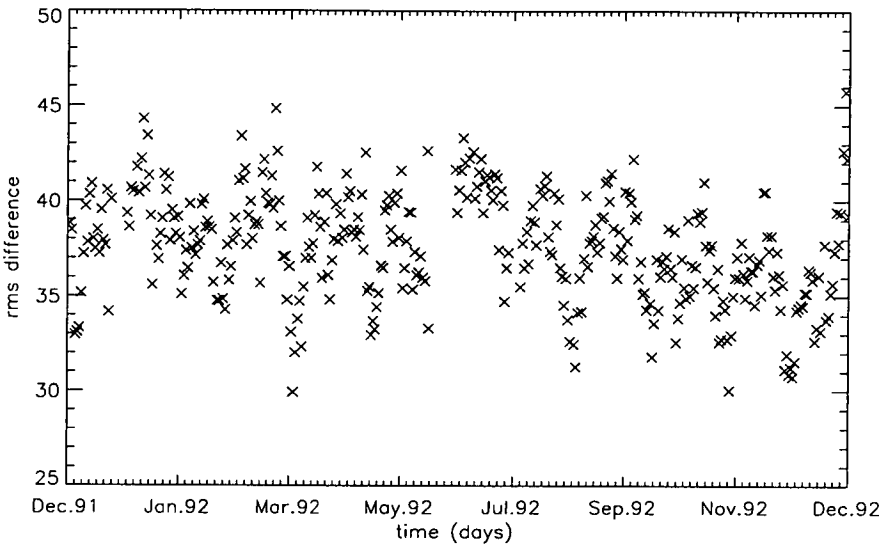

Figure 3.10: rms difference between MLS and NVAP for all available days from 1st December 1991 to 31st December 1992.

strong, as in boreal winter when it is not. This suggests that, as stated by Read *et al.*, (1995), the effect of high cirrus clouds from deep tropical convection is not a significant problem.

The best-fit line for the correlation plots of NVAP total precipitable water against MLS mixing ratio (like that in figure 3.9 a) does not pass through the origin and intercepts on the y axis at an average value of 35.5 ppmv over the year. This is a similar value to that reported by W. G. Read, personal communication, (1997) who compared the current analysed product with the new improved MLS UTH retrieval and noted that MLS had a moist bias of about 40 ppmv everywhere.

3.1.5 ECMWF

This section provides a brief overview of the ability of the ECMWF forecasting scheme to produce analyses of the water vapour field consistent with those just described. The ECMWF humidity fields come from the re-analysis data described in chapter 2.

Seasonal averages of relative humidity are plotted in figure 3.11. The ITCZ in

DJF is mostly south of the equator as expected, with breaks over the Eastern Pacific and Atlantic ocean. The SPCZ is more pronounced than that in MLS data but compares well to the NVAP field. In JJA the ITCZ extends right round the world and there is no break in the Western Indian ocean as was indicated by NVAP. The SPCZ is well pronounced, extending to just past the date line and the northern branch of the ITCZ is much more pronounced than in MLS and NVAP. Vespirini (1998) noted that the double ITCZ was a systematic defect of the ECMWF analyses that is not very well marked in observations. Although it is perhaps a more persistent and well marked feature in the ECMWF field than in the MLS or NVAP fields, there is some observational evidence from NVAP and MLS to support it.

Enhanced moisture over the monsoon region is not well represented by ECMWF. Although there is excess moisture during JJA compared with DJF, its position is too far south, being centred over the Indian ocean rather than over the continent as in MLS and NVAP. Enhanced moisture over Panama in JJA compares well with MLS and joins with the ITCZ as the NVAP field showed. In DJF, the dry tongue off the western coast of South America compares well to that in the MLS field, but in JJA, the feature is rather too moist. This has been noted by Vespirini (1998) who attributed it to biased data rather than to a shortcoming of the model.

Seasonal means also indicate some asymmetry between the hemispheres as far as summer moistening is concerned. 30% humidity extends to about 40°N compared with only about 25°S. Zonal means are presented for both seasons in figure 3.12 and show the characteristic displacement of the peak relative humidity towards the summer pole. The peak value in the northern hemisphere is higher than the southern, and the northern hemisphere as a whole is moister than the southern in their respective summers.

The main difference between the ECMWF compared with NVAP and MLS is that in JJA (southern hemisphere winter) the RH beyond 50°S increases from 10% to 45% at 90°S. A corresponding increase from 15-25% takes place in the northern hemisphere winter. The difference is due to the temperature of the Antarctic being colder than the Arctic, therefore the air can hold less water vapour and its relative humidity increases. The difference between southern and

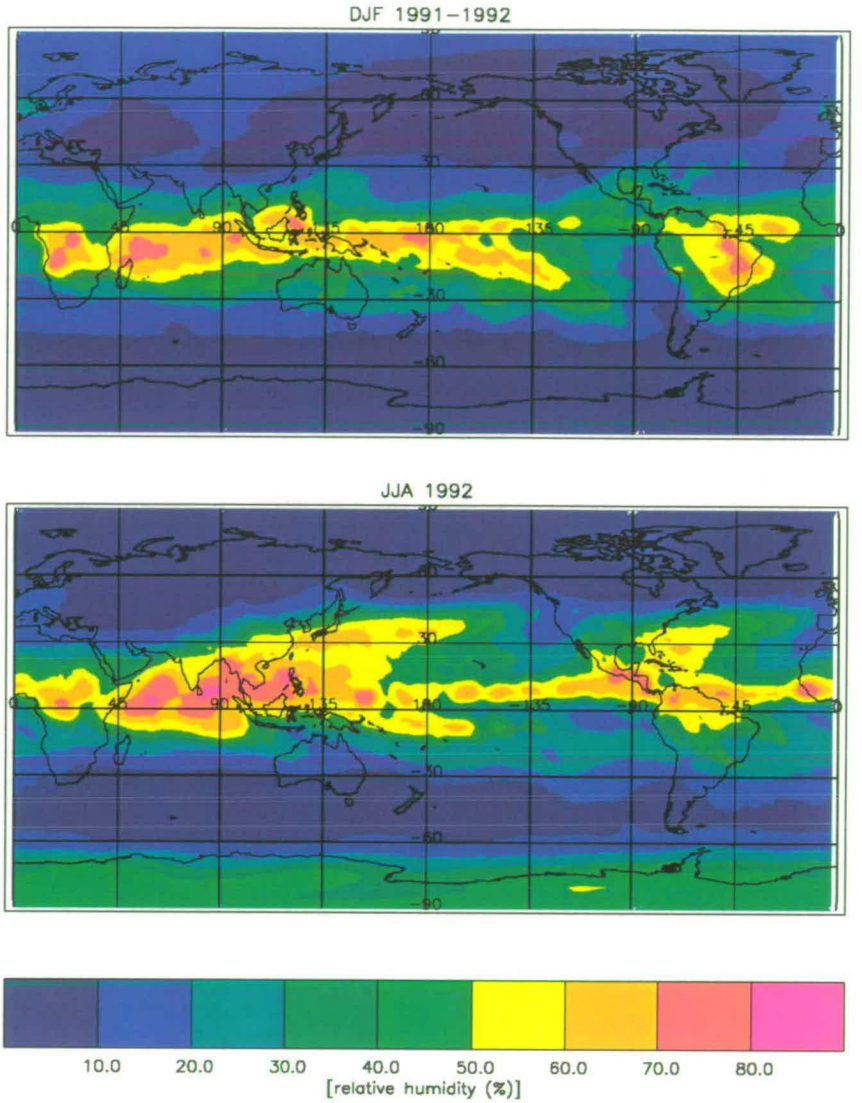

Figure 3.11: Seasonally averaged ECMWF relative humidity (%) at 200 hPa for December–January 1991/2 (DJF) and June–August 1992 (JJA).

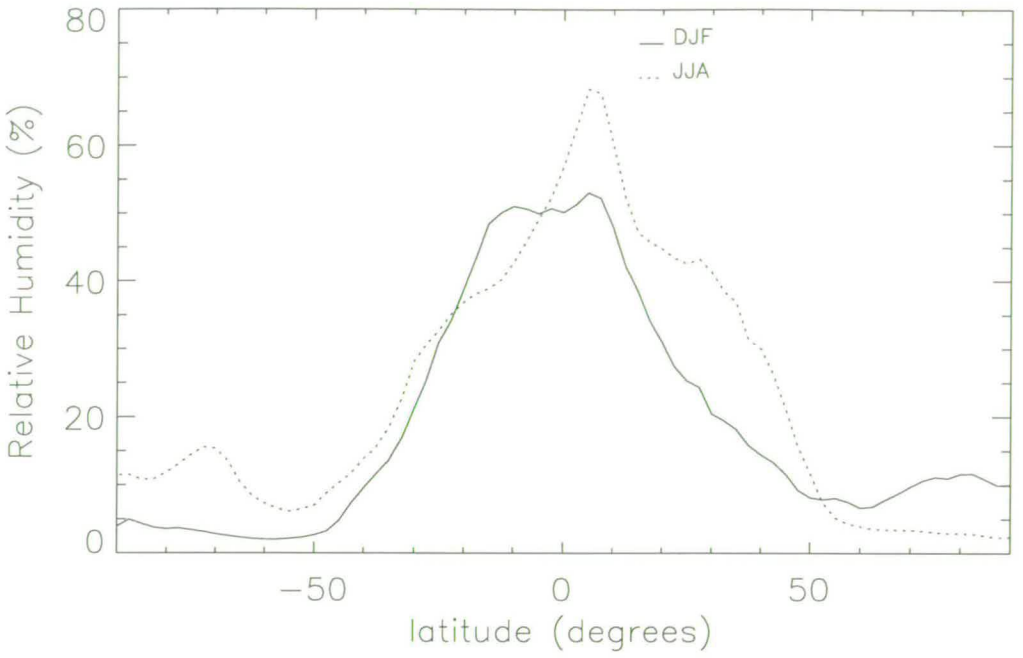

Figure 3.12: Seasonally averaged zonal mean ECMWF relative humidity (%) at 200 hPa for December–January 1991/1992 (DJF) and June–August 1992 (JJA).

northern hemisphere winters was noted by Kelly *et al.* (1991) and discussed in an earlier part of this chapter.

Points that were furthest from the line of best fit of ECMWF and MLS had a similar location to those that came from the NVAP and MLS correlation. Both data sets include TOVS measurements, so results can be expected to be similar. MLS reported more moisture than ECMWF in the Indonesian region due to the dry bias of TOVS in cloudy conditions. ECMWF was too moist in the equatorial dry zone due to the moist biasing known to affect TOVS specifically in this area.

3.2 Conclusions

MLS and NVAP reproduce the large-scale distribution features which are common to most other datasets and which reflect the effects of the Hadley circulation upon upper tropospheric moisture. The ITCZ was seen to be more pronounced in the NVAP field than in the MLS field, and the zonal mean to be much more sharply peaked. This is partly due to the spatial resolution of the NVAP measurements

being much greater than those of MLS. Water vapour in the upper troposphere decreases from its maximum values near the equator to minimum values near the poles. The north-south movement of the peak values of water vapour follow the movement of the inter-tropical convergence zone from north of the equator in northern hemisphere summer to south of the equator in southern hemisphere summer.

Outside the tropics, the summer hemisphere is moister than the winter hemisphere reflecting the increased strength of Hadley cell subsidence over the winter hemisphere. The hemisphere as a whole is moistened in its respective summer, and this hemispheric moistening is stronger for the northern hemisphere than for the southern. The effect is stronger for NVAP than for MLS. A wintertime asymmetry between northern and southern hemispheres which has been observed, in SAGE II and HIRS data can also be seen with MLS and NVAP.

Both NVAP and MLS see moistening associated with the Asian monsoon. That from MLS is slightly further west relative to NVAP. Although ECMWF shows an increase in relative humidity related to the monsoon, its position is further south and not confined to the continent as both MLS and NVAP are. Moistening is also associated with the Indonesian fountain though to a lesser extent than for the monsoon. Both of these regions will be investigated in further detail in chapter 6 to investigate their respective roles in stratosphere-troposphere exchange.

Tropospheric rivers that can be seen on the NVAP map cannot be seen on the MLS map. Most of the contribution to the atmospheric rivers is from the atmosphere below 500 hPa which is at the bottom of the NVAP column but well below the MLS measurements. It may also be that the horizontal resolution of MLS measurements is not great enough to capture the atmospheric rivers. Intrusions of dry air off the western coasts of continents however, are noticeable in both MLS and NVAP.

The average correlation between MLS and NVAP during the period from December 1991–December 1992, is 0.74 and suggests that there is good agreement between the two fields. Some differences are to be expected since the MLS measurement is centred at 215 hPa and the NVAP field is a column integral between 300 and 500 hPa. Much of the similarity is due to the water vapour at 215 hPa being strongly related to that below through convective processes.

Those points which do not agree so well, lie within the tropical region and over the oceans where the radiosonde coverage (which comprise NVAP) is more sparse. In regions of deep cumulus convection there are some discrepancies between the two datasets due to the dry bias introduced by the TOVS measurements which comprise part of the NVAP dataset. MLS, which is capable of measuring in these cloudy regions reports them as being moister than is suggested by NVAP. The region of the equatorial dry zone was reported to be moister in NVAP than MLS and is due to contamination of TOVS radiances by small amounts of precipitable water in the 300-100 hPa layer.

The rms difference between MLS mixing ratios and the NVAP equivalent mixing ratio shows that the measurements generally fall within plus or minus 40 ppmv of the best fit line. There is no seasonal trend to this which shows that even when there is increased cloudiness due to the Asian summer monsoon, the measurements from MLS do not appear to deteriorate. This would be in agreement with Read *et al.*, (1995) that cirrus clouds do not have a significant effect on MLS measurements.

In summary, this chapter has shown that MLS reproduces the main features of the water vapour field in the upper troposphere well. Most differences between the MLS field and that from SSM/I, TOVS, or HIRS II, can be attributed to differences in measuring height and vertical resolution, horizontal resolution, and to the differences in the ability of the instruments to report in cloudy conditions. The ability of MLS to measure in cloudy conditions gives it an advantage over other instruments. It is clear from this chapter, that MLS can make a new and important contribution to the knowledge of the water vapour field in this region.

Chapter 4

Variability in the Tropics

4.1 Introduction

The tropics play an important role in climate studies. It is here that the deep convection and detrainment take place which form the central issue in the debate about the drying of the upper troposphere (Lindzen, 1990) and it is here that much transfer between the troposphere and the 'stratospheric overworld' (Hoskins, 1991) takes place.

The atmospheric circulation in the tropics is driven by the large latent heat changes which accompany phase changes of water. Knowledge of the distribution of water vapour in the tropics and its variation over time is of importance to understanding the tropical circulation. Since the tropical circulation influences the subtropics and mid-latitudes an understanding of it may aid climate and weather predictions on a global scale. In addition, the response of the tropical circulation to changes in humidity is often used as an indication of the possible climatic changes which may result from global warming.

It is also here however that the use of radiosonde data is most limited. Profiles are confined largely to northern hemisphere landmasses with the result that the water vapour field in the upper troposphere of the tropical region has been poorly observed. MLS, which has provided almost daily coverage of the tropical region since its launch in 1991, can make an important contribution to the observations of water vapour in this area.

This chapter explores the temporal variation of water vapour with a focus upon intraseasonal time-scales. In section 4.3 the variability of the water vapour field in the tropical upper troposphere is described and it is argued that some of the

observed features are related to the Madden-Julian oscillation (MJO). Hence to provide the background to this, the literature concerning the MJO is first reviewed in section 4.2.

4.2 The Madden-Julian Oscillation

This section provides an introduction to the Madden-Julian oscillation upon which the next two chapters focus.

The Madden-Julian oscillation comprises large-scale circulation anomalies associated with convective anomalies which move eastwards. The dynamical signal in for example zonal wind and surface pressure, exhibits a period of 30-60 days and affects all longitudes. The circulation anomalies travel with speeds of about 10ms^{-1}. The convective signal on the other hand is confined in longitude and has a broader time-scale of 30-95 days (e.g. Salby and Hendon, 1994 and Kiladis and Weickmann, 1992). The coupled convective anomalies move eastward at $3\text{-}6\text{ms}^{-1}$. The dynamical signal can be detected at all times of the year but the convective behaviour is seasonally affected, being stronger in the summer hemisphere. Although the relationship between the circulation and convection is uncertain, evidence suggests that the interactions between the two are vital to the existence and eastward propagation of the MJO (Zhang and Hendon, 1997).

Figure 4.1 taken from Madden and Julian (1972), is a schematic representation of the MJO showing the relationship between the circulation and enhanced convection. The diagram shows the easterly movement of convection along with an easterly movement of low pressure and increased tropopause height. The convection is seen to be strongest over the Indonesia and the western Pacific. A negative pressure anomaly over East Africa and the Indian Ocean is seen at time F and the circulation cell reaches to the dateline. At G, the pressure anomaly has spread eastwards, the circulation cell reaches beyond the dateline and convection is enhanced. At H, the enhanced convection moves to Indonesia and westerly winds are also prominent. At A, the circulation cells are approximately symmetric, convection is strong and centred over the Western Pacific. At B, the cell to the west of the convection weakens, pressure rises over the Indian ocean, and the convection also weakens. Weak convection is still present at C. At D, divergence

in the upper troposphere in located over the Atlantic and there is no accompanying low-level convergence. Time E represents the final phase of the cycle with two asymmetric circulation cells (Madden and Julian, 1972).

As noted above, the convective anomalies are strongest over the warm pool of the Indian ocean, the Maritime Continent and the west Pacific and are observed to migrate eastwards. Often a southwards development along the South Pacific Convergence Zone (SPCZ) is seen. The SPCZ is a band of persistent cloud that extends in a southeasterly direction from New Guinea to about 30°S, 120°W. It also has a northwesterly component which merges with the ITCZ. The location of the SPCZ may be determined by SST gradients, and land-sea distributions may affect its strength. The SPCZ is most active during southern summer and its location and strength vary on both interannual and intraseasonal time-scales. The 500 hPa vertical velocity field from ECMWF data (Vincent, 1994) showed that the position, location and strength of the SPCZ varies seasonally with the SPCZ being most pronounced in December-February and least pronounced in June-August. More details on the SPCZ can be found in the review by Vincent, (1994).

Kiladis and Weickmann (1992) found that the zonal portion of the SPCZ contained a pronounced summertime peak in outgoing longwave radiation (OLR) within the MJO range. Rui and Wang (1990) used 10 years of OLR data from NOAA polar orbiting satellites and found that during strong MJO events 'moist', OLR anomalies move from the equator towards the south eastern Pacific. Matthews *et al.*, (1996) looked at 10 years of gridded, daily OLR data from the AVHRR and found that virtually all MJOs cause the enhancement or excitation of convection along the SPCZ. Similarly, in northern summer, MJO events propagate north-eastwards into the west Pacific. This north-eastwards development is far less pronounced than the south-eastward development in southern summer.

During the summer monsoon, over India and south-east Asia, northward propagation dominates over the eastward propagation. During El Niño, the SPCZ tends to be north and east of its average position and during La Niña it lies south and west of its general position.

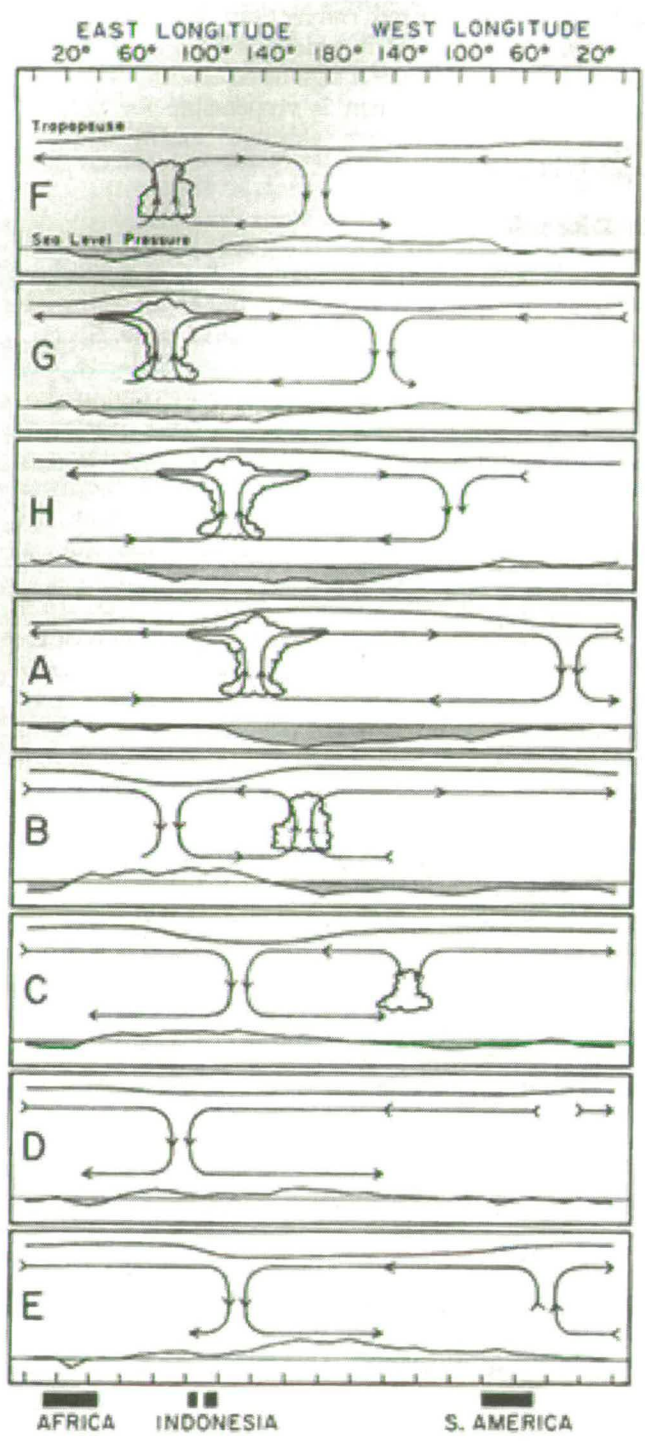

Figure 4.1: Schematic diagram illustrating the longitude-height structure of the MJO. Clouds indicate regions of enhanced convection. The time interval between successive pictures is about 6 days. The mean pressure disturbace is plotted at the bottom of each chart with the negative anomalies shaded. The relative tropoause height is indicated at the top of each chart. (Madden and Julian, 1972)

4.2.1 Structure and Generation of the MJO

The structure of the oscillation is not completely understood. According to Hendon (1988), it has some of the characteristics of an equatorially trapped Kelvin wave but it also has a meridional component indicating that some other mechanism is also present. In addition, a free, dry Kelvin wave would have a greater phase speed than that observed. The presence of precipitation could slow down the dry Kelvin wave but still the meridional component cannot be accounted for (Hendon, 1988). Hendon and Salby (1994) constructed a life cycle of the MJO using out-going longwave radiation data from the Advanced Very High Resolution Radiometer (AVHRR), wind fields from the National Meteorological Center and the European Centre for Medium- Range Weather Forecasts, and temperatures from the Microwave Sounding Unit. They found that the MJO had characteristics of a coupled Rossby-gravity wave propagating eastwards along with the convective anomaly at $5ms^{-1}$, and a Kelvin wave propagating from the convective anomaly, eastwards at $10ms^{-1}$. Hendon and Salby, (1996) interpreted this as a forced response west of the dateline and a radiating response east of the dateline.

Convective Instability of the Second Kind

Many studies have focused upon the feedback between the tropical circulation and the MJO involving cumulus convection and Convective Instability of the Second Kind (CISK) as a mechanism for exciting a Kelvin wave. Normally in CISK, a low level convergence field lifts the moist surface air to the lifting condensation level and convection is initiated. Latent heat release in turn forces large-scale motion and enhances the low-level convergence, thereby maintaining and intensifying convection.

With wave-CISK, a wave (Kelvin wave) induces surface convergence at C in figure 4.2, between the high and low pressure perturbations. High pressure initially forms at C, the centre of convergence of the Kelvin wave, convection is initiated, and further surface convergence is induced to the east. Hence as the convergent centre of the Kelvin-wave moves eastwards, so too does the convection. The region of maximum moisture convergence is located to the east of the convection

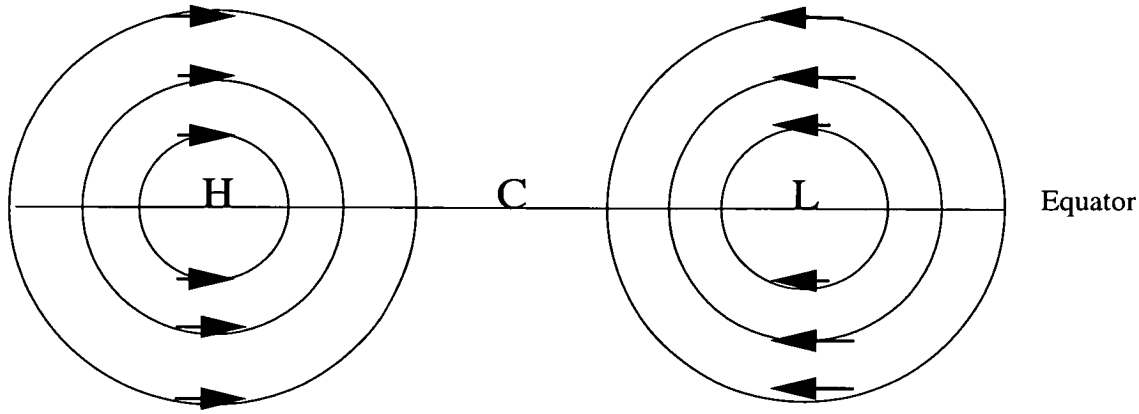

Figure 4.2: Horizontal velocity perturbations associated with a Kelvin wave. Convection is induced at the centre of convergence C of the Kelvin wave. Wind arrows are not drawn to scale. (Figure based on Matsuno, 1966).

and leads in time the variation in convection.

This idea of wave-CISK forms the basis of a possible mechanism for the MJO as illustrated in figure 4.3 a. An equatorial disturbance could be dispersed eastwards by Kelvin waves or westwards by Rossby waves. Convection develops in the region of convergence (at C in the figure). With CISK as a heating source, the Kelvin wave can be maintained and even enhanced and the convergence centre and convective centre propagate eastwards. Rossby waves disperse the dying cloud clusters westwards. When the disturbance passes over warm water, it is amplified through CISK due to the extra moisture. Over cold water, the moisture supply is reduced and the amplitude of the disturbance is decreased. The CISK excitation can provide sufficient energy to overcome the dissipation and so the disturbance can continue to propagate.

Lau and Peng (1987) tested this idea with model experiments and found that a CISK heat source causes Kelvin wave modes to be enhanced and the disturbances to propagate eastwards at speeds of about $20ms^{-1}$. The phase speed for the propagation is faster than observed. They also found the amplitude of the CISK heating to be dependent on the east-west sea surface temperature gradient. The idea of wave-CISK as a possible mechanism for the MJO was investigated in

more detail by Chang and Lim (1988) who used a 5-level model to confirm that Kelvin wave-CISK modes have the correct propagation and overall structure but that there are features in the observed and simulated oscillations that are not accounted for by the Kelvin wave-CISK modes.

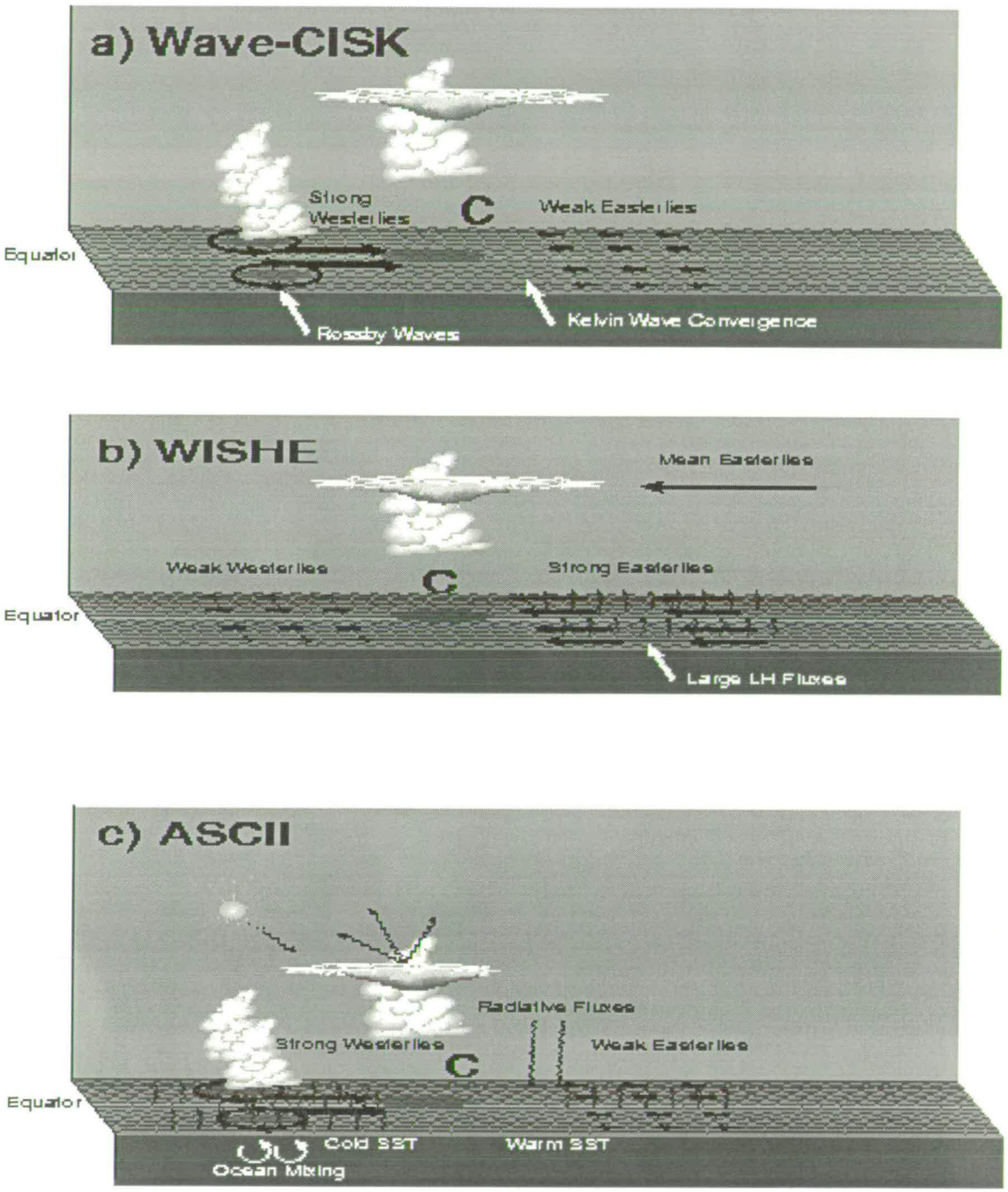

Figure 4.3: Schematic illustration of the theories of the intraseasonal oscillation. a) Wave-CISK, b) Wind-induced surface heat exchange (WISHE), and c) air-sea convective intraseasonal interaction (ASCII). (Figure taken from Flatau *et al.*, 1997)

Cloud Organisation

Chao and Lin (1994) propose an explanation of the intraseasonal oscillation based upon the observational work by Nakazawa (1988) and Sui and Lau (1992). The observations showed that the convective region associated with the intraseasonal oscillation consists of one or more 'super cloud clusters'. The super cloud clusters have a horizontal extent of about 5000 km and periods of about 10 days. They comprise a synoptic scale ensemble of mesoscale cloud clusters at different stages in development and with lifetimes of 2-3 days (e.g. Lau *et al*, 1991). New cloud clusters appear to the east of existing cloud clusters. The super cloud cluster moves eastwards and the individual cloud clusters within it move westwards (see figure 4.4). Chao and Lin (1994) suggest that the origin of the intraseasonal oscillation is a convective region which starts over the Indian Ocean and moves eastwards until the sea surface temperature (SST) becomes too cold to support it. When the warm SST's extend into the Eastern Pacific during El Niño years, the convective region can move further eastwards. After the convective region has reached the mid-pacific and decayed, a new one begins in the Indian Ocean and this cycle repeats at 40-50 day intervals. The super cloud clusters are generated by a tele-induction mechanism whereby a new cloud cluster is initiated by an existing cloud cluster. The new cloud cluster (800-1200 km on the eastern side of the existing one) receives moisture from the east and the existing cloud cluster decays. The process of new cloud clusters being generated to the east and the decay of existing ones gives rise to an eastward moving envelope, the super cloud cluster. Chao (1995) discusses the idea of wave-CISK as an explanation for the MJO and maintains that the super cloud cluster explanation for the MJO can overcome some of the inadequacies of the wave-CISK explanation.

Hendon and Liebman (1994) used data from the same sources as Hendon and Salby (1994) (see above) to examine the connection between convection and the MJO and in particular, whether the MJO organises convection or whether convection plays a part in generating the MJO. They conclude that large scale disturbances in the circulation are coupled to convection and a positive feedback results through frictional wave-CISK. Hendon and Liebman question the role of super cloud clusters in the excitation and propagation of the MJO. Although they

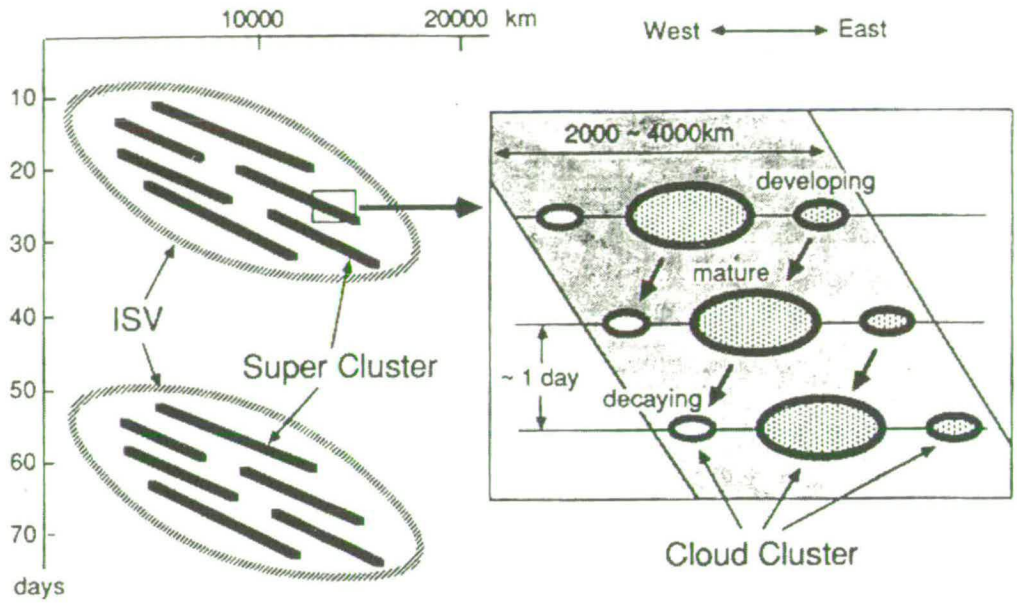

Figure 4.4: Intraseasonal Variability (ISV) comprising of super cloud clusters (slanting lines). These super cloud clusters are enlarged on the right to show development, growth and decay of the smaller westward moving cloud clusters, Nakazawa (1988)

find synoptic scale disturbances reminiscent of the super cloud clusters, they find that they only account for 5-20 % of the variance and therefore conclude that it is unlikely that the super cloud clusters play an important role in the evolution of the MJO. Cho *et al.*, (1994) considered the organisation of cumulus clouds into cloud clusters and how this would effect a Kelvin wave. Their results suggested that rather than the cumulus convection itself, it is the organisation of cloud clusters that is an important part of the dynamical processes leading to the MJO. They did not consider the role of super cloud clusters in their study.

Dunkerton and Crum (1995) examined 10 years of OLR on temporal scales of supercloud clusters (2-15 days) and of the intraseasonal envelope (30-60 days). They find that the role of supercloud clusters is relevant to some but not all MJO events and that the enhancement of convective activity on spatial and temporal scales smaller than that of superclusters is more important. Similarly, Kiladis *et al.*, (1994) also focused on shorter period convection. They analysed OLR over Borneo and the region 150-160°E on 6-30 day timescales and found that the bulk of intraseasonal variability in convection and the low-level circulation falls within

this range.

Wind-Induced Surface Heat Exchange

The evaporation-wind theory (also known as wind-induced surface heat exchange WISHE) as an alternative to the wave-CISK theory of the MJO was put forward by Emanuel (1987) and independently by Neelin *et al.*, (1987). Evaporation from the sea surface depends on wind speed and the greater the wind speed, the greater the evaporation. The theories propose that regions of convection force easterly winds to the east of the convection and westerly winds on the western side. This is illustrated in figure 4.3 b. These winds are superposed upon the mean easterly winds in the tropics and so the westerly winds are retarded and the easterly winds enhanced. Thus, evaporation will be greater on the eastern side and reduced on the western side. The theory accounts for the observed eastwards propagation of the MJO, its equatorially trapped nature and its low phase speed.

The WISHE theory is based upon the assumption that mean surface winds in the tropics are easterly. This assumption is criticised by Wang (1988). Wang found there to be pronounced longitudinal variation in zonal winds and in the region of the Indian ocean where the convective anomalies originate, winds are often westerly (see also Emanuel, 1988) and Neelin, 1988). Results from the TOGA COARE intensive observation period (Lin and Johnson, 1996) suggest that maximum surface fluxes tend to develop towards the west of the convective system because westerly wind bursts are usually stronger than easterlies. Flatau *et al.*, (1997) incorporate these findings into a new theory of the intraseasonal oscillation which they call air-sea convective intraseasonal interaction (ASCII), illustrated in figure 4.3 c, along with the theories of wave-CISK (a) and WISHE (b) for comparison. Like WISHE, surface fluxes are important to maintain the convection but in ASCII, the surface forcing is generated by the cloud cluster itself. As with wave-CISK, strong westerlies are generated beneath the cloud cluster. The presence of the cloud cluster causes the SST to drop due to evaporation, oceanic vertical mixing and the cloud shielding the sea from sunlight. East of the cluster where winds are easterly, SST increases. Convection then develops in the convergent region (C) of the Kelvin wave in a similar manner to wave-CISK. Unlike WISHE, regions of weak surface winds, rather than strong

surface winds, favour the further development of convection.

Using ECMWF data, Jones *et al.*, (1998) examined the association between the MJO and intraseasonal variations in surface heat fluxes and SST in the Indian and Pacific oceans. They showed that intraseasonal variations in convection and the large-scale circulation strongly modify the ocean surface heat fluxes of net shortwave radiation and latent heat. As observed by Hendon and Salby (1994) and Jones and Weare (1996) they found clear skies and minimum surface wind speeds along with maximum low level moisture convergence to be present before the onset of convection. As convective anomalies move eastwards, net surface shortwave radiation decreases and surface latent heat fluxes increase resulting in negative surface fluxes and negative SST. This can be seen in figure 4.3 c. Like Flatau *et al.*, (1997) they conclude that the results are at odds with the WISHE theory of the MJO and that an important relationship exists between the MJO and SST which should be incorporated into theories.

Other research has shown that eastward propagating modes can occur even when surface winds are assumed to be at rest. Then the eastwards propagation arises from enhancement of Kelvin waves over Rossby waves. Neelin *et al.* suggest that the evaporation-wind mechanism may combine with another mechanism to excite the MJO.

Jones and Weare (1996) investigated the evaporation-wind theory as a mechanism for maintaining the MJO and whether it coexists with wave-CISK. Using ISCCP data to look at the convection field, and ECMWF data to calculate surface heat fluxes, they concluded that behaviour of low-level moisture convergence was consistent with the wave-CISK mechanism. They observed heat fluxes that were negative on the eastern side of convection in contrast to the evaporation-wind theory which requires them to be positive. They conclude that observations support the wave-CISK mechanism but not the evaporation-wind mechanism and they cast doubt upon the idea that the two theories may coexist.

Figure 4.5 illustrates the conclusions of Jones and Weare. Initially, organised convection leads to a circulation with convergence in the lower troposphere and divergence in the upper troposphere. In part a, convergence to the east of the convection provides moisture and forces the organised convection to propagate eastward to situation b by wave-CISK (see figure 4.2). In b, surface evaporation

anomalies are positive on the western side of the convection and negative on the eastern side. Convection induces new surface convergence to the east, and wave-CISK continues to propagate the wave eastwards, even though westerly winds (eastward propagation) tend to be retarded by evaporation. Propagation continues until at d, the region of maximum surface evaporation is located where the maximum convection was situated 4 days earlier.

Hendon and Glick,(1997) analysed OLR from NOAA's polar orbiting satellite and surface fluxes of latent heat and radiation from ECMWF operational analyses. Their findings do not support the requirements for WISHE but are in support of frictional wave-CISK. Sperber *et al.* (1996) used satellite derived outgoing longwave radiation and reanalysis from the National Center for Environmental Prediction/National Center for Atmospheric Research to verify intraseasonal variability simulated in the Goddard Laboratory for Atmospheres and the UKMO atmospheric general circulation models. They find that WISHE is not responsible for the eastward propagation of the MJO and that frictional wave-CISK is not necessary to maintain the eastward propagation of the MJO.

4.3 Variability of MLS Water Vapour at 215 hPa

The following section will examine the variability of MLS water vapour in the tropical region by analysing time-series. The region between 32°N and 32°S is covered by the MLS instrument in both viewing directions and consequently, barring instrument failures, there are daily measurements of water vapour in the tropics.

Time-series of 520 days in length from the 1st December 1991 until the 3rd of May 1993 were created by interpolating the data using the regression retrieval and space-time interpolation method used by Jackson *et al.*, (1990). Footprints were interpolated onto grid points spaced every 5° in longitude around latitude circles at 20°N, 10°N, the equator, 10°S, and 20°S. Those that fell within a given 'search radius' (chosen to be 2150 km) of the grid points were given a weighting based upon the distance from it. The search radius of 2150 km corresponds to about 18° of latitude at the equator. The MLS orbit spacing is 15° at the equator and so the search radius therefore always captures a footprint. A scaling distance

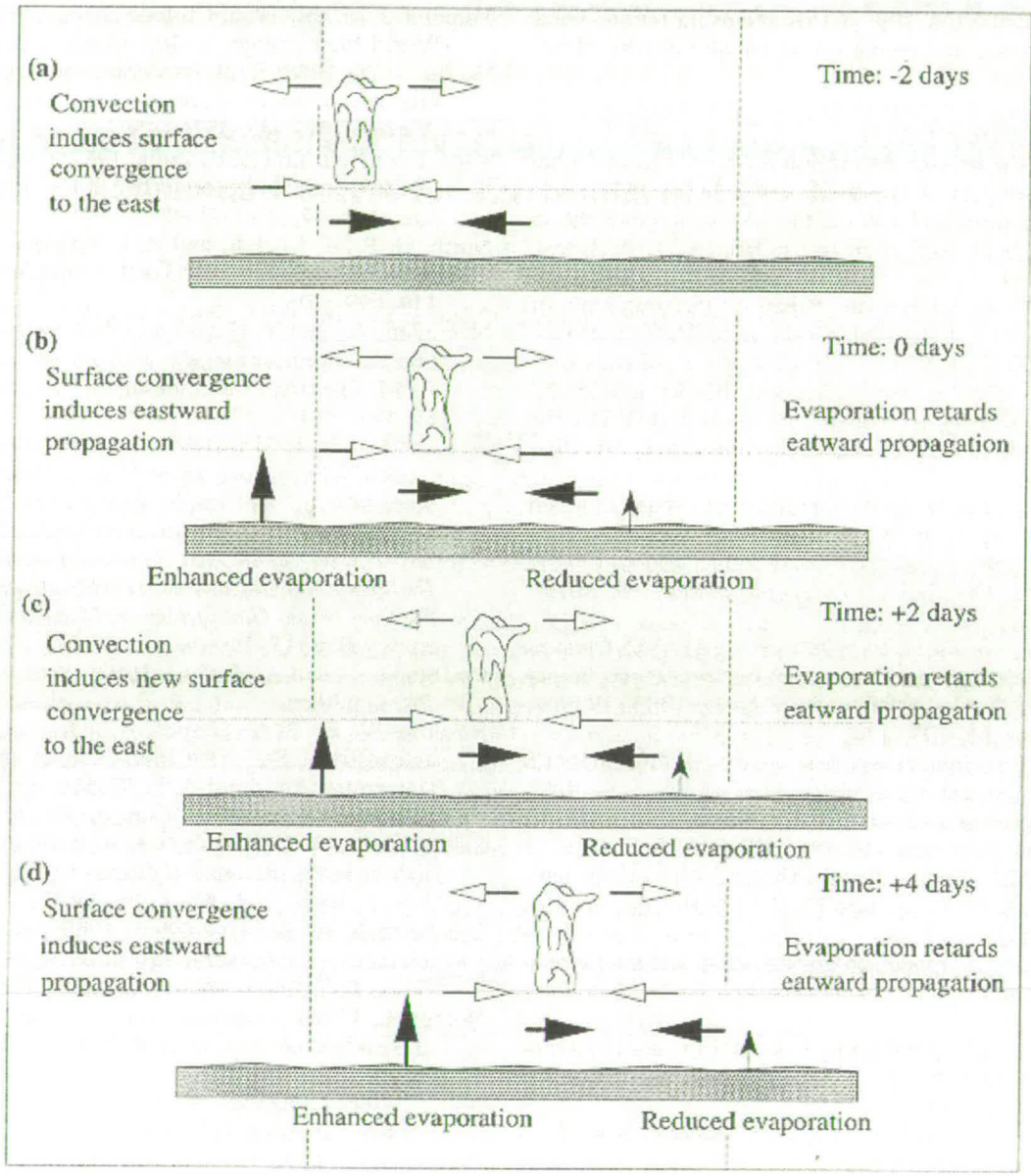

Figure 4.5: Propagation due to wave-CISK. Convection induces surface convergence to the east (a) which induces eastward propagation (b), in turn inducing new surface convergence (c) and eastward propagating (d), Jones and Weare,(1996)

of 1000 km was used meaning that footprints 1000 km away from the given grid point have a weighting of 1/e whereas any that fall directly on the grid point have a weighting of 1. This method of interpolation was used for MLS water vapour in the stratosphere by Black (1997).

Much of the following section uses Fourier transform and lag correlation techniques which require a dataset with no missing data. Data gaps were filled in time with a Kalman filter (Rodgers, 1996). When data is missing, the Kalman filter predicts the water vapour concentration based on the previous measurements, the amount by which the concentration changes from day to day and the error on the measurements. The filter is run both forwards and backwards in time and the two predictions are combined. Usually the data gaps were only of one or two days during the satellite yaw manoeuvres but there were some longer gaps when the instrument experienced technical difficulties. For the purposes of display, gaps longer than 4 days were masked. In all analysis, the Kalman filtered data was used.

4.3.1 The Annual Cycle

Longitude-time sections have been plotted for the selected latitudes in figures 4.6 to 4.14. The annual cycle is evident in each longitude-time section and has a pronounced longitudinal variation. To isolate the annual cycle so that it can be studied in more detail, it was removed by least squares fitting it to a sine wave with a cosine component to take account of phase differences.

The northern hemisphere latitudes, 20°N and 10°N are shown in figures 4.6 and 4.8 respectively. The two latitudes are similar in that the highest water vapour mixing ratios occur between 50°E and 120°E over the Indian Ocean and SE Asia from May to September when convection is strong. 10°N is overall more humid than 20°N where mixing ratios of 70 ppmv are reached during winter. Figures 4.7 and 4.9 show the variation with longitude in the amplitude of the annual cycle for 20°N and 10°N respectively. The variation with longitude is similar in both cases with the amplitude of the annual cycle being greatest in the region influenced by the Indian monsoon. At 20°N, 90°E, over the Bay of Bengal, it accounts for 80% of the variance in water vapour. This is considered in more detail in table 5.1. A secondary maximum occurs over Panama as Newell *et al.*, (1997) noted. Minima

occur in both cases over the Atlantic and eastern Pacific Oceans.

At the equator (fig. 4.10) the range of mixing ratios is narrower than the other latitudes. This may be a result of the position of the intertropical convergence zone (ITCZ) which is rarely situated at the equator itself (Philander *et al.* 1996). The maximum mixing ratios are located over the Indian Ocean and Indonesia. The minimum mixing ratios occur over the Eastern Pacific and are subject to an East-West migration on annual time-scales, resulting in lower values extending further west in June-August and further east from November-January.

The variation of the annual cycle with longitude is shown in figure 4.11. Its amplitude like the range, is least pronounced at the equator and again this is probably related to the off-equatorial position of the ITCZ. The maximum occurs at 90°W, off the coast of South America where it accounts for 53% of the variance. Table 5.1 looks at this in more detail. Water vapour variations in the region 80-90°W, 0-10°S have been shown by Newell *et al.,* (1997) to be closely related to the El Niño variations in sea surface temperature and also to anomalous changes in sea surface temperature which account for about 56% of the water vapour fluctuation. A secondary maximum occurs at 90°E, south of the Bay of Bengal, as was the case with the Northern Hemisphere latitudes. The minimum amplitude arises in the western Pacific ocean, which is warm all year round.

Longitude-time plots for 10°S and 20°S are shown in figures 4.12 and 4.14 respectively. Relative humidity is greater over Indonesia and South America during summer and lowest over the Eastern Pacific in winter. Mixing ratios are much higher at 10°S than at 20°S. A clear annual cycle can be seen over the African continent and South America in both plots and is illustrated more clearly in the corresponding figures 4.13 and 4.15, which show the variation in the strength of the annual cycle with longitude. Figure 4.13 for 10°S reveals further local maxima over Indonesia and South America and an anomalous peak over the Mid-Pacific. Figure 4.15 for 20°S shows the annual cycle to be strong over Africa and South America but there is a much less pronounced variation between 80°E and 280°E than at 10°S.

The influence of the cold Eastern Pacific in suppressing convection and giving rise to a drier upper troposphere and of the warm western Pacific leading to a moister upper troposphere is evident in figure 4.12. This constitutes the Walker

circulation with rising air in the west and subsiding air in the east. The influence of the Walker circulation on upper tropospheric water vapour from MLS has been noted by Newell *et al.* (1996) in two short periods of data from 17th September to 22nd October 1991 and 7th February to 14th March 1994. Here, the presence of the Walker circulation can be seen to be a more persistent feature. Mixing ratios over the Western Pacific show a similar east-west migration to that at the equator, with low humidity found further west during winter, when the ocean is colder. Eastward moving features during the summer months originate over the warm Indian ocean and are quickly terminated once they reach the Eastern Pacific. These have a higher frequency than the annual cycle and are investigated by analysing the time-series with a focus on intraseasonal time-scales.

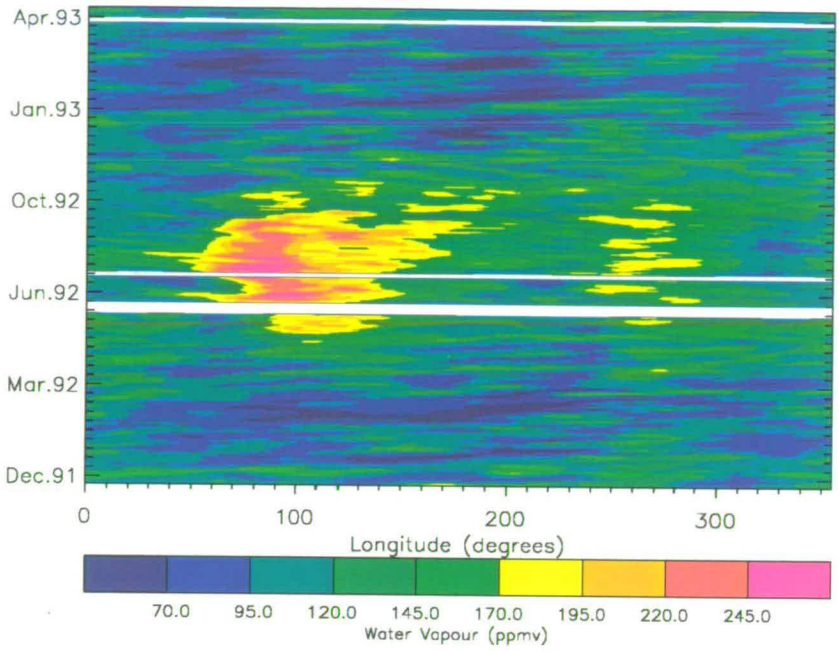

Figure 4.6: Longitude-time sections of water vapour mixing ratios at 215 hPa and 20 °N. Data have been Kalman filtered and a mask applied to gaps longer than three days.

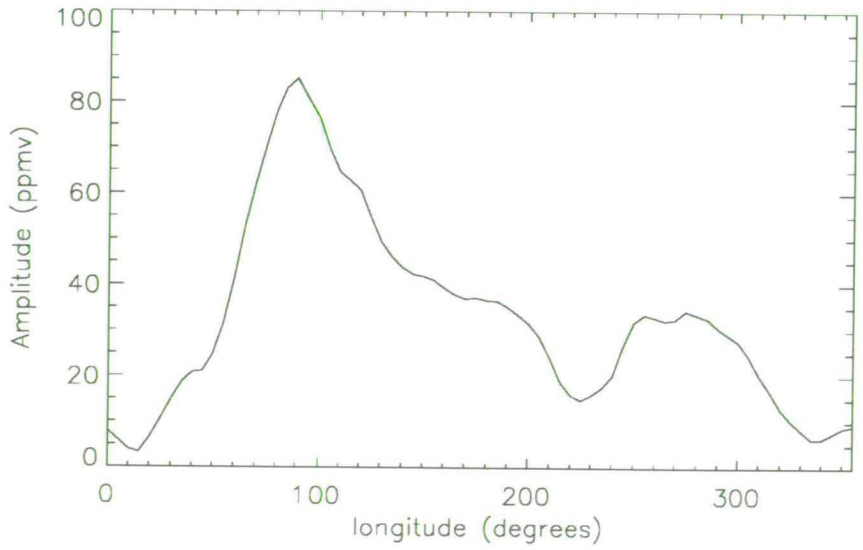

Figure 4.7: Variation in amplitude of the annual cycle with longitude for 20°N and 215 hPa.

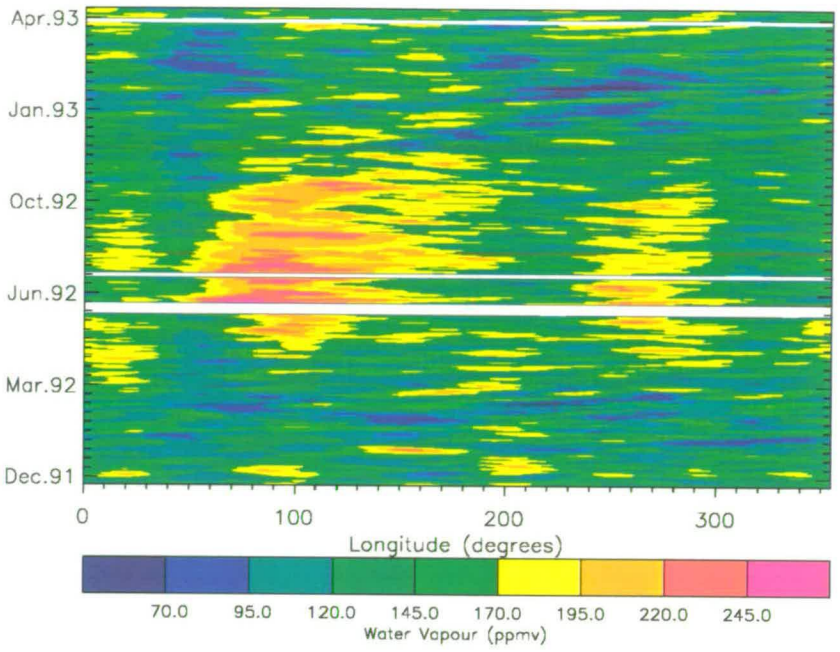

Figure 4.8: As for figure 4.6 but for 10°N.

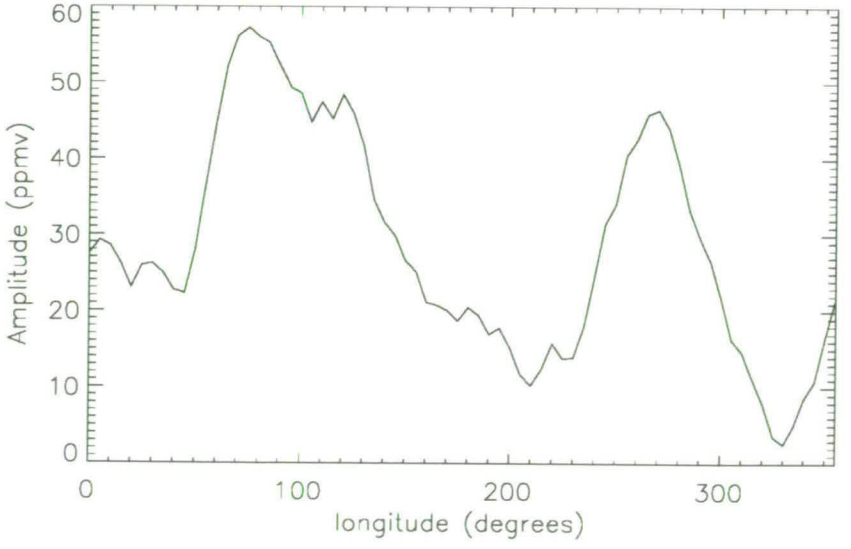

Figure 4.9: As for figure 4.7 but for 10°N

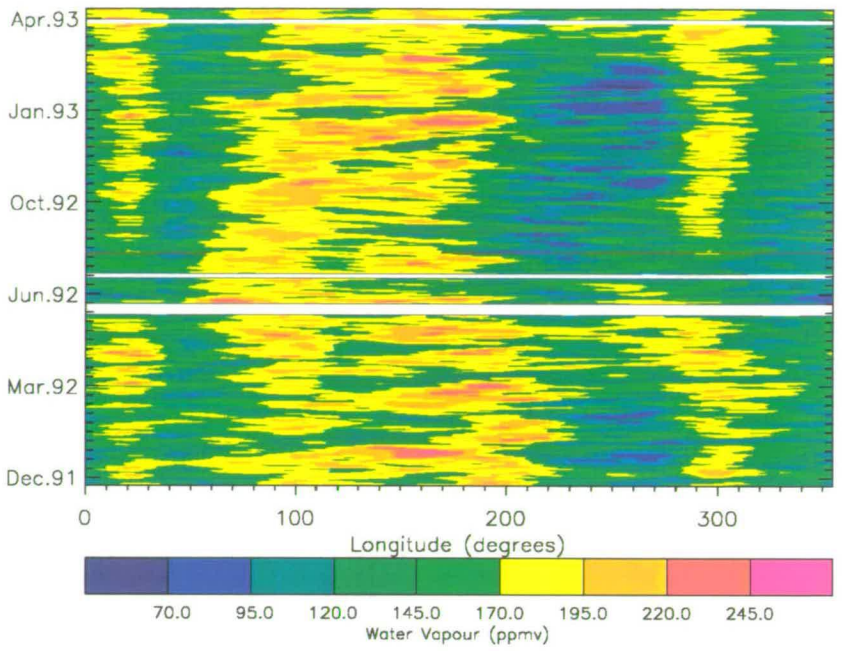

Figure 4.10: As for figure 4.6 but for 0°.

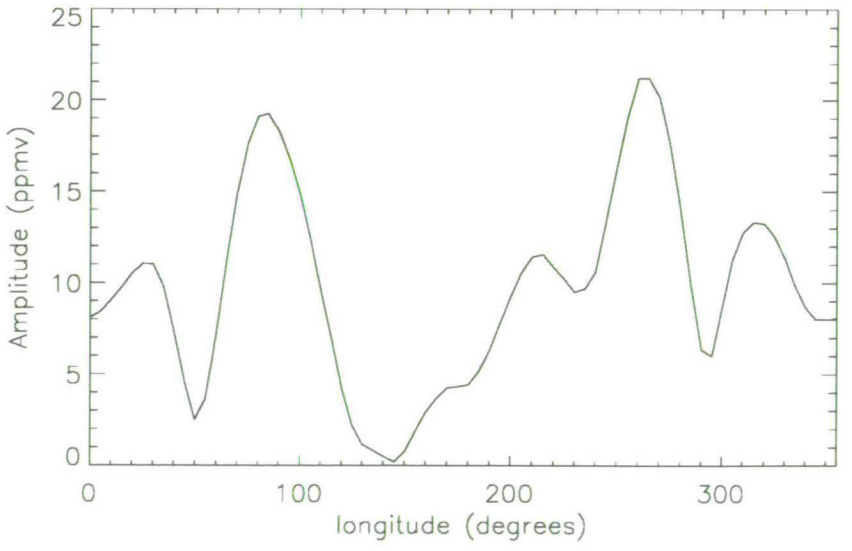

Figure 4.11: As for figure 4.7 but for 0°

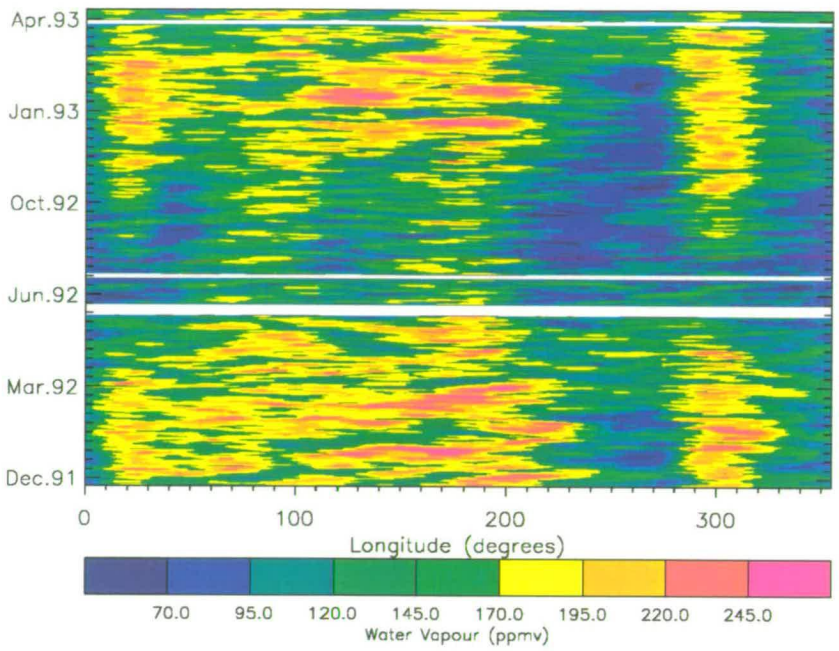

Figure 4.12: As for figure 4.6 but for 10°S.

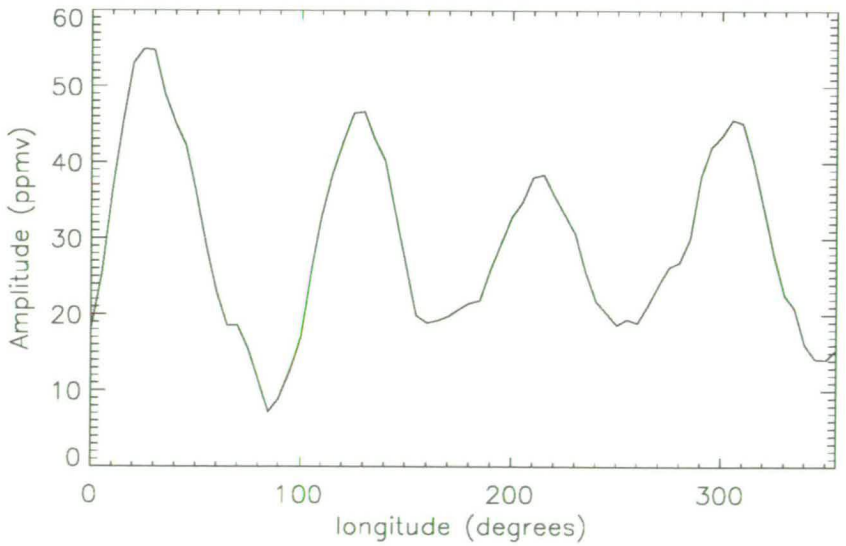

Figure 4.13: As for figure 4.7 but for 10°S

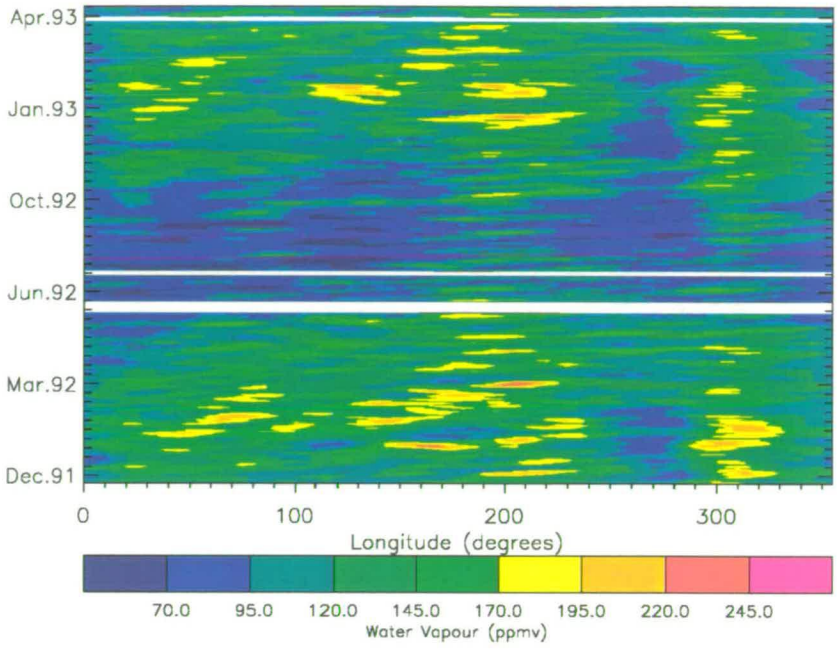

Figure 4.14: As for figure 4.6 but for 20°S.

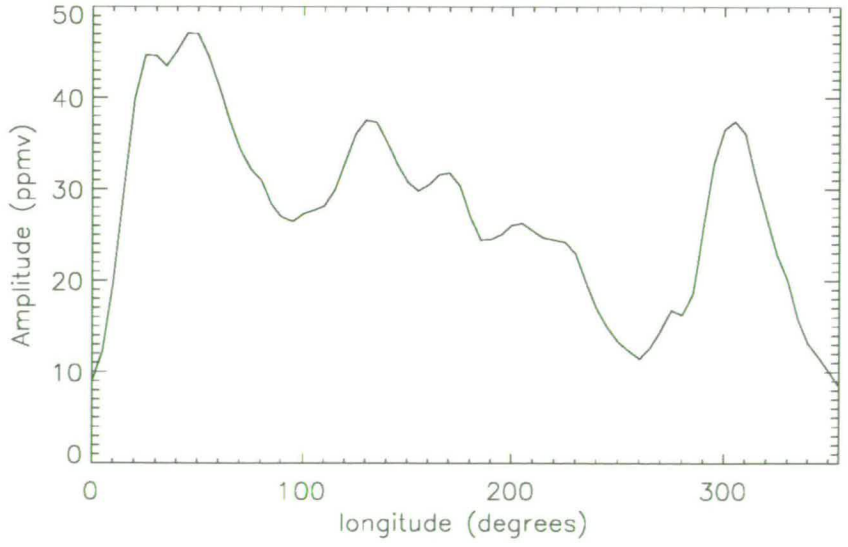

Figure 4.15: As for figure 4.7 but for 20°S

4.3.2 Intraseasonal Variability

One of the main modes of variability in the tropics is the Madden-Julian Oscillation (MJO) (Madden and Julian, 1971). The MJO comprises large scale circulation anomalies associated with convective anomalies which propagate eastwards at 3-6ms^{-1}. The dynamical signal of the MJO in for example zonal wind or surface pressure has a period of 30-60 days and can be detected across the tropics. The convective signal (seen in outgoing longwave radiation) has a broader range of 30-95 days (e.g. Kiladis and Weickmann, 1992 and Salby and Hendon, 1994) and is strongest in the Indian Ocean and Western Pacific.

Eastward moving features are apparent in the water vapour fields (figure 4.12) and are most prominent at 10°S in southern summer. The moist anomalies at 10°S cover longitudes from 90°E to 245°E (115°W). One such feature begins at 105°E and travels to 190°E in about 22 days, thus moving with a speed of about 5ms^{-1}.

At the equator during southern summer there are similar eastward moving features to those at 10°S but they are less intense and during southern winter, there are only limited signs of eastward propagation. Similar propagation of moist anomalies occurs in summer at 10°N with a more limited longitudinal extent, being confined mostly to the Indian Ocean. There is also evidence for the eastward movement of dry features between 130 and 280°E in northern hemisphere winter at 10 and 20°N. In this section however, the eastward moving moist features and their relationship to the MJO will be discussed. The discussion will focus on 10°S, where the anomalies are associated with the highest mixing ratios.

Figure 4.16 shows the lag correlogram at 160E, 10°S based on the 520 days of data used for figure 4.12. The annual cycle and low frequency variability was removed from each longitude using a 150 day Butterworth filter (appendix A). This is a more effective method than that of least squares fitting, which removes only a single sine component. The filter removes all periods greater than 150 days. Also shown is the red noise background spectrum computed from lag-one autocorrelation (Gilman *et al.*, 1963). The data have anticorrelation < -0.2, at lags of 20–35 days, well above the red spectrum and significant at the 95% level. This is suggestive of waves of period 40-70 days and this interpretation is sup-

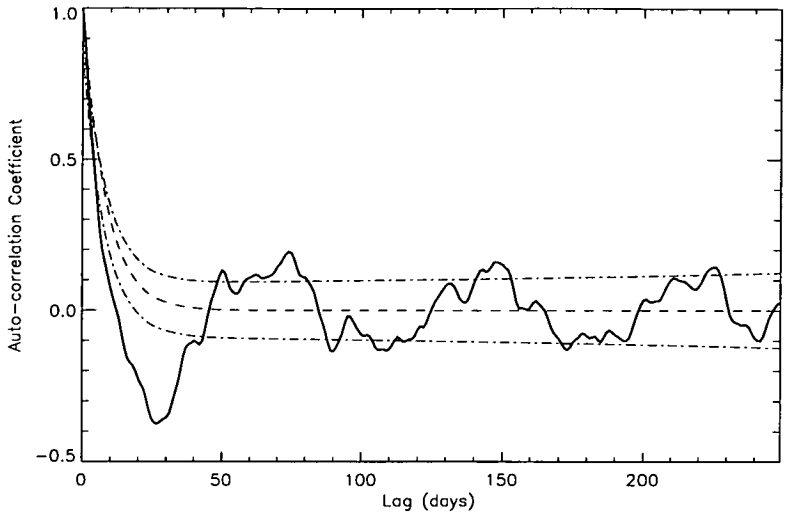

Figure 4.16: Auto-correlation of the time-series at 160° E, 10 °S (continuous line) and red noise (dashed line)

ported by the existence of positive correlations at lags of 40-70 days. Inspection of figure 4.12 suggests that these correlations arise from features which are only apparent in the southern summer months and since only slightly over one cycle is apparent in each year, very high correlations cannot be expected. Moreover the magnitude of the correlation at the wave period will be necessarily less than that at the half period.

By cross-correlating the time-series at each longitude with a reference longitude (chosen to be 160°E) using different lags, the eastward propagation and the cyclical nature is clearly illustrated (see fig. 4.17). At longitudes to the west of 160°, the higher correlation coefficients correspond to negative lags and east of 160°E the lags are positive. The propagation speed can be more easily estimated from this plot. Between 105° and 190° the correlation coefficient is greater than 0.4 and remains at this level for 22 days. This gives a propagation speed of $4.9 \mathrm{ms}^{-1}$. Around the dateline, there appears to be a discontinuity with almost a 180° phase shift. This may be due to the increased propagation speed of convective anomalies or circulation that has been widely observed east of the

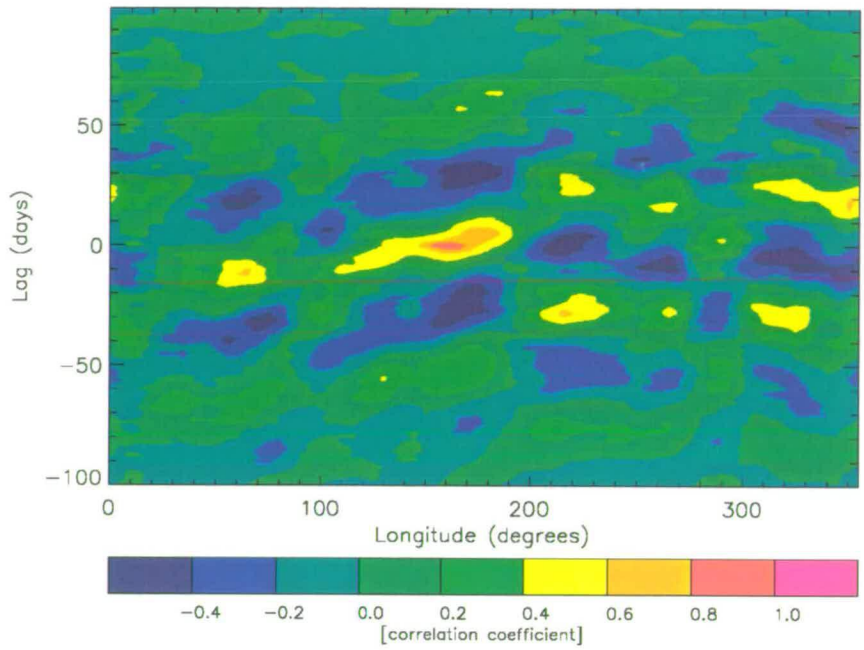

Figure 4.17: Cross correlation of each longitude with 160°E and 10°S at different lags.

dateline (e.g. Hendon and Salby, 1994). West of the dateline, surface zonal winds move eastwards along with convection at $5ms^{-1}$, but east of the dateline, phase speeds increase to $10ms^{-1}$. The cross correlation plot is very similar to the extended empirical orthogonal functions (EEOF) of the same data, shown in Clark *et al*, (1998). They interpreted EEOF 1 and 2 as an eastward propagating mode, and EEOF 3 and 4 as a zonally symmetric mode. The discontinuity around the dateline in figure 4.17 fits with this interpretation.

Figure 4.18 shows how the power at each frequency varies with longitude for 10°S. The strongest signal corresponds to frequency of 0.014 days $^{-1}$ or time-period of 70 days and falls within that associated with the convective signal of the MJO. Variability with periods of 70 days have also been noted in ocean studies. For example in the depth of the 20°C isotherm in the western Pacific (e.g. Kessler *et al.*, 1995; McPhaden and Taft; 1988, Hendon *et al.*, 1998). The power spectrum was tested for significance at 95% by computing the signal to red noise ratio and comparing it with the chi-squared distribution following the method of Gilman *et al.*, (1963). At 70 days, values greater than 112 $ppmv^2$ are

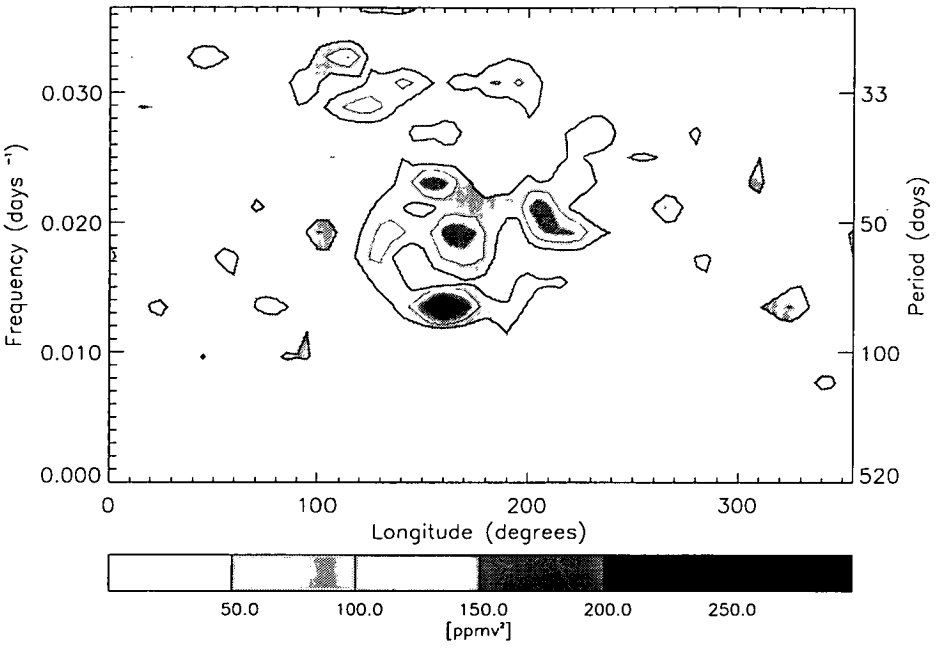

Figure 4.18: Variation in power at each wavenumber for each longitude around a latitude circle at 10 °S (contour intervals are 50 ppmv^2).

significant. The signal is confined in longitude from 140 to 180 °E. This area, over the Western Pacific, has been shown to exhibit strong intraseasonal variability in outgoing longwave radiation (OLR) which is often used to infer deep convection. Salby and Hendon (1994) examined 10 years of outgoing longwave radiation data from the Advanced Very High Resolution Radiometer (AVHRR) and found that intraseasonal behaviour was coincident with centres of climatological convection and warm sea surface temperature, with maxima over the Indian Ocean and Western Pacific and secondary maxima over the Eastern Pacific, Africa and South America. They noted that most of the intraseasonal variance occurred over the Indian Ocean. This contrasts with the signal in water vapour which is dominant over the Western Pacific. The absence of signal in the water vapour field over the Indian Ocean indicates that convective moistening is not reaching the 215 hPa level.

A filter of similar width to that used in studies of OLR (e.g. Salby and Hendon, 1994; Zhang and Hendon, 1997) was applied to the water vapour data. A 30-85 day Butterworth band-pass filter was chosen to capture the eastward moving

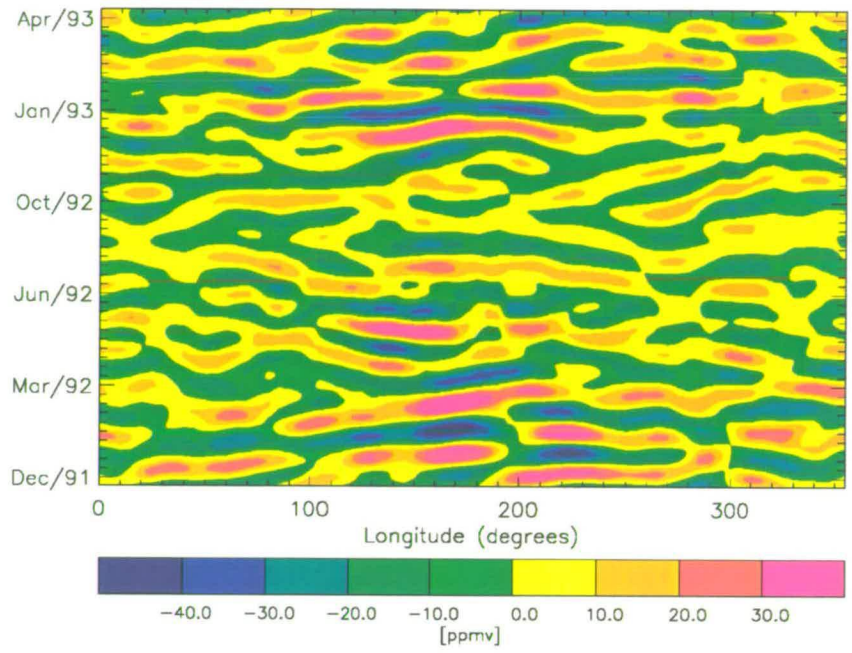

Figure 4.19: 30-85 day band-pass filtered Hovmoller plot at 10°S

disturbances that were identified from the unfiltered data. Figure 4.19 shows the 520 day Hovmoller plot at 10°S after the 30–85 day filter has been applied. Similar discontinuities to those in 4.17 can be seen east of the dateline in December 1991 to March 1992 and to a lesser extent from December 1992 to March 1993. When applied to 520 days of data at 10°S, 160°E it accounted for 38% of the total power compared with 21% for the annual cycle. Mixing ratios in this band vary by ± 60 ppmv and the precision of the measurements is ± 5 ppmv. At the equator, intraseasonal activity occurring in the 30-85 day band accounts for 35% less power than at 10°S.

At 10°S the water vapour anomalies, consistent with the OLR signal Salby and Hendon (1994), possess a strong seasonality which is apparent in the time longitude section (figure 4.12). The eastward propagating anomalies are strong from December to March and virtually absent from June to October when the ITCZ has migrated north of the equator. This is reflected in the differing percentage variance for which the filter band accounts throughout the year. Over a 120 day period in December-March 1991/92 (see figure 4.20) intraseasonal variability

accounts for 63% of the power compared with 26% for April-July and 7% for August-November.

Interannual Variations

There have been suggestions that the MJO varies in strength from year to year and that this may be related to the ENSO phenomenon (e.g. Lau and Chan, 1986). With this in mind, the behaviour of upper tropospheric water vapour was investigated for other years. The data gaps, which have increased in length as the spacecraft and instrument have aged make later years more difficult to study. Longitude-time sections for southern summer periods are shown for 10°S for all the available MLS data in figures 4.20 to 4.24. The summer of 1994–95 is left out as there was very little data available.

In most years, mixing ratios greater than 170 ppmv never extend further east than 210°E (150°W). Knutson and Weickmann (1987) noticed similar behaviour in OLR and proposed that low sea surface temperatures or descending motion associated with the Walker circulation suppress further eastward development. In 1991–1992, an El Niño year (Trenberth, 1997) (fig. 4.20), mixing ratios of between 170 and 195 ppmv reach as far as 240°E (120°W), signs of eastward propagation are the most apparent and the 30-85 day MJO filter band accounts for 63% of the variance. The greater extent of the anomalies in 1991–1992 may be a result of the Eastern Pacific being warmer due to El Niño and more favourable for convection.

In the following year, (1992–1993 shown in fig. 4.21) 52% of the variance can be explained by intraseasonal activity and there are signs of eastward propagation albeit more limited in extent. The summer of 1993/94 (fig. 4.22) has the same range of mixing ratios as 1991/92 but even less sign of eastward propagation.

1996/97 (fig. 4.24) was a La Niña year (Trenberth, 1997) when the Eastern Pacific is anomalously cold. It may be expected that convection would be suppressed and mixing ratios low but, from the limited data available, mixing ratios can be seen to be as high as those in 1991/92, and there may even be signs of eastward propagation in late February and early March. Mixing ratios under these La Niña conditions are not as low as in 1995–96 (see fig. 4.23) when mixing ratios of less than 70 ppmv were reached over the Eastern Pacific and remained

below 245 ppmv for the whole period.

Although in 1991–1992 the strongest MJO event coincided with an El Niño event, it is not possible to say that strong MJO events necessarily occur under El Niño conditions. Weak MJO events do not seem to be related to La Niña conditions. Salby and Hendon (1994) found that the convective signal was absent during the strong ENSO cycle of 1982-1984 even though it was evident in the weaker ENSO episode of 1986-87. The relationship between the occurrence of MJO events and ENSO conditions warrants further investigation.

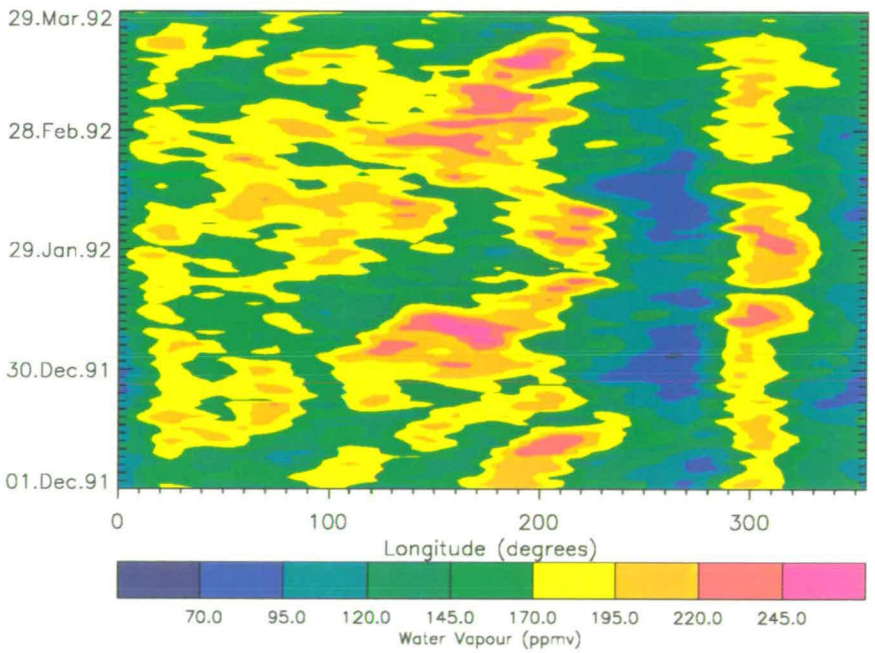

Figure 4.20: Time-longitude sections at 10°S for 120 days of southern summer. Data have been Kalman filtered and a mask applied to gaps longer than three days.

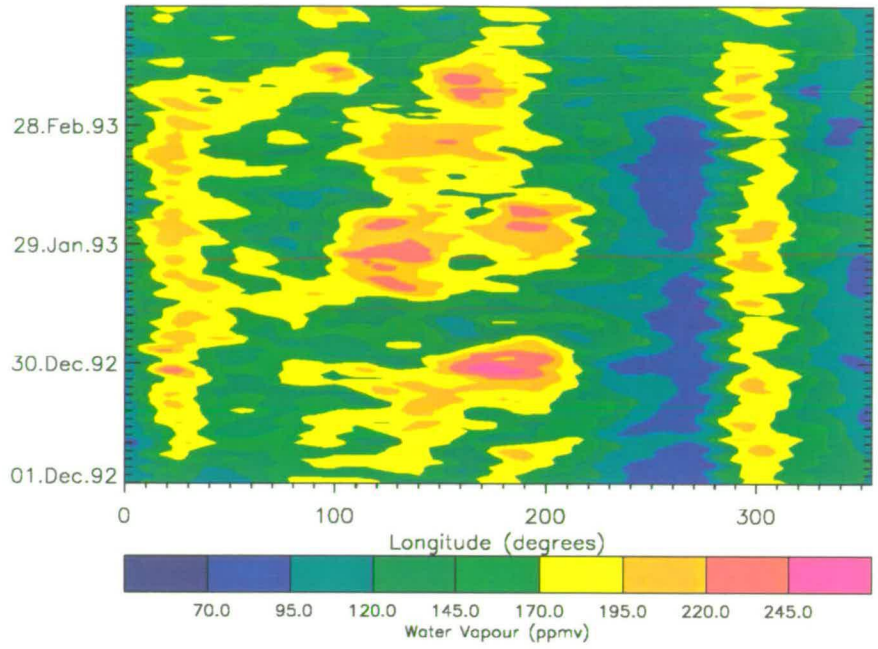

Figure 4.21: As for figure 4.20 but for 1992/93

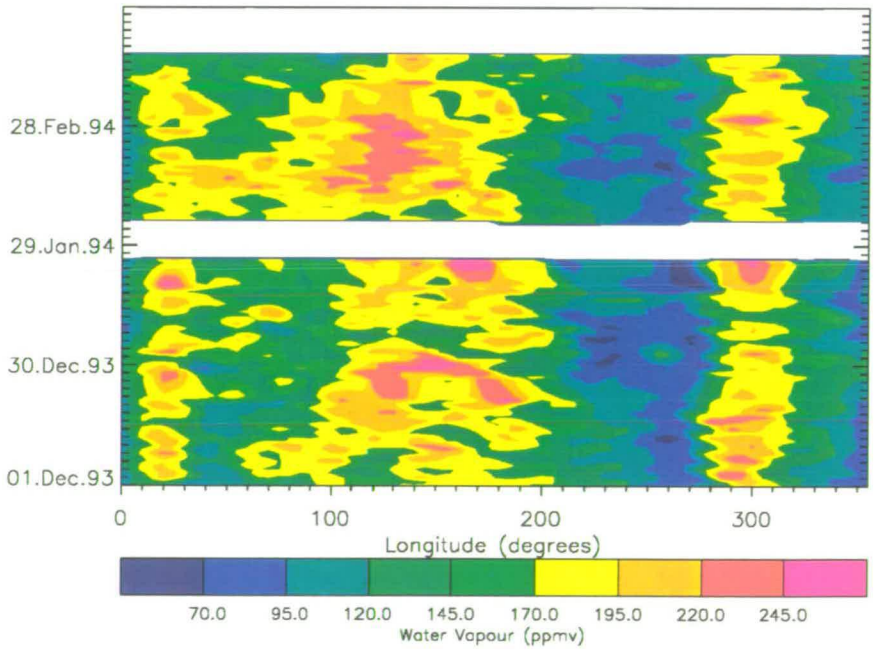

Figure 4.22: As for figure 4.20 but for 1993/94

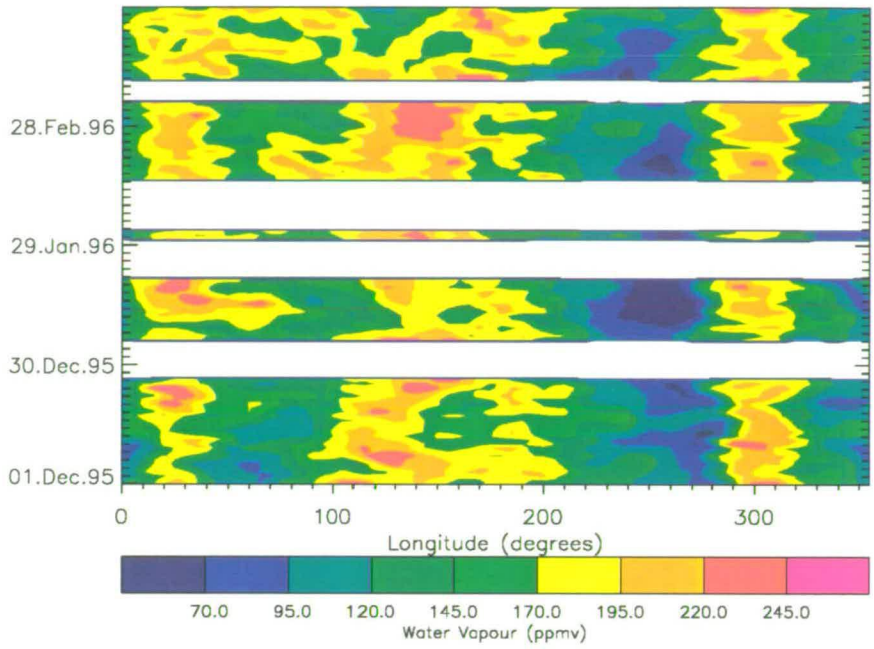

Figure 4.23: As for figure 4.20 but for 1995/96

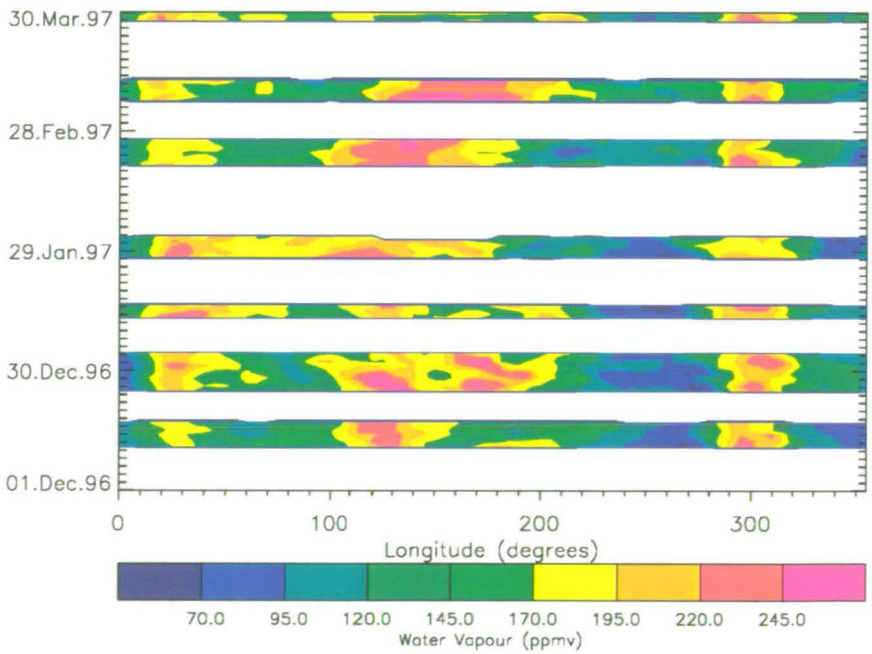

Figure 4.24: As for figure 4.20 but for 1996/97

4.4 Conclusions

This chapter has focused upon the upper troposphere in the tropical region between 20°N and 20°S. The construction of time-series and the methods of time-series analysis used in the chapter have allowed the investigation of temporal variability on a range of timescales. The annual cycle and its variation with longitude have been examined in more detail than previously and water vapour has been found to exhibit variability on intraseasonal timescales.

The annual cycle can account for up to 80% of the variability of water vapour in the tropics. It is most pronounced over the landmasses of South America and central Africa. In general, the oceans have a moderating effect on the annual cycle but local maxima occur in regions influenced by the Asian monsoon and over Indonesia and the Central Pacific.

The time-longitude section for 10°S revealed regions of high water vapour mixing ratios which moved eastwards at $5ms^{-1}$ across longitudes from 90-245°E and which were most prominent from December to March 1991–1992. Lag correlations of the 520 day time-series at 10°S showed there to be a cycle with period of 40-70 days and power spectrum analysis shows the power to be concentrated at periods from 30-85 days at longitudes from 140-180°E; the strongest signal being found at 160°E.

Wavenumber-frequency analysis presented in Clark *et al.*, (1998) revealed that the power in this 30-85 band was concentrated into two main frequency bands, 70 days and 30-60 days. The power at 70 days was at zonal wavenumber 1 and was subsequently interpreted as being a zonally symmetric mode. The power in the 30-60 day range was at eastward wavenumbers 1-3 and interpreted as a propagating mode (Clark *et al.*, 1998). EEOF analysis revealed eastward propagation between 75°E and 200°E with a period of 55 days, and a further oscillation at 35 days with no identifiable propagation and broadly distributed in longitude. These EEOF plots were similar in appearance to the cross-correlation and filtered longitude-time section and have a discontinuity over the dateline with the eastern hemisphere out of phase with the western.

The 30-60 day propagating mode is likely to be a Kelvin wave response to the broader timescale oscillation in tropical convection associated with the MJO.

Standing components to tropical convection which have been observed in OLR and 150 hPa divergence (e.g. Hsu *et al.,* 1990; Zhu and Wang,1993; Zhang and Hendon, 1997), may account for the power at 35 and 70 days.

The main finding of this chapter is that water vapour in the tropical upper troposphere at 215 hPa varies on intraseasonal timescales. It is proposed that this is related to the convective anomalies of the Madden-Julian oscillation. To strengthen the suggested association with convection, the water vapour field will be compared with other meteorological variables in the next chapter. Sequences of days within an 'MJO' event will be studied and compared in detail with synoptic maps so that the evolution and development of the eastward moving features can be followed.

Chapter 5

Relation to Other Meteorological Fields

The aim of this chapter is to examine other datasets in order to establish a firmer link between the eastward moving features identified in the previous chapter, and the MJO. Firstly, NVAP and ECMWF data are examined to see whether the eastward moving features are apparent in other datasets or whether they are uniquely observed by MLS. The annual cycles which are also evident in these plots will be compared and contrasted with the equivalent from MLS.

Dynamical quantities from the ECMWF reanalysis will also be examined to determine a physical explanation of the variability in the MLS field. The lifecycle of an MJO event will be studied and compared with ECMWF and NVAP data. Finally, two other levels of MLS data will be examined to investigate the vertical structure of the eastward moving features.

5.1 Moisture Fields

This first section examines the equivalent longitude-time sections of total precipitable water and relative humidity and compares annual and intraseasonal features to those from MLS.

5.1.1 NVAP Total Precipitable Water

The longitude-time plot for total precipitable water from NVAP for 20°N is shown in figure 5.1. There is a short gap in January 1992 where values were virtually zero, indicating some problem with the data. As with the plot of MLS UTH (fig.

4.6) at this latitude, the TPW is highest between 50 and 120°E, during the time of strong convection which occurs over the Indian sub-continent during summer. The high degree of similarity between this plot and the equivalent from MLS is reflected in a high correlation coefficient of 0.80. The annual cycle in TPW at 20°N (fig. 5.2) varies with longitude in a similar manner to the MLS mixing ratios (fig 4.7). The amplitude, being greatest at 90°E and accounting for 83% of the variance, is the strongest throughout the tropics (see table 5.1). A secondary maximum occurs over South America, as can be seen in the longitude-time section and which compares well with that in MLS data.

As with MLS UTH at 215 hPa, NVAP TPW show that 10°N (fig. 5.3) is more humid than 20°N (fig. 5.1). The high mixing ratios over the Indian Ocean and South-East Asia in MLS data (fig. 4.8) are noticeable as greater TPW in the longitude-time section for NVAP data. The NVAP field shows there to be more moisture across the Pacific Ocean between 140-240°E than is indicated in the MLS field. Also more moist is the region 0-40 and 345-360°E (i.e. 15°W-40°E) over northwest Africa. These areas of higher moisture may be caused by shallower convection moistening the 500-300 hPa layer which does not reach and moisten the 215 hPa level. These differences cause the correlation coefficient to be 0.65; much lower than the correlation at 20°N. The annual cycle has maximum amplitude at 90°E (c.f.75° for MLS, table 5.1) where it accounts for 64% of the variance. The overall variation with longitude, illustrated in figure 5.4, is very similar to that in MLS data (fig. 4.9) with large peaks over Africa and off the coast of Panama, and deep minima over the eastern Pacific and the Atlantic oceans.

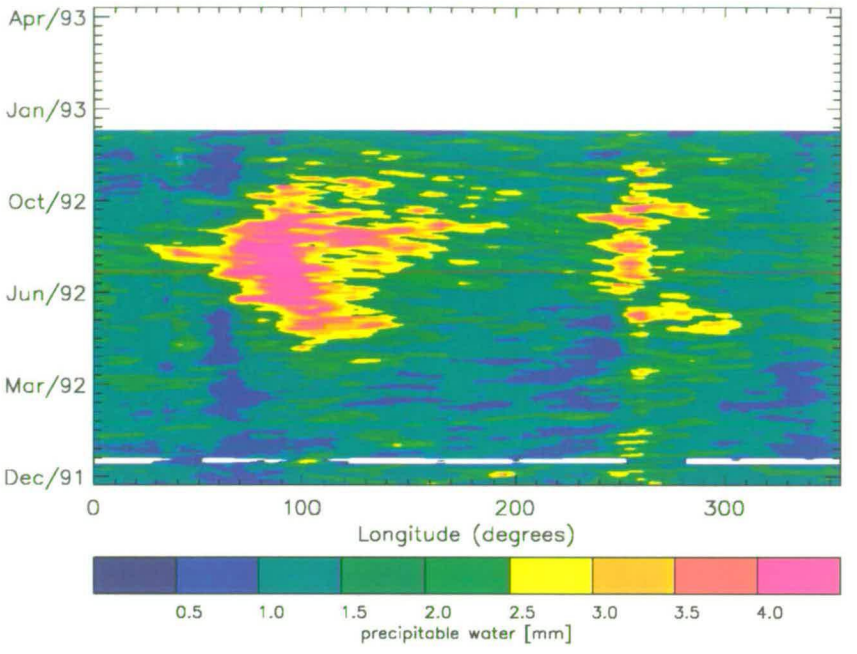

Figure 5.1: Time-longitude section of NVAP, 300-500 hPa precipitable water at 20°N.

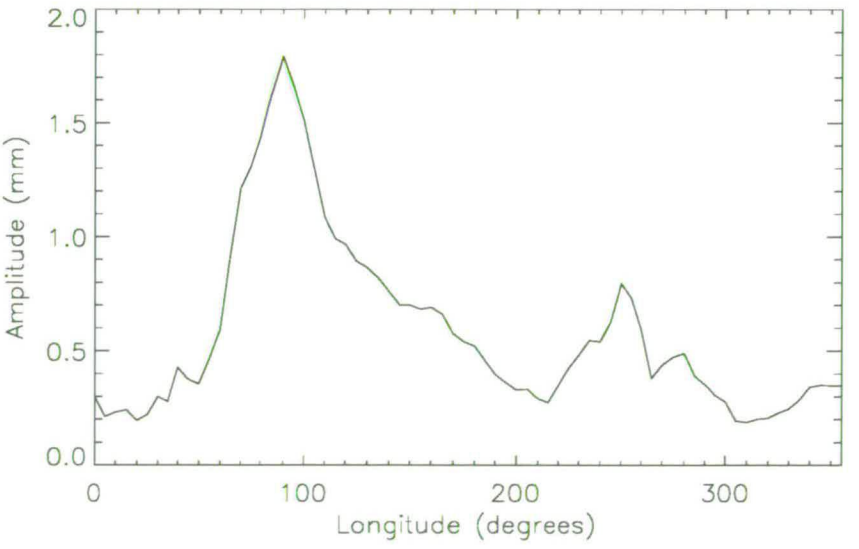

Figure 5.2: Variation with longitude of the annual cycle in NVAP, 300-500 hPa precipitable water at 20°N.

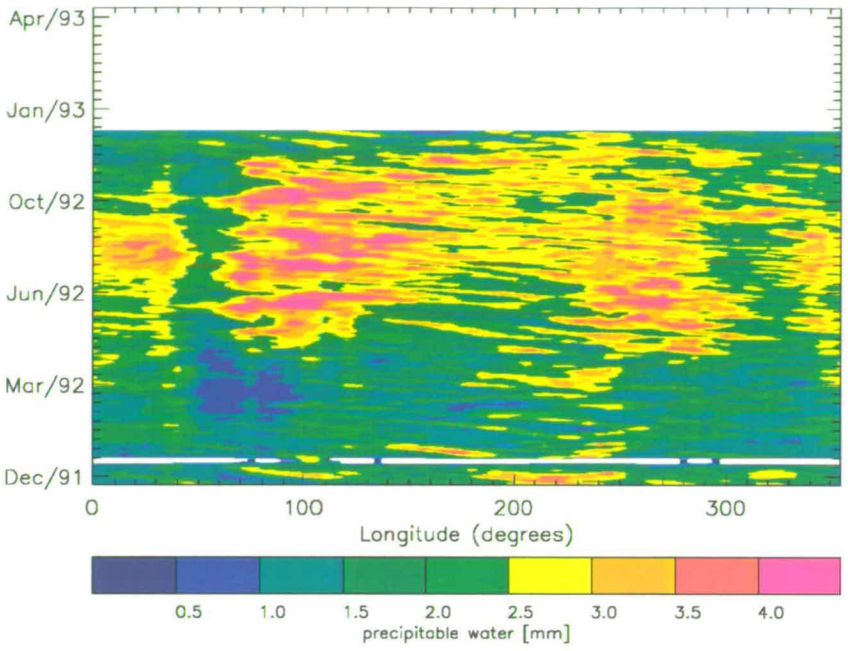

Figure 5.3: As for figure 5.1 but for 10°N

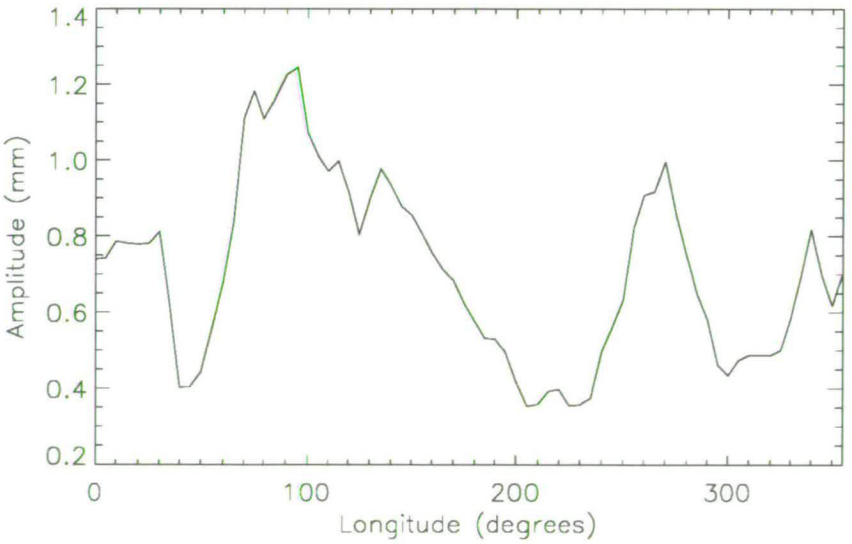

Figure 5.4: As for figure 5.2 but for 10°N.

The longitude-time section for the equator is shown in figure 5.5. Africa, South America and Asia can be seen to be moist all year round. There is also a great deal of moisture over the Pacific extending all the way across the eastern Pacific to South America between March and June. There is slight evidence for this in the MLS data (fig, 4.10) but it is much less marked. It appears that there will be a similar East-West migration of low TPW over the western Pacific as was seen in MLS data. The correlation coefficient between MLS and NVAP at the equator is 0.61, even less than at 10°N.

The variation in amplitude of the annual cycle around the latitude circle is strikingly different in NVAP data (fig 5.6) than in MLS data (see fig. 4.11). In NVAP, the annual cycle is most pronounced in a broad region over the Pacific Ocean from 180°E to about 250°E and contrasts with the much narrower peak in MLS data at 260°E. The broad peak corresponds to the region of high TPW which occurs from March to June and which has no such counterpart at 215 hPa. A secondary maximum occurs over South America, as is the case in MLS data, but whereas the annual cycle in UTH has a further maximum over Africa, this is much less obvious in NVAP data.

At 10°S (fig 5.7) TPW is highest over Africa, the Indian Ocean, western Pacific and South America between December and April. The lowest values of TPW are located over the eastern Pacific between April and October during southern hemisphere winter. In contrast to the eastern Pacific at the equator, the eastern Pacific at 10°S, remains dry throughout the year. The correlation coefficient of 0.74 reflects the high degree of similarity between the NVAP TPW and MLS fields.

The high TPW amounts over South America and low TPW amounts over the eastern Pacific is indicative of the Walker circulation which is evident for most of the year, except during June when TPW falls over South America. The variation with longitude of the annual cycle (fig 5.8) is very similar to that of MLS (fig. 4.13) with maxima over Africa, Indonesia, South America and over the Eastern Pacific. On shorter time-scales, the eastward moving features between 75 and 230°E during the winter months of 1991–1992 that are noticeable in the MLS field (see fig. 4.12), are also evident in the NVAP field. This implies that the features at 215 hPa depend on processes such as convection which take place

below. Intraseasonal variability of cloud liquid water from SSM/I has been noted by Weng *et al.* (1997) in a time-longitude section averaged between 10°N and 10°S.

At 20°S the TPW field is similar to the MLS water vapour field, the correlation coefficient being 0.71. TPW is on average, lower than at 10°S. The highest quantities are again over the continents and over the western Pacific and the lowest over the eastern Pacific. The annual cycle, although generally weaker than at 10°S varies with longitude in a similar way (see fig. 5.10) and compares well with the equivalent from MLS. It is greatest at 45°E and there are further maxima over Indonesia and South America.

In all cases, the patterns of TPW are very similar to those of UTH and this is reflected by the correlation coefficients. The high correlation coefficients indicate the similarity between the annual cycles in both fields. The highest correlation coefficient is at 20°N where the annual cycle is also maximum. The lowest correlation coefficient is at the equator, due mainly to the annual cycle in MLS data being a minimum here, but also caused by the excess of moisture over the eastern Pacific in NVAP compared with MLS.

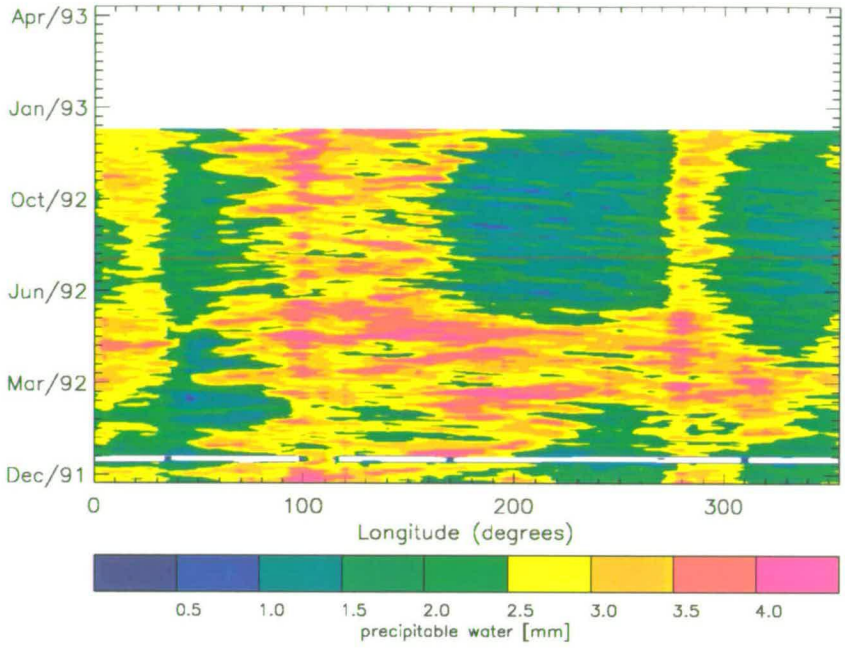

Figure 5.5: As for figure 5.1 but for 0°

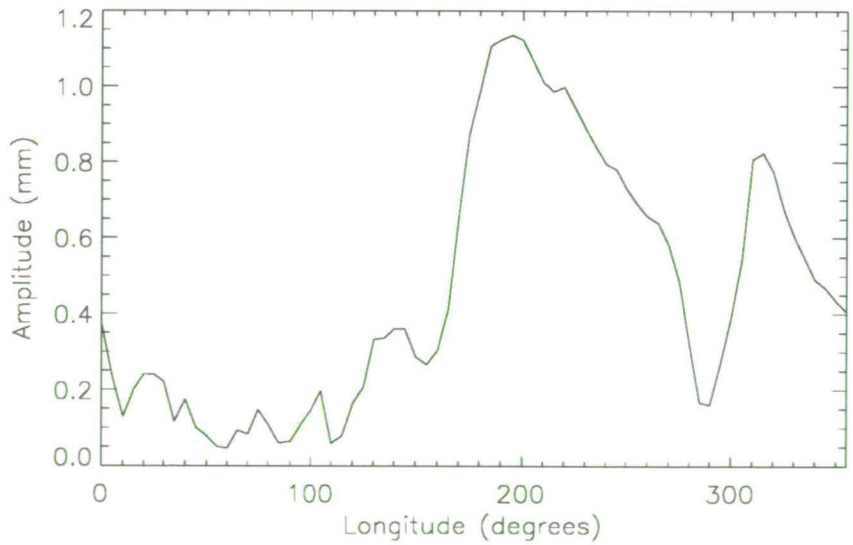

Figure 5.6: As for figure 5.2 but for 0°.

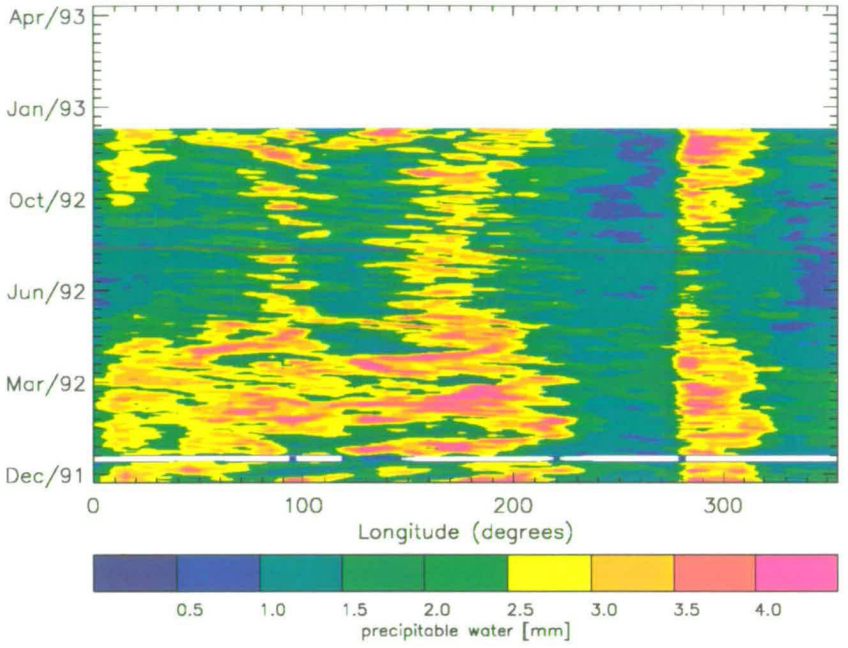

Figure 5.7: As for figure 5.1 but for 10°S

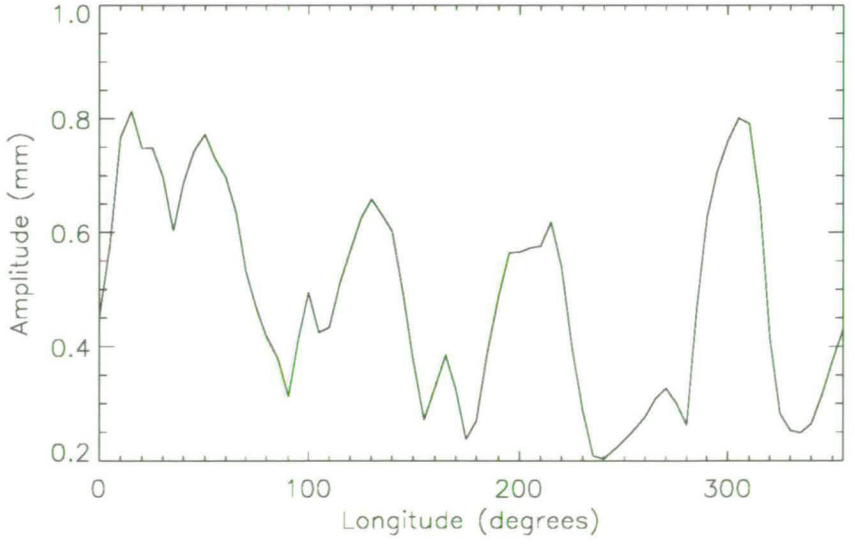

Figure 5.8: As for figure 5.2 but for 10°S.

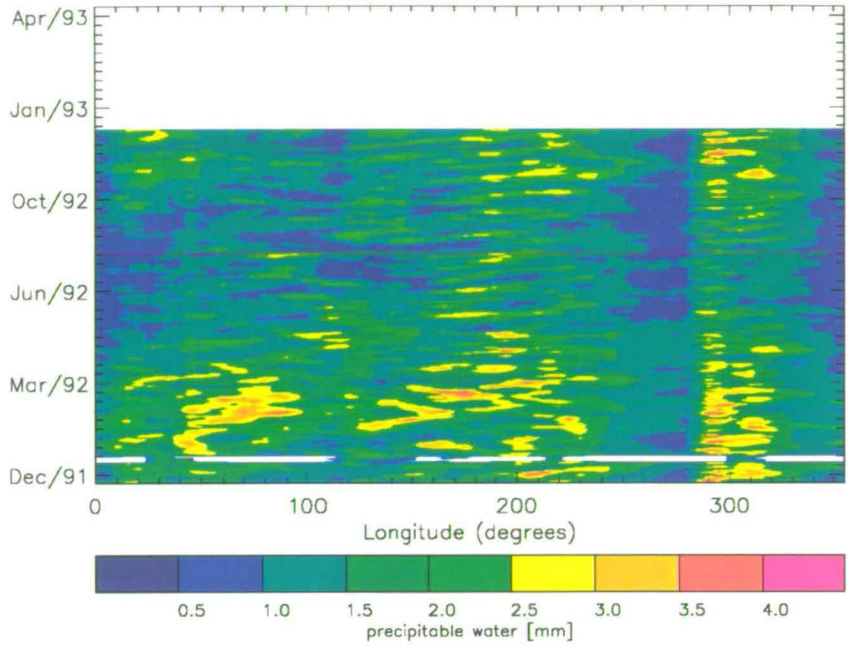

Figure 5.9: As for figure 5.1 but for 20°S

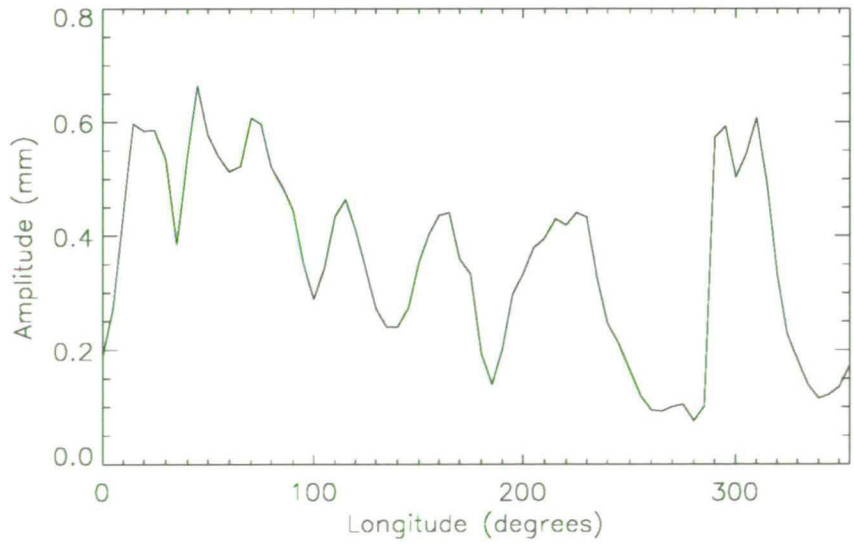

Figure 5.10: As for figure 5.2 but for 20°S.

Latitude (°)	Longitude of Maximum Amplitude (°)			Maximum % Variance accounted for		
	MLS	NVAP	ECMWF	MLS	NVAP	ECMWF
20 N	90 E	95E	95E	80	83	84
10 N	75 E	90E	70E	61	64	79
0	85 W	160W	160W	54	65	65
10 S	25 E	40E	80W	76	50	54
20 S	45 E	45E	45E	64	50	70

Table 5.1: Table showing the strength and position of the largest annual cycle at each latitude.

5.1.2 ECMWF Relative Humidity

In the northern hemisphere, (figs. 5.11 and 5.13) the features seen in longitude-time plots of ECMWF relative humidity (RH) at 200 hPa are similar to those seen in MLS UTH and NVAP TPW. Over Africa and south-east Asia, RH values are high during summer and much lower during winter. Over oceanic regions ECMWF RH remains comparatively low all year round. 10°N is generally moister than 20°N, as observed in both MLS and NVAP datasets. Over south-east Asia at 10°N, the ECMWF moist area is much less confined in area than in MLS and NVAP. At 10°N, the moist area extends right across the Pacific Ocean which is indicated in both MLS and NVAP fields as being much drier. This causes the secondary maximum in the annual cycle to be broadly peaked (from 180–280°E) in comparison to that in MLS UTH and NVAP TPW where the peak extends from 230–290°E. The maximum annual cycle which occurs at 20°N, 95°E accounts for around 80% of the variance; this being the largest amplitude seen throughout the tropics (see table 5.1). The position and percentage variance accounted for compare well with MLS UTH and NVAP TPW. At 10°N the position of the maximum annual cycle in ECMWF RH is similar to that in MLS UTH and NVAP TPW but it accounts for 15% more variance.

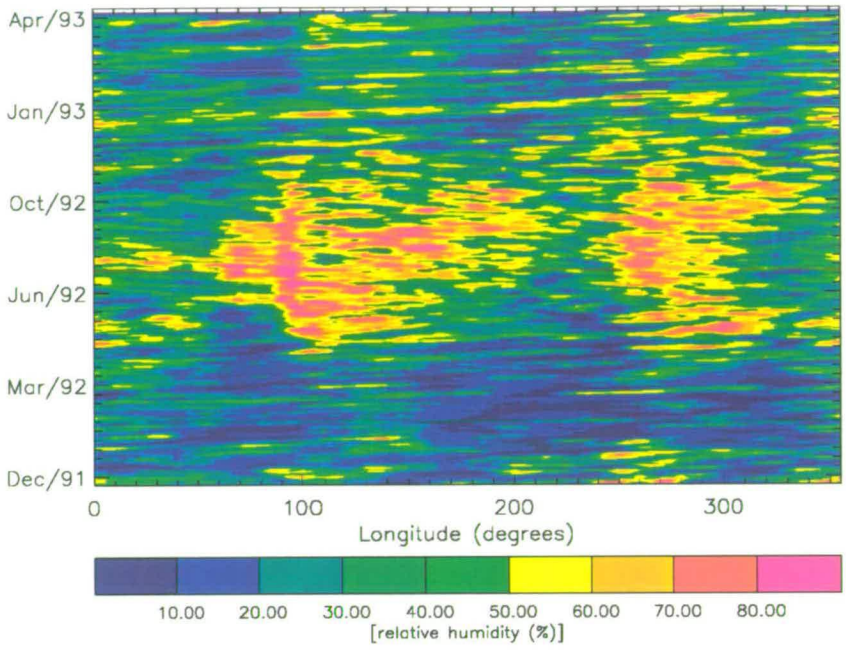

Figure 5.11: Longitude-time section for ECMWF relative humidity at 200 hPa and a latitude of 20°N.

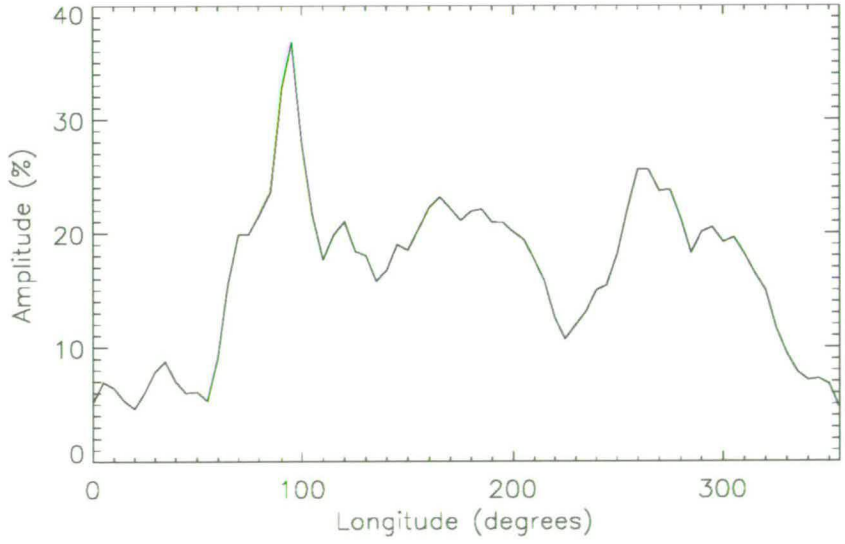

Figure 5.12: Variation with longitude of the annual cycle in ECMWF, 200 hPa relative humidity at 20°N.

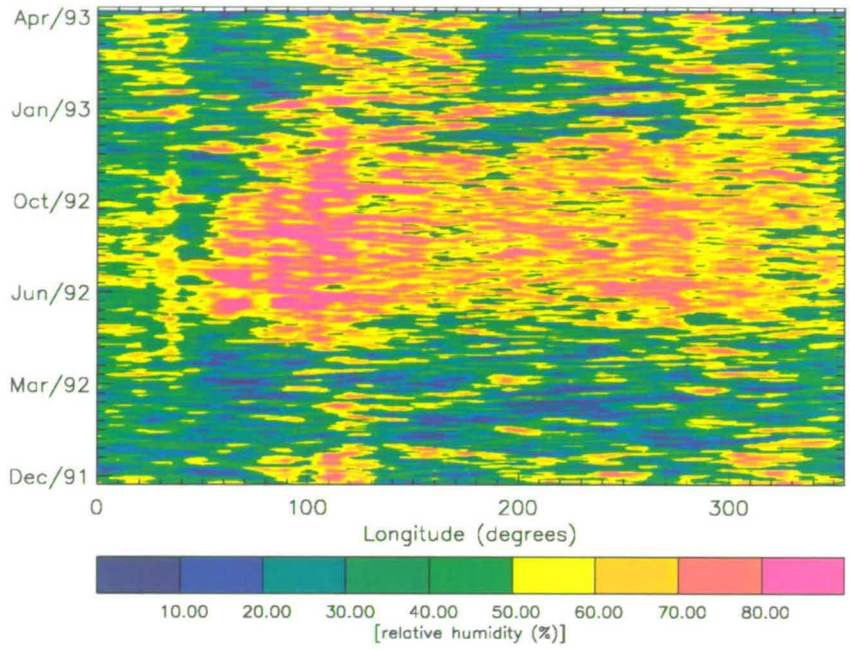

Figure 5.13: As for figure 5.11 but for 10°N.

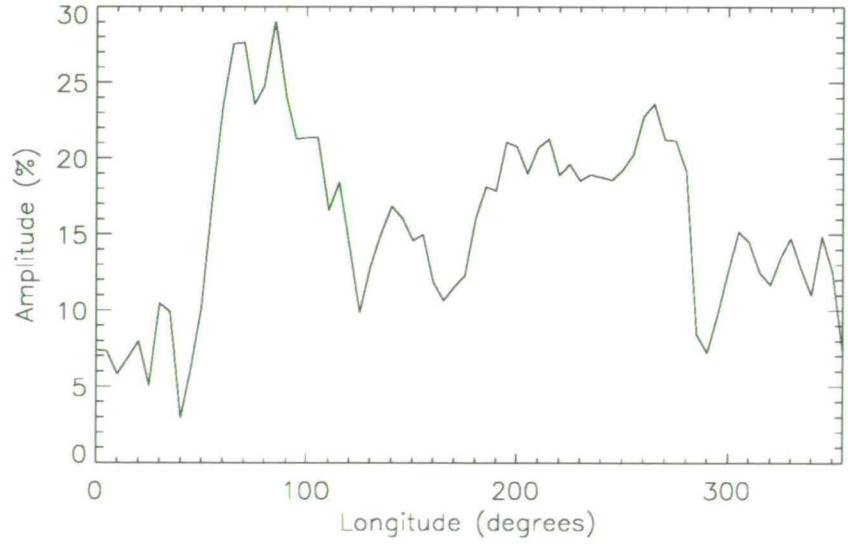

Figure 5.14: As for figure 5.12 but for 10°N.

Latitude (°)	Correlation with MLS	
	NVAP	ECMWF
20 N	0.80	0.71
10 N	0.65	0.55
0	0.61	0.52
10 S	0.74	0.60
20 S	0.71	0.68

Table 5.2: The correlation coefficients of the NVAP and ECMWF longitude-time sections with the MLS longitude-time sections for each latitude.

One difference between the ECMWF-RH field and the MLS-UTH and NVAP-TPW fields at the equator (fig. 5.15) is that the region 30-60°E which is dry in both NVAP and MLS, has relatively high RH values. The eastern Pacific is moister during February to May in both ECMWF and NVAP than it is in MLS. The differences between ECMWF and MLS fields are reflected in the correlation coefficient of 0.52 which is significantly lower than the corresponding correlation coefficient between MLS and NVAP of 0.61 (see table 5.2). The maximum annual cycle accounts for 65% of the variance, a comparable figure to that from NVAP and occurs in the same place, but its position contrasts markedly with that in the MLS data. Despite this, the longitudinal variation in amplitude of the annual cycle is more similar to MLS than is NVAP, with local maxima over South America, the Bay of Bengal and Africa and minima over Indonesia, the western Pacific and far eastern Pacific just off the coast of South America. The NVAP field has greater vertical depth than both the MLS and ECMWF fields and this may account for some of the difference. Signs of eastward propagation are less evident in the ECMWF field at the equator than in the MLS or NVAP fields at the equator.

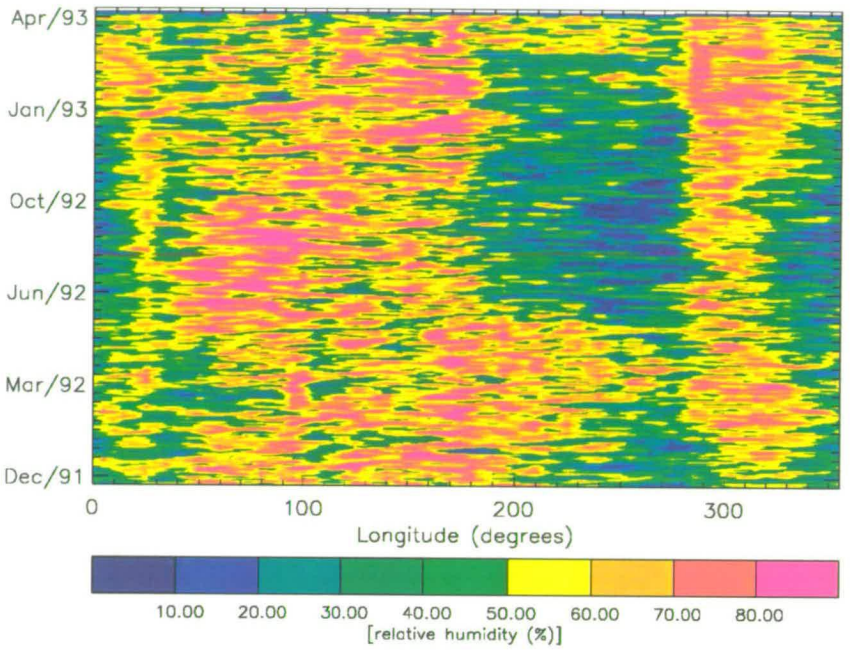

Figure 5.15: As for figure 5.11 but for 0°.

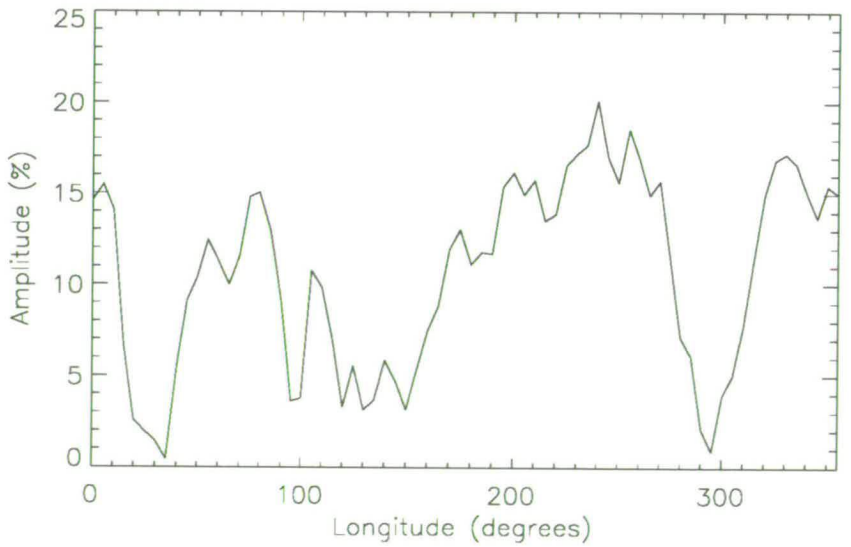

Figure 5.16: As for figure 5.12 but for 0°.

The longitude-time section for 10°S can be found in figure 5.17. At 100°E, a band of high RH is present throughout the year. This feature is visible in the MLS and NVAP fields although the NVAP and MLS fields indicate a greater drying in southern winter. The Walker circulation is most pronounced during southern summer and weakens between April and July. This seasonal variation can be noted in both UTH and TPW. The annual cycle exhibits similar behaviour with longitude to both TPW and UTH. Eastward moving moist features are also evident, most prominently in southern summer 1991-1992. These lack the contrast between moist and the following drier time that NVAP and MLS showed, and as a result are less easy to resolve into individual events. The eastwards extent, from Africa, across the Indian Ocean to 230°E compares well with MLS and NVAP. That the ECMWF analysis scheme can capture these intraseasonal features is important to predicting and modelling ENSO events.

Although much drier than 10°S, the RH field at 20°S is moister than the TPW and UTH fields. It is correlated with MLS with a value of 0.68. The annual cycle accounts for most variance at 45°E in agreement with both MLS and NVAP data.

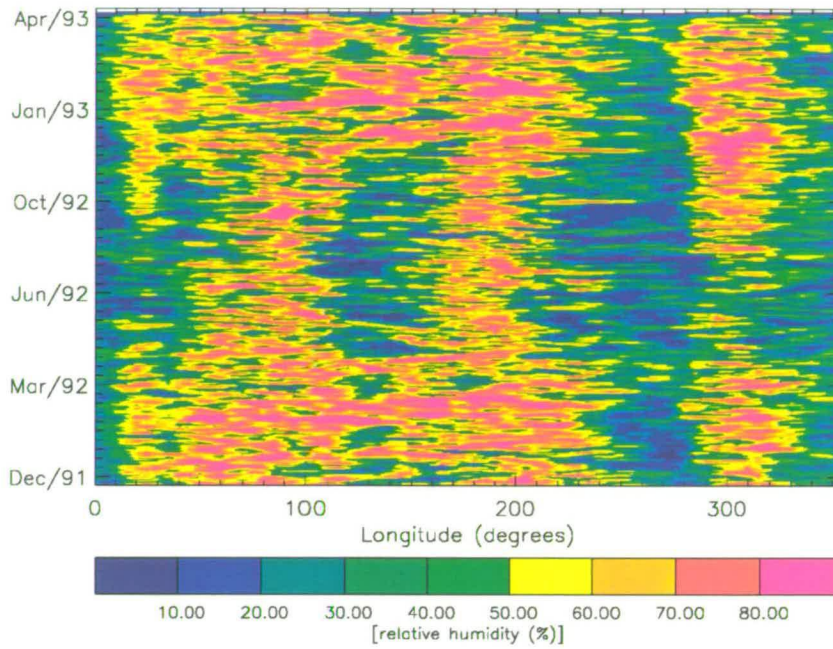

Figure 5.17: As for figure 5.11 but for 10°S.

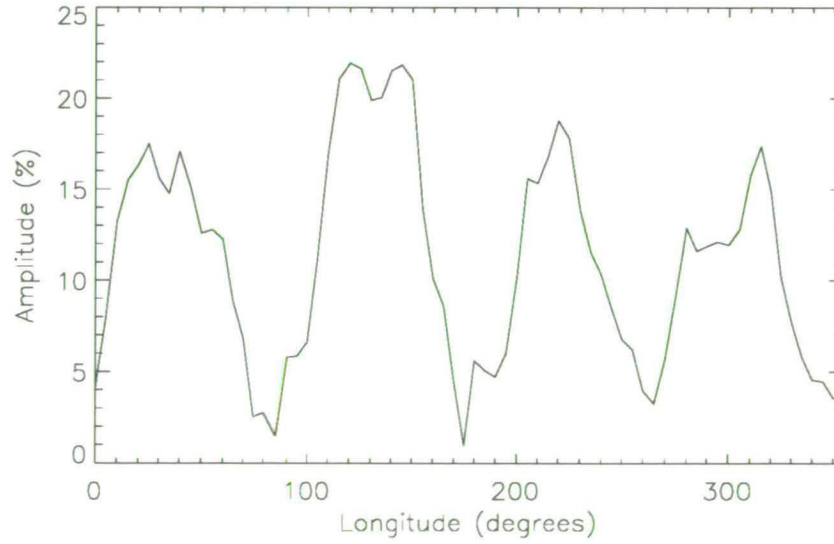

Figure 5.18: As for figure 5.12 but for 10°S.

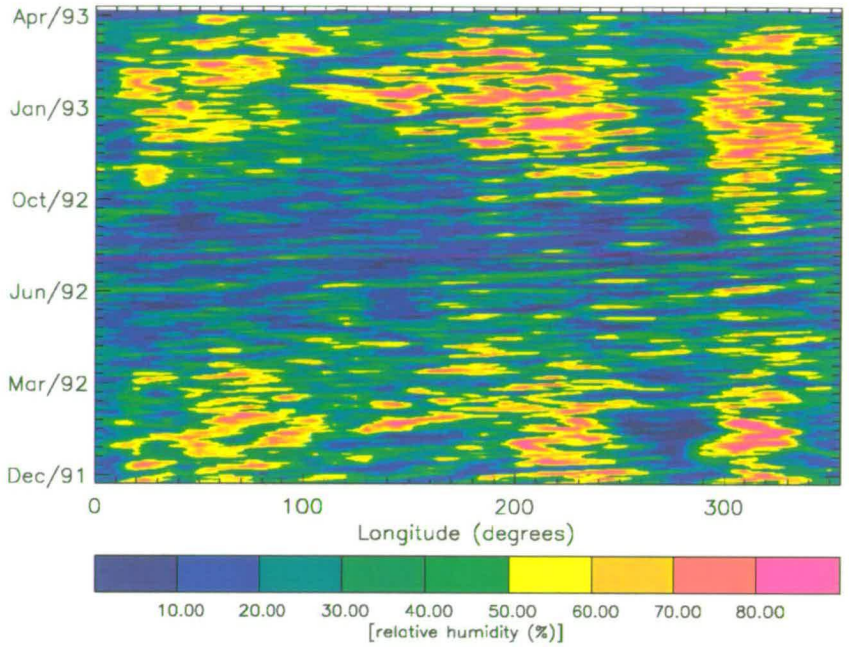

Figure 5.19: As for figure 5.11 but for 20°S.

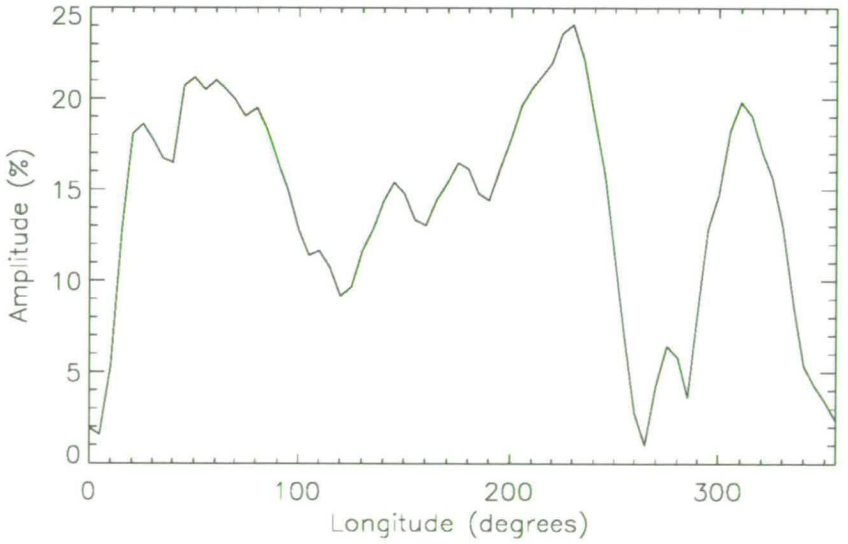

Figure 5.20: As for figure 5.12 but for 20°S.

5.1.3 Summary

Overall, the NVAP TPW is more correlated with the MLS UTH field than the RH from ECMWF analysis. This is somewhat surprising since the NVAP TPW values are based upon a column of the atmosphere from 500-300 hPa, 100 hPa lower than the MLS measurement, whereas the ECMWF is for 200 hPa. Moreover, the NVAP column values are dominated by the moisture content at 500 hPa. The similarity between MLS and NVAP is a reflection on the convection which brings moisture through the NVAP column to the 215 hPa level. It gives confidence to the MLS retrieval and particularly that the features seen in the MLS field are not due to cirrus cloud contamination.

The comparison shows some deficiencies in the ECMWF analysis. Since the ECMWF analyses have little input in the upper troposphere, areas where the analysis is good are due to reasonable simulation of upward transport or where radiosondes have given accurate information. Similarities between ECMWF and the other two fields give confidence in the ECMWF convection schemes and the retrieval in MLS. Differences highlight shortcomings of the ECMWF convection scheme.

The ECMWF analysis of relative humidity compares reasonably with fields from MLS and NVAP. Correlation is better in the northern hemisphere where the annual cycle is stronger, and because of the more extensive radiosonde network in the northern hemisphere providing more input data.

The position of the maximum annual cycle compares well with MLS and NVAP, but there are some differences in the variation of annual cycle over longitude. Maxima over South America extend into the central Pacific where MLS and NVAP data show the water vapour values to be low and the annual cycle to be suppressed. Longitude-time sections at 10°N and at the equator showed the eastern Pacific to be too moist. This could be due to the Walker circulation not being strong enough and therefore not producing sufficient contrast in moisture between the western and eastern Pacific. A similar problem in predicting the moist/dry contrast of the tropics and subtropics has been noted and attributed to the under-prediction of the strength of the Hadley circulation (e.g. Salathé and Chesters, 1995; Soden and Bretherton, 1994). The variation in amplitude of the

annual cycle with longitude is better represented at 10°S, where the eastern Pacific is moister than usual and contrasts less with the western. That the ECMWF model can represent the signs of the eastward propagation of moist anomalies and the enhanced moisture over the eastern Pacific at 10°S, which is attributed to the MJO, is important for the prediction of El Niño.

5.2 The Lifecycle of the MJO

In this section, the lifecycle of the MJO in upper tropospheric water vapour at 215 hPa is examined and compared with ECMWF vertical velocity. The same features are looked for in the NVAP TPW and ECMWF RH fields.

The evolution of the MJO in the water vapour field from MLS is illustrated by a sequence of maps of 5 days averaged water vapour taken through a cycle in December–February 1991. This is compared with mid-tropospheric vertical velocity (500 hPa) from ECMWF reanalysis, also averaged over 5 days. Both quantities are plotted in figure 5.21 where water vapour mixing ratios greater than 170 ppmv are shaded in grey and upward vertical velocity more negative than -0.05Pas^{-1} is coloured black. The dates indicate the middle of each pentad.

From 17th - 22nd December, mixing ratios greater than 170 ppmv are spread out in a band along the equator. Several small pockets of vertical velocity are strung out along the equator from Africa as far as 135°W and there is indication of the South Pacific Convergence Zone (SPCZ). On the 27th December, the distribution of high water vapour begins to shift from Africa and the Indian Ocean towards Indonesia. Similarly, the distribution of pockets of vertical velocity has shifted from Africa and the Indian Ocean towards Indonesia. Both the SPCZ and the ITCZ are well pronounced in the vertical velocity field.

On the 1st January, there is a large vertical velocity pocket over the western Pacific and a corresponding area of high mixing ratio is beginning to develop. By 6th January, the moist area has moved eastwards from Indonesia to become centred over the western Pacific and vertical velocity is still strong at this time.

On the 11th January the pocket of vertical velocity begins to break up but water vapour mixing ratios remain high and continue to migrate eastwards and to intensify along the SPCZ. The SPCZ remains a strong characteristic in both

the vertical velocity and water vapour fields until 5th February but lingers as a feature in water vapour for a further 5 days. On the 10th February, the small pockets of vertical velocity have returned to Africa and the Indian Ocean and mixing ratios have begun to increase here also. Finally, water vapour disperses from the SPCZ.

This correspondence between water vapour and vertical velocity illustrates a strong relationship between high mixing ratios and convection and indicates that the convective system as a whole moves eastwards rather than the water vapour being advected along at the 215 hPa level. The patterns of water vapour mixing ratio are similar to those in OLR during the MJO in March/April 1988 described by Matthews *et al.* (1996). Both begin as a low intensity band along, and mostly south of the equator which becomes organised over Indonesia and the western Pacific and is followed by development in a south-easterly direction along the SPCZ. Again, the SPCZ remains prominent in the water vapour field for longer than in OLR. Knutson and Weickmann, (1987) noted the development of OLR from the Indian Ocean to the SPCZ. Rui and Wang (1990) found that development along the SPCZ occurred in strong MJO events and Matthews *et al.* (1996) found that enhancement or excitation of convection along the SPCZ is observed in virtually all MJO's from 1979-88.

5.2.1 NVAP and ECMWF

Similar eastward movement from Africa, across the Indian Ocean and development along the SPCZ can also be seen in the NVAP TPW field (see fig. 5.22). During 17th-22nd of December, a band of TPW $>$ 2.5 mm is spread out along the equator. The 27th December contains a large amount of bad data (recognised by the TPW amount being virtually zero) but it can be seen that values of TPW are beginning to increase over Indonesia. On 1st January, TPW amounts have decreased over Africa and the Indian Ocean and there is a large area of high TPW over the western Pacific. On the 6th January, the moist area has increased in size and moved slightly eastwards and southwards. On the 11th January as with the vertical velocity field, the pocket of high TPW has become more fragmented. Eastward movement continues and development begins along the SPCZ. TPW remains low over the Indian Ocean and Indonesia until 5th February, then TPW

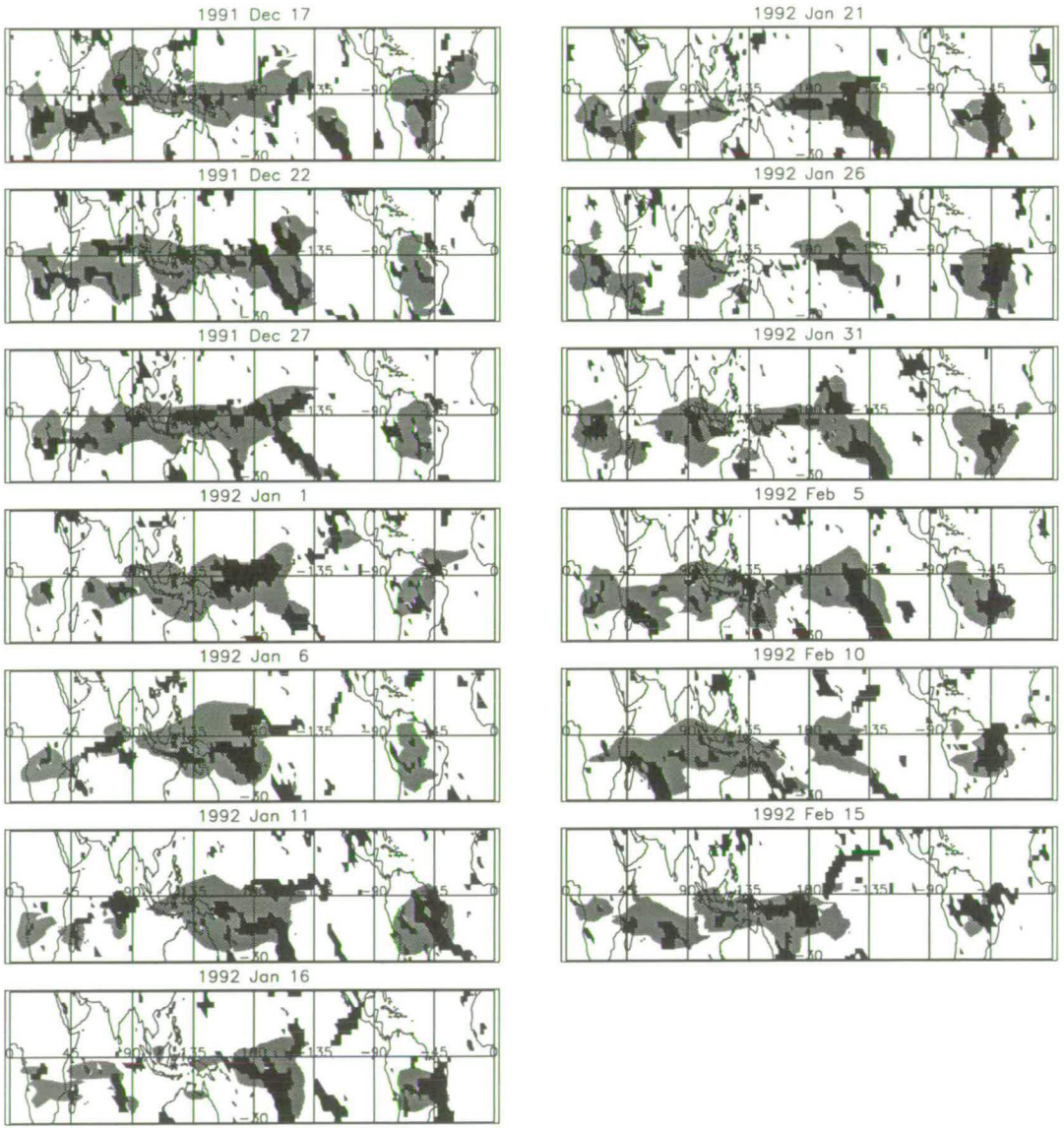

Figure 5.21: 5 day averaged water vapour mixing ratios, at 215 hPa, greater than 170 ppmv (grey) and ECMWF vertical velocity at 500 hPa, less than -0.05Pas^{-1} (black). Dates indicate the middle of the pentad.

begins to increase over Indonesia again. On the 10th February, the SPCZ (as in MLS data) is still pronounced and by the 15th February, it finally disperses from the SPCZ.

In general, pentad fields of ECMWF RH lack the contrast between moist and dry areas although the moisture has the same spatial distribution. Throughout the ECMWF sequence (fig. 5.23), Africa and the Indian Ocean are seen to be much more moist than in MLS or NVAP data. The translation of moisture from Africa across the Indian Ocean is more difficult to see.

On 17th December, the ECMWF relative humidity field shows many similarities with the MLS UTH and NVAP TPW fields. For example, a band of high relative humidity extends from Central Africa into the Indian Ocean and the high RH which extends from India south-eastwards along the Indonesian island chain is well represented. The band continues into the western Pacific, along the ITCZ and SPCZ before breaking up over the eastern Pacific. Enhanced moisture returns over South America and extends along the ITCZ, mostly north of the equator, across the Atlantic to North Africa. This Atlantic part of the ITCZ remains well pronounced in the ECMWF field throughout the entire sequence, similar to NVAP data but in contrast to MLS mixing ratios. In the ECMWF field however, the ITCZ is shown to be as moist as the western Pacific, illustrating the lack of contrast in relative humidity values. Salathé and Chesters (1995) noted that ECMWF accurately depicted the locations of the extreme features in UTH but failed to capture their full intensity. Likewise, the Pacific ITCZ and SPCZ are well marked throughout the ECMWF series more consistently than in the MLS field (Vespirini, 1998).

On the 6th January when mixing ratios reach their most intense over the western Pacific there is no such increase in relative humidity although there is, for the only time, almost a complete absence of the western Pacific part of the ITCZ. ECMWF data also reveal a suppression of convection over Indonesia and the western Pacific as an absence of high relative humidity on 16th and 21st January. This compares well with MLS data and has been widely noted to occur in MJO events (e.g. Rui and Wang, 1990).

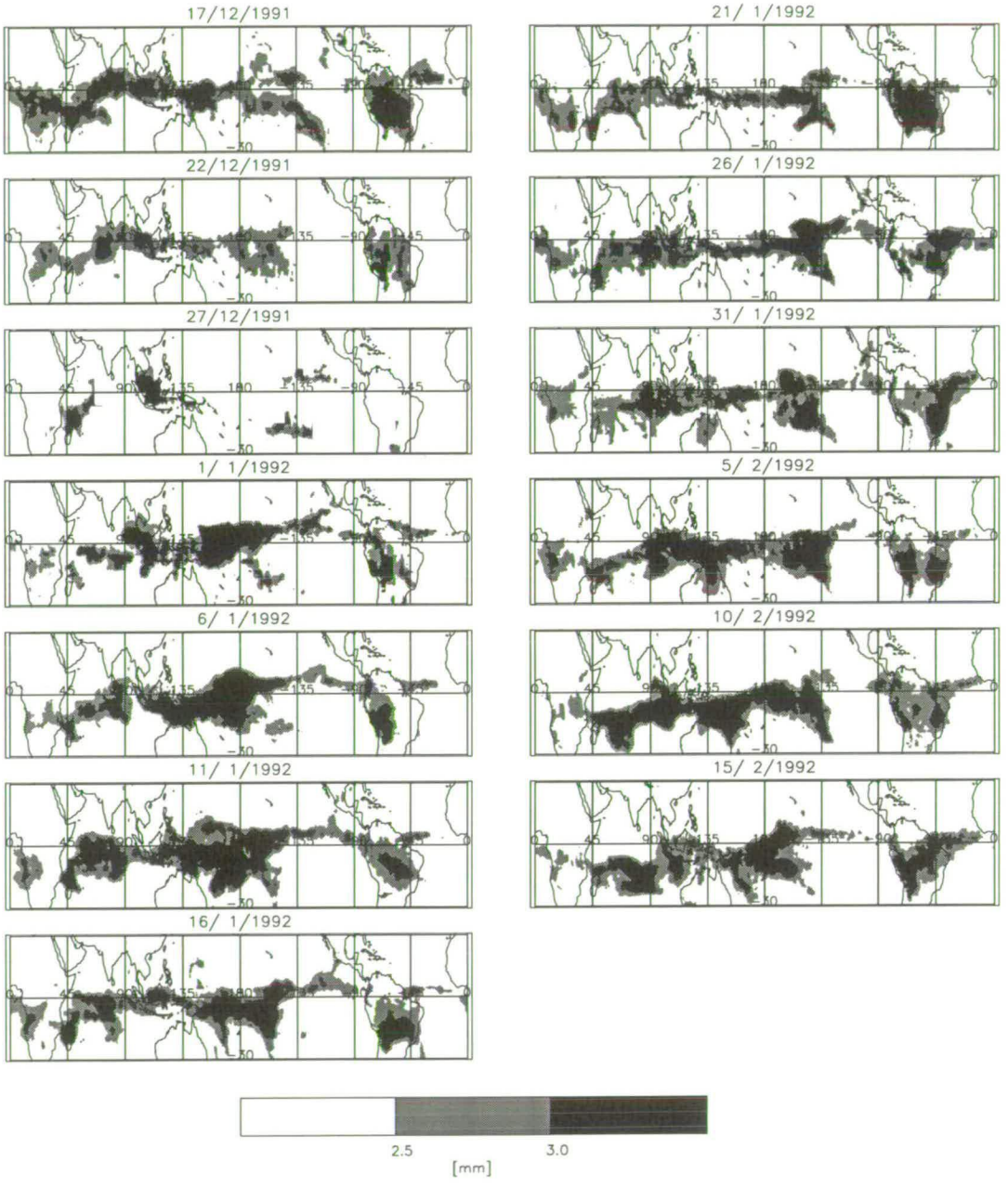

Figure 5.22: 5 day averaged NVAP TPW (mm). Dates indicate the middle of the pentad.

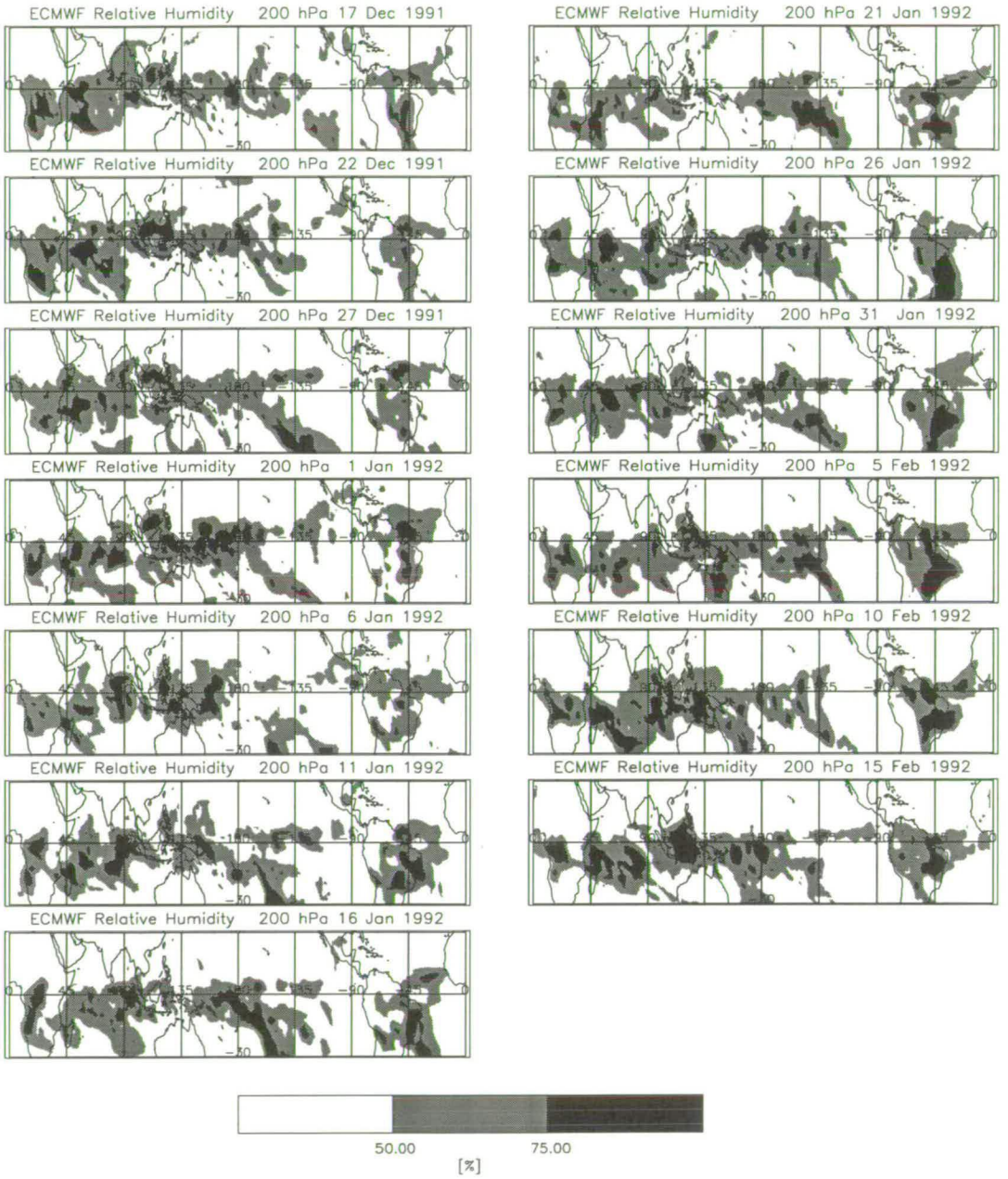

Figure 5.23: 5 day averaged ECMWF relative humidity (%). Dates indicate the middle of the pentad.

5.3 Westerly Wind Bursts

The high water vapour mixing ratios in the upper troposphere appear to be related to surface, westerly wind bursts. Wang (1988) showed that although the mean surface winds in the tropics are easterly, they are often westerly in the region where convective anomalies associated with the MJO originate. Zhang (1996) found that deep convection tended to occur in surface (850 hPa) westerly wind perturbations and Hendon and Glick (1997) showed that westerly wind anomalies were related to enhanced evaporation.

A time-series of ECMWF zonal winds at 850 hPa and 10°S is presented in figure 5.24. Regions of westerly wind are evident during southern summer in both 1992 and 1993 and are well correlated with the eastward moving moist features in the time-longitude plot of water vapour (figure 4.12). The longitudinal extent of the westerly winds in 1992 (from 40-200 °E) corresponds well with the more evident eastward propagation in the water vapour field of this year. The westerly wind bursts described here also fit the pattern of wind bursts described by Verbickas (1998) based on the ECMWF reanalysis data. She found that the wind bursts generally had speeds greater than $5ms^{-1}$, occurring between November and April, and had longitudinal extents of 500-8000 km.

Enhanced water vapour at 215 hPa is also simultaneous with strong easterly (negative) winds at 200 hPa during the northern hemisphere winter months when the MJO is active. This is shown in figure 5.25. Upper level zonal winds are therefore easterly when the lower level winds are westerly, a pattern that was noted by Madden and Julian (1971) and Kiladis *et al.*, (1994) who found there to be a baroclinic structure during MJO events, with easterly anomalies overlying westerlies.

In contrast to the zonal winds at 10°S, westerly wind bursts at the equator (not shown) are weaker and have a limited longitudinal extent. Similarly, Zhang and Hendon (1997) who also used 850 hPa zonal winds from the ECMWF analysis showed that the maximum intraseasonal variance in zonal wind was south of the equator and concentrated in the western Pacific, and Verbickas (1998) noted that there was a tendency for westerly wind bursts to occur in the southern hemisphere. This is an important reason for the mixing ratios being higher at 10°S than at

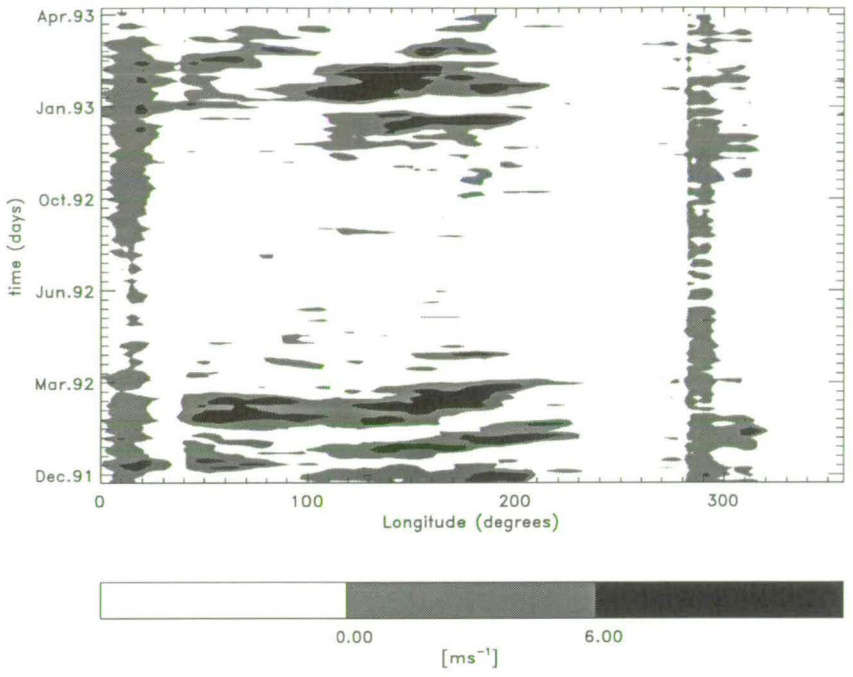

Figure 5.24: Time-longitude section of ECMWF zonal winds at 10°S and 850 hPa

the equator and a further indication that the high mixing ratios are a result of enhanced evaporation and convection. The fact that the largest variances do not lie on the equator appears to be in conflict with those theories which attribute the MJO to moist Kelvin waves, as remarked by Zhang and Hendon (1997).

5.3.1 Cyclone Pairs

Often, westerly wind bursts develop from the interaction between a pair of tropical cyclones which form on both sides of the equator. These 'cyclone pairs' were considered by Keen (1982) to be dynamically related if the initial formation of the northern and southern systems occurred within 9 days of each other, if the initial latitudinal separation was not more than 22 degrees, and if the longitudinal difference ranged from +9° (with the northern system east of the southern system) to -17° (with the northern system west of the southern). According to this definition, cyclone pairs are predicted to occur with a frequency of 2.4 events per year. Applying a stricter definition of a cyclone pair, where there must be simultaneous development within 5° of the equator at the same longitude, results

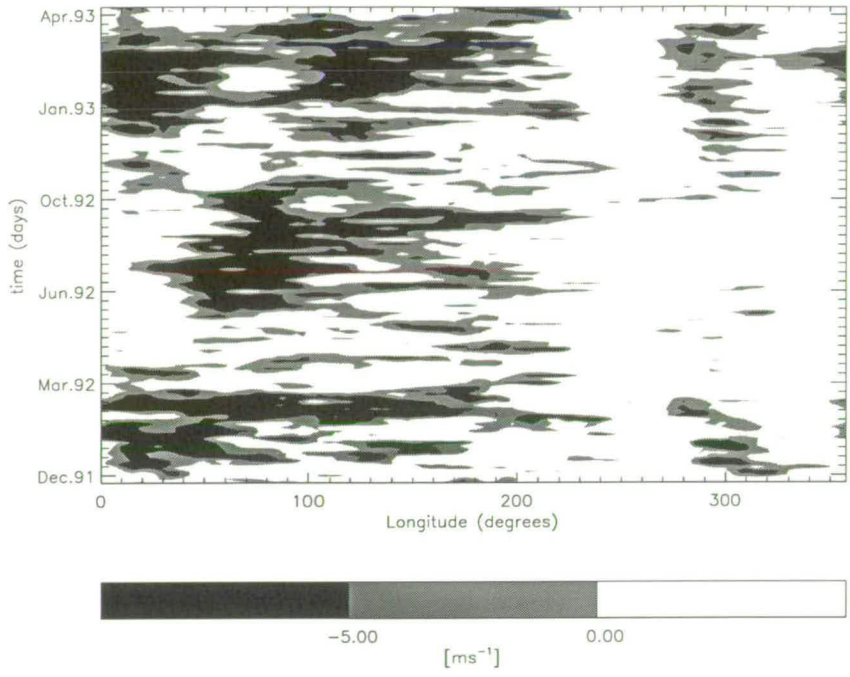

Figure 5.25: Time-longitude section of ECMWF zonal winds at 10°S and 200 hPa

in occurrence once every 2-5 years (e.g. Lander, 1990; Harrison and Geise, 1991).

Having established that westerly wind bursts are present during times of enhanced water vapour, wind fields are now examined during the lifecycle of the MJO. A sequence of 5 day averaged 850 hPa wind fields can be found in figure 5.26 for the series of days taken through the MJO event described in section 5.2. On 17th December, surface westerly winds are situated around 170°E and just south of the equator. The upper tropospheric winds (200 hPa, not shown) are easterly in the region 130-150°E. At the surface, there is little sign of westerly wind bursts again until the 1st January. Upper tropospheric winds however, are easterly between 90-180°E on 22nd December but have a suppressed region around 140°E on 27th December.

On 22nd December, there are signs of an upper tropospheric anticyclone pair, with the northern one being situated at 120°E, 10°N and the southern one being situated at 130°E, 10°S. The northern anticyclone collapses by 27th December, and the southern one has moved south into the SPCZ.

Westerly winds at the surface become strong on the 1st January along the equa-

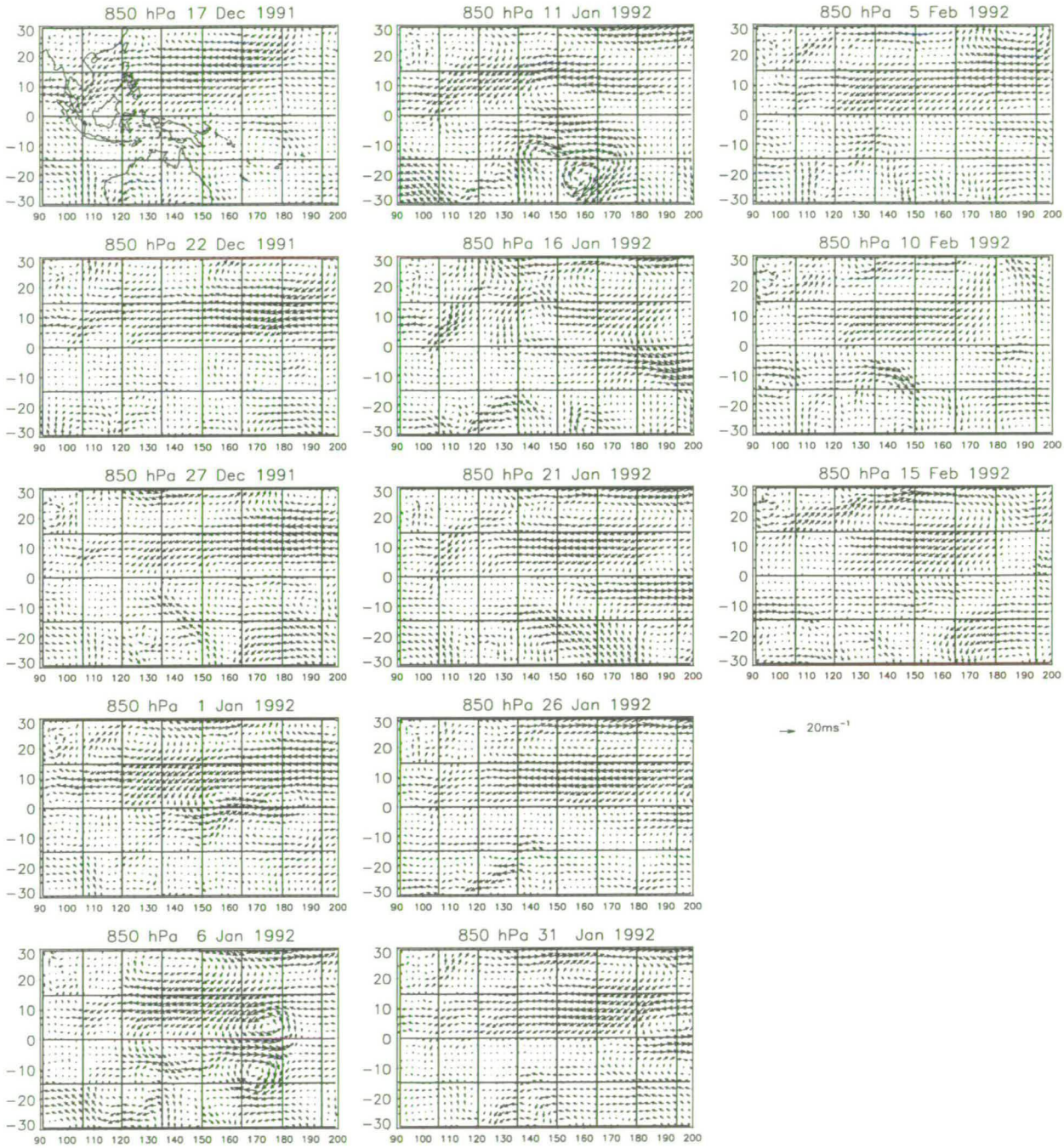

Figure 5.26: 5 day averaged 850 hPa ECMWF wind fields.

tor and between 135-185°E. A characteristic tropical cyclone pair then develops on the 6th January, with the northern one being centred at 170°E, 5°N and the southern one at at 170°E, 10°S. The upper level flow directly above this region is divergent, with strong easterlies to the west, and an anticyclone to the east in the northern hemisphere.

The southern-most cyclone of the pair moves southwards and channels westerly flow from the equator to 15°S. Westerly winds remain in the region of 160°E until 21st January, and beyond the dateline until 10th February. The westerlies return to west of the dateline on 5th February where they are associated with a developing cyclone at 135°E, 15°S. This leads to strong westerly winds from 90-150°E, 10°S by the following pentad.

The development of the cyclone pair on 6th January, coincides with the enhanced water vapour in the region of the dateline or slightly to the west, and with the two vertical velocity centres either side of the equator (see fig. 5.21). The water vapour mixing ratios are perhaps the highest on this day, signifying the peak in convection. The position of the cyclone pair with respect to the convective centre varies throughout the cycle of the MJO (e.g. Rui and Wang, 1990), but this would be in agreement with Kiladis *et al.*, (1994) who find the cyclones at the time of the peak in OLR.

The formation of the cyclone pair leads to westerly flow being maximised just south of the equator. This westerly flow just off the equator was also seen in the longitude-time section. Harrison and Vecchi (1997) noted that off-equatorial westerly wind bursts commonly occurred along with tropical cyclone pairs. The appearance of cyclone pairs (figure 5.26) in the lower troposphere or anticyclone pairs in the upper troposphere is often a sign of Rossby wave activity (see figure 5.27) (e.g. Matsuo, 1966; Knutson and Weickmann, 1987; Lau *et al.*, 1988). The significance of the occurrence of the cyclone pair in this case is therefore that it may explain the off-equatorial maximum of the westerly winds in the longitude-time section, accounting for the enhanced water vapour at 10°S, and it may signify that Rossby-wave activity is taking place.

Harrison and Geise (1991) noted that the development of near-dateline, cyclone pairs were associated with warm ENSO phases, and Keen (1982) remarked that the cyclone pairs encouraged the advancement of warm water and pushed

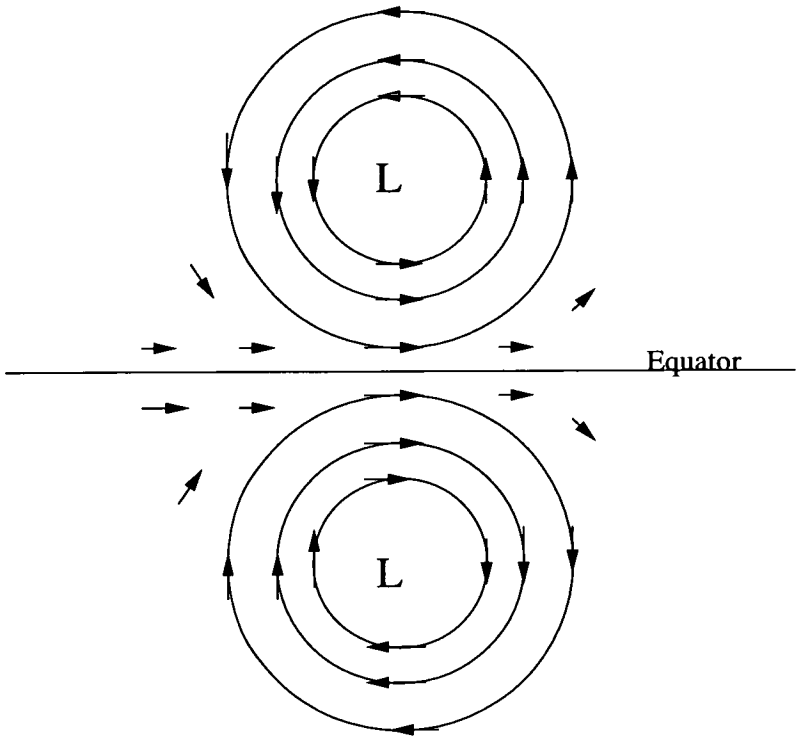

Figure 5.27: Horizontal velocity perturbations associated with a Rossby wave. Wind arrows are not drawn to scale. (Figure based on Matsuno, 1966).

the equatorial westerlies 20-40° further east. The development of cyclone pairs, westerly wind bursts and the MJO are intimately related to ENSO. It is thought that westerly wind events may play a role in the early stages of development of an El Niño, by decreasing the easterly trade winds in the central and western Pacific and initiating equatorially trapped Kelvin waves in the ocean. The near-dateline development observed here might therefore be expected since 1992 was an El Niño year. Hence, the formation of the cyclone pair may have encouraged the significant eastwards propagation of the westerly winds in this year and the eastwards extension of the intraseasonal water vapour anomalies.

5.4 Vorticity and Divergence

Regions of positive vorticity and negative divergence signify converging air and would be expected to occur at the base of convection, coincident with areas of divergence at its outflow. If the regions of high water vapour mixing ratios are related to convection, vorticity and divergence should be correlated with water

vapour.

Due to the irregular nature of the vorticity field, the vertical average of 150 hPa, 200 hPa and 250 hPa was examined but there were no evident eastward moving patterns which might be related to the features in water vapour in figure 4.12.

A longitude-time section of divergence at 10°S, averaged over 200, 150 and 250 hPa is shown in see figure 5.28. A similar longitude-time section is shown for 100 hPa in figure 5.29 which is not a vertical average and shows just the areas of strong divergence. In both figures, divergence is taking place over South America at about 320°E, about 20°E of the high mixing ratios at 200 hPa. A region of convergence (negative divergence) corresponding to the subsiding branch of the Walker circulation is evident at about 280°E over the eastern Pacific in figure 5.28. It is particularly strong in southern summer from December 1991-March 1992 and from October 1992-March 1993. The influence of the Walker circulation was seen in the MLS water vapour field at 10°S to be particularly strong during these times.

Over the central Pacific (200–250°E), strong divergence is taking place . It is likely that this indicates convective outflow resulting from the enhanced convection over the western Pacific and corresponding to the rising arm of the Walker circulation. As was the case over South America, it is displaced slightly eastwards relative to the maximum in the water vapour field. The eastward displacement between the water vapour fields and the divergence fields at both 100 hPa and 200 hPa may be a result of the strong westerly winds at 200 hPa in the region east of the dateline. It would be expected however, that the westerly wind would likewise have had this effect on the water vapour at 215 hPa.

There is evidence of convective outflow with an eastwards extent, which stretches from 120-260°E and which is prominent in February to March 1992. This feature is most pronounced at 100 hPa (fig. 5.29) although a similar feature can be seen, albeit less clearly, at 200 hPa. Again, there is an offset between the divergence and the water vapour field by about 20°E. Convergence at 850 hPa can also be related to this structure (not shown).

The tops of convective clouds are usually estimated to reach no higher than 150 hPa so the presence of these features in the divergence field at 100 hPa (which approximates the tropopause) is somewhat surprising and indicates that

the convection is much deeper than expected. The deep convection will be examined in conjunction with stratosphere-troposphere exchange in the following chapter.

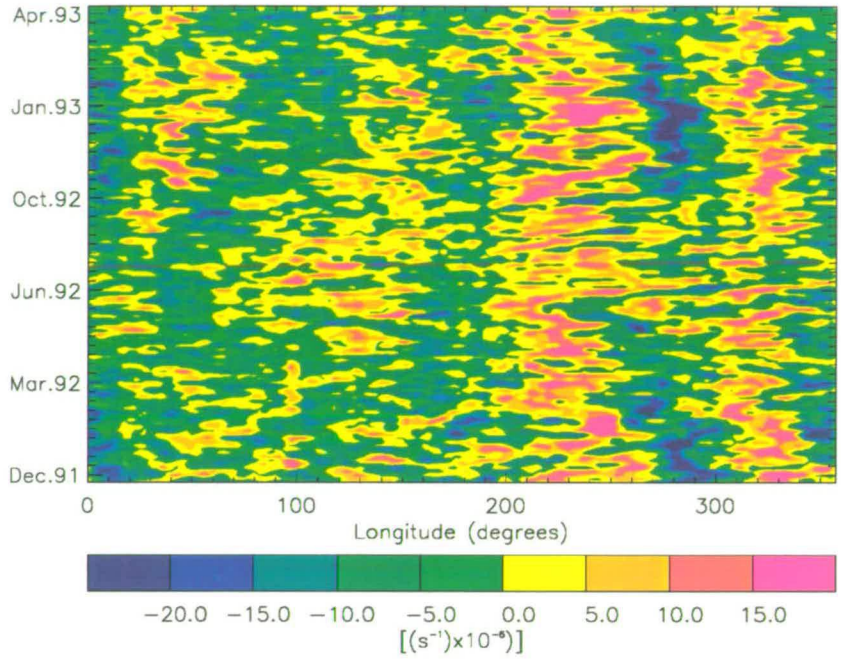

Figure 5.28: Time-longitude section of ECMWF divergence, averaged from 250 hPa, 200 hPa and 150 hPa at 10°S.

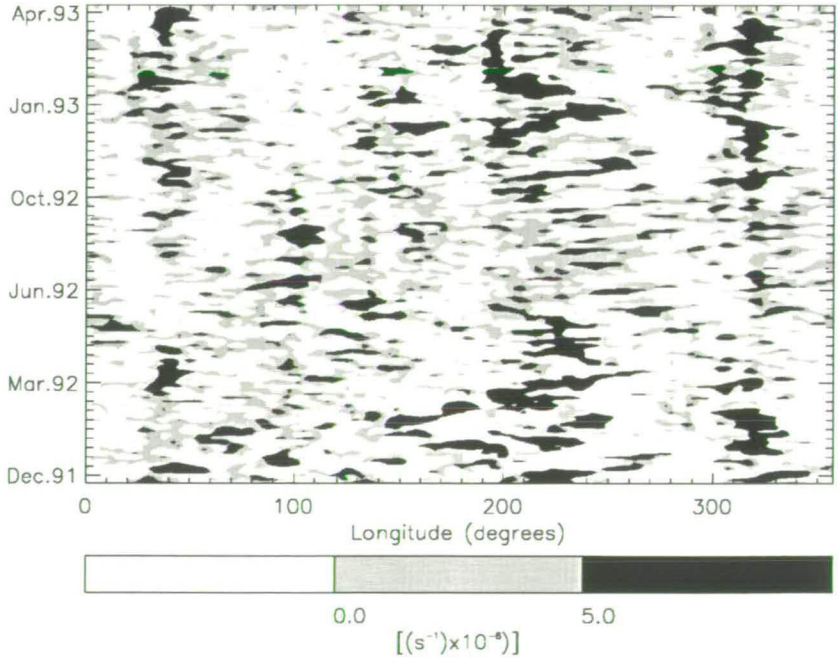

Figure 5.29: Time-longitude section of ECMWF divergence, at 100 hPa at 10°S.

5.5 316 hPa and 147 hPa Water Vapour

The water vapour retrieval at 147 hPa and 316 hPa is less reliable than at 215 hPa and has therefore not been used throughout the thesis. We now return to MLS measurements and examine the 147 hPa and 316 hPa levels for signs of the MJO. As before, longitude-time sections and 5-day averaged maps have been constructed.

Longitude-time sections at 10°S for 316 and 147 hPa made in the same way to those for 215 hPa are shown in figures 5.30 and 5.32 respectively. The 316 hPa level is more moist than 215 hPa with mixing ratios that range from 160–370 ppmv and 70–245 ppmv respectively. The 147 hPa level is drier that the 215 hPa level and mixing ratios range from 30-86 ppmv. At both 316 hPa and 147 hPa, patterns are similar to those at 215 hPa, with high water vapour values over continents in summer and low values over the continents in winter and over the oceans. The position of South America is particularly striking in all three levels.

At 316 hPa, the eastern Pacific is dry throughout most of the year except for a small increase in moisture during March and April. This moistening was not revealed to the same extent by NVAP data which includes some water vapour near this level. It is also much more pronounced than that occurring at 215 hPa and 147 hPa suggesting that it is due to shallower convection which does not reach these higher levels.

The longitudinal variation in the strength of the annual cycle is similar at all 3 levels. The annual cycle accounts for maximum variance over Africa, 25–30°E. At 316 hPa it accounts for 85%, at 215 hPa for 82% and at 147 hPa for 75% of the variance. Secondary maxima are found over Indonesia, the Mid-Pacific, and South America. The minimum annual cycle is found over the Indian Ocean (90°E) at 147 hPa and 215 hPa compared with over the western Pacific (160°) at 316 hPa.

Eastward moving features are evident in the longitude-time sections of both levels. At 147 hPa they appear to have a clearer eastwards propagation than at 215 hPa and at 316 hPa. As before, pentad maps are examined to reveal the evolution of highest values of water vapour. The patterns of water vapour at 316 hPa (figure 5.34) and 147 hPa (figure 5.35) are similar to those at 215 hPa.

They show that the moist regions are over Central Africa, South America and the western Pacific and Indonesia. The eastern Pacific is dry at both levels. Convection over the Atlantic branch of the ITCZ, although it appears at 316 hPa, never reaches 147 hPa indicating that the convection there is shallower. That both levels are similar to 215 hPa supports the assertion that the patterns are due to translating convection rather than to the advection of water vapour along the 215 hPa level.

The power spectrum analysis at 316 hPa shows the 70 day peak to be more pronounced than the 50-60 day peak in a similar way to the power spectrum of 215 hPa. At 147 hPa, the 50-60 day peak dominates over the 70 day peak. Clark *et al.*, (1998) ascribed the 70 day peak to a zonally symmetric mode and the 50-60 day peak to a propagating mode. This interpretation combined with the characteristics of the eastward propagation in the longitude-time sections would suggest that the 147 hPa level displays an enhancement of the propagating mode over the zonally symmetric mode. At 316 hPa, on the other hand, more of the intraseasonal variability rests in the zonally symmetric mode.

At 215 hPa the 30–85 day filter band accounted for 38% of the total variance at 160°E and the annual cycle for 21%. At 316 hPa the annual cycle accounts for 24% and the MJO for 32%, and at 147 hPa the annual cycle and intraseasonal activity account for 17% and 38% respectively (see table 5.3). At all three levels, the MJO accounts for more variability than the annual cycle in the region of 160°E.

Whereas the strength of the annual cycle decreases with height, the MJO accounts for increasing variance on ascending to 147 hPa. The intraseasonal convective anomalies were also more clearly visible than the ITCZ at 147 hPa. One interpretation of this is that the intraseasonal convective anomalies reach a greater height than the climatological convection. This could explain the observation that the divergence field shows intraseasonal convective outflow at levels higher than expected.

Height (hPa)	**Percent of Variance accounted for by**	
	Annual Cycle	Intraseasonal
316	24	32
215	21	38
147	17	38

Table 5.3: Percentage variance accounted for by the annual cycle and MJO at 160°E and 316 hPa, 215 hPa and 147 hPa levels of MLS data.

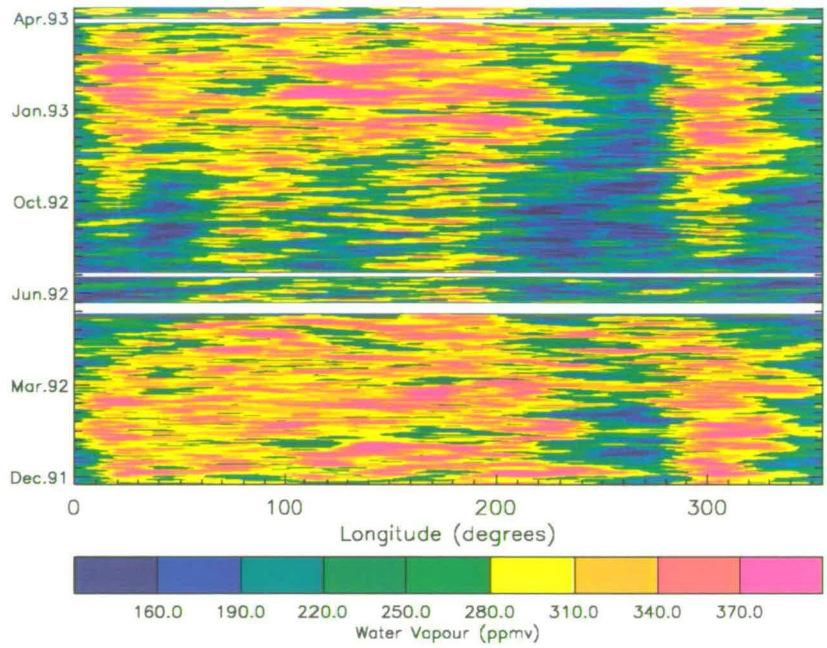

Figure 5.30: Longitude-time sections of water vapour mixing ratios at 316 hPa and 10°S. Data has been Kalman filtered and a mask applied to gaps longer than three days.

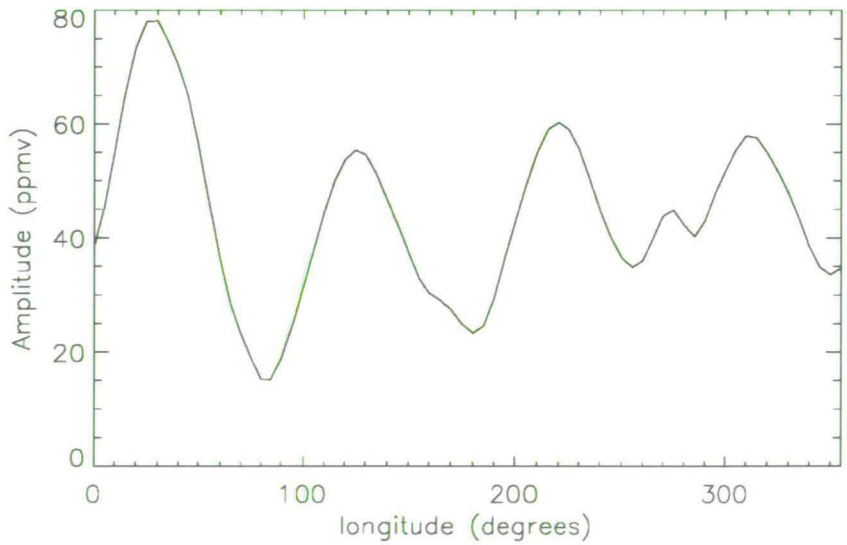

Figure 5.31: Variation in amplitude of the annual cycle with longitude for 10°S and 316 hPa.

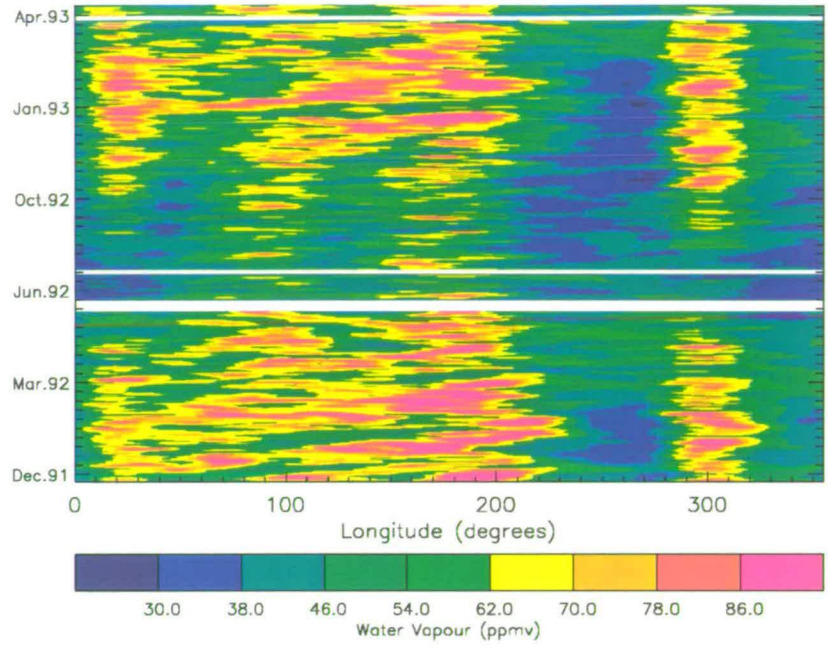

Figure 5.32: Longitude-time sections of water vapour mixing ratios at 147 hPa and 10°S. Data has been Kalman filtered and a mask applied to gaps longer than three days.

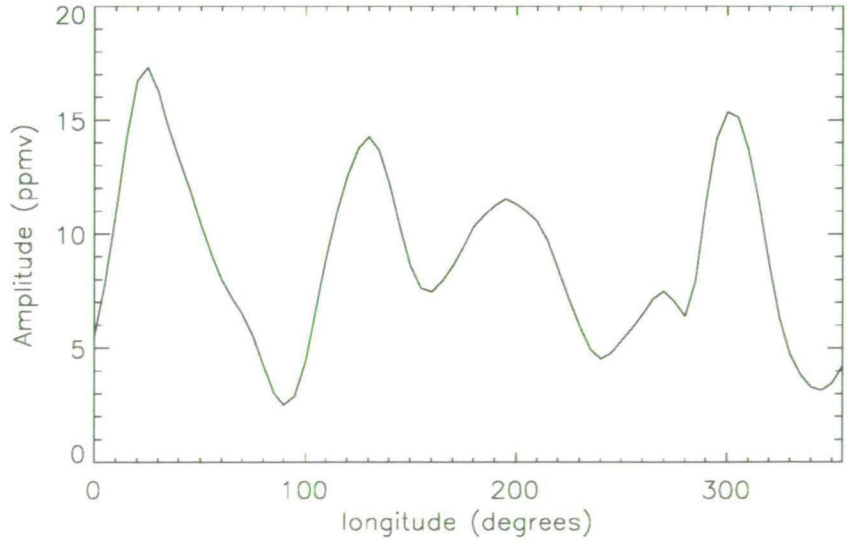

Figure 5.33: Variation in amplitude of the annual cycle with longitude for 10°S and 147 hPa

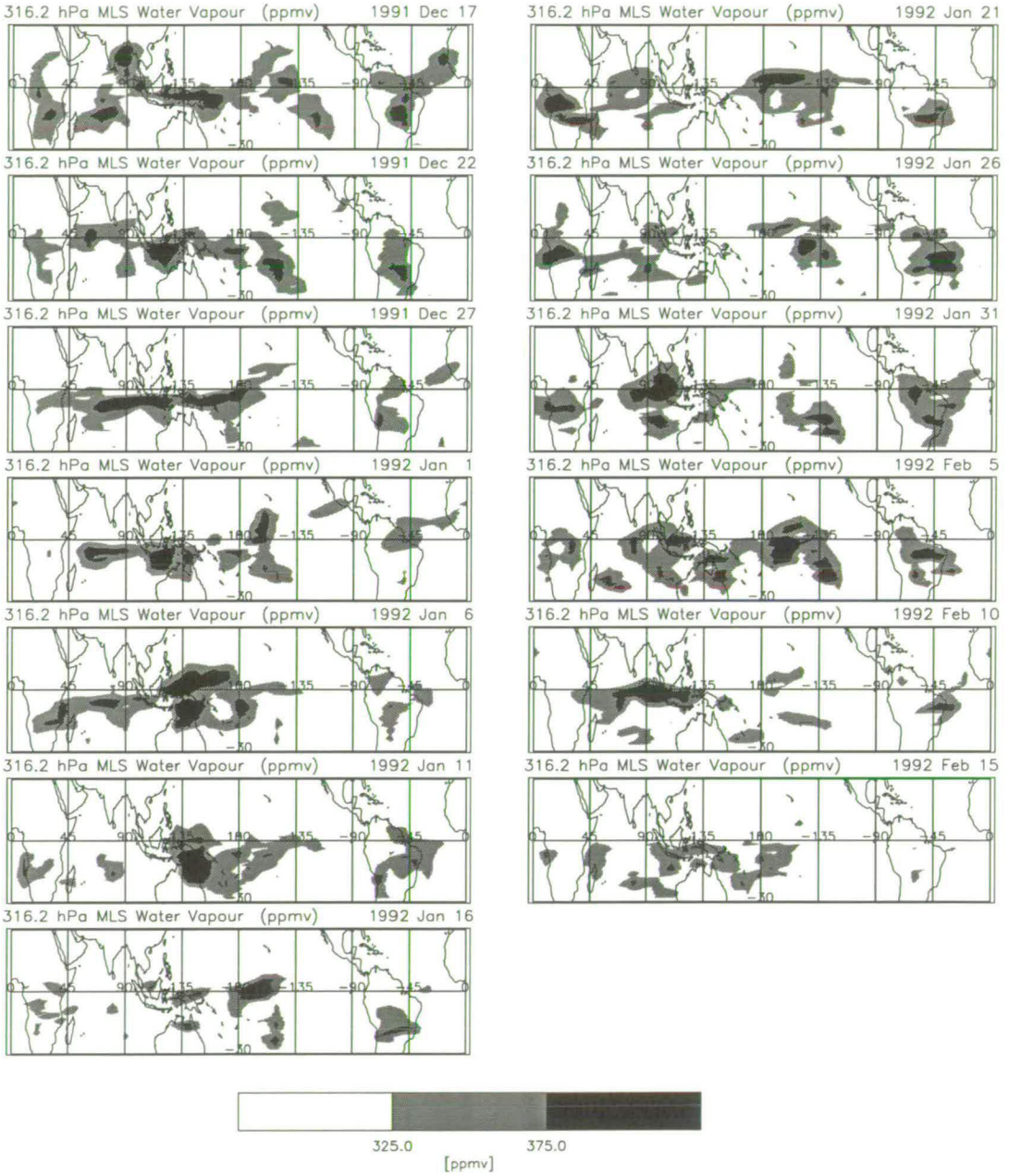

Figure 5.34: 5 day averaged MLS water vapour mixing ratios (ppmv) at 316 hPa. Dates indicate the middle of the pentad.

5.5.1 Summary

Attempts to associate the variability with convection and account for apparent eastwards propagation can be summarised as follows.

- The movement of water vapour from Africa to the western Pacific and its development down the SPCZ is characteristic of the MJO and compares well with observations of OLR, often used to infer convection.
- Pockets of upward motion, as illustrated by 500 hPa ECMWF vertical velocity, move concomitantly with water vapour, showing the water vapour to be associated with slowly translating convection.
- Slowly translating UTH is apparent in MLS data at levels above and below 215 hPa. Similar patterns are also found in NVAP data.
- Water vapour is correlated with ECMWF 850 hPa westerly wind bursts over the region in question. The formation of a cyclone pair in this case, accounts for the off-equatorial position of the westerly wind bursts.
- The longitude-time section of upper-level divergence suggests that large-scale moist regions may be associated with enhanced convection.

5.6 Conclusions

The annual cycle in UTH at 215 hPa was seen to be well correlated with both NVAP data, representing total precipitable water in the column below, and with MLS data on levels above and below. It was also well represented by ECMWF, but with some discrepancies over the eastern Pacific where TOVS introduces a moist bias. The intraseasonal cycle that was identified in longitude-time sections at 215 hPa and discussed in chapter 4 can also be noticed in different datasets. Eastward moving features are apparent in NVAP data, revealing the depth of the structure, and leading to confidence that MLS is 'seeing' water vapour rather than the results being due to contamination by cirrus clouds. MLS data at 316 hPa and 147 hPa also reveal such structures.

The magnitude of the intraseasonal signal increases with height and the propagating mode shows enhancement over the zonally symmetric mode. The annual

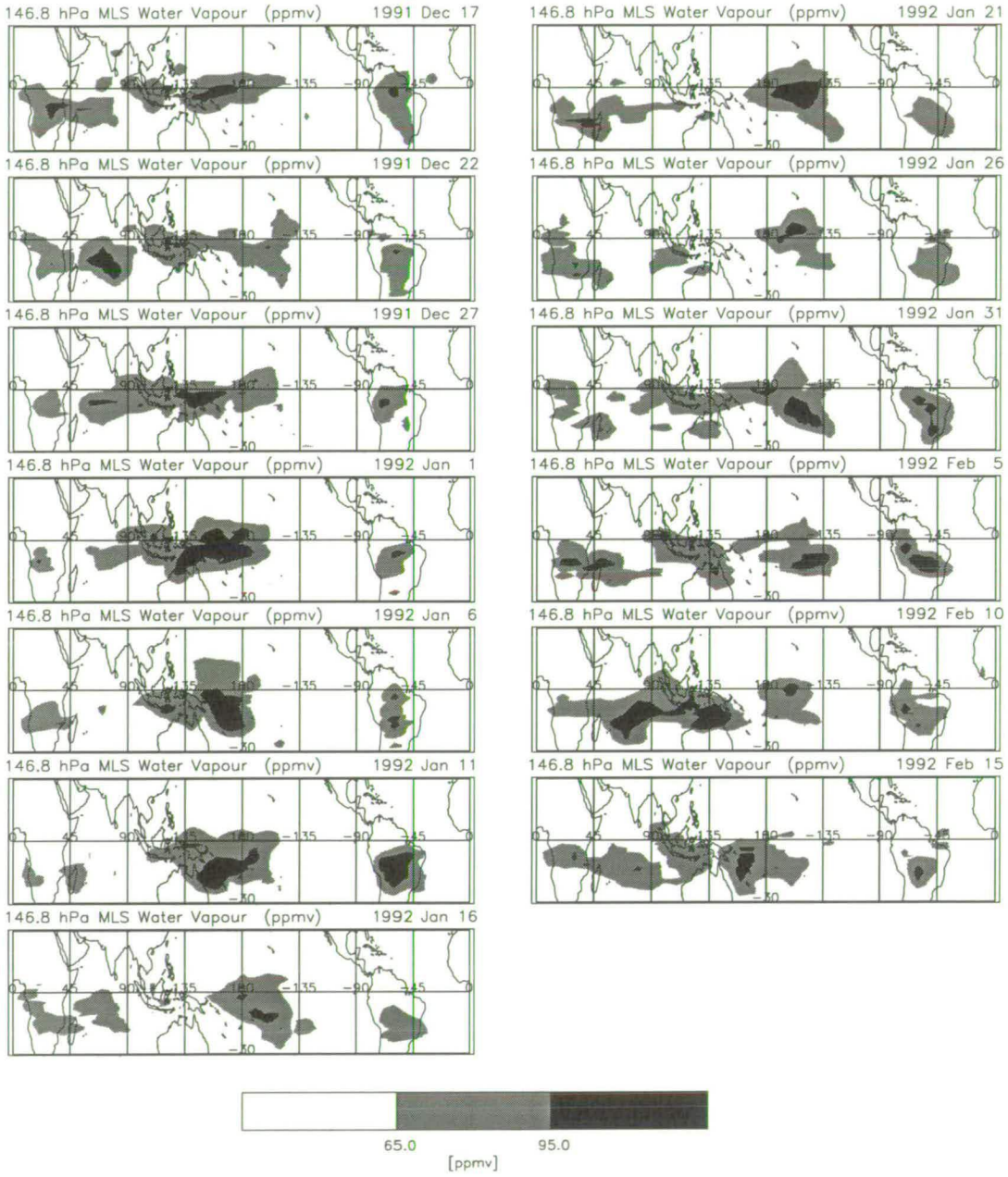

Figure 5.35: 5 day averaged MLS water vapour mixing ratios (ppmv) at 147 hPa. Dates indicate the middle of the pentad.

cycle, in contrast, decreases in strength with height and this leads to the idea that the intraseasonal convective anomalies reach greater heights than the climatological convection. The divergence field shows that some of these events reach the 100 hPa level. The possible role of the MJO in stratosphere-troposphere exchange will be examined in the following chapter.

There is some evidence for the intraseasonal cycle in the longitude-time section of ECMWF relative humidity at 10°S but similar features were not present at the equator. The 5-day averaged fields showed that ECMWF does not show sufficient contrast between dry and moist times and regions. In previous studies this has been ascribed to a shortcoming of the model's convective scheme. The lack of contrast in moisture between the western and eastern Pacific suggests that, like the Hadley circulation, the Walker circulation may also be underestimated by the model. Because of the importance of the MJO to El Niño and to forecasting, it is important that this should be improved in the ECMWF model.

Comparisons with dynamical quantities derived from ECMWF data were aimed at revealing areas of strong convection to help confirm the cause of the variability. The eastward moving moist features were correlated with westerly wind bursts at 850 hPa which lead to enhanced evaporation and are known to play an important part in generating and maintaining the MJO. The formation of cyclone pairs was also noted to occur during an MJO event and is related to the off-equatorial position of the maximum westerly wind bursts and encourages the development of moist anomalies east of the dateline.

Sequences of water vapour maps through an eastward moving event showed a similar lifecycle to that seen in many studies of OLR during MJO events. Upward motion in the mid-troposphere was strong when mixing ratios were high which implied that convective processes are leading to a moist upper troposphere. Water vapour at 215 hPa moved from the Indian Ocean, intensified over the western Pacific and moved down the SPCZ. This movement was associated with pockets of upward motion indicating the translation of convective centres. Similar lifecycles were seen in 315 hPa mixing ratios and NVAP total precipitable water in the column below, further supporting the association with convection. Similarly, convection that reaches 147 hPa also displays this eastward translation and development along the SPCZ which is characteristic of the MJO.

The correlation with westerly wind bursts, development of cyclone pairs, similarity between the lifecycle of OLR and water vapour and its correspondence with vertical velocity all support the association of the eastward moving features with the convective anomalies of the MJO.

The results presented in chapters 4 and 5 may give some indication to the possible mechanisms involved in the MJO. The spatial resolution and the altitude of the MLS measurements means that small-scale water vapour anomalies associated with small-scale and lower altitude convection cannot be resolved and therefore it is not possible to comment on the cloud-organisation of the MJO. It is hoped that when this work is extended to include analysis of outgoing longwave radiation, the cloud-organisation of the MJO can be investigated.

Two important results presented in this chapter were the occurrence of low-level westerly wind bursts at the time of enhanced water vapour (figure 5.24), and the development of a cyclone pair also in the lower troposphere (figure 5.26). The appearance of westerly wind bursts in this case would appear not to fit with the WISHE theory of the MJO which requires winds to be easterly, but westerly winds are an important part of both wave-CISK and ASCII theories. The westerly wind bursts in this case were seen to be maximum off the equator in contradiction to Kelvin wave dynamics as mentioned in section 5.3. However, westerly wind bursts in an equatorial Rossby mode would have maximum variance off the equator (e.g. Wheeler and Kiladis, 1999) and furthermore, the appearance of cyclone pairs in the lower troposphere (figure 5.26) or anticyclone pairs in the upper troposphere is a sign of Rossby wave activity (see figure 5.27) (e.g. Matsuo, 1966; Knutson and Weickmann, 1987; Lau *et al.*, 1988).

Equatorial Kelvin wave theory requires that low-level (850 hPa) westerly winds and high pressure are found to the west of 850 hPa easterly winds and low pressure perturbations (see figure 4.2). This is accompanied by divergence on the western side and convergence on the eastern side. Pressure perturbations were not examined in the thesis but the 850 hPa wind fields in figure 5.26 show this pattern on the 1st and 6th January in the region of the dateline at the equator. This is accompanied by positive and negative divergence anomalies centred on the equator near the dateline revealed by 5 day averaged ECMWF divergence fields (see figure 5.36) at 850 hPa. Hence, it can be concluded that there is evidence of

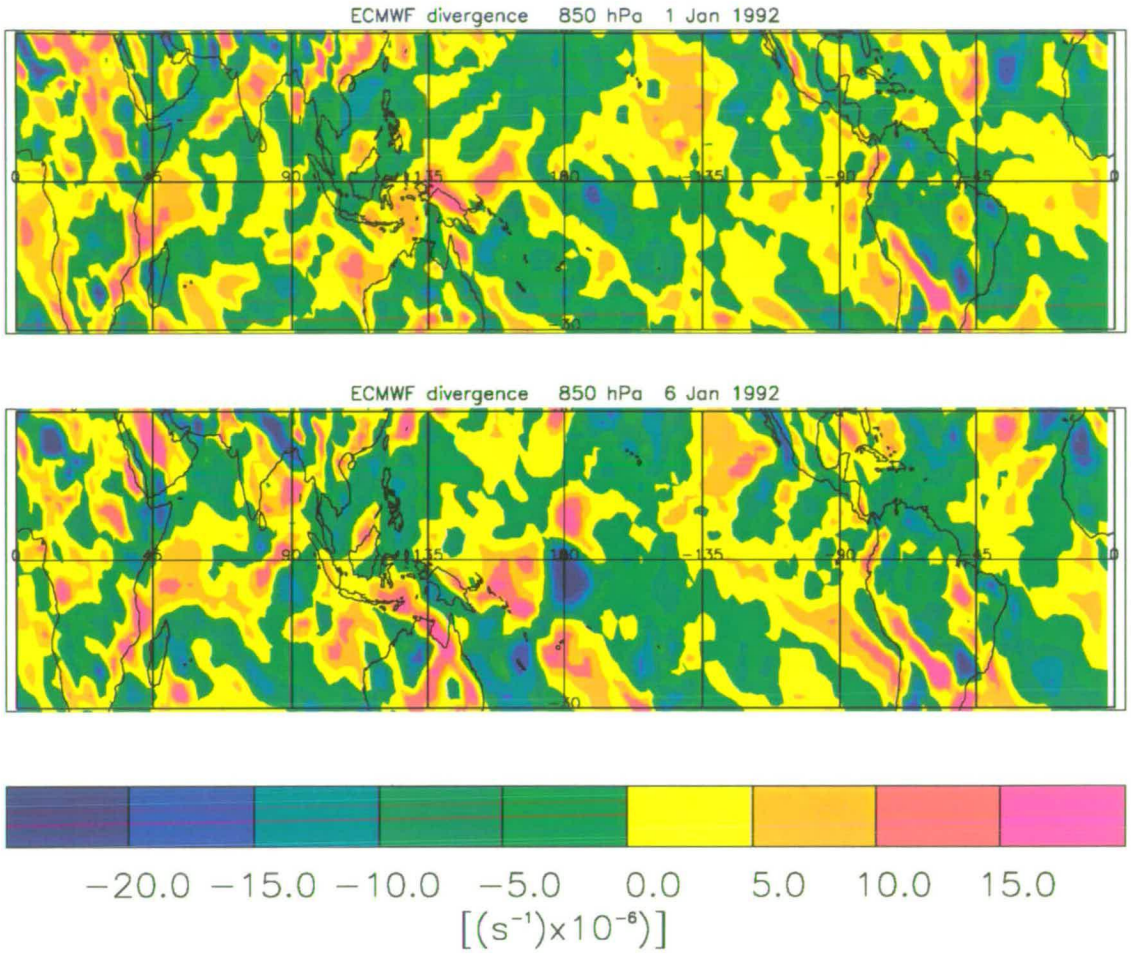

Figure 5.36: 5 day averaged ECMWF 850 hPa divergence . Dates indicate the middle of the pentad.

Kevin wave activity during this particular MJO event.

According to the results presented in this thesis, any appropriate theory for the MJO should include both Rossby and Kelvin wave modes. Although wave-CISK and ASCII theories both involve Kelvin waves to induce eastward propagation, Rossby waves figure in the wave-CISK explanation only (see figure 4.3) and the results presented here would appear to support the wave-CISK explanation despite the off-equatorial position of maximum variance of water vapour and westerly winds. A more detailed analysis would focus on the time-lag between the maximum in surface convergence and the maximum in convection and their positions relative to each other. The maximum surface convergence of moisture should lead in time, and be found further to the east of the maximum in convection to

confirm the presence of the Kelvin wave-CISK mechanism.

The ASCII theory also involves an interaction with sea surface temperature; sea surface temperature is lower underneath the cloud cluster and warmer to the east of it. Presently, it is not possible to comment further on the mechanism of ASCII but future work will involve a detailed analysis of SST to address this issue. This will focus on determining the position of maximum sea surface temperature in relation to the enhanced convection and centre of maximum surface convergence. The observation that SSTs are warmer to the east of the enhanced convection would be evidence in support of ASCII.

Chapter 6

Water Vapour in the Lower Stratosphere

6.1 Introduction

A new non-linear retrieval of water vapour from the 183 GHz channel on MLS has recently become available and is described in chapter 2. The retrieval extends stratospheric measurements to two extra levels, 68 hPa and 100 hPa, although data at 100 hPa are considered to be less reliable. This chapter presents results based on this new retrieval and explores the relationship between water vapour in the upper troposphere and lower stratosphere.

The non-linear retrieval, together with upper tropospheric measurements from the 205 GHz channel, can potentially enable profiles of water vapour to be constructed upwards of 316 hPa. Using both sets of data, patterns of water vapour in the tropical upper troposphere are compared with those in the lower stratosphere and used to examine aspects related to stratosphere–troposphere exchange. Previous chapters have focussed upon the variability of water vapour in the upper troposphere and a 30-85 day cycle was identified with the deep convective anomalies of the MJO. Evidence that stratosphere-troposphere exchange may take place within the deep convective events of the MJO is examined.

The first part of this chapter presents an overview of water vapour in the lower stratosphere and describes the current ideas of stratosphere-troposphere exchange. The next section looks at seasonal zonal means of water vapour at 68 hPa. Section 6.3 examines the variability of water vapour in the tropical lower stratosphere and how it relates to that in the upper troposphere. The lower

stratosphere and the MJO is discussed in section 6.5.

6.1.1 The Tropopause

The tropopause defines the boundary between the troposphere and the stratosphere. There are many ways to define the position of the tropopause (Highwood and Hoskins, 1998). The 'lapse-rate' definition is used most often and is based on the fact that the temperature lapse rate in the troposphere is much larger than in the stratosphere. By convention, the World Meteorological Organisation (WMO) defines the lapse-rate tropopause as, "The lowest level at which the temperature lapse rate decreases to 2 K km^{-1} or less and the lapse rate average between this level and the next 2 km does not exceed 2 K km^{-1}."

In the tropics, the tropopause coincides roughly with an isentropic surface of 380 K and in the extratropics with a surface of constant potential vorticity (PV). Using the conventional definition of PV, (see chapter 1) the extratropical tropopause has a value of 2PVU (Potential Vorticity Units, 1PVU= $10^{-6}\ m^{-2}\ s^{-1}\ K\ kg^{-1}$). The tropopause has a quasi-impermeable nature, acting as a barrier to adiabatic motion where θ and PV are conserved, but being permeable to diabatic motion.

Isentropes slope downwards and polewards and intersect the tropopause as shown in figure 6.1. In the tropics the 380 K isentrope is typically found at 100 hPa and varies by less than 10 hPa annually. In the extratropics, the height of the tropopause is maximum in winter and minimum in summer associated with changes in the strength of the stratospheric polar vortex. In the northern hemisphere the mean position of the tropopause moves upwards from winter to summer and in the southern hemisphere, this shift takes place between 30°S and 40°S (Appenzeller *et al.*, 1996).

The use of figure 6.1 enabled Holton *et al.*, (1995) to classify different types of stratosphere–troposphere exchange (STE). The shaded area in figure 6.1 denotes the 'lowermost stratosphere' where isentropic surfaces cut through the tropopause. In this region, STE occurs along isentropic surfaces as shown by the wiggly lines in fig 6.2. This mechanism for STE is important in the extratropics. Above 380 K is the 'overworld' (Hoskins, 1991) where isentropes lie entirely within the stratosphere. The overworld cannot be reached from the tro-

posphere without crossing an isentropic surface. In the tropics therefore, STE takes place through diabatic ascent in overshooting cumulonimbus convection as shown in figure 6.2.

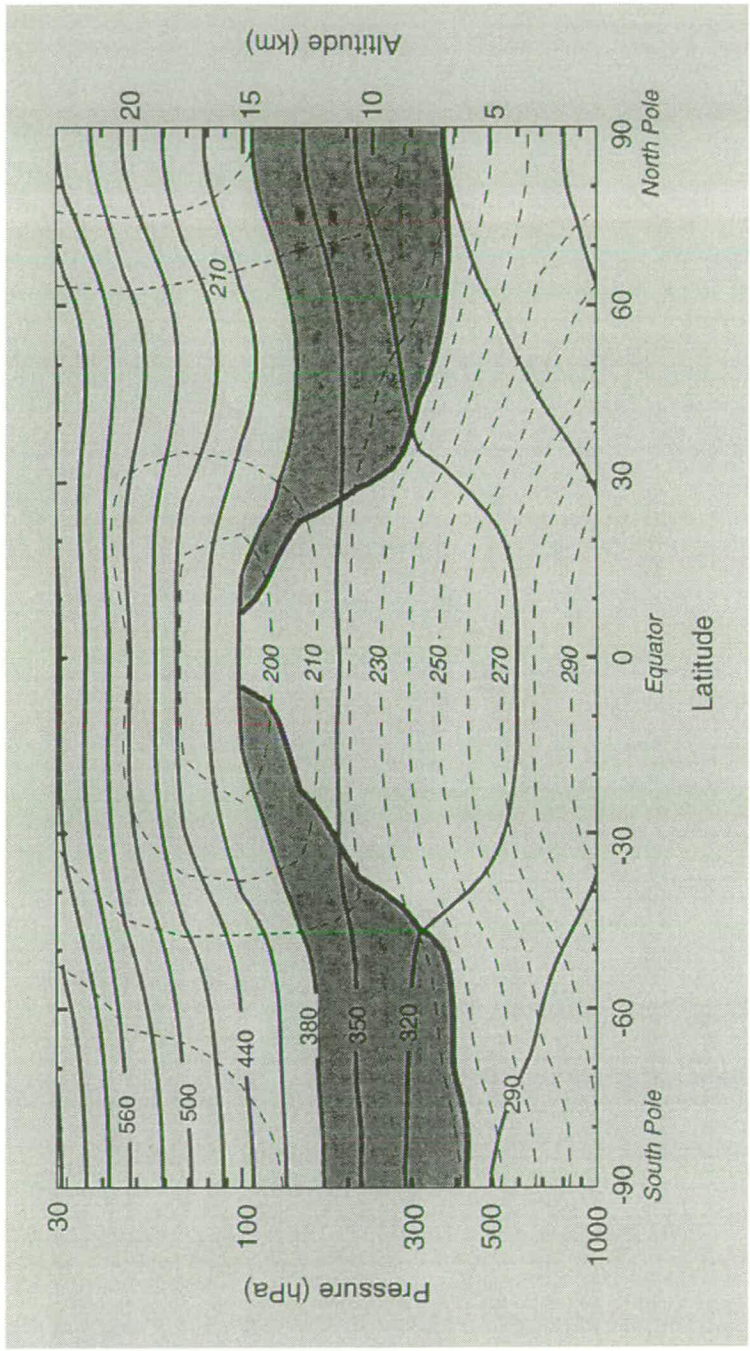

Figure 6.1: Latitude-altitude cross section for January 1993 showing longitudinally averaged potential temperature (solid contours) and temperature (dashed contours) from UKMO data. The heavy line denotes the 2-PVU potential vorticity contour which approximates the tropopause outside the tropics. The shaded area indicates the "lowermost stratosphere" whose potential temperature surfaces span the tropopause (Figure taken from Holton *et al.*, 1995.)

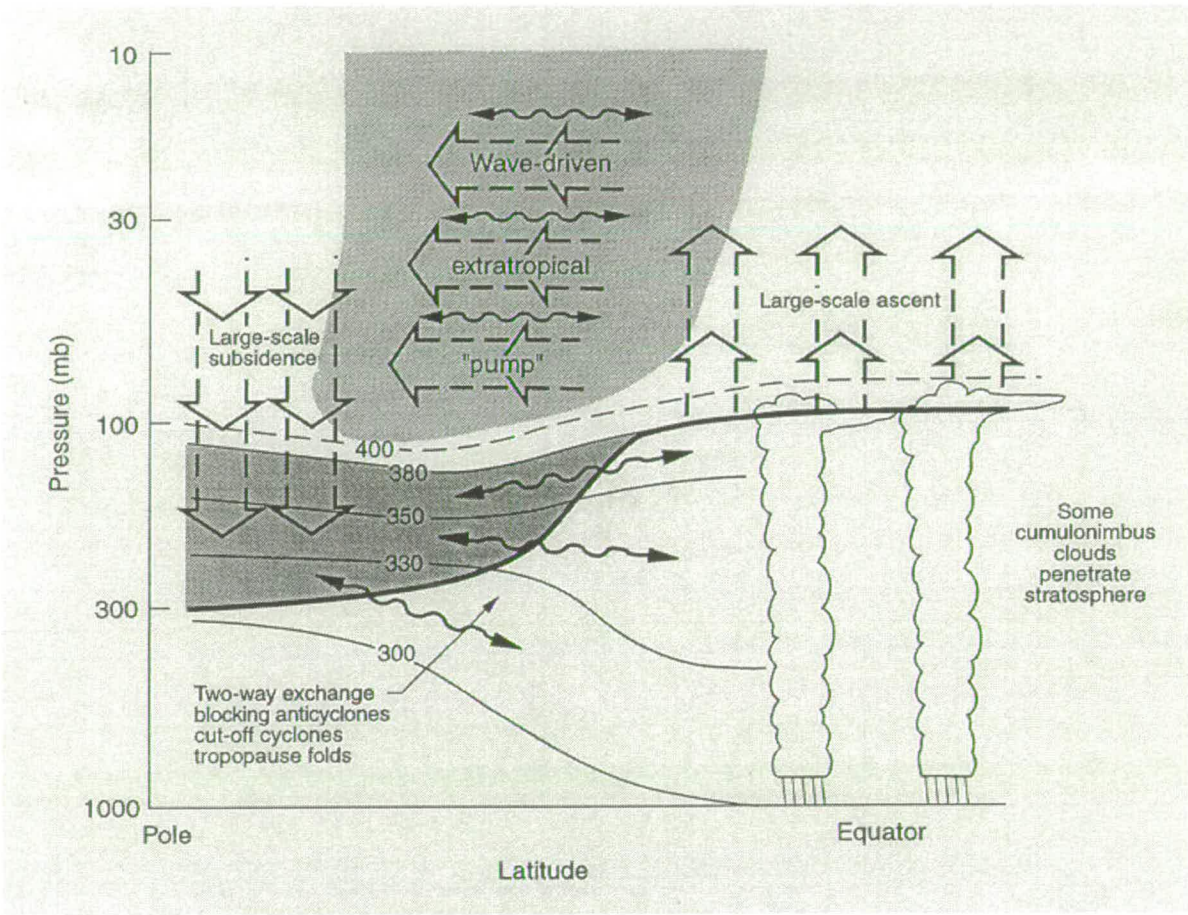

Figure 6.2: Dynamical aspects of STE. The heavy line indicates the tropopause, the thin lines are isentropic surfaces in Kelvins. The heavy shaded region denotes the "lowermost stratosphere" where isentropic surfaces span the tropopause and isentropic exchange by tropopause folding occurs. The region above the 380 K surface is the "overworld" in which isentropes lie entirely in the stratosphere. Light shading denotes the "extratropical pump". The wavy double headed arrows denote meridional transport by eddy motions. The broad arrows show transport by the global scale circulation. (Figure taken from Holton *et al.*, 1995.)

6.1.2 Stratosphere–Troposphere Exchange in the Tropics

Water Vapour in the Lower Stratosphere

In contrast to the troposphere where water vapour mixing ratios decrease with height due to the decrease in temperature, mixing ratios in the stratosphere increase with height due to methane oxidation. Typically mixing ratios have a value of 3-6 ppmv, much lower than tropospheric values, which, even just below the tropopause, are in the region of 70 ppmv.

Brewer (1949) analysed stratospheric water vapour measurements made over England with a frost-point hygrometer. He found the observed mixing ratios to be lower than the minimum saturation mixing ratio (q_s) at the local tropopause. To account for this dryness, he proposed a circulation whereby air enters the stratosphere from the troposphere in the tropics, drifts polewards and descends in the extratropics. The tropical tropopause which is high and cold acts as a 'cold trap' to 'freeze dry' the air as it rises through. Consequently air from the tropopause is much drier than surrounding air in the stratosphere which has been moistened by methane oxidation. The freeze drying procedure remains the most plausible explanation for the dryness of the lower stratosphere.

Mastenbrook (1974) and Kley *et al.* (1979) found mixing ratios in the tropical, lower stratosphere that were too low to be explained by the mean tropopause temperature. Kley *et al.* (1979) found mixing ratios of 3 ppmv at about 21 km or 46 hPa above Panama which would require a tropopause temperature of 189 K. The local temperature of the tropopause was only 193 K and could not therefore have been responsible for drying the air. Kley *et al.* therefore suggested that the air must have entered the stratosphere at a different location.

Observations (e.g. Kley *et al.*, 1979; Kley *et al.*, 1982) also showed that the minimum mixing ratios or hygropause, was found 2–3 km above the local tropopause. Kley *et al.*, (1982) proposed that overshooting convective clouds could hydrate the lower stratosphere by sublimation of ice crystals but did not observe any convective towers which reached as high as the hygropause. Jones *et al.* (1986) used data from LIMS and SAMS instruments on the Nimbus 7 satellite to investigate whether water vapour mixing ratios in the stratosphere were consistent with a source via the oxidation of methane. They inferred an average water vapour mix-

ing ratio on injection into the stratosphere of 2.6–2.8 ppmv and an equivalent temperature at 60 hPa of 186 K to produce these values.

Newell and Gould-Stewart (1981) defined areas where the air could enter the stratosphere as being regions where the air was 190.6 K at 100 hPa, cold enough to dry the air to 3 ppmv. They introduced the term 'stratospheric fountain' and identified the most likely times and locations for the stratospheric fountain as being the Western Pacific, northern Australia, Indonesia and Malaysia from November–March, and over the Bay of Bengal and India during the monsoon. Once in the stratosphere, air could be transported rapidly in the zonal direction and only slowly in the vertical thereby explaining the dryness over Panama as Kley *et al.*, (1979) observed.

The stratospheric fountain idea could not explain the elevated hygropause and an alternative mechanism whereby tropical convective systems could cool the stratosphere was proposed by Danielsen (1982). Some convective events are strong enough to overshoot both the tropopause and their equilibrium level. As their buoyancy becomes negative, they subsequently decelerate and sink. Throughout this time, the air parcel is mixing with the stratospheric air and a large cirrus anvil forms (approx. 200 km^2). In addition to the temperature minimum at tropopause level, a second minimum occurs at the top of the anvil, resulting in a 'Σ' shaped temperature profile and hence accounting for the observed water vapour minimum well above the tropopause. The difference between radiative heating at the base and cooling at the top produces upward heat fluxes and downward ice crystal fluxes. The sedimentation of the ice crystals from the top acts to dehydrate the region. Thus, tropospheric air is introduced to the stratosphere, but results in dehydration.

Based on model simulations, Potter and Holton (1995) suggested that convectively generated buoyancy waves could induce vertical parcel displacements which promote the formation of ice crystals in the lower stratosphere. In the simulations, clouds formed upwind of the convective region and subsequent precipitation of the ice crystals led to dehydration as with Danielsen's hypothesis. Potter and Holton's method however, does not require convection to penetrate the tropopause or reach the hygropause.

Dynamical Control

It has long been known (e.g. Eliassen, 1951; Dickenson, 1968) that the extratropical stratosphere and mesosphere act non-locally upon the tropical stratosphere. The effect, known as the "extratropical pump", is responsible for large-scale ascent and mass transfer from the tropical upper troposphere to lower stratosphere. Its relation to stratosphere-troposphere exchange is illustrated in figure 6.2.

Rosenlof and Holton, (1993) used the downward control principle [1] to examine the rate of mass transfer across the 100 hPa surface. They used momentum and temperature fluxes from 10 years of daily geopotential heights from UKMO analyses and found that upwelling was limited to equatorward of 15°N and 15°S except during southern hemisphere winter when it extends to 30°S. In the NH winter stratosphere at high latitudes, the stronger forcing of planetary waves results in stronger downwelling in the high latitudes and hence stronger, compensatory upwelling in the tropics. Consequently this results in more mass transfer across the tropical tropopause in NH winter (DJF) than during SH winter (JJA). It also drives tropical temperatures below radiative equilibrium and produces an annual cycle in tropical temperatures near the 100 hPa level, with lowest temperatures in NH winter and highest temperatures in NH summer. Yulaeva *et al.*, (1994) observed this annual cycle in 12 years of global satellite data from the MSU-4.

A consequence of the annual cycle in tropopause temperatures is that mixing ratios of air that has entered the stratosphere from the tropical troposphere should also have an annual cycle, in phase with that of temperature. Mote *et al.* (1995) used satellite observations from MLS, HALOE and SAGE II to show that stratospheric water vapour varies seasonally in phase with the annual cycle in tropopause temperatures. Stratospheric air is marked with an 'entry mixing ratio' q_e set by the temperature at the tropopause. Due to the only relatively weak mixing between tropics and extratropics, layers of air retain this water vapour signal up to two years; this is known as the 'tape recorder' effect (Mote *et al.*, 1996)(see figure 6.3). The lowest mixing ratios occur after January when the 100 hPa equatorial temperature is a minimum. The annual cycle in water vapour or 'tape signal' propagates upwards with time and can still be observed

[1] under steady state conditions, the extratropical mass flow across an isentropic surface is controlled by the momentum forcing above the surface

near 20 hPa (see figure 6.3).

This upward advection of the seasonal minimum explains the elevated hygropause found in many previous studies (see discussion above), and sets of balloon profiles (Ovarlez *et al.*, 1996) show a vertical structure consistent with the tape recorder hypothesis.

The implied ascent rates just above the tropical tropopause were calculated to be about 0.2 mms^{-1} in northern summer and about 0.4 mms^{-1} in northern winter with the annual maximum (0.5 mms^{-1}) occurring just south of the equator in December or January. The greater ascent rate in northern hemisphere winter than northern hemisphere summer is as expected from dynamical constraints.

The Role of Convection

A uniform rising motion across the tropics, would result in a thick layer of cirrus clouds forming near the tropopause. Since this is not observed, it has been suggested (e.g. Robinson, 1980) that upward flow across the tropopause must be associated entirely with deep convection that penetrates the stratosphere. Tropical convective systems could dry the stratosphere through mechanisms such as that proposed by Danielsen, (1982) (see discussion above). Cumulonimbus clouds may also lead to hyperventilation whereby deep cumulonimbus clouds inject a greater mass of dry air into the stratosphere than can be taken up by the action of the extratropical pump.

The primary aim of the Stratosphere-Troposphere Exchange Project Tropical Experiment (STEP Tropical) (Russell *et al.*, 1993) was to investigate stratosphere-troposphere exchange and the dehydration process in the region and season with the coldest average tropopause temperatures. Aircraft, carrying Lyman-Alpha hygrometers, (see section 2.1) were deployed in the western Pacific and northern Australia during the winter monsoon (January-February) 1987. A total of 14 missions were carried out.

Kelly *et al.*, (1993) found the minimum mixing ratios at 375 K to be about 2.4 ppmv over Darwin in January to February. Danielsen (1993) found that, during the break-monsoon, overshooting cumulonimbus towers do mix stratospheric air with tropospheric, and Kelly *et al.*, (1993) showed that the ice crystals fall out without evaporating, hence providing strong observational evidence in sup-

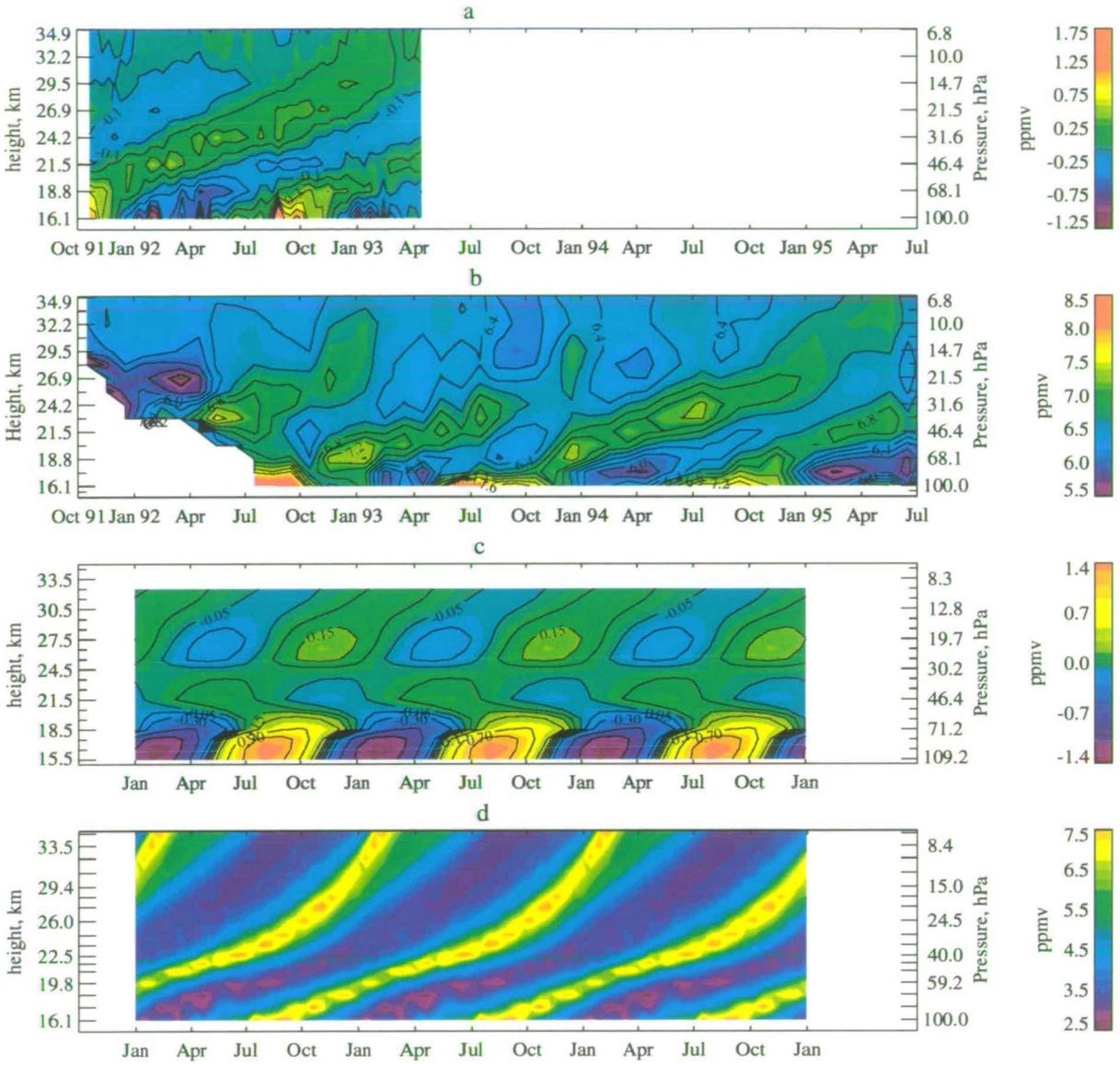

Figure 1

Figure 6.3: Time-height sections of water vapour mixing ratio from a) MLS, b) HALOE c) SAGE II and d) trajectory analysis. See Mote *et al.* (1996) for details.

port of Danielsen's 'hyperventilation' idea. The resulting air had mixing ratios of 1.5-2.0 ppmv.

During the active phase of the monsoon cloud tops reached heights of around 16.5 km and temperatures of 185.5 K were recorded, implying saturation mixing ratios of 1.6 ppmv. During the break phase cloud tops were higher than during the active phase, and the corresponding temperatures were colder. Heights of 16.9 km and cloud top temperatures of 183 K implied a saturation mixing ratio (q_s) of 1.1 ppmv.

The widespread nature of monsoon convection means it could be a significant contributor to the transport of tropospheric air into the stratosphere. Pfister *et al.*, (1993), reveal that monsoon tropical cyclones mixed tropospheric air directly into the stratosphere, at heights of around 18 km, by means of detrainment from small and numerous overshooting turrets. In these cases, injected stratospheric air is dehydrated to the observed environmental stratospheric values. They observed one anomalously high mixing ratio of 10 ppmv at about 16.5 km. These overshooting turrets are significant because they deposit tropospheric air into the lowest 2 km of the stratosphere over several days.

STEP results showed that convection does transport tropospheric air into the stratosphere. Most ice crystals were observed to sediment out, and this showed that the cold-trap dehydration mechanism does take place in convective systems. It is still unknown whether convective events occur sufficiently often to dominate over the tropical stratospheric mass and water vapour budget and whether or not they result in hyperventilation (Holton *et al.*,1995).

Recently, Jackson *et al.* (1998) used HALOE measurements to show that mixing ratios of less than 2.4 ppmv enter the stratosphere in December, January and February from 0–10°N in the region of 140–170°E. This happened along with an upward distortion of the 375 K surface and a temperature minimum of about 192 K, indicating that deep convection is taking place. They also found sporadic exchange at 10°S resulting in stratospheric mixing ratios of 2.4–2.8 ppmv. Most exchange however, was found to occur at 10°N and to spread southwards. Although most STE takes place in December, January and February (DJF) isolated incidences of STE are found in March, April and May (MAM). One such example in MAM 1994 showed an upward distortion of the 375 K surface and a seasonal

temperature minimum of 193K; this temperature being still 4.5K warmer than the temperature required to saturate to 2.4 ppmv. More persistent STE takes place in September, October and November (SON) between 10°S and 20°N at 120°E, with air entering with mixing ratios of 3.6–4.0 ppmv in SON at 10–20°N.

Using 100 hPa Temperatures

In later parts of this chapter, the ECMWF 100 hPa temperatures will be used to calculate saturation mixing ratios to identify regions where possible freeze drying may take place. There are some hazards involved with the use of 100 hPa temperatures as a proxy to tropopause temperatures and these are to be outlined briefly here.

Mote *et al.*, (1996) reported a discrepancy between the lowest average mixing ratio in the tropical region and the UKMO temperatures at the 100 hPa level. The lowest mixing ratio observed was 3.0 ppmv (at 46 hPa) requiring a temperature of 189.6 K at 100 hPa, and the highest mixing ratio was 4.2 ppmv which would require a temperature of 191.6 K. UKMO temperatures in the area 30°N to 30°S were too high to explain the observed mixing ratios and only a few grid points were cold enough to saturate the air to the observed mixing ratios.

Mote *et al.* suggest that hyperventilation may explain this discrepancy. Air introduced into the stratosphere by cumulonimbus clouds which are sub-grid-scale in size would imply lower temperatures than those which were represented by the UKMO model. This hyperventilation is most likely to occur in Northern Hemisphere summer when the pumping rate is minimum, and particularly in the Asian monsoon region where deep convection is prevalent.

Figure 6.4 shows the ECMWF temperatures averaged over the area between 30°N and 30°S (top curve), and the minimum temperature occurring in the same area (bottom curve), for each day. The horizontal line indicates the 189.6 K corresponding to a saturation mixing ratio (q_s) of 3.0 ppmv, the lowest reliable value of q_s observed at 46 hPa by UARS instruments reported by Mote *et al*, (1996). Area-averaged ECMWF temperatures for the period December 1991– April 1993 (figure 6.4) range from 195-199.5 K compared with a UKMO temperature range of 196-200 K. The minimum temperature occurring in the area for each day is the lower curve in figure 6.4. The minimum temperature ranges from 184-193 K in

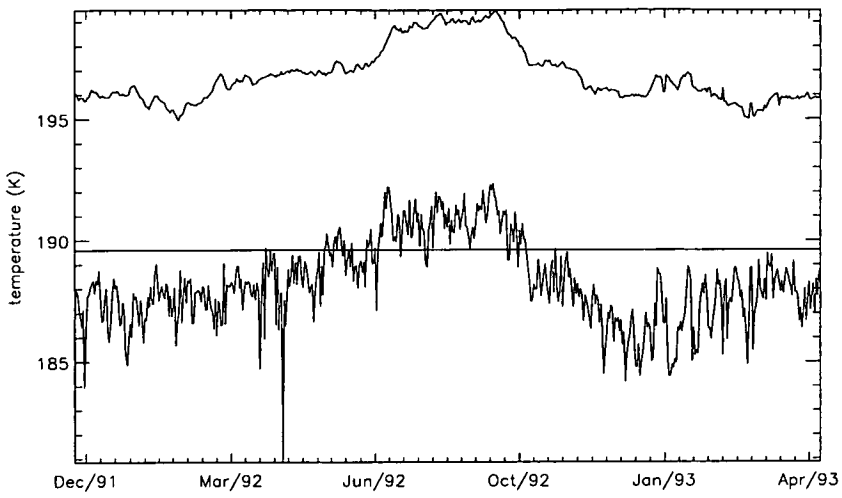

Figure 6.4: ECMWF 100 hPa temperatures for the area averaged between 30°N and 30°S (top curve) and the minimum temperature occurring in the same area (bottom curve) on each day. The horizontal line indicates the 189.6 K corresponding to the saturation mixing ratio (q_s) of 3.0 ppmv observed by Mote *et al*, (1996).

ECMWF compared with 186-196 K in UKMO; minimum ECMWF temperatures are 2 K lower than UKMO. Although the area-averaged ECMWF temperatures are still too high to account for the 3.0 ppmv mixing ratio, there are many more times in the ECMWF data than in the UKMO data when individual grid-points are cold enough.

The use of 100 hPa temperatures as a proxy for tropopause temperatures can lead to the calculated minimum saturated mixing ratio (q_s) being higher than observed if the tropopause lies below the 100 hPa level (Fredrick and Douglass, 1983). This is a result of q_s being proportional to temperature and inversely proportional to pressure. When the temperatures at 100 hPa are higher than the tropopause temperatures and the pressure of the tropopause is higher than 100 hPa these conditions lead to a higher calculated q_s. This is often the case in northern hemisphere summer (JJA). In northern hemisphere winter (DJF) the tropopause is often above 100 hPa. In this case, 100 hPa temperatures are greater than the tropopause temperatures as before, but this time the pressure of the tropopause is lower than 100 hPa and the two effects cancel. 100 hPa

temperatures are a better approximation to tropopause temperatures in northern hemisphere winter than in northern hemisphere summer.

6.2 Water Vapour at 68 hPa

Seasonal averages of water vapour at 68 hPa from MLS are shown in figures 6.5 and 6.6. As expected for this height in the stratosphere, the seasonal averages are largely zonal in structure reflecting rapid zonal mixing. In DJF (figure 6.5) a drier region with mixing ratios of around 3.4 ppmv is located over the 'stratospheric fountain' region of Indonesia and the western Pacific. Additionally, it is dry over Panama, extending southeastwards to the coast of Chile. Similarly, a dry region is located over Indonesia and the western Pacific in HALOE data at 100 hPa (Jackson *et al.*, 1998) and there is an area off the coast of Panama which extends southeastwards. There is no equivalent dry area off the coast of Panama in the HALOE field at 83 hPa.

In MAM (figure 6.5), the lowest water vapour values lie along, and mostly north of the equator. In JJA (figure 6.6), the equatorial region remains dry (though not as dry as in MAM) and the structure remains predominately zonal except for a moister area (4.0 ppmv) evident in the Asian monsoon region persisting until SON (figure 6.6). This moistening associated with the Asian monsoon was noted by Jackson *et al.*, (1998) to occur at 128 hPa, 100 hPa and 83 hPa and to be in contrast with the climatology presented by Rind *et al.*, (1993) from SAGE II data which did not reveal this at either 150 hPa or 100 hPa. The moist region observed by MLS at 68 hPa is centred further east, is more localised and persists for longer than that at 83 hPa in HALOE data. The monsoon moistening being still evident at 68 hPa is higher than has previously been observed with MLS data.

6.3 The 'Tape Recorder' and the Upper Troposphere

In a similar way to Mote *et al.*, (1996) time-height sections have been constructed for the lower stratosphere, but in addition, levels in the upper troposphere have been added. Missing data have been filled with a Kalman filter appropriate to

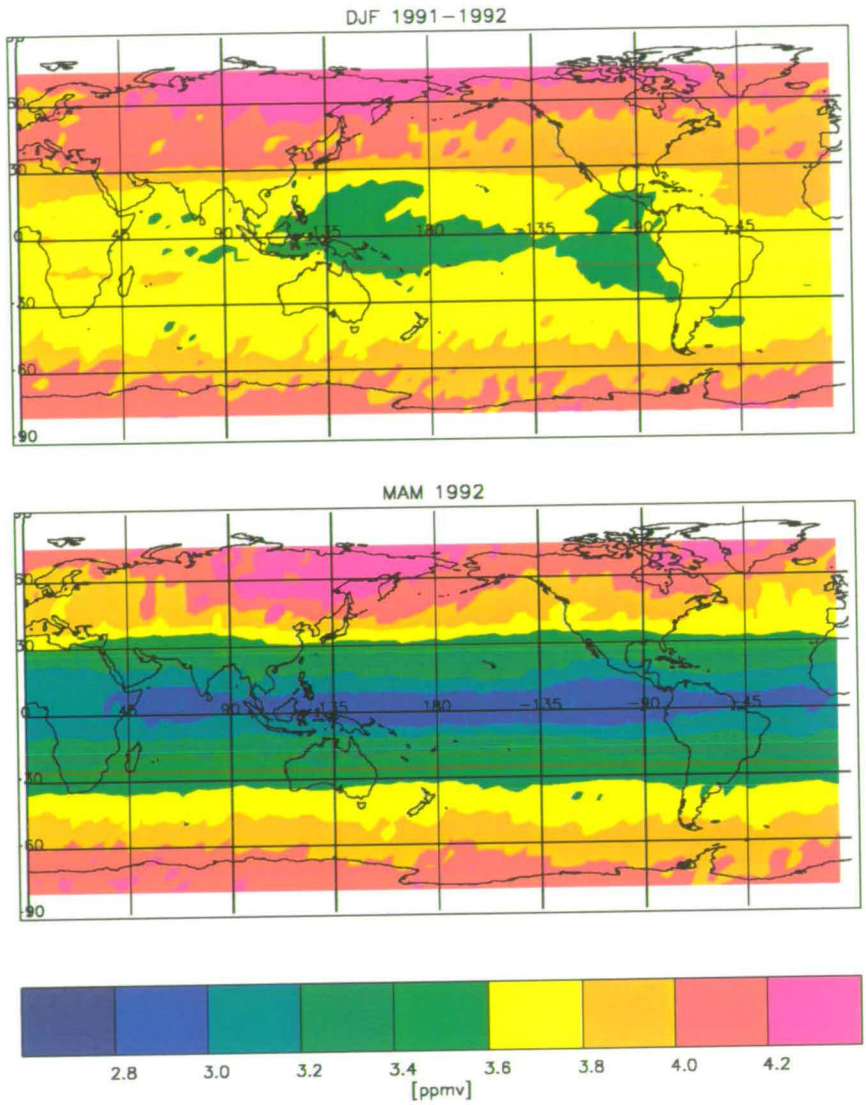

Figure 6.5: Seasonally averaged MLS water vapour (ppmv) at 68 hPa for December–February 1991/2 (DJF) and March–May 1992 (MAM).

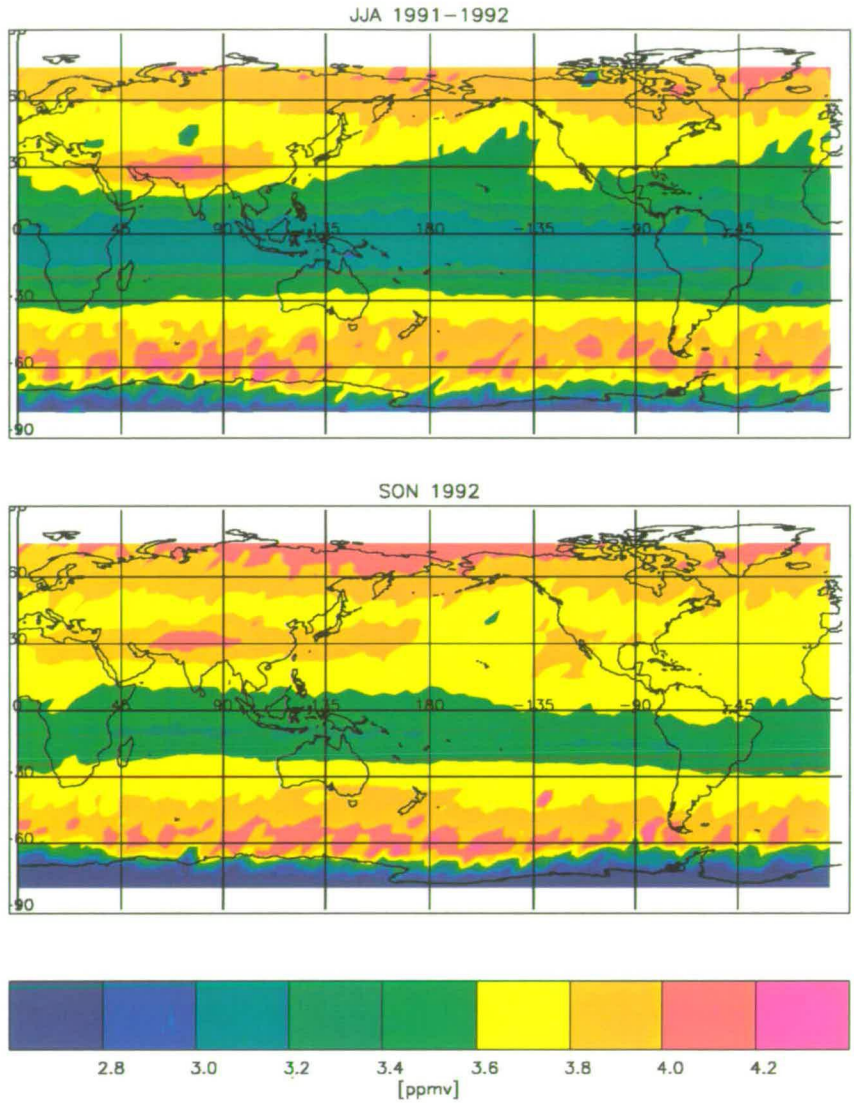

Figure 6.6: Seasonally averaged MLS water vapour (ppmv) at 68 hPa for June–August 1992 (JJA) and September–November 1992 (SON).

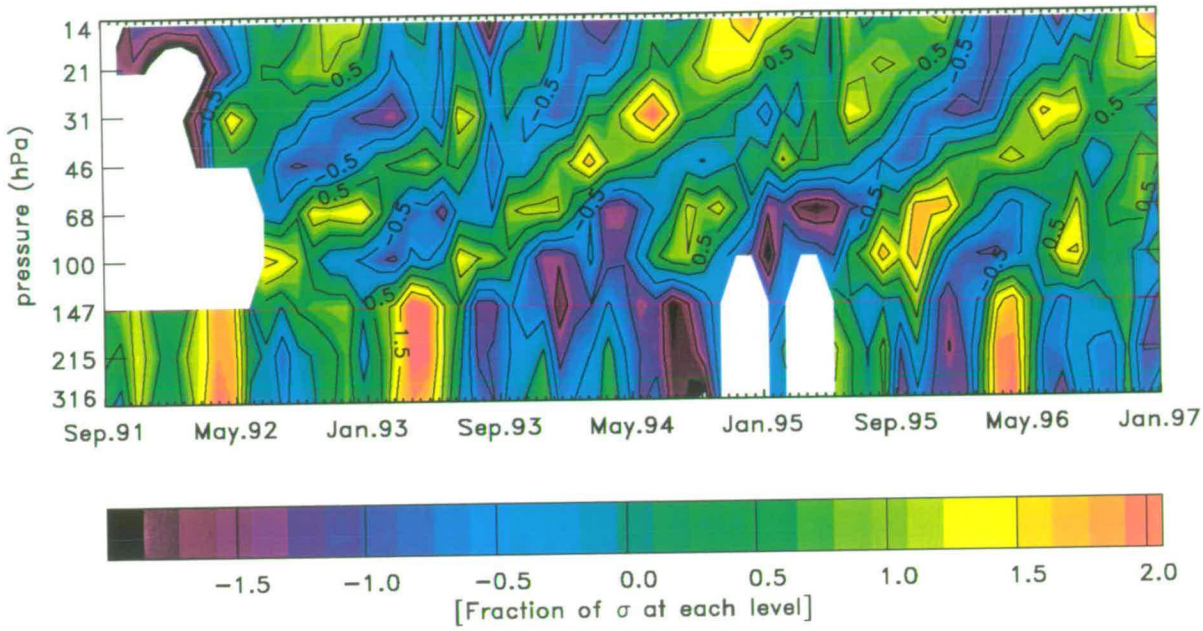

Figure 6.7: Time-height section of zonal mean water vapour between 12°N and 12°S. Stratospheric water vapour comes from HALOE (version 18) and tropospheric water vapour from the 205 GHz channel. The plot shows deviations from the time-mean expressed as a fraction of the standard deviation (w.r.t. time) at that level. Measurements in both stratosphere and troposphere are 30 day averages.

the level. The plots show deviations from the time-mean at each level, expressed as a fraction of the standard deviation at each level.

Figure 6.7 presents a time-height section comprising HALOE measurements (version 18) in the lower stratosphere and MLS 205 GHz measurements in the upper troposphere. The time-height section begins in September 1991 and ends in January 1997. Because HALOE take several days to cover latitudes from 12°N to 12°S, measurements are binned every 30 days. In the lower stratosphere, the plot shows the characteristic tape signal with alternating dry and moist bands propagating upwards from the 100 hPa level. Moist plumes in the upper troposphere appear to attach onto moist fingers in the lower stratosphere. Three such examples of this can be seen in the figure, one in May 1992, one in spring 1993 and one in May 1996. Likewise, dry plumes in the troposphere extend as dry bands in the stratosphere.

A similar time-height section is shown in figure 6.8 for the period September 1991–April 1993. This figure is composed of stratospheric measurements from the non-linear retrieval (MLS 183 GHz radiometer) and tropospheric measurements as before from the 205 GHz radiometer on MLS. Measurements are daily, excepting yaw days and times when there were difficulties with the instrument. Two moist and three dry tape signals can be seen in this plot.

A positive anomaly (figure 6.8) in the upper troposphere is evident during NH winter and spring (November–May 1992) but is interrupted by a dry anomaly in February 1992. Another moist anomaly begins in NH winter of 1993. Moist plumes in the upper troposphere are shortly followed by moist tape signals in the lower stratosphere with a delay of about 2 months. Dry anomalies in the upper troposphere are found in NH summer and autumn from June to November but are overlaid by a moist tape signal in the stratosphere. The relationship between positive anomalies and moist tape signal is less clear than in the 30 day averaged plot and there appears not to be a simple relationship between the two.

The relationship between the moist plumes and the tape signal can be further elucidated by examining the tape recorder for the northern and southern hemisphere tropics independently. The two figures 6.9 and 6.10 show time-height sections where measurements are binned from 5-15°N and 5-15°S respectively. Although the stratospheric tape signals are similar, variations in the upper troposphere are very different.

For the northern tropics, a moist upper troposphere occurs between May and November (local summer-autumn) when the ITCZ is in the northern hemisphere. A particularly moist plume is evident in July and is related to the Asian monsoon. The moist tape signal in the lower stratosphere begins in September, about 1 month after the maximum in the upper troposphere. The northern upper troposphere is dry from late November to April and joins with a dry tape signal.

In the southern hemisphere, the pattern in the upper troposphere is reversed to that in the northern hemisphere reflecting the movement of the ITCZ to the southern hemisphere in local summer. The tape signal in the stratosphere remains unaffected, and the moist and dry times in the troposphere are now out of phase with those in the stratosphere. The upper troposphere is moist from November to April, (when it was dry in the NH) and dry tape signal can be seen in the

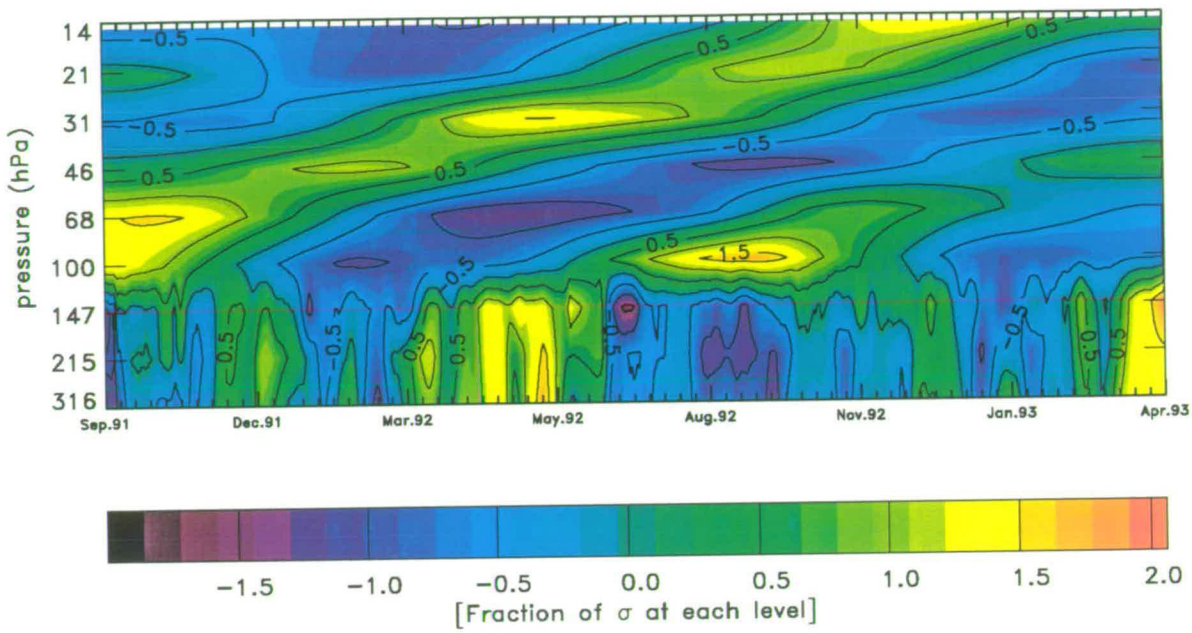

Figure 6.8: Time-height section of zonal mean water vapour between 12°N and 12°S. Stratospheric water vapour comes from the non-linear retrieval and tropospheric water vapour from the 205 GHz channel. The plot shows deviations from the time-mean expressed as a fraction of the standard deviation (w.r.t. time) at that level.

lower stratosphere. The upper troposphere is dry from May to November (when it was moist in the NH) and a moist tape signal is seen above.

Rosenlof *et al.*, (1997) found that maximum mixing ratios on the 390 K potential temperature surface ($\sim$ 100 hPa) occurred in July and August for 10-50°N and in October to November for 10-50°S. In the northern hemisphere tropics, the maximum on the 390 K surface seen by HALOE and presented by Rosenlof *et al.* happens about a month after the maximum UTH (147 hPa) seen in MLS data and presented by Sandor *et al.*, (1998). In the southern hemisphere the maximum stratospheric water vapour was seen about 10 months after the maximum southern hemisphere values of UTH. The results presented here are consistent with the findings of Rosenlof *et al.* and Sandor *et al.* and provide observational evidence in support of the assertion by Rosenlof *et al.* that more air enters from the northern upper troposphere than from the southern.

Analysis of the zonal mean also suggests that more moist air enters from the

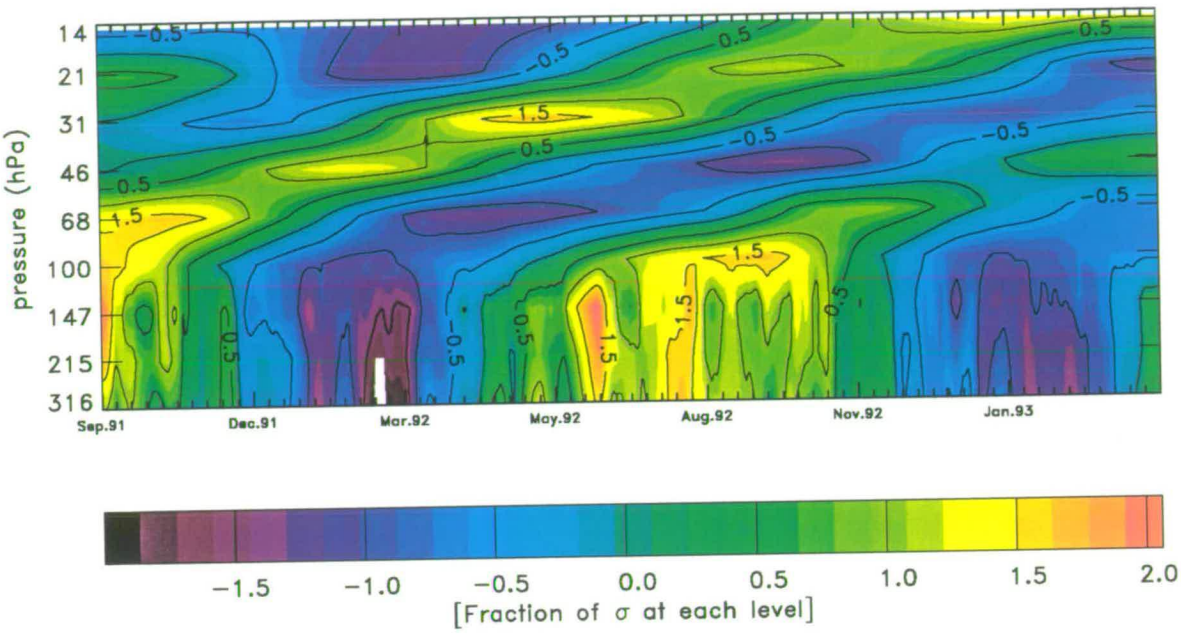

Figure 6.9: As for figure 6.8 but for measurements binned between 5 and 15°N.

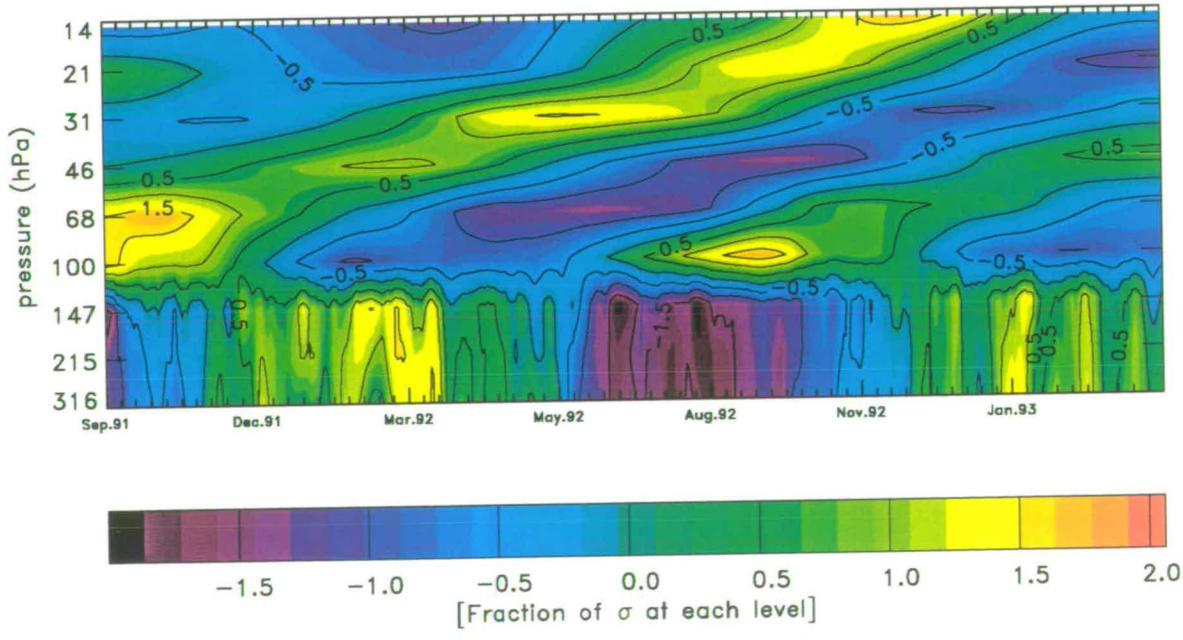

Figure 6.10: As for figure 6.8 but for measurements binned between 5 and 15°S.

northern hemisphere than from the southern although quantative calculations are need to confirm this. Figure 6.11 shows the zonal mean water vapour at 100 hPa from September 1991-April 1993. Both the dry and the moist regions are offset from the equator, being centred at 10-20°N. At 68 hPa (figure 6.12), the position of the entry of dry air and moist air is also displaced off the equator into the northern hemisphere. It is however nearer to the equator than at 100 hPa. Similar results were seen by Randel *et al.*, (1998) who noted that the annual cycle in water vapour observed by HALOE is centred over the equator at and above 68 hPa but in the NH subtropics at 100 hPa.

The zonal mean also shows that transport from the tropics to the midlatitudes takes place. This occurs at both 100 and 68 hPa but is much more pronounced at 100 hPa. Air moves into the midlatitudes more quickly and with less mixing in the northern hemisphere than in the southern hemisphere, a fact also noted by Rosenlof *et al.*, (1997) in HALOE data. At 100 hPa, the 4.0 ppmv contour for example, only reaches to 30°S in comparison to 50°N. Similarly the dry 3.0 ppmv contour reaches only 10°S compared with 30°N. The 3.6 ppmv contour level (at 100 hPa) is located around 55°N on the 15th January when MLS yaws from north to south. This contour level has reached 70°N at the end of March when MLS next turns to look south. This gives a horizontal transport speed of 0.3 $m\ s^{-1}$. Data from HALOE (Randel *et al.*, 1998) showed strong transport into the northern hemisphere middle and high latitudes at 100 hPa but little latitudinal spreading occurred at 68 hPa and above with the annual cycle remaining within 30°N-S.

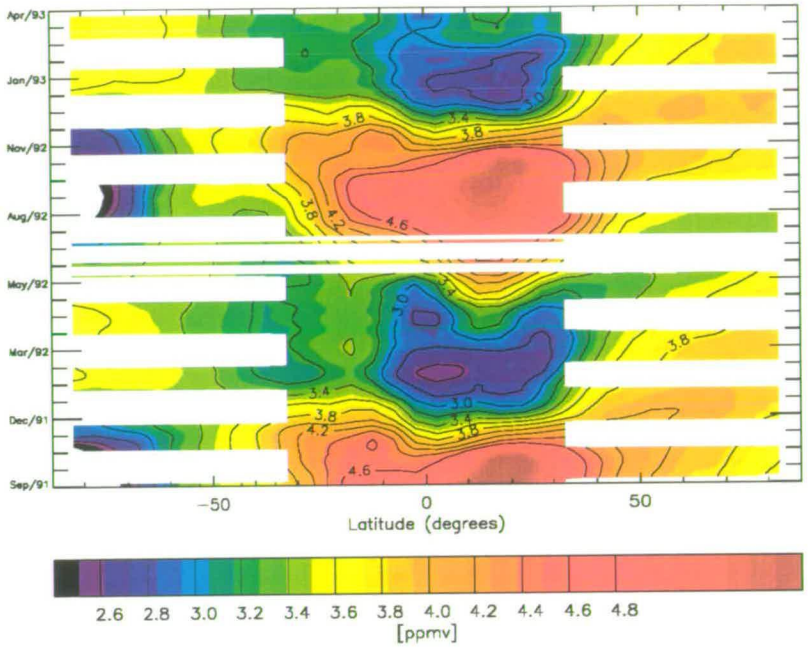

Figure 6.11: Zonal mean water vapour (ppmv) at 100 hPa.

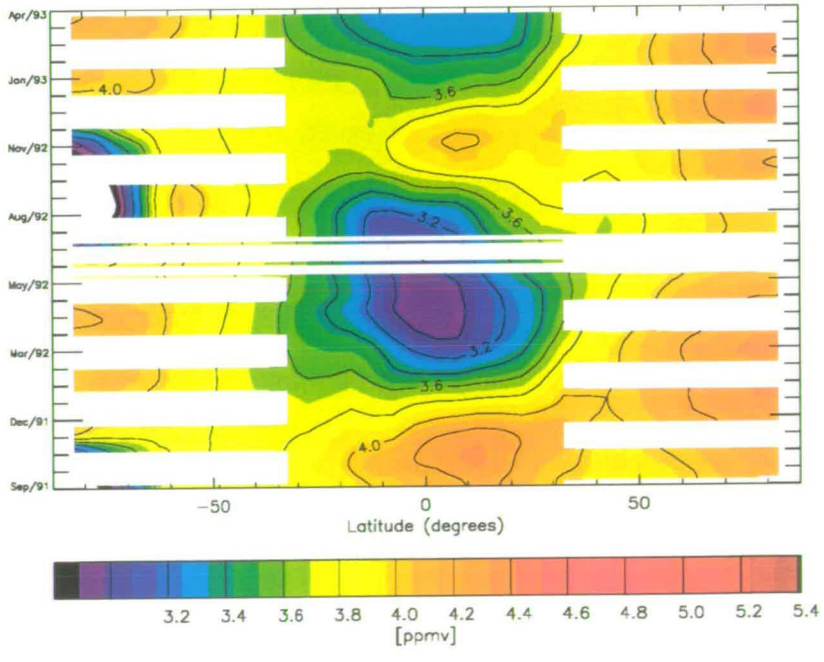

Figure 6.12: Zonal mean water vapour (ppmv) at 68 hPa.

At 68 hPa there is some transport out of tropics, but only to about 40°N and, as at 100 hPa, there is more mixing in the southern hemisphere than in the northern hemisphere. More limited mixing with the midlatitudes takes place at 68 hPa than at 100 hPa due to the upward advection in the tropical pipe being much more rapid than the horizontal mixing (Plumb, 1996). The tropical pipe is more leaky in the tropopause region, and mixing with the midlatitudes is more evident at 100 hPa than above. Trepte and Hitchman (1992) analysed the dispersal of volcanic aerosol and found that poleward transport occurred readily at altitudes within a few kilometres of the tropopause but that in the altitude range 21-28 km ($\sim$ 46 hPa and above), aerosols remained within 20° of the equator.

Mixing of water vapour from the tropics to mid-latitudes appears from figure 6.11 to be greater in winter 1992-1993 than in winter 1991-1992 when the phase of the QBO changes from easterly to westerly. In 1991-1992, the 3.9 contour band extends to 70°N remaining unmixed but in 1992-1993, the same contour interval breaks off into isolated patches, which are found up to 80°N. The phase of the QBO is illustrated in figure 6.13 showing a time-height section of ECMWF zonal wind averaged between 12°N and 12°S. The magnitude of the winds are similar to those from the UKMO analyses presented in Swinbank and O'Neill (1994). Winds are easterly from December 1991 until December 1992 and are then westerly for the remainder of the time series.

Trepte and Hitchman (1992) noted the effect of the QBO on transport of aerosols. When the westerly shear was present, there was an increase in aerosol transport to the midlatitudes. The easterly phase encourages ascent in the tropical pipe and transport to midlatitudes is suppressed but in the westerly phase when ascent is slower, there is more time for mixing with mid-latitudes. The QBO is also manifest in the degree of moistening seen at 68 hPa. In 1992, the moistening at 68 hPa is much less severe than in 1991. In 1992, when the phase is westerly, more mixing takes place with mid-latitudes at 100 hPa, resulting in less being taken up in the tropical pipe to 68 hPa.

At both 100 hPa and 68 hPa, the northern hemisphere is moister than the southern as Kelly *et al.*, (1990) and Kelly *et al.*, (1991) observed from aircraft measurements (see discussion in section 3.1.2), and Rosenlof *et al.* (1997) and Pan *et al.*, (1997) observed in satellite measurements from HALOE and SAGE

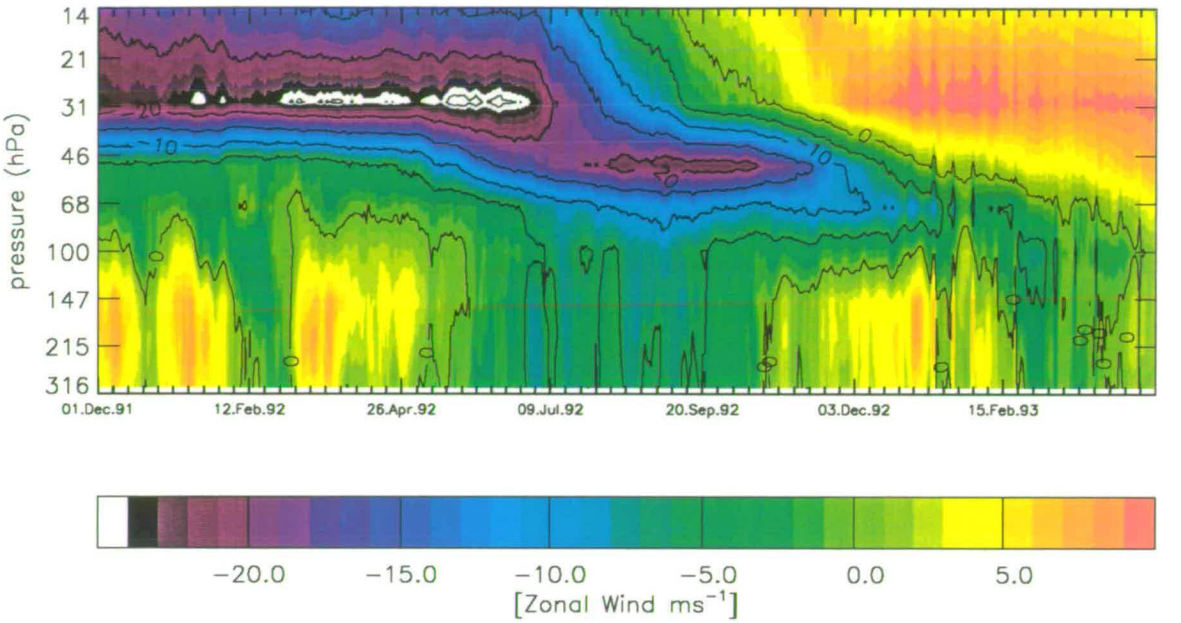

Figure 6.13: Time-height section of mean zonal wind from ECMWF averaged between 12°N to 12°S.

II respectively. In the zonal mean (fig. 6.11) dehydration in the SH polar vortex can be seen to be much stronger than in the NH vortex. When mixing ratios are high in the tropics between June and September, the vortex is particularly dry. The mixing of the moist tropical air with the dry polar air results in the southern hemisphere being drier than the northern hemisphere. This agrees very well with the zonal mean at 390 K from HALOE measurements presented by Rosenlof *et al.*, (1997).

6.4 Evolution of the Tape Signal

The time-height sections which reveal the tape recorder effect are based on the average water vapour mixing ratio in the latitude bin from 12°N to 12°S. They give no information about the local distribution of water vapour and how it changes. At both 100 hPa and 68 hPa, there is still regional structure to the water vapour field and it is this regional structure and its development over time that is described here.

The time-height section for the entire tropical region (figure 6.8) shows that the 100 hPa level is moist from 8th September to 30th November 1991. It then becomes dry and remains dry until 14th May 1992. This is followed by a moist tape signal which is present until December 1992. Sequences of days are studied throughout the entire period for which there is data from the 183 GHz channel on MLS, (September 1991-April 1993) focusing on the transitions from moist to dry or from dry to moist tape signals.

6.4.1 Drying, 1991-1992

100 hPa

This section begins by looking at the change from moist to dry tape signal seen at 100 hPa in figure 6.8 and occurring in December 1991. Towards the end of the moist period high mixing ratios greater than 5.50 ppmv retreat, from their extent across almost the entire tropics, gradually back to the northern hemisphere. High mixing ratios remain for longest over India but disappear entirely by 3rd December, coinciding with the cessation of deep convection at 215 hPa associated with the Asian monsoon.

A sequence of pentads at 100 hPa for days during the moist-dry transition is shown in figure 6.14. Mixing ratios of 2.4-2.8 ppmv are apparent at the beginning of the sequence, mostly north of the equator. Also plotted (figure 6.15) for the same sequence of days, is the ratio of the MLS mixing ratios (r) to ECMWF saturation mixing ratios (r_s) calculated from ECMWF temperatures i.e. r/r_s. Most of the longitudinal structure in these maps is imposed upon the field by the ECMWF temperatures.

When this fraction is less than 1, the observed mixing ratio is less than the saturation mixing ratio. This may indicate that the air parcel has already passed through its minimum temperature at a different time or location or that the tropopause is lying below the 100 hPa level. The parcel may have become saturated below the 100 hPa level in the previous NH autumn. This saturated air would be transported upwards by the large-scale circulation, becoming less saturated as the temperature increases. This accounts for most of the air in the tropics.

When the ratio r/r_s is approximately equal to 1, freeze drying in situ is probably

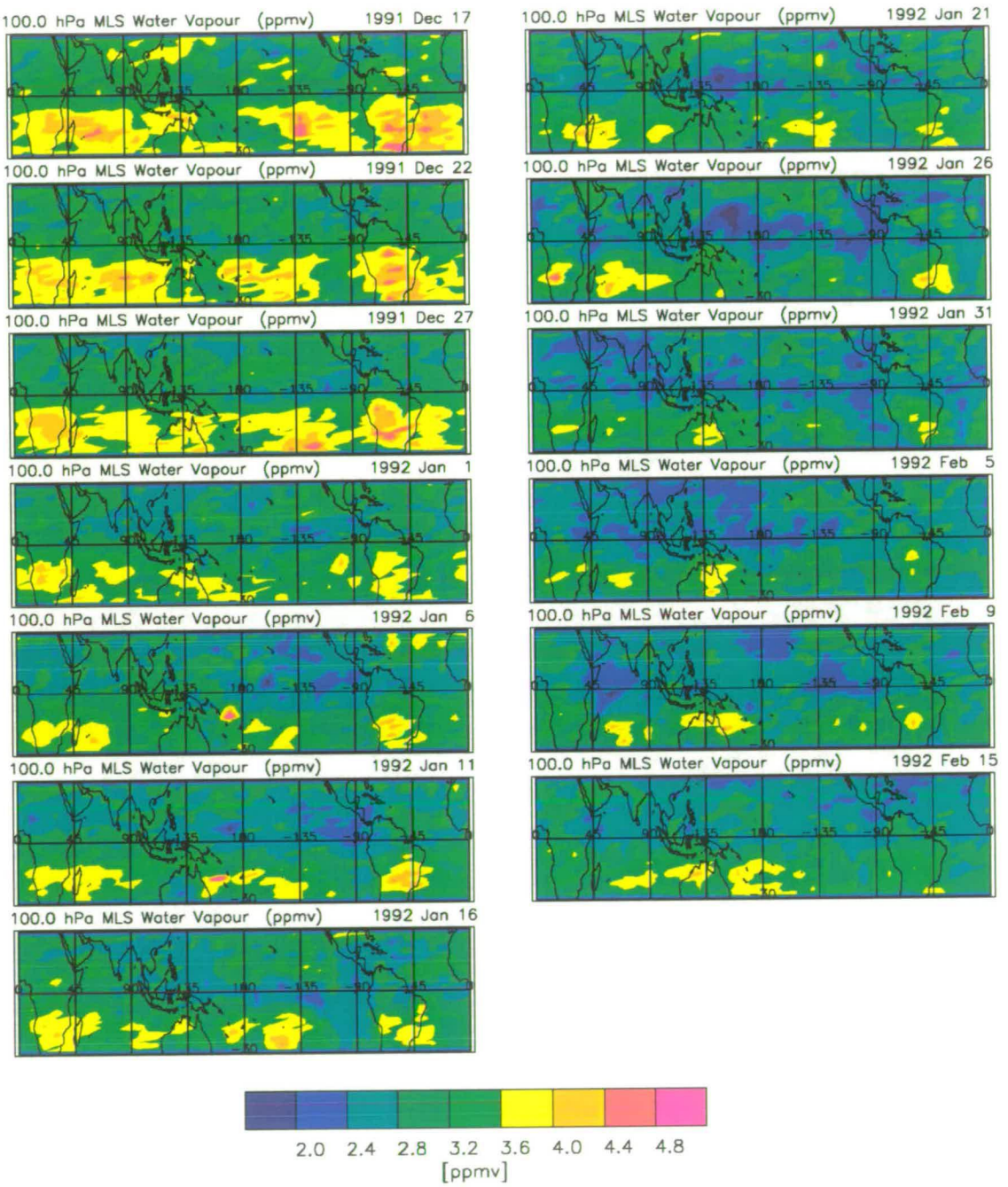

Figure 6.14: Sequence of 5 day averaged water vapour at 100 hPa showing the transition from moist to dry in 1991-1992.

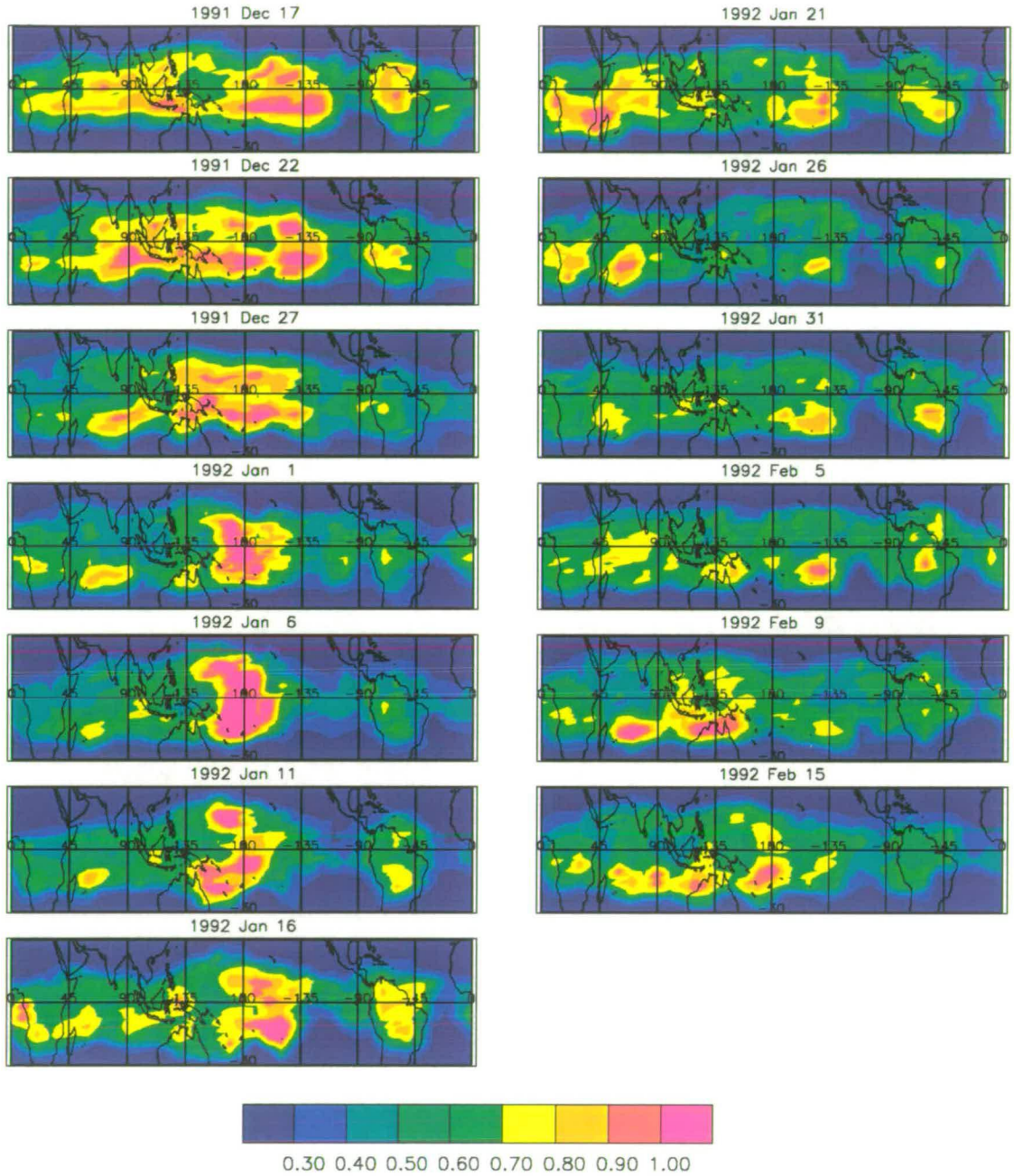

Figure 6.15: Ratio of MLS mixing ratio to possible ECMWF saturation mixing ratios at 100 hPa (r/r_s) based on 5 day averaged 100 hPa temperatures and 5 day averaged 100 hPa mixing ratios during the moist to dry transition 1991-1992.

taking place at this level or nearby. This is occurring in a wide region over the western Pacific but does not have a related pattern in the water vapour field at 100 hPa, though it does show similarities with the water vapour at 215 hPa and 147 hPa (see 5.21).

On January 11th, mixing ratios of between 2.0 and 2.4 ppmv can be noted in the region of Panama, and on January 21st, in the Northwestern Pacific ocean off the coast of the Philippines. They appear not to be related to freeze-drying processes. There is evidence for some in situ, freeze-drying over the western Pacific but this does not appear to lead to dry features in the water vapour field at 100 hPa. Moister areas remain in the southern hemisphere over the continents but eventually the whole tropics becomes covered with mixing ratios of around 3.2 ppmv.

When the ratio is greater than 1, the observed mixing ratio is greater than saturation mixing ratio, indicating that the mixing ratio has been measured too large, or that the temperature is too low. In this sequence of days, the problem affects the western Pacific. This may result from retrieval errors or from an under-estimate of temperature by the ECMWF model. In this case, it is more likely that the water vapour is too high, caused by being mostly the climatology from SAGE II.

68 hPa

At 68 hPa, the moist to dry transition takes place about 1 month after 100 hPa. Five day averages are therefore examined for the next sequence to that at 100 hPa, beginning on 20th February and shown in figure 6.16.

Around 20th February, particularly dry air (2.8 ppmv) enters over SE Asia and Indonesia. This is followed by an eastward and southwards expansion but the dry air remains confined to a 15°N-5°S band along the equator until the middle of June, well after the end of the sequence shown here.

The easternmost edge of the 2.8-3.0 ppmv contour band on 20th February is at 105°E and has moved to 160°E by the 2nd pentad, moving with a speed of $14 ms^{-1}$. The zonal wind averaged over an area (5-10°N and 70-110°E) enclosing this 2.8-3.0 ppmv region during these 5 days is just 4.2 ms^{-1}. The zonal wind can't therefore account for the movement of the 2.8-3.0 ppmv contour band during

the 5 day period. Averaged over the entire sequence of days, the zonal wind in the Indonesian and SE Asian region (0-20°N, 90-135°E) is -0.4ms^{-1}. The zonal wind is not strong enough to account for the spread of dry air around the latitude circle. This suggests that dry air must be mixing over the surface continually. It is interesting to note however, that the stratospheric fountain region is the first location to see these low mixing ratios.

From May onwards (figure 6.20) intermittently, high values of water vapour can be seen over India, spreading to south-east Asia, but mixing ratios less than 2.8 ppmv remain over the western Pacific until the middle of August.

6.4.2 Drying, 1992-1993

The moist-dry transition is now examined for 1992-1993 and compared with 1991-1992.

100 hPa

Five day averaged maps were examined for 1992-1993 (not shown) and there are some similarities with 1991-1992. Mixing ratios between 5.0 and 5.5 ppmv remain as far south 15°S for about 45 days and then retreat back to the northern hemisphere to be replaced by mixing ratios of 4.0 ppmv. Localised areas over Indonesia and Australia have values of around 3 ppmv. Then bands of 3.0 ppmv air extend across the equator by the 3rd week in November. Mixing ratios of 2.4-2.8 ppmv then begin to appear over India, south east Asia and Panama. Values of 2.0-2.4 ppmv appeared at the beginning of December in 1991/1992 and persisted until the beginning of March. In 1992/1993, they appeared at the end of December and persisted only until the end of January. This dry tape signal is not associated with such low mixing ratios as were present in the previous year. Values remain around 2.8 ppmv with isolated patches of drier air in the northern hemisphere and of moister air over the southern hemisphere continents. In winter 1991, drier areas were larger and lasted for longer.

68 hPa

Intermittently, drier intrusions (3.4 ppmv) appear over Australia and Indonesia from 6th November onwards. Mixing ratios greater than 4.0 ppmv remain over

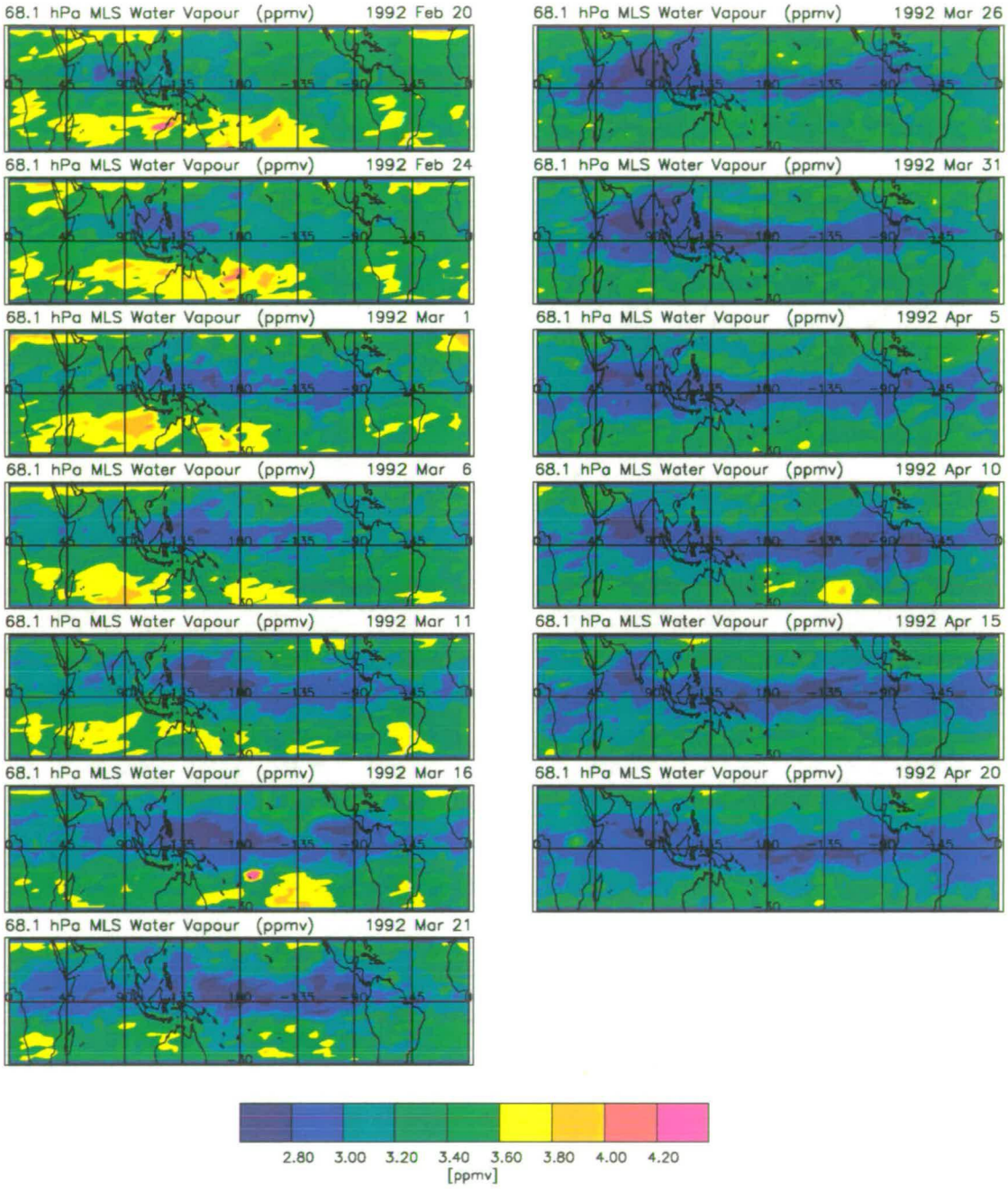

Figure 6.16: Sequence of 5 day averaged water vapour at 68 hPa showing the transition from moist to dry in 1992.

the northern Atlantic, India and South America. Mixing ratios of 3.0 ppmv do not occur until March 6th over Indonesia (figure 6.16). Although mixing ratios of 2.8-3.0 ppmv were prominent at 68 hPa from 20th February 1992 until August, values this low are seen on only 2 pentads in 1993 (16th and 21st March).

As at 100 hPa this 'dry' event is not as dry as 1991/1992. The difference in the dryness may be related to the phase of the QBO. When the QBO is in its easterly phase, as it is during winter 1991-1992 (see figure 6.13), lower equatorial temperatures and greater ascent rates are implied (Carr *et al.*, 1995). During the westerly phase of the QBO, temperatures are higher and ascent rates lower. This was the case in winter 1992-1993. The easterly phase of the QBO can therefore account for the lower mixing ratios in 1991-1992 (related to the colder temperatures). The easterly phase of the QBO may also encourage deep convection (Collimore *et al.*, 1998) to overshoot the tropopause and hence lead to a drier lower stratosphere.

6.4.3 Moistening, 1992

The transition from the dry to the moist tape signal which takes place at 100 hPa around April 1992 is now examined. Sequences of 5 day averages are described for both the 100 and the 68 hPa levels and also for the 215 hPa level in the upper troposphere.

215 hPa

The water vapour field for 215 hPa shown in figure 6.17, has much more localised structure than at the stratospheric levels. Intense convection is sporadic over India and south east Asia from April onwards and becomes a persistent feature from the middle of May as indicated by the mixing ratios of 220 ppmv and greater. The high mixing ratios are associated with the monsoon convection, and coincide with the moistening beginning at 100 hPa. Unlike at 100 hPa, the moisture remains well confined to the monsoon region. The moist areas over the western Pacific have no counterpart at 100 hPa, either as dry or as moist features.

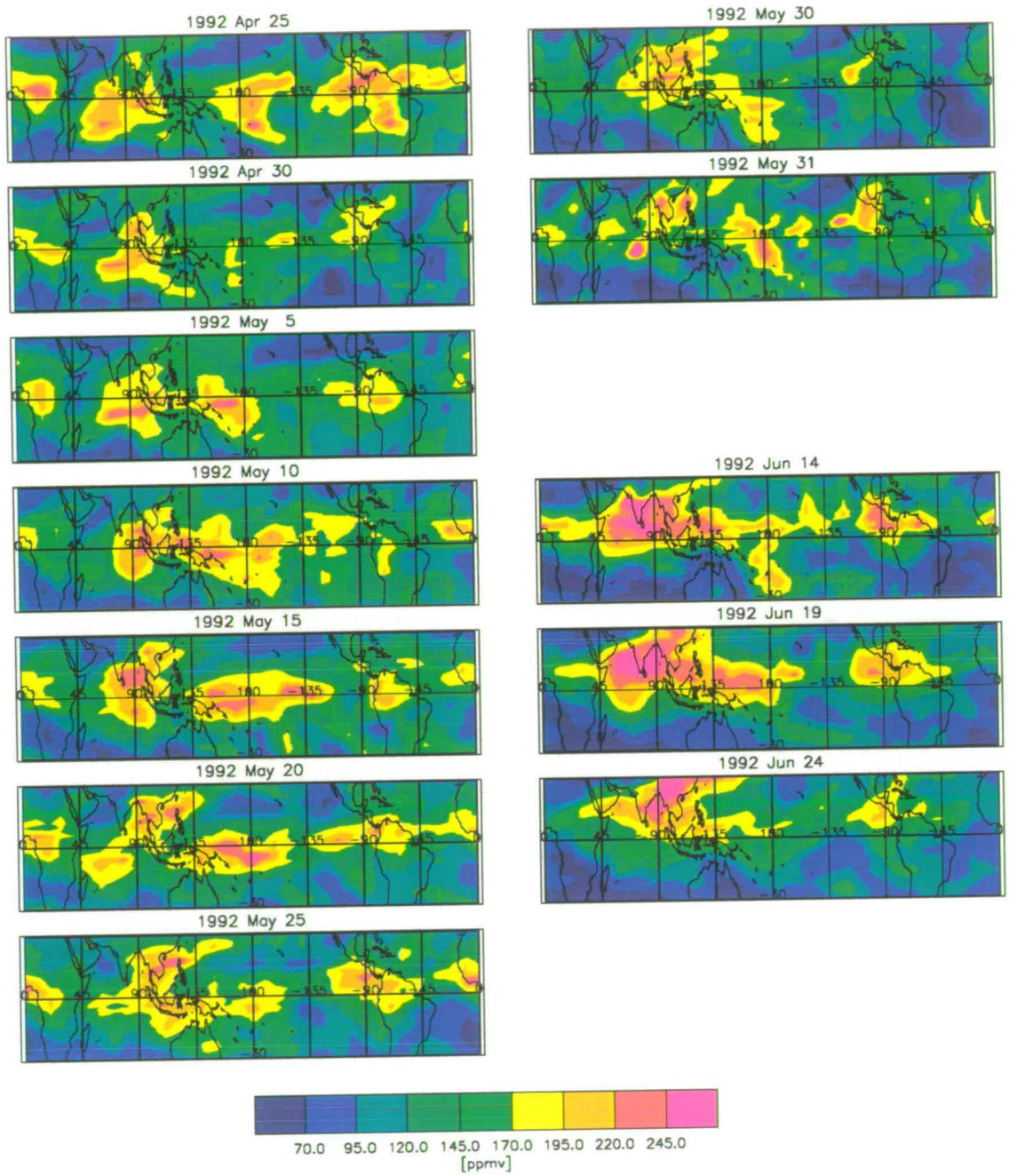

Figure 6.17: Sequence of 5 day averaged water vapour at 215 hPa showing moistening spreading from the monsoon region.

100 hPa

As seen in the time-height section (figure 6.8) around the 14th May the 100 hPa level becomes moist again. Sequences of 5 day averages, shown in figure 6.18, reveal that this moistening begins over India and south-east Asia towards the end of April. Mixing ratios of 4.0-4.4 ppmv are first observed over the Indian monsoon region and spread eastward and southward. The easternmost edge of this 4.0-4.4 ppmv contour band can be seen to move from 160°E on 15th May to about 225°E on the 30th May, therefore moving with a speed of about 5 m s^{-1}. The average ECMWF zonal wind in this region (10-20°N, 160-240°E) is a comparable 6 m s^{-1} and could therefore account for this movement. Intermittently, mixing ratios of 4.0-4.4 ppmv are observed over Africa and Panama which also spread laterally and join to form a band across the northern tropics.

Mixing ratios greater than 4.8 ppmv are first observed in the Asian monsoon region on 30th May and subsequently over Africa and Panama on June 14th. The zonal wind averaged in the region 10-20°N, 45-90°E appears to account for the spread of 4.8 ppmv mixing ratios from India across the Indian Ocean to Africa but the emergence of this high mixing ratio band over Panama is independent.

Although the zonal winds can account for some of the movement of moisture, they cannot account for the spread of moisture across the entire northern hemisphere tropics. It would appear that high mixing ratios are initially introduced over the monsoon region but that further moisture upwells in locations other than India and South East Asia, particularly Panama and possibly Central Africa. The saturation mixing ratios are now examined to investigate this further.

Figure 6.19, for the same sequence of pentads, maps the ratio of the MLS mixing ratios to ECMWF saturation mixing ratios calculated from ECMWF temperatures i.e. r/r_s. As discussed previously, when this fraction is less than 1, the observed mixing ratio is less than the saturation mixing ratio. In the previous sequence during the moist-dry transition, this was interpreted as an indication that the air parcel saturated below 100 hPa and was transported upwards under the influence of the extratropical pump. In this sequence of days however, the regions of low relative humidity may be the remnants of the previous dry period. In other words, the air parcels passed through their minimum temperature in the

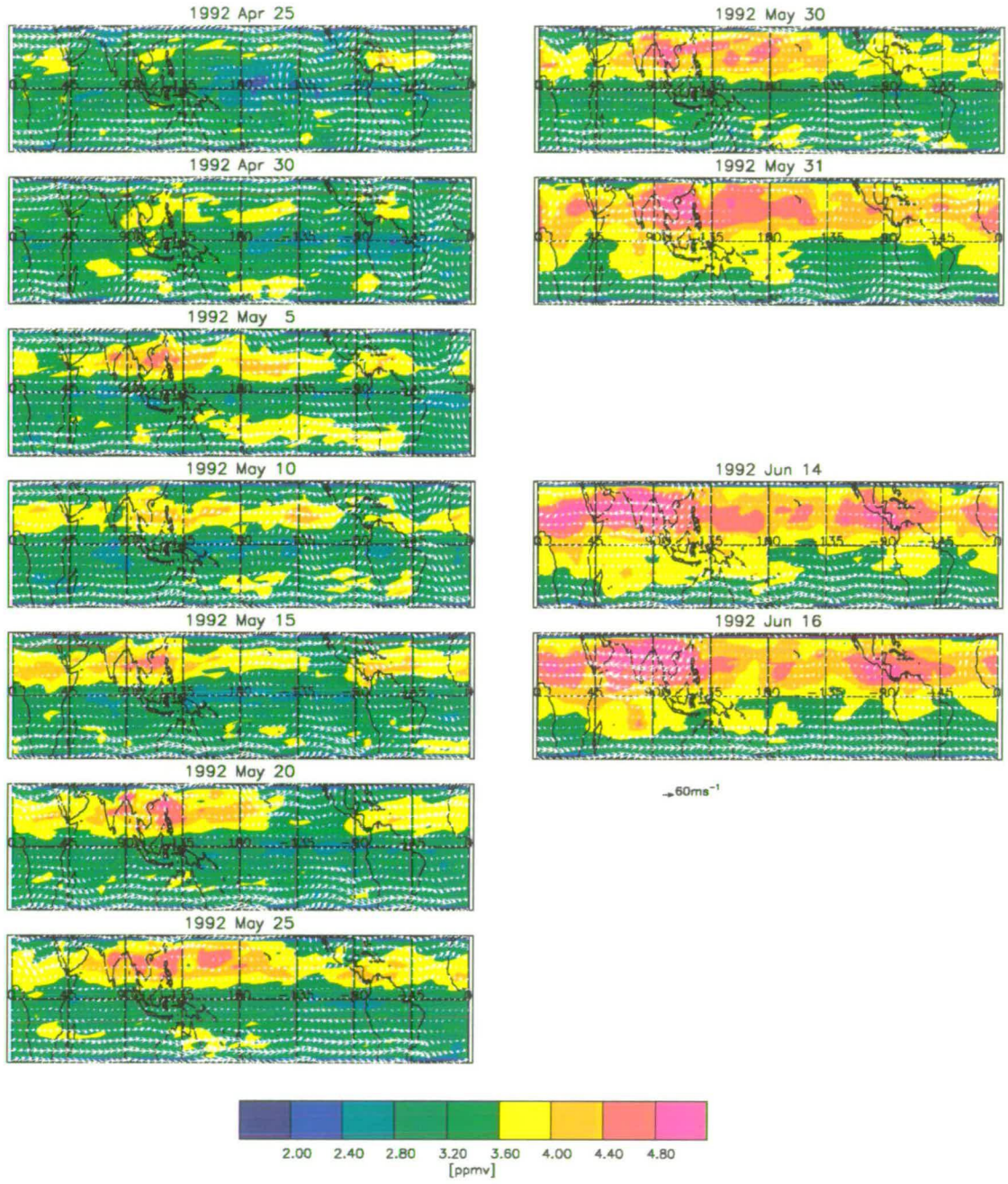

Figure 6.18: Sequence of 5 day averaged water vapour at 100 hPa showing moistening spreading from the monsoon region. Also shown are 5 day averaged ECMWF winds.

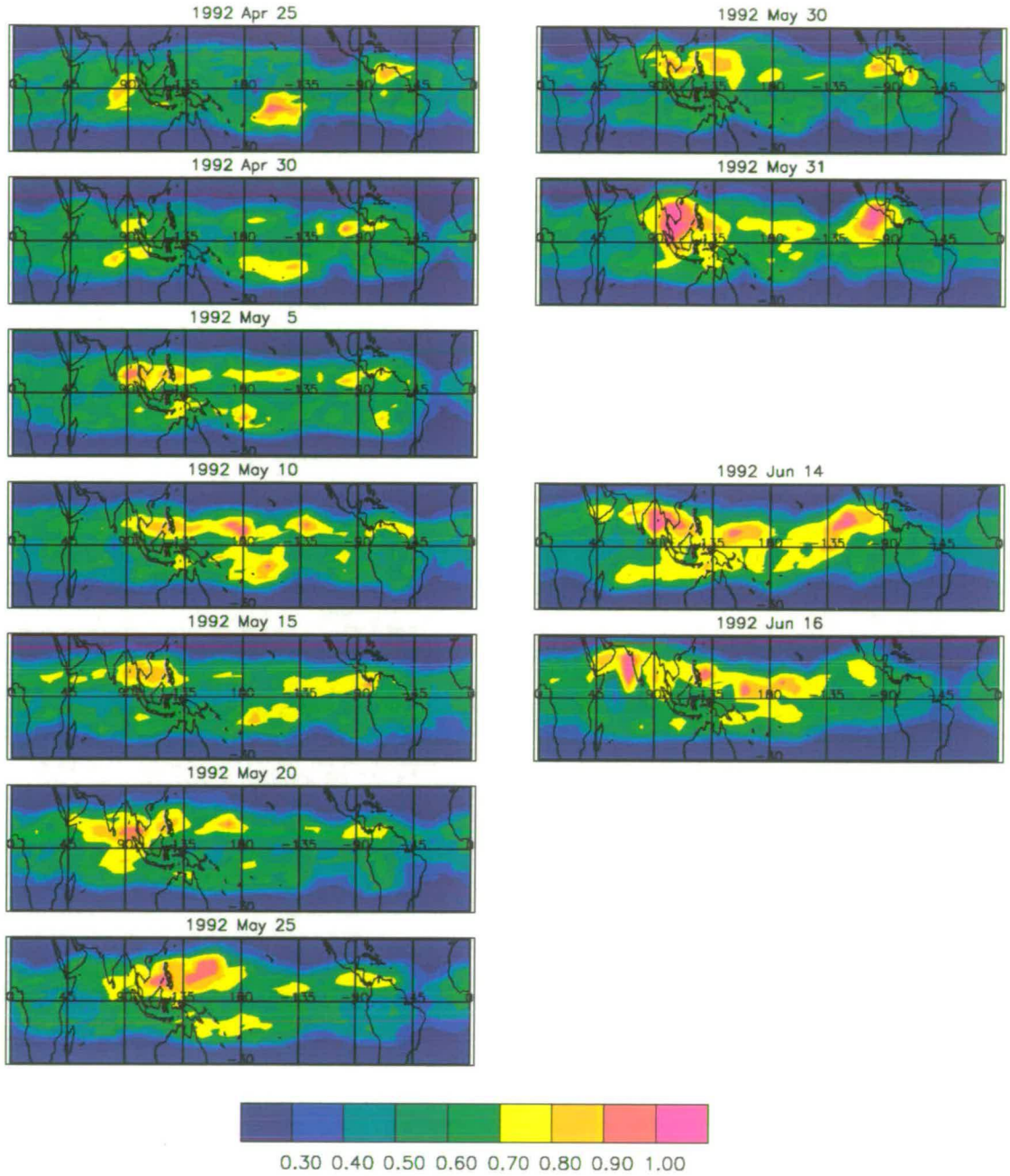

Figure 6.19: Ratio of MLS mixing ratio to possible ECMWF saturation mixing ratios at 100 hPa, based on 5 day averaged temperatures and 5 day averaged mixing ratios.

previous DJF.

When the ratio r/r_s is approximately equal to 1, freeze drying in situ could be taking place. Values of 0.9 are found over the Asian monsoon region from 5th May, coinciding with the appearance of mixing ratios of 4.4-4.8 ppmv in figure 6.18. The ratio r/r_s is 1.0 or greater on 31st May and 14th June over the Asian monsoon region and over Panama. This indicates that localised incidences of freeze drying in situ could be taking place.

On 31st May mixing ratios of 4.8 ppmv were apparent over SE Asia, and on the 14th June, mixing ratios of 4.8 ppmv first became prominent over Panama (see figure 6.18). The mixing ratios in both of these regions are high at 215 hPa (figure 6.17) suggesting that deep convection and saturation is taking place in both Asia and Panama, and is introducing air with a higher mixing ratio than before. The observation of moistening over the Asian monsoon region is in agreement with Jackson *et al.*, (1998) but Jackson *et al.*, found that the relative humidity is less than 50% and concluded that there is probably no saturation in this region. There is however, considerable uncertainty in the 100 hPa temperatures, and in both the HALOE and MLS mixing ratios so this must be interpreted with caution.

These results along with the observation that the zonal wind cannot account for the movement of water vapour from Asia across the entire northern tropics suggest that moistening initially takes place over the monsoon region and spreads laterally to Africa and to the eastern Pacific under the influence of the zonal wind. Further moistening takes place over Panama and also spreads laterally to join that from Asia so filling the tropical region with moister air.

68 hPa

Similarly to 100 hPa, moistening after the dry tape signal begins over India (see figure 6.20). In May, values of 3.6-3.8 ppmv are noticeable against a background of 3.2 ppmv. By the middle of June, mixing ratios of 4.0 ppmv appear sporadically, and more consistently in later NH summer. These water vapour values spread westwards from India to Africa under the influence of the zonal wind which in the region 15-30°N and 80-110°E is an average of -10ms^{-1}. Moisture continues to enter over SE Asia and then over Panama. Moistening also approaches the equator from the south, but more slowly, leaving a band about 5°S of the equator

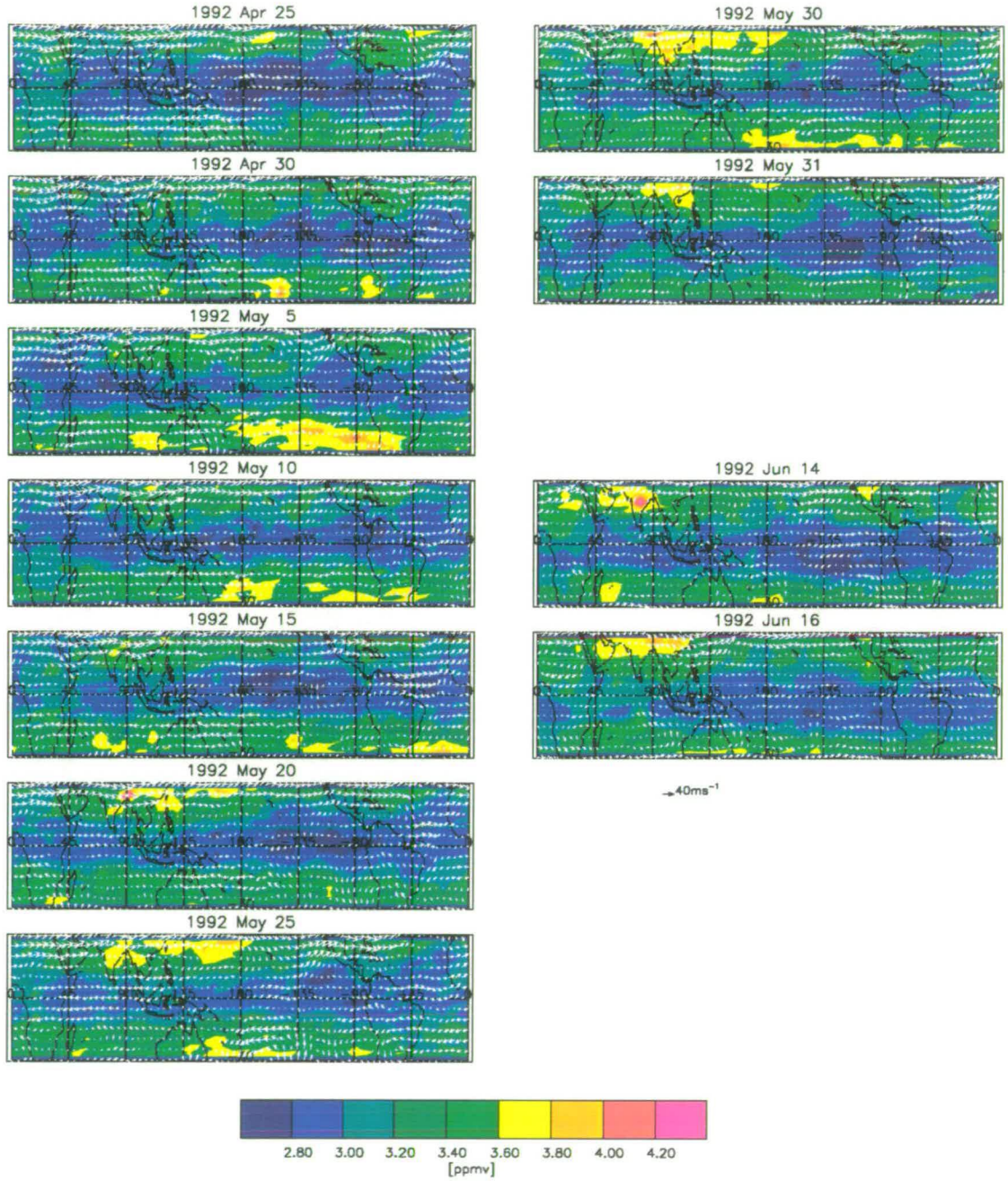

Figure 6.20: Sequence of 5 day averaged water vapour at 68 hPa showing moistening spreading from the monsoon region. Also shown are 5 day averaged ECMWF winds.

which remains at 3.2 ppmv.

6.4.4 Summary

Time-height sections of water vapour from MLS and from HALOE showed that the stratospheric tape signal was in phase with upper tropospheric variability in the northern hemisphere, but out of phase with the southern hemisphere. The zonal mean at 100 hPa showed that the annual cycle in water vapour is initiated in the northern hemisphere. Both low and high mixing ratios spread from the northern hemisphere tropics into the southern hemisphere tropics and into the mid-latitudes. Transport is more rapid into the northern hemisphere mid-latitudes and remains relatively unmixed. More mixing takes place in the southern hemisphere, notably with dehydrated air in the polar vortex. This mixing with the vortex and the fact that less moist air enters the southern hemisphere in the tropics results in the southern hemisphere being drier than the northern hemisphere as many studies have shown. The effects of the QBO in encouraging upward transport during the easterly phase and increasing mixing with the midlatitudes during the westerly phase was also noted. It resulted in the 68 hPa level being much drier in winter 1992-1993 than in winter 1991-1992. Transport out of the tropics is, as expected, much greater at 100 hPa than at 68 hPa due to the tropical pipe being more leaky at lower altitudes.

As the tropical region begins to get drier, moist areas continue to remain over the southern hemisphere continents. The first region to become dry is the Indonesian fountain region followed by Panama and the western coast of North America. Eventually, dry air is found in a band along the equator with the most northerly extent over Panama and Indonesia. Jackson *et al.,* (1998) also note that most STE takes place in the NH and spreads southwards. Here it was shown that although freeze drying does take place in situ over the western Pacific, the dry features are more likely to result from upward propagation of air that was saturated below the 100 hPa level.

At the end of a dry tape signal, pentad fields reveal moisture to originate over the Asian monsoon region from April onwards. This is also evident at 68 hPa in the seasonal means for JJA and SON. Further moist air enters over Panama as was seen in pentad fields at both 100 hPa and 68 hPa, and in the seasonal mean

for SON at 68 hPa. This moister air then spreads southwards and eastwards. The hydrating effect on the lower stratosphere of the Asian monsoon is in agreement with observational evidence from HALOE at 128 hPa, 100 hPa and 83 hPa, presented by Jackson *et al.*, (1998) but which was not evident in SAGE II data (Rind *et al.*, 1993). MLS sees this moistening effect at 68 hPa, higher than has previously been observed. In contrast to Jackson *et al.*, results presented here suggest that entry over the monsoon region could be accompanied by freeze drying processes. There appears also to be some moistening effect at 100 hPa and 68 hPa associated with the Australian monsoon.

Some differences in observed dryness exist from year to year. Winter 1991-1992 was much drier than 1992-1993 and this was attributed to the easterly phase of the QBO in 1991-1992, lowering the temperature of the tropopause and encouraging deep convection.

6.5 The Lower Stratosphere and the MJO

In the previous chapter, eastward propagation was seen in longitude-time sections of upper tropospheric water vapour at 215 hPa, and this eastward propagation was also present at 147 hPa. This was associated with the deep convection of the MJO. This section examines whether any of these deep convective events transport water vapour through the tropopause to the stratospheric overworld and whether this can be seen in the 100 hPa water vapour field.

Longitude-time sections at 10°S are shown for 100 hPa in figure 6.21 and for 68 hPa in figure 6.23. As before, the fields have been Kalman filtered to fill missing days and a mask applied to gaps of more than three days. At 100 hPa, mixing ratios range between 3.4 and 4.1 ppmv and at 68 hPa between 3.0 and 4.1 ppmv. Both spatially and temporally, the fields in the stratosphere have much less variance than those in the troposphere. Mote *et al.*, (1996) showed water vapour to have a large annual cycle at the tropical tropopause. This is apparent in the longitude-time sections. Least squares fitting showed the annual cycle to account for more than 90% of the variance at most longitudes. Low mixing ratios are found from May–January at 100 hPa and from February–September at 68 hPa. The annual cycle is out of phase at the two levels by about 3 months

due to the tape signal which propagates slowly upwards. This contrasts with the troposphere where adjacent pressure levels vary in phase due to rapid transport through cumulonimbus convection.

The amplitude of the annual cycle varies much less across longitude in the stratosphere than in the troposphere where land-sea contrasts have a strong influence. Figures 6.22 and 6.24 show the variation in strength of the annual cycle with longitude for 100 hPa and 68 hPa respectively. Since the climatology is based on a monthly zonal mean, all longitudinal variation must be introduced by the MLS measurements. The peak in the annual cycle occurs over South America at 68 hPa and over the Eastern Pacific at 100 hPa where it accounts for 95% and 98% of the variance respectively. The peak at 100 hPa corresponds to that in 100 hPa temperatures from the ECMWF re-analysis. At 68 hPa, a secondary maximum is located over Africa and a minimum amplitude (87% of the variance) over the Western Pacific (120°E). The minimum over the western Pacific, and the maxima over Africa and South America at 68 hPa agree well with those in the troposphere suggesting that not all the information about the underlying surface has been lost. This remaining influence of land and sea may be an important consideration in stratosphere-troposphere exchange.

The variation of the annual cycle across longitude at 68 hPa shows more similarity with that in the troposphere than does the 100 hPa level. This is surprising as it would be expected that 100 hPa would be more similar to the troposphere since it is closer to it. 100 hPa lacks the pronounced minimum over the Western Pacific and a there is a much less marked increase in amplitude over Africa. The lack of similarity between 100 hPa and the troposphere may be an indication that the field at 100 hPa is not a significant improvement on the climatology.

Mote *et al.*, (1998) created similar time-longitude sections by binning measurements within 2.5° of latitude either side of the equator. They removed periods longer than 90 days using a high-pass filter and showed only the short-term variability in their paper. Wavenumber-frequency analysis illustrated some power to be in eastward travelling wavenumber 1 at periods from 10-25 days and 30-70 days, the latter they identify as an evanescent response to the MJO signal at 215 hPa. The power in this MJO band drops by approximately 4 orders of magnitude between 215 and 100 hPa due to the decrease in mixing ratio with height,

and by another order of magnitude between 100 and 68 hPa and as a result, at 68 hPa the MJO band accounts for very little of the total variance.

Since Mote *et al.*, (1998) find an evanescent response to the MJO signal in the lower stratosphere, this section focuses on whether any of the convective events associated with the MJO in the upper troposphere result in troposphere-stratosphere exchange.

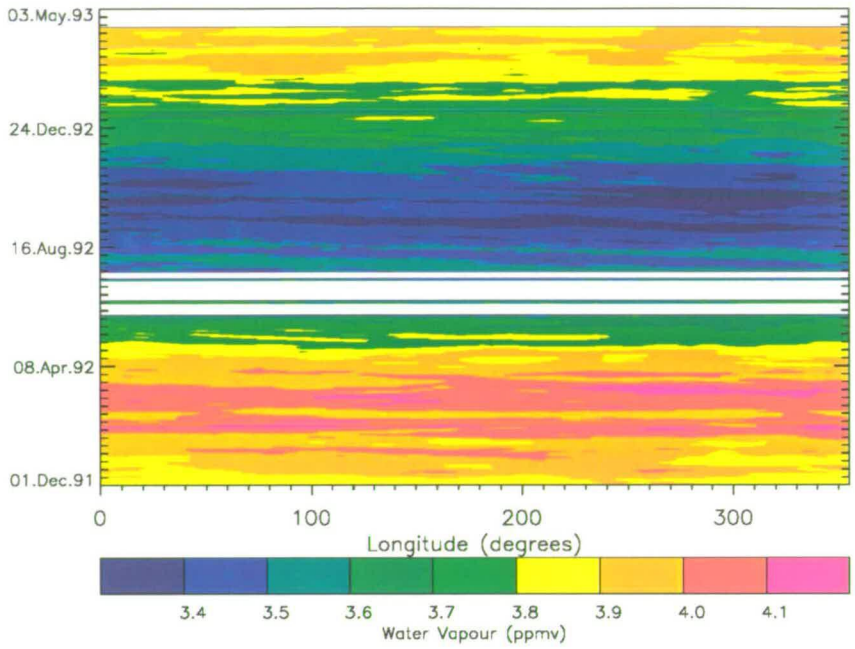

Figure 6.21: Longitude-time sections of water vapour mixing ratios at 100 hPa and 10°S.

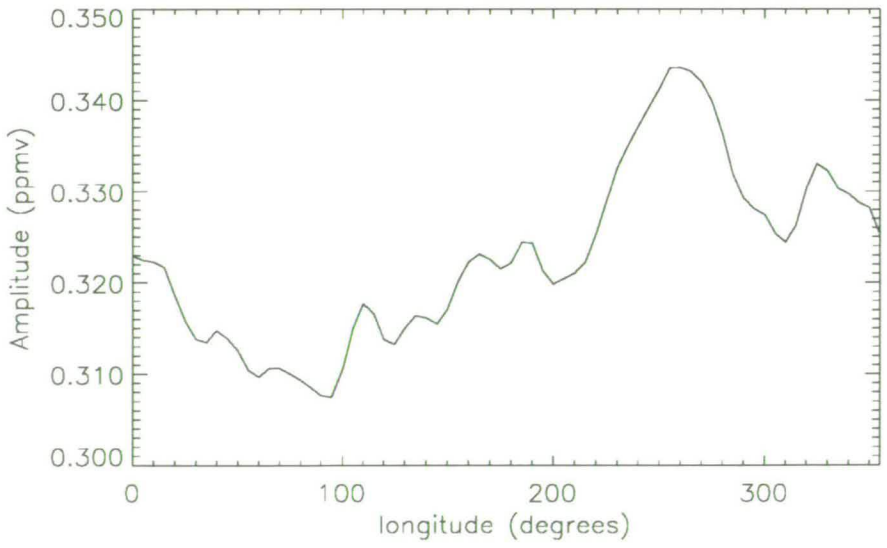

Figure 6.22: Variation in amplitude of the annual cycle with longitude for 10°S and 100 hPa

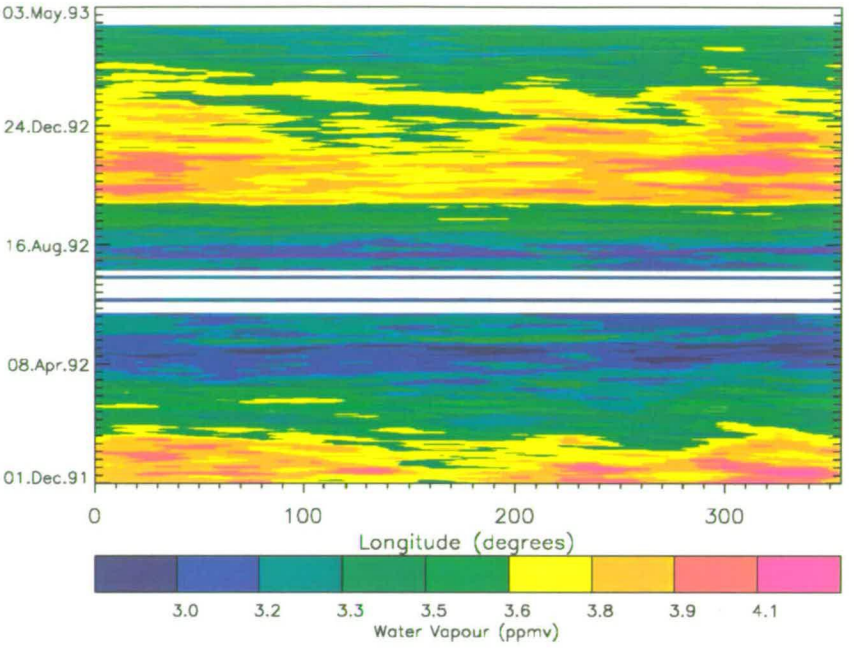

Figure 6.23: As for figure 6.21 but for 68 hPa.

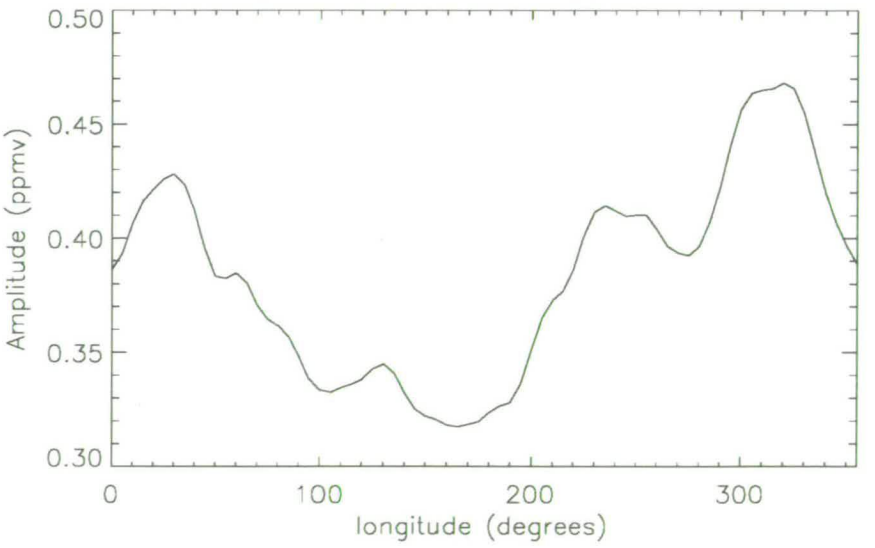

Figure 6.24: As for figure 6.24 but for 68 hPa

6.5.1 STE and Convection

In the previous chapter, the lifecycle of the MJO was studied using sequences of 5 day averages during an eastward moving event in December 1991–February 1992. Events were linked with deep convection. Here, the same sequences of 5 days are examined to see if the deep convection in the troposphere affects the stratosphere or results in stratosphere-troposphere exchange. The sequence of 5-day averaged fields fall at the time of the moist-dry tape transition discussed earlier in the chapter. Figure 6.14 shows the 5-day averaged water vapour fields at 100 hPa.

Five day averaged temperature fields are shown in figure (6.25) for the sequence of days when deep convection was noted. Sharp temperature gradients are seen around 20°N and 20°S. Temperatures of about 190 K are seen across the central tropics except for the far eastern Pacific, Atlantic ocean and central Africa. On the 1st January, temperatures fall to 188 K over the western Pacific and then on the 6th January, temperatures less than 188 K can be seen. These particularly cold temperatures occur along with deep convection in the upper troposphere. Throughout the rest of the sequence, except for tiny localised areas on 21st January and 5th February, temperatures this low are not observed again and remain above 192 K.

Figure 6.26 shows 5 day averaged mean potential temperature between the equator and 10°S at 100 hPa. At the beginning of this sequence, the potential temperature at 100 hPa has a range of about 9 K with the minimum temperature of 369 K occurring at about 180°E. On 1st January, a fall in potential temperature of 3 K takes place around 180°E. The potential temperature falls by a further 3 K on 6th January. Similarly on these days, figure 6.27 shows the 375 K surface to be at a pressure of below 95 hPa in the region of the dateline i.e there is an upward distortion of the 375 K surface. This, along with the fall in potential temperature at 100 hPa, is indicative of deep convection (e.g. Pfister *et al.*, 1993; Jackson *et al.*, 1998).

These dates correspond to the regions of high water vapour found in pentad maps of water vapour at 215 hPa and 147 hPa (see figure 5.21). In particular, the 6th of January was a time of deep convection in the upper troposphere and

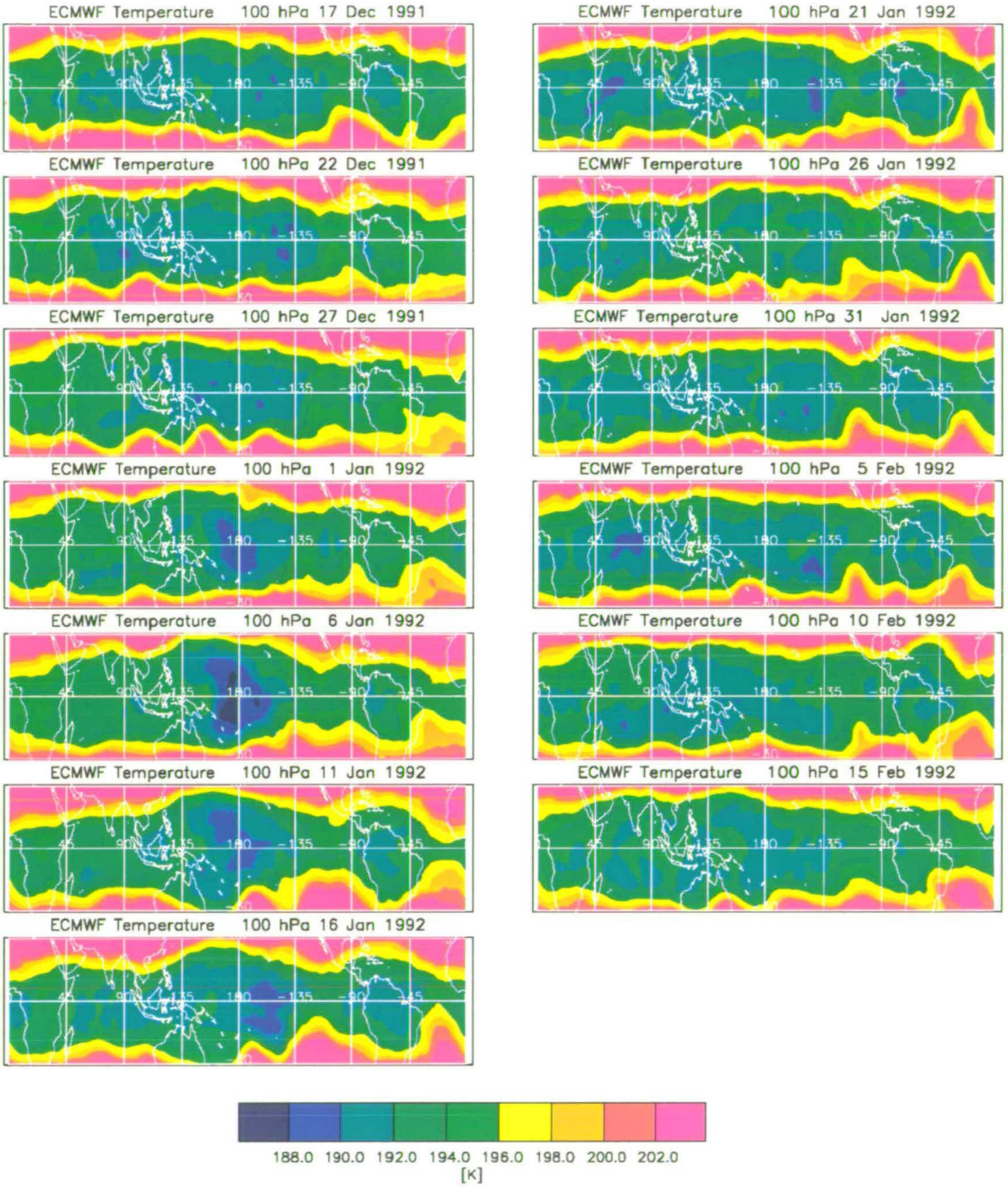

Figure 6.25: 5 Day averaged ECMWF temperature at 100 hPa.

the time when cyclone pairs developed at 850 hPa. Signs of dehydration or moistening are not observed in the water vapour field at 100 hPa for these days. However, since the isentropic surface is uplifted to 95 hPa, this would imply that the convective outflow is also at this level. The lack of discernible features at 100 hPa should not be taken as proving that stratosphere-troposphere exchange is not taking place because of high dependence of the 100 hPa measurements on the zonal mean climatology.

6.6 Conclusions

This chapter has presented some initial results from the new non-linear retrieval of water vapour in the lower stratosphere.

Seasonal averages of water vapour at 68 hPa showed that the field was largely zonal in structure with lower mixing ratios at the equator and higher mixing ratios towards the poles (excluding the southern polar vortex in JJA and SON). Departures from zonal symmetry can still be found at this level. The stratospheric fountain region was seen to be dry in DJF and the Asian monsoon region to be moist in JJA and SON. The affects of the monsoon and the stratospheric fountain reach higher in the stratosphere than has previously been reported.

Zonal mean water vapour at 100 hPa and 68 hPa compared well with previous studies of water vapour. Transport from the tropics to the midlatitudes was greater at 100 hPa than at 68 hPa due to the tropical pipe being more leaky at the lower altitude. Air moves into midlatitudes more quickly and with less mixing in the northern hemisphere than in the southern. Mixing in the southern hemisphere with air from the polar vortex results in the southern hemisphere being drier than the northern, in agreement with many studies.

Time-height sections of water vapour from MLS and from HALOE showed that the stratospheric tape signal was in phase with upper tropospheric variability in the northern hemisphere, but out of phase with the southern hemisphere. This suggests that more water vapour gets into the stratospheric overworld from the northern hemisphere than from the southern. Greater transfer of air into the northern hemisphere than the southern has been suggested by Rosenlof *et al.*, (1997) and was revealed in zonal mean water vapour at 390 K from HALOE.

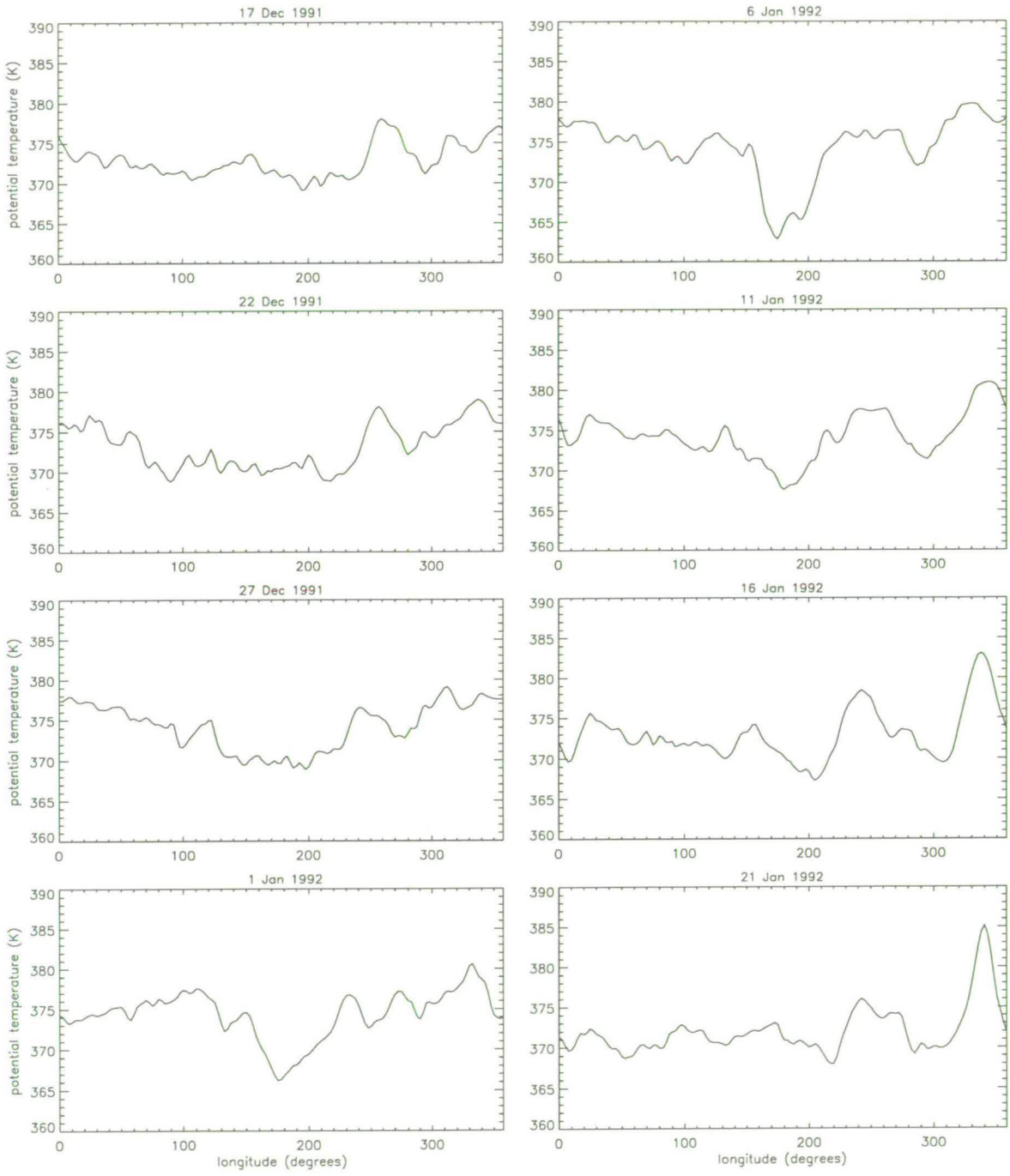

Figure 6.26: 5 Day averaged meridional mean of ECMWF potential temperature between 0 and 10°S at 100 hPa.

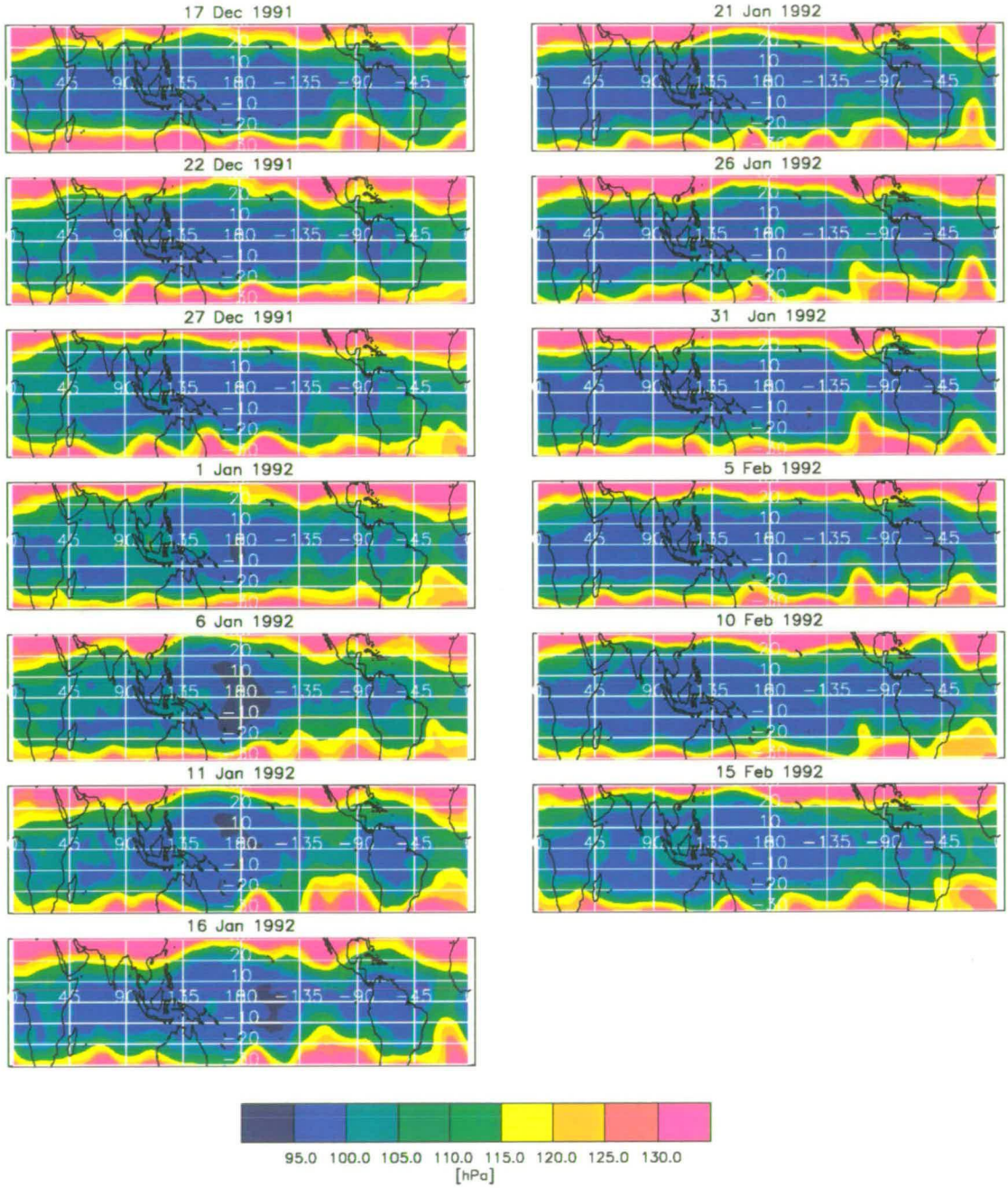

Figure 6.27: 5 Day averaged ECMWF pressure of the 375K isentropic surface.

The maxima and minima at the tropics were seen in the northern hemisphere before the southern. A zonal mean at 100 hPa from MLS confirms this, with both the tropical maxima and minima being offset from the equator at 10-20°N and the maxima and minima being seen in the northern hemisphere before the southern. The maxima and minima at 68 hPa were offset also, but were closer to the equator than at 100 hPa.

One advantage of the new non-linear MLS retrieval over HALOE and SAGE II is that the tropical region is covered more frequently, hence allowing daily maps of the water vapour field to be drawn. Five day averaged maps during the transition from 'dry to moist' or 'moist to dry' tape signals confirmed that the northern hemisphere temporally leads the southern. In particular, SE Asia and India are the first regions to become moist during the time of the monsoon, closely followed by Panama. Occasionally, though it seems not necessarily, these injections of air are accompanied by freeze drying processes. Following the initial appearance of the moister air in the locations just mentioned the water vapour spreads zonally and is accompanied by further mass transfer in other locations until the whole northern tropics and the southern tropics north of 10°S become moist. Similarly dry air appears initially over Indonesia and the Western Pacific followed by Panama and upward transfer continues in other locations to fill the tropics north of 10°S. The most northerly extent of the low mixing ratios is over Indonesia and the western Pacific.

Some differences exist from year to year which may be related to the phase of the QBO. In 1991-1992, when the phase of the QBO was easterly the 5 day averaged fields at 100 hPa and 68 hPa showed that both levels were drier and that the dryness lasted for longer than in 1992-1993 when the QBO phase was westerly. The effects of the QBO were also noticeable in the zonal mean. The maximum in water vapour at 68 hPa was greater in 1992 than in 1993 due to more upward advection within the tropical pipe in 1992 when the QBO was easterly. Transport out of the tropics into midlatitudes was enhanced by the westerly phase of the QBO, an effect evident in the 100 hPa field.

As in previous chapters the variability of water vapour in the lower stratosphere was also examined using longitude-time sections. Longitude-time sections showed that the lower stratospheric water vapour was dominated by the annual cycle

which accounts for at least 90% of the variance. The variation in the strength of the annual cycle with longitude at both 68 and 100 hPa shows there to be some remaining influence of topography with larger annual cycles over south America and suppressed annual cycles over the eastern Pacific. The longitudinal structure to the water vapour field must come from the measurements themselves as the a priori is a zonal mean. Hence, the variation with longitude of the annual cycle being similar to that in the troposphere is a good indication that the retrieval is producing believable values. At 68 hPa there is better agreement with the troposphere than at 100 hPa which seem to confirm that there are some problems with the retrieval at 100 hPa.

Mote *et al.*, (1998) showed temporally-filtered longitude-time sections at 68 hPa and 100 hPa which had similar eastward moving features to those at 215 hPa. Wavenumber-frequency analysis showed that they had a 30-70 day time period. The divergence field at 100 hPa presented in chapter 5 indicated that there was convective outflow at around the 100 hPa level associated with the eastward moving features. In this chapter, 5-day averaged fields were investigated for evidence that some of these deep convective events associated with the MJO resulted in transfer of water vapour to the stratospheric overworld. Specifically, on the 1st and 6th January 1992, high water vapour concentrations were observed over the western Pacific at 215 hPa, coinciding with the formation of cyclone pairs at 850 hPa. That convection was reaching the stratosphere on these days, was signalled by a drop in 100 hPa temperature and an upward distortion of the 375 K isentropic surface over the western Pacific. The meridional mean of potential temperature at 100 hPa indicated that it fell over a narrow range of longitudes from 160-180°E.

The 100 hPa water vapour field did not display spatial features which correlated well with the temperature field or with the water vapour field at 215 hPa. This could be taken as an indication that the moisture content of the lower stratosphere is not altered significantly during this event. The annual cycle dominates the water vapour field, accounting for more than 90% of its variance and it is therefore difficult to see smaller amplitude variances above this. It may also be that the retrieval at 100 hPa is not sufficiently sensitive to smaller-scale changes in mixing ratio. Evidence suggests that convective events of the MJO do period-

ically penetrate the stratosphere but it remains unclear by how much they alter the moisture content. It may be such events which trigger the weak evanescent signal of the MJO that Mote *et al.*, (1998) describe.

Chapter 7

Conclusions and Further Work

This chapter summarises the main findings of this thesis and highlights areas that are interesting for further research.

Primarily, this thesis exploited the water vapour product from the 205 GHz channel on UARS MLS. The measurements are most sensitive at 215 hPa, but some realistic information is obtainable at 316 hPa and at 147 hPa as this thesis demonstrated. As an extension to this work in the upper troposphere, the non-linear retrieval of water vapour from the 183 GHz MLS, which extended stratospheric measurements to 68 hPa and 100 hPa, was also investigated.

In chapter 1, the radiative role and the importance of water vapour to the climate was outlined. Global measurements of water vapour, particularly in the tropical upper troposphere, were seen to be necessary to aid the understanding and prediction of climate change. In chapter 2, MLS was shown to be a useful means for acquiring the data, providing many advantages over radiosondes and other satellites.

In chapter 3, MLS was found to reproduce the large-scale features of the water vapour field, comparing well with previous research and with the NASA water vapour dataset (NVAP). Many of the differences between MLS data and NVAP data can be explained by the different type of measurement, MLS being mixing ratios at 215 hPa and NVAP being total column water vapour between 300 hPa and 500 hPa. The similarity between them reflects the importance of convective processes in maintaining the moisture budget of the upper troposphere. The main regions of difference occur in the convective regions of the Asian monsoon and Indonesian fountain where MLS measurements are more moist than NVAP. This

can be attributed to the TOVS field, (which contributes to NVAP) introducing a dry bias in cloudy conditions and possibly to some effects of cirrus contamination in the MLS measurements.

ECMWF humidity analysis was also shown to reproduce the moisture field well. The main problems are a lack of contrast between dry and moist times and locations. The contrast between tropics and subtropics being due to an under-prediction of the strength of the Hadley circulation, is a trait that has been widely noted. The lack of contrast between Western and Eastern Pacific noted here could similarly be due to an under-prediction in the strength of the Walker circulation. Generally however, the ECMWF field compared well with the MLS field, and this can be put down to the success of the convective parameterisations in the model.

Much of the thesis focused upon variability of water vapour in the tropical region. Time series were constructed which allowed variability to be studied on a range of timescales. The annual cycle and its variation with longitude was investigated in more detail than in previous research and an intraseasonal variability in water vapour in this height range, was seen for the first time. This intraseasonal cycle was demonstrated to be related to the convective anomalies of the Madden-Julian oscillation.

Water vapour in the tropical region was seen to exhibit an annual cycle which had a strong longitudinal variation and was most pronounced over the landmasses of South America and Africa. The oceans tend to have a moderating effect on the annual cycle but secondary maxima occur in regions influenced by the Asian monsoon, and over Indonesia and the central Pacific. The influence of land and sea weakens with increasing height but its affects can still be observed in the lower stratosphere at both 100 hPa and 68 hPa.

Longitude-time sections revealed eastward moving moist anomalies which were demonstrated to be related to the convective anomalies of the MJO. The moist anomalies were most prominent at 10°S from December 1991 to March 1992; this period coinciding with an El Niño. Power spectrum analysis showed that these features had a time-period of 30-85 days with a peak at 70 days. The 70 day peak was interpreted by Clark *et al.,* (1998) as a zonally symmetric mode, and the

variability in the 50-60 day range as a propagating mode. This interpretation fits retrospectively with the cross-correlation and the filtered longitude-time section which revealed both a propagating and a non-propagating mode.

Similar eastward moving features were seen in the other MLS levels, 316 hPa and 147 hPa. This demonstrates not only the dependence on convective processes, but also gives credence to the retrieval at these levels. Although the intraseasonal cycle dominates over the annual cycle in the region of 160°E at all three levels, its dominance increases at higher levels as the amplitude of the annual cycle decreases and that of the intraseasonal cycle increases. This is due to the convective anomalies reaching greater altitude than the climatological convection. Moreover, the power spectrum shows enhancement of the propagating mode over the zonally symmetric mode at the 147 hPa level.

Evidence was presented which linked the eastward moving features in the water vapour field with the convective anomalies of the MJO. Sequences of days taken through a moist event showed movement of water vapour from Africa, across the Indian Ocean, intensification over Indonesia and the Western Pacific and development down the SPCZ. This is characteristic of MJO events and compares well with the outgoing longwave radiation field described in many studies. A detailed comparison of the OLR field with the water vapour field is an important area for future work. These water vapour fields were compared with ECMWF mid-tropospheric vertical velocity and with low level wind fields. The water vapour was seen to be high and to occur in the same location as the convection as indicated by the upward movement in the vertical velocity field. Westerly wind bursts were correlated with the eastward moving moist anomalies. The westerly wind bursts were maximised off the equator in the southern hemisphere and were associated with the unusual development of a cyclone pair.

Future work should be directed towards linking all the meteorological fields together in a more quantitative sense. A more sophisticated comparison between water vapour and zonal winds, possibly involving singular value decomposition, may indicate whether convection leads westerly wind bursts or whether westerly wind bursts lead water vapour. Does the convection force the westerly wind bursts, or do the westerly wind bursts force the convection? This is important in trying to establish the mechanism for the MJO. Analysis of velocity potential

may be an improvement upon divergence and vorticity fields in which eastward moving features were difficult to identify. Correlation between OLR and water vapour should be examined both in longitude-time sections and as 5 day averaged fields. Again, the phase relationship between water vapour and OLR should be investigated to see if there is a time lag between the expected enhanced water vapour and reduction in OLR. Sea surface temperature fields in the tropics would also be interesting to analyse in conjunction with the water vapour and the OLR fields with the hope of establishing the relationship among them.

In 1992, an El Niño year, the eastward extent of the moist anomalies was greater than in the other years, and the water vapour mixing ratios were higher. Future work in this area should include a more detailed assessment of the interaction between the MJO and El Niño and their combined effects on the water vapour field. An examination of the interaction between the MJO and the Asian monsoon is likewise, an interesting area of further research. The eastwards moving dry features which are apparent at 10°N in the northern hemisphere winter also require explanation.

Occasionally, the convective events of the MJO resulted in an overshooting of the 100 hPa level which is taken to be an approximation to the tropopause. This was signalled by a sudden fall in 100 hPa temperatures and an upward distortion of the 375 K potential temperature surface. It may be such events as this which lead to the evanescent signal of the MJO found by Mote *et al.* (1998). It remains unclear as to the extent to which these convective penetrations change the moisture content of the lower stratosphere, due to the uncertainty of the retrieval at 100 hPa.

Seasonal averages of water vapour at 68 hPa showed an expected zonal structure but some departures from zonal symmetry were observed. During DJF dry areas were found in the region of the 'stratospheric fountain' and around Panama and enhanced moisture was noted in the Asian monsoon region in JJA. The effects of the monsoon and the stratospheric fountain reach higher in the stratosphere than has previously been observed.

Time-height sections and zonal means of water vapour showed that the stratospheric tape signal was in phase with the northern hemisphere but out of phase

with the southern hemisphere. The zonal mean revealed air to spread from the northern hemisphere to the southern hemisphere tropics and to mix with midlatitude air in both hemispheres. Transport to mid-latitudes is enhanced when the phase of the QBO is westerly and is greater at 100 hPa than at 68 hPa due to the tropical pipe being more leaky at the lower altitude. Air moves into midlatitudes more quickly and with less mixing in the northern hemisphere than in the southern. Mixing in the southern hemisphere with air from the polar vortex results in the southern hemisphere being drier than the northern in agreement with studies from HALOE and from SAGE II. That these results are in agreement with previous studies is an important indication of the validity of the new non-linear retrieval.

Unlike HALOE and SAGE II, MLS samples the tropical region on a daily basis, excepting instrument failures. Five day averaged maps allowed the transition from dry to moist tape signals at 100 hPa and 68 hPa, to be examined. At the end of a dry tape signal, moistening initiates over the Asian monsoon region and other locations follow subsequently. Following the initial appearance of the moister air in the locations just mentioned the water vapour spreads zonally and is accompanied by further mass transfer in other locations.

From the five day averaged maps, it can be concluded that at the end of a moist signal, the 'stratospheric fountain' region, western Pacific and Panama are the first places to become dry. The importance of the stratospheric fountain region is therefore that it temporally leads the stratosphere in becoming dry, but that mass transfer from troposphere to stratosphere is not confined to this region. Trajectory analysis would allow the movement of water vapour to be closely followed and hence the extent to which water vapour enters at other locations or is transported from the source regions could be determined. This is an important area for future work. It is also hoped that the new version 5 ozone from MLS could be used along with water vapour to give further information about transport in the lower stratosphere.

Appendix A

The Butterworth Filter

The annual cycle and low frequency variability can be effectively removed using a Butterworth low-pass filter (Ersoy, 1997). The Butterworth filter has the form

$$filter = \frac{1}{1 + [D/D_0]^{2n}} \tag{A.1}$$

where D is the frequency image, D_0 is the cutoff frequency and n is the order of the filter. The frequency response at the cutoff frequency is equal to 50% of the maximum.

Similarly, a band-pass filter can be defined with a centre frequency C:

$$filter = \frac{1}{1 + [(D - C)/D_0]^{2n}} \tag{A.2}$$

The ability of the filter to remove the annual cycle is shown for 25°S, 10°S in figure A.1 where the annual cycle is strong, and in figure A.2 where the annual cycle is weak. Over most of the time-series, the annual cycle is a good fit to the data. Errors are largest at the ends of the time-series due to applying Fast Fourier transforms to a series of finite length.

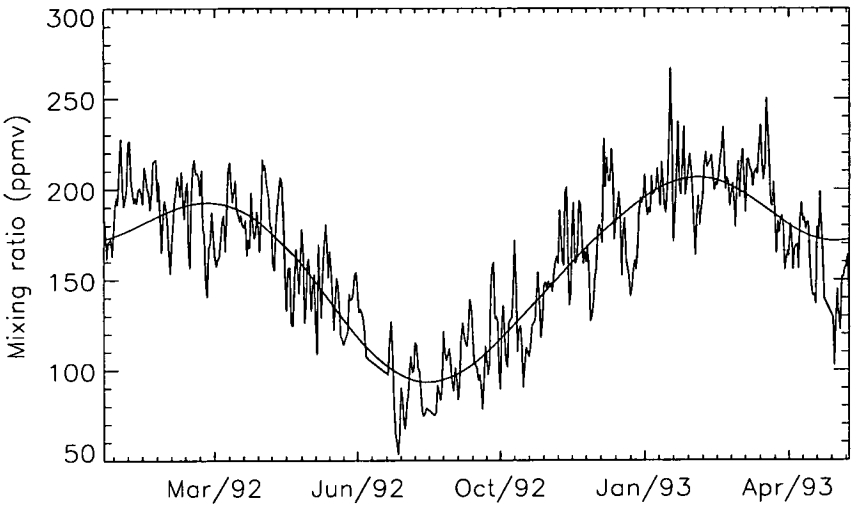

Figure A.1: The 150 day Butterworth high-pass filter applied to the MLS UTH time-series at 25°E, 10°S where the annual cycle is pronounced.

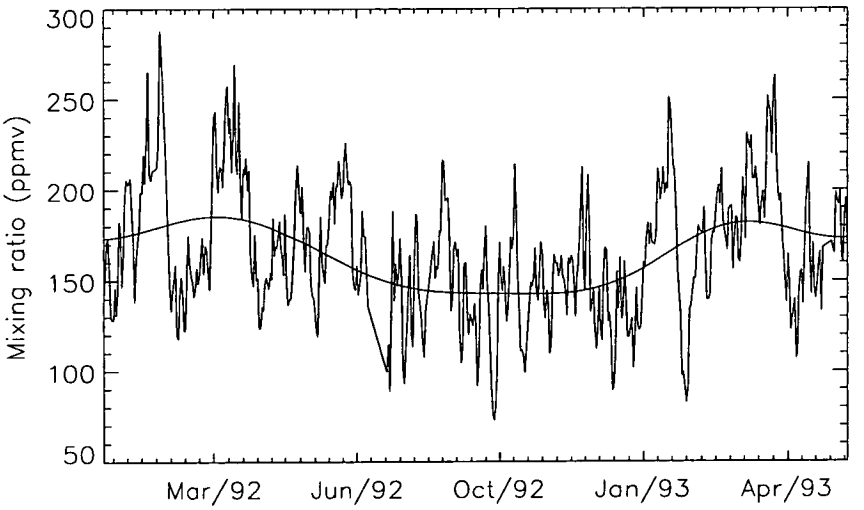

Figure A.2: As for figure A.1 but for 160°E where the annual cycle has a small amplitude.

References

Appenzeller, C., Holton, J.R., Rosenlof, K.H., 1996: The seasonal variation of mass-transport across the tropopause, *J. Geophys. Res.*, **101**, pp 15071–15078.

Arking, A., 1990: Feedback processes and climate response to proceedings of the conference on climate impacts of solar variability, NASA conference publications CP-3086.

Arking, A., 1991: The radiative effects of clouds and their impact on climate, *Bull. Amer. Meteor. Soc.*, **72**, pp 795–813.

Barath, F., M. Chavez, R. Cofield, D. Flower, M. Frerking, M. Gram, W. Harris, J. Holden, R. Jarnot, W. Kloezeman, G. Klose, G. Lau, M. Loo, B. Maddison, R. Mattauch, R. McKinney, G. Peckham, H. Pickett, G. Siebes, F.Soltis, R. Suttie, J. Tarsala, J. Waters, W. Wilson 1993: The Upper Atmosphere Research Satellite Microwave Limb Sounder Instrument, *J. Geophys. Res.*, **98**, pp 10751–10762.

Betts, A.K., 1990: Greenhouse warming and the tropical water budget, *Bull. Amer. Meteor. Soc.*, **71**, pp 1464–1465.

Black, R., 1997: Trajectory mapping of water vapour measured by the microwave limb sounder, Ph.D Thesis, University of Edinburgh, pp 231–233.

Blackwell, K.G., J.P. McGuirk, 1996, Tropical upper tropospheric dry regions from TOVS and rawinsondes, *J. Appl. Meteorol.*, **35**, pp 464–481.

Brewer, A.M., 1949: Evidence for a world circulation provided by the measurements of helium and water vapour distribution in the stratosphere, *Q.J.R. Meteorol. Soc.*, **75**, pp 351–363.

Bond, S.T. 1996: The Potential effect of cirrus on microwave limb sounder retrievals, Ph.D Thesis, University of Edinburgh.

Carr, E.S., R.S. Harwood, P.W. Mote, G.E. Peckham, R.A. Suttie, W.A. Lahoz, A. O'Neill, L. Froidevaux, R.F. Jarnot, W.G Read, J.W. Waters, R. Swinbank, 1995: Tropical stratospheric water vapour measured by the microwave limb sounder (MLS), *Geophys. Res. Letts.*, **22**, pp 691–694.

Cess, R.D., G.C. Potter, J.P. Blanchett, G.J. Boer, A.D. Del Genio, M. Déqué, V. Dymnikov, V. Galin, W.L. Gates, S.J. Ghan, J.T. Kiehl, A.A. Lacis, H. Le Truet, Z.X. Li, X-Z. Liang, B.J. McAvaney, V.P. Meleshko, J.F.B. Mitchell, J.J. Morcrette, D.A. Randall, L. Rikuo, E. Roeckner, J.F. Royer, U. Schlese, D.A. Sheinin, A. Slingo, A.P. Sokolov, K.E. Taylor, W.M. Washington, R.T. Wetherald, I. Yagai, M-H. Zhang, 1990: Intercomparison and interpretation of climate feedback processes in 19 atmospheric General Circulation Models, *J. Geophys. Res.*, **95**, pp 16601–16616.

Chaboureau, J-P., Chédin, A.S. Noëlle, 1998: Remote sensing of the vertical distribution of atmospheric water vapour from the TOVS observations: Method and validation, *J. Geophys. Res.*, **103**, pp 8743–8752.

Chang, C.-P., H Lim, Kelvin Wave CISK, 1988: A possible Mechanism for the 30-50 Day Oscillation, *J. Atmos. Sci.*, **45**, pp 1709–1720.

Chao, W.C., 1995: A Critique of Wave-CISK as an explanation for the 40-50 Day Tropical Intraseasonal Oscillation, *Journal of the Meteorological Society of Japan*, **73**, pp 677–684.

Chao, W.C., S.-J. Lin, 1994: Tropical Intraseasonal Oscillation, Super cloud Clusters and Cumulus Convection schemes, *J. Atmos. Sci.*, **51**, pp 1282–1297.

Chen, T.C., J.M. Chen, J. Pfaendtner, J. Susskind, 1995: The 12-24 Day Mode of Global Precipitation, *Monthly Weather Review*, **123**, pp 140–152.

Chen, T.C., H. van Loon, M-C. Yen, 1996a: An Observational Study of the Tropical-Subtropical Semiannual Oscillation, *Journal of Climate*, **9**, pp 1993–2002.

Chen, T.C., J. Pfaendtner, J.M. Chen, C.K. Wickle, 1996b: Variability of the Global Precipitable Water with a Timescale of 90-150 Days, *J. Geophys. Res.*, **101**, pp 9323–9332.

Cho, H-R., K. Klaus Fraedrich, J.T. Wang, 1994: Cloud Clusters, Kelvin Wave-CISK, and the Madden-Julian Oscillations in the Equatorial Troposphere, *J. Atmos. Sci.*, **51**, pp 68–76.

Chou, M-D., 1994: Coolness in the Tropical Pacific during an El Niño Episode, *Journal of Climate*, **7**, pp 1684-1692.

Clark, H.L., R.S. Harwood, P.W. Mote, W.G. Read, 1998: Variability of water vapour in the tropical upper troposphere as measured by the Microwave Limb Sounder on UARS, *J. Geophys. Res.*, **103**, pp 31695–31707.

Collimore, C.C., M.H. Hitchman, D.W. Martin, 1998: Is there a quasi-biennial oscillation in tropical deep convection? *Geophys. Res. Letts.*, **25**, pp.333–336.

Danielsen, E.F., 1982: A dehydration mechanism for the stratosphere, *Geophys. Res. letts.*, **9** pp 605–608.

Danielsen, E.F., 1993:In situ evidence of rapid, vertical, irreversible transport of lower tropospheric air into the lower tropical stratosphere by convective cloud turrets and by larger-scale upwelling in tropical cyclones, *J. Geophys. Res.*, **98**, pp 8665–8681.

Del Genio, A.D., W. Kovari-Jr, M.-S. Yao, 1994: Climatic implications of the seasonal variation of upper tropospheric water vapour, *Geophysical Research Letters*, **21**, pp 2701–2704.

Dickenson, R.E. 1968: On the excitation of and propagation of zonal winds in an atmosphere with Newtonian cooling, *J. Atmos. Sci.*, **25**, pp 269–279.

Dunkerton, T.J., F.X. Crum, 1995: Eastward propagating ~2- to 15-day equatorial convection and its relation to the tropical Intraseasonal oscillation, *J. Geophys. Res.*, **100**, pp 25781–25780.

Douglas, P. 1996: The Potential effect of cirrus on microwave limb sounder retrievals, Ph.D Thesis, University of Edinburgh.

Eliassen, A., 1951: Slow thermally or frictionally controlled meridional circulation in a circular vortex, *Astrophys Norv*, **5(2)**, pp 19–60.

Elliot, W.P., D.J. Gaffen,. 1991: On the utility of radiosonde humidity archives for climate studies, *Bull. Amer. Meteor. Soc.*, **72**, pp 1507–1520.

Elliot, W.P., M.E. Smith, J.K. Angell, 1990: Monitoring tropospheric water vapour changes using radiosonde data, Elsevier, Oxford.

Elson, L.S., W.G. Read, J.W. Waters, P.W. Mote, J.S. Kinnersley, R.S. Harwood, 1996: Upper Tropospheric Water Vapour from UARS MLS,*Bull. Amer. Meteor. Soc.*, **101**, pp 9001–9015.

Emanuel, K.A. 1987: An air-sea interaction model of intraseasonal oscillations in the tropics, *J. Atmos. Sci.*, **44**, pp 2324–2340.

Emanuel, K.A. 1988: Reply (to comments by Wang on "An air-sea interaction model of intraseasonal oscillations in the tropics", *J. Atmos. Sci.*, **44**, pp 3528–3530.

Ersoy, O., 1997: Fourier-related transforms, fast algorithms and applications, Prentice Hall, London, pp 233–234.

Ferranti, L., T.N. Palmer, F.Monteni, E. Klinker, 1990: Tropical–extratropical interaction associated with the 30-60 day oscillation and its impact on medium and extended range prediction, *J. Atmos. Sci.*, **47**, pp 2177–2199.

Flatau, M. P.J. Flatau, P. Phoebus, P,P Niiler, 1997: The feedback between equatorial convection and local radiative and evaporative processes: The implications for intraseasonal oscillations, *J. Atmos. Sci.*, **54**, pp 2373–2386.

Frederick, J.E., and A.R. Douglass, 1983: Atmospheric temperature near the tropical tropopause: Temporal variations, zonal asymmetry and implications for stratospheric water vapour, *Mon. Wea. Rev.*, **111**, pp 1397–1403.

Fu, R., R.E. Dickinson, B. Newkirk, 1997: Response of the upper tropospheric humidity and moisture transport to changes of tropical convection. A comparison between observations and a GCM over and ENSO cycle, *Geophys. Res. Letts.* **24** , pp 2371–2374.

Gill, A.E., 1982: Atmosphere-Ocean Dynamics, Academic Press, London.

Gilman, D.L., F.J. Fuglister, J.M. Mitchell, Jr., 1963: On the power spectrum of "red noise", *J. Atmos. Sci.*, **20**, pp 182–184.

Hansen, J.E., A.A. Lacis, 1991:*Nature*, **349**, pp 467.

Harries, J.E., J.M. Russell, A.F. Tuck, L.L Gordley, P. Purcell, K. Stone, R.M. Bevilacqua, M. Gunson, G. Nedoluha, W.A. Traub, 1996: Validation of measurements of water vapour from the Halogen Occultation Experiment (HALOE), *J. Geophys. Res.*, **101**, pp 10205–10216.

Harrison, D.E., B.S. Geise, 1991: Episodes of surface westerly winds as observed from islands in the western tropical Pacific, *J. Geophys. Res. oceans*, **96**, pp 3221–3237.

Harrison, D.E., G.A. Vecchi, 1997: Westerly wind events in the tropical Pacific, 1986-95, *Journal of Climate*, **10**, pp 3131–3156.

Hendon, H.H., 1988: A Simple Model of the 40-50 Day Oscillation, *J. Atmos. Sci.*, **45**, pp 569–584.

Hendon, H.H., B. Liebman, 1994: Organisation of Convection Within the Madden-Julian Oscillation, *J. Geophys. Res.*, **99**, pp 8073–8083.

Hendon, H.H., B. Liebman, J.D. Glick, 1998: Oceanic Kelvin waves and the Madden-Julian Oscillation, *J. Atmos. Sci.*, **55** pp 88–101.

Hendon, H.H., M.L. Salby, 1994: The Life-Cycle of the Madden-Julian Oscillation, *J. Atmos. Sci.*, **51**, pp 2225–2237.

Hendon, H.H., M.L. Salby, 1996: Planetary-scale circulations forced by intraseasonal variations of observed convection, *J. Atmos. Sci.*, **53**, pp 1751–1758.

Highwood, E.J., B.J Hoskins, 1998: The tropical tropopause, *Q.J.R. Meteorol. Soc.*, **124**, pp 1579–1604.

Holton, J., 1992: Introduction to dynamic meteorology, 3rd edition, Academic Press, London.

Holton, J.R., P.H. Haynes, M.E. McIntyre, A.R. Douglas, R.B Rood, L. Pfister, 1995: Stratosphere–Troposphere Exchange, *Reviews of Geophysics*, **33(4)**, pp 403–439.

Houghton, J.T., G.J. Jenkins, J.J. Ephraumus,1990: Climate change, the IPCC scientific assessment, Cambridge University Press, Cambridge.

Hoskins, B.J. 1991:Towards a PV-theta view of the general circulation, *Tellus, Ser. A*, **43**, pp 27–35.

Hsu, H-H., B.J. Hoskins, F-F. Jin, 1990: The 1985/86 intraseasonal oscillation and the role of the extratropics, *J. Atmos. Sci.*, **47**, pp 823–839.

IPCC 1996: Intergovernmental Panel on Climate Change 1995, the science of climate change, Edited by J.T. Houghton, Cambridge University Press, Cambridge.

Jackson, D.L., G.L. Stephens, 1995: A study of SSM/I-derived columnar water vapour over the global oceans, *Journal of Climate*, **8**, pp 2025–2038.

Jackson, D.R., R.S. Harwood, E. Renshaw, 1990: Tests of a Scheme for Regression Retrieval and Space-Time Interpolation of Stratospheric Temperature from Satellite Measurements, *Q.J.R. Meteorol. Soc.*, **116**, pp 1449–1470.

Jackson, D.R., S.J. Driscoll, E.J Highwood, J.E. Harries, J,M. Russell III, 1998: Troposphere to stratosphere transport at low latitudes as studied using HALOE observations of water vapour 1992–1997, *Q.J.R. Meteorol. Soc.*, **124**, pp 169–192.

Jones, C., B.C. Weare, 1996: The role of low-level moisture convergence and ocean latent heat fluxes in the Madden and Julian Oscillation: An observational analysis using ISCCP data and ECMWF analyses, *J. Climate*, **9**, pp 3086–3104.

Jones, C., D.E Waliser, C. Gautier, 1998: The influence of the Madden-Julian oscillation on ocean surface heat fluxes and sea surface temperature, *J. Climate*, **11**, pp 1057–1072.

Jones, R.L., J.A. Pyle, J.E. Harries, A.M. Zavody, J.M. Russell III, J.C. Gille, 1986: The water vapour budget of the stratosphere studied using LIMS and SAMS satellite data, *Q.J.R. Meteorol. Soc.*, **112**, pp 1127–1143.

Jones, R.L., J.F.B. Mitchell, 1991: Is water vapour understood?, *Nature*,**353**, pp 212.

Keen, R.A., 1982: The Role of cross-equatorial tropical cyclone pairs in the southern oscillation, *Mon. Wea. Rev.*, **110**, pp 1405–1416.

Kelly, K.K, A.F. Tuck, T. Davies,1991: Wintertime asymmetry of upper tropospheric water between the northern and southern hemispheres, *Nature*,**353**, pp 244–247.

Kelly, K.K., M.H. Proffitt, K.R. Chan, M. Loewenstein, J.R. Podolske, S.E. Strahan, J.C. Wilson, D. Kley, 1993: Water vapour and cloud water measurements over Darwin during the STEP 1987 tropical mission, *J.Geophys. Res.*, **98**, pp 8713–8724.

Kessler, W.S., M.J. McPhaden, K.M. Weickmann, 1995: Forcing of intraesasonal Kelvin waves in the equatorial Pacific, *J.Geophys. Res. oceans.*, **100**, pp 10613–10631.

Kiladis, G.N., K.M. Weickmann, 1992: Circulation anomalies associated with tropical convection during northern winter, *Mon. Wea. Review.*, **120**, pp 1900–1923.

Kiladis, G.N., G.A. Meehl, K.M. Weickmann, 1994: Large-scale circulation associated with westerly wind bursts and deep convection over the western equatorial Pacific, *J.Geophys. Res.*, **18**, pp 18527–18544.

Kley, D., E.J. Stone, W.R Henderson, J.W. Drummond, W.J. Harrop, A.L. Schmeltekopf, T.L. Thompson, R.H. Winkler, 1979: *In situ* measurements

of the mixing ratio of water vapour in the stratosphere, *J. Atmos. Sci.*, **36**, pp 2513–2524.

Kley, D., A.L. Schmelekopf, K. Kelly, R.H. Wrinkler, T.L. Thompson, M. McFarland, 1982: Transport of water vapour through the tropical tropopause, *Geophys. Res. letts.*, **9**, pp 617–620.

Knutson, T.R., K.M. Weickmann, 1987: 30-60 day atmospheric oscillations: Composite life cycles of convection and circulation anomalies, *Mon. Wea. Review.*, **115**, pp 1407–1436.

Lahoz, W.A., M.R. Suttie, L. Froidevaux, R.S Harwood, C.L. Lau, T.A. Lungu, G.E. Peckham, et al., 1996: Validation of UARS microwave limb sounder 183 GHz H_2O Measurements, *J. Geophys. Res.*, **101**, pp 10129–10149.

Lander, M.A., 1990: Evolution of the cloud pattern during the formation of tropical cyclone twins symmetrical with respect to the equator, *Mon. Wea. Review.*, **118**, pp 1194–1202.

Lau, K.-M., L.Peng, 1987: Origin of Low-Frequency (Intraseasonal) Oscillations in the Tropical Atmosphere, Part I: Basic Theory, *J. Atmos. Sci.*, **44**, pp 950–972.

Lau, K.M., P.H. Chan, 1986: The 40-50 day oscillation and ENSO - a new perspective, *Bull. Amer. Meteorol. Soc.* **67**, pp 533–534.

Lau, K.-M., T. Nakazawa, C.H. Sui, 1991:Observations of cloud cluster hierarchies over the tropical western Pacific, *J.Geophys. Res.*, **96**, pp 3197–3208.

Lau, K.-M., F.C. Chang, 1992: Tropical intraseasonal oscillation and its prediction by the NMC operational model, *J. Climate*, **5**, pp 1365–1378.

Lau, K.-M., C.-H. Ho, M.-D Chou, 1996: Water vapour and cloud feedback over the tropical oceans: Can we use ENSO as a surrogate for climate change? *Geophys. Res. Letts.*, **23**, pp 2971–2974.

Lin, K., R.H. Johnson, 1996: Kinematic and thermodynamic characteristics of the flow over the western Pacific warm pool during TOGA COARE, *J. Atmos. Sci.*, **53**, pp 695–715.

Lindzen, R.S., 1990a: Some coolness concerning global warming, *Bull. Amer. Meteor. Soc.*,**71**, pp 288–299.

Lindzen, R.S., 1990b: Response, *Bull. Amer. Meteor. Soc.*, **71**, pp 1465–1467.

Lindzen, R.S., 1991: *Nature*, **349**, pp 467.

Madden, R.A., P.R. Julian, 1971: Detection of a 40-50 Day Oscillation in the Zonal Wind in the Tropical Pacific, *J. Atmos. Sci.*, **28**, pp 702–708.

Madden, R.A., P.R. Julian, 1972: Description of global scale circulation cells in the tropics with a 40-50 day period, *J. Atmos. Sci.*, **29**, pp 1109–1123.

Madden, R.A., P.R. Julian, 1994: Observations of the 40-50 Day Tropical Oscillation - A review, *Monthly Weather Review*, **122**, pp 814–837.

Mastenbrook, H.J., 1974: Water vapour measurements in the lower stratosphere, *Can. J. Chem.*, **52**, pp 1527–1531.

Matsuno, T., 1966: Quasi-geostrophic motions in the equatorial area, *J. Meteorol. Soc. Japan*, **44**, pp 25–43.

Matthews, A.J., B.J. Hoskins, J.M. Slingo, M. Blackburn, 1996: Development of Convection along the SPCZ within a Madden-Julian Oscillation, *Q.J.R. Meteorol. Soc.*, **122**, pp 669–688.

McPhaden, M.J., B.A. Taft, 1988: Dynamics of seasonal and intraseasonal variability in the eastern equatorial Pacific, *J. Phys. Oceanogr.*, **18**, 1713–1732.

Mote, P.W., K.H. Rosenlof, J.S. Holton, R.S. Harwood, J.W. Waters, 1995: Seasonal variations of water vapour in the tropical lower stratosphere, *Geophys. Res. Letts.* , **22**, pp 1093–1096.

Mote, P.W., K.H. Rosenlof, M.E. McIntyre, E.S. Carr, J.C Gille, J.S. Holton, J.S. Kinnersley, H.C. Pumphrey, J.M Russell III, J.W. Waters, 1996: An atmospheric tape recorder: The imprint of tropical tropopause temperatures on stratospheric water vapour, *J. Geophys. Res.*, **101**, pp 3989–4006

Mote, P.W., H.C. Pumphrey, T.J. Dunkerton, 1998: Sub-seasonal variations in lower stratospheric water vapour, *Geophys. Res. letts.*, **25**, pp 2445–2448.

Nakazawa, T., 1988: Tropical Super Cloud Clusters Within Intraseasonal variations over the Western Pacific, *J. Meteor. Soc. Japan*, **66**, pp 823–839.

Neelin, J.D., I.M. Held, K.H. Cook, 1987: Evaporation-wind feedback and low frequency variability in the tropical atmosphere, *J. Atmos. Sci.*, **44**, pp 2341–2348.

Neelin, J.D., 1988: Reply (to comments by Wang on "An air-sea interaction model of intraseasonal oscillations in the tropics", *J. Atmos. Sci.*, **44**, pp 3526–3527.

Newell, R.E., S. Gould-Stewart, 1981: A Stratospheric Fountain? *J. Atmos. Sci.*, **38**, pp 2789–2796.

Newell, R.E., N.E. Newell, Y. Zhu, C. Scott, 1992: Tropospheric rivers? A pilot study, *Geophys. Res letts.*, **19**, pp 2401–2404.

Newell, R.E., Y. Zhu, E. V. Browell, W. G. Read, J. W. Waters,1996: Walker circulation and tropical upper tropospheric water vapour, *J. Geophys. Res.*, **101**, pp 1961–1974.

Newell, R.E., Y. Zhu, W.G. Read, J.W. Waters, 1997: Relationship between tropical upper tropospheric moisture and eastern tropical Pacific sea surface temperature at seasonal and interannual time scales, *Geophys. Res letts.*, **24**, pp 25–28.

Ovarlez, J., H. Ovarlez, H. Teitelbaum, 1996: *In situ* water vapour measurement, and a case study of the drying mechanism of the tropical lower stratosphere, *Q.J.R. Meteorol. Soc.*, bf 122, pp 1447–1458.

Ovarlez, J., P. vanVelthoven, 1997: Comparison of water vapour measurements with data retrieved from ECMWF analyses during the POLINAT experiment, *J. App. Met.*, bf 36, pp 1329–1335.

Pan, L., S. Solomon, W. Randel, J-F. Lamarque, P. Hess, J. Gille, E-W Chiou, M. P. McCormick, Hemispheric asymmetries and seasonal variations of the lowermost water vapour and ozone derived from SAGE II data, *J. Geophys. Res*, **102**, pp 28177–28184.

Pfister, L., K.R. Chan, T.P Bul, S. Bowden, M. Legg, B. Bary, K. Kelly, M. Proffitt, W. Starr, 1993: Gravity waves generated by a tropical cyclone during the STEP Tropical Field Program: A case study, *J. Geophys. Res*, **98**, pp 8611–8638.

Philander, S.G.H., D. Gu, D. Halpern, G. Lambert, N.-C. Lau T. Li, R.C. Pacanowski, 1996: Why the ITCZ is mostly north of the equator, *Journal of Climate*, **9**, pp 2958–2972.

Plumb, R.A., 1996: A "tropical pipe" model of stratospheric transport, *J. Geophys. Res*, **101**, pp 3957–3972.

Potter, B.E., F.R. Holton, 1995: The role of monsoon convection in the dehydration of the lower tropical stratosphere, *J. Atmos. Sci.*, **52**, pp 1034–1050.

Pumphrey, H.C., D.Rind., J.M. Russell III, J.E. Harries, 1998: A preliminary zonal mean climatology of water vapour in the stratosphere and mesosphere, *Adv. Space Res.*, **21**, pp 1417–1420.

Pumphrey, 1999: Validation of a prototype water vapour retrieval for UARS MLS, *J. Geophys. Res., in press.*

Ramanathan, V., W. Collins, 1991: Thermodynamic regulation of ocean warming by cirrus clouds deduced from observations of the 1987 El Nino, *Nature*, **349**, pp 500–503.

Randel, D,L., T.H. Vonder-Haar, M.A. Ringerud, G.L. Stephens, T.J. Greenwald, C.L. Combs, 1996: A New Global Water Vapour Dataset, *Bull. Amer.Meteor.Soc.*, **77**, pp 1253–1245.

Randel, W.J., F. Wu, J.M. Russell III, A. Roche, J.W. Waters, 1998: Seasonal cycles and QBO variations in stratospheric CH_4 and H_2O observed in UARS HALOE data, *J. Atmos. Sci.*, **55**, pp 163–185.

Raval, A., V.Ramanathan, 1989: Observational determination of the greenhouse effect, *Nature.*, **342**, pp 758–761.

Read, W.G., J.W. Waters, D.A. Flower, L. Froidevaux, R.F. Jarnot, D.L. Hartmann, R.S. Harwood, R.B. Rood, 1995:Upper tropospheric water vapour from UARS MLS, *Bull. Amer. Meteor. Soc.*,**76**, pp 2381–2389.

Reber, C.A., 1993: The Upper Atmosphere Research Satellite (UARS), *Geophys. Res letts.*, **20**, pp 1215- 1218, special issue.

Rind, D., E.W Chiou, W.Chu, J.Larsen, S Oltmans, J.Lerner, M.P McCormick, L McMaster, 1991: Positive water vapour feedback in climate models confirmed by satellite data, *Nature*, **349**, pp 500–503.

Rind, D., E.W Chiou, W.Chu, S Oltmans, J.Lerner, J.Larsen, M.P.McCormick, L McMaster,1993: Overview of the Stratospheric Aerosol and Gas Experiment II water vapour observations: method, validation and data characteristics, *J. Geophys. Res*, **98**, pp 4835-4856.

Rodgers, C.D., Inverse methods for atmospheric sounding: Theory and practise, World Scientific Publishing Co. Ltd., 1996, pp 103–110, *in Preparation.*

Robinson, G.D., 1980: The transport of minor atmospheric constituents between troposphere and stratosphere, *Q.J.R. Meteorol. Soc.*, bf 106, pp 227–253.

Roche, A.E., K.B. Kumer, J.L. Mergenthaler, G.A. Ely, W.G. Uplinger, J.F. Potter, T.C. James, L.W. Sterrit, The cryogenic limb array etalon spectrometer (CLAES) on UARS: Experiment description and performance, *J. Geophys. Res.*, **98**, pp 10763–10775.

Rosenlof, K.H., J.R. Holton, 1993: Estimates of the stratospheric residual circulation using the downward control principle, *J. Geophys. Res.*, **98**, pp 10465–10479.

Rosenlof, K.H., A.F. Tuck, K.K. Kelly, J.M Russell III, M.P McCormick, 1997: Hemispheric asymmetries in water vapour and inferences about transport in the lower stratosphere, *J. Geophys. Res.*, **102**, pp 13235–13253.

Rui, H., B. Wang, 1990: Development Characteristics and Dynamic Structure of Tropical Intraseasonal Convection Anomalies, *J. Atmos. Sci.*, **47**, pp 357–379.

Russell, J.M. III, L.L. Gordley, J.H. Park, S.R. Drayson, W.D. Hesketh, R.J. Cicerone, A.F. Tuck, J.E. Frederick, J.E. Harries, P.J. Crutzen, 1993: The Halogen Occultation Experiment, *J. Geophys. Res.*, **98**, pp 10777–10798

Russell, P.B., L. Pfister, H.B Selkirk, 1993: The Tropical Experiment of the Stratosphere-Troposphere Exchange Project (STEP): Science objectives, operations and summary findings, *J. Geophys. Res.*, **98**, pp 8563–8589.

Salathé, E.P. and D. Chesters, 1995: Variability of moisture in the upper troposphere as inferred from TOVS satellite observations and the ECMWF model analysis in 1989, *Journal of Climate*, **8**, pp 120–132.

Salathé, E.P., D. Chesters, Y.C. Sud, 1995: Evaluation of the upper tropospheric moisture climatology in a General Circulation Model using TOVS radiance observations, *Journal of Climate*, **8**, pp 2404–2414.

Salby, M.L., H.H. Hendon, 1994: Intraseasonal behaviour of clouds, temperature and motion in the tropics, *J. Atmos. Sci.*, **51**, pp 2207–2224.

Sandor, B.J., W.G. Read, J.W. Waters, K.H. Rosenlof, 1998: Seasonal behaviour tropical to mid-latitude upper tropospheric water vapour from UARS MLS, *J. Geophys. Res.*, **103**, pp 25935-25947.

Schmetz, J., O.M. Turpeinen, 1988: Estimation of the upper tropospheric humidity field from METEOSAT water vapour image data. *J. Applied Meteorology*, **27**,pp 889–899.

Schmetz,J. and L. van de Berg, 1994: Upper tropospheric humidity observations from Meteosat compared with short-term forecast fields, *Geophysical Research Letters*, **21**, pp 573–576.

Shea, D.J, H. van Loon, J.W. Hurrell, 1995: The Tropical-Subtropical Semiannual Oscillation in the Upper Troposphere, *International Journal of Climatology*, **15**, pp 975–983.

Shine, K.P., A. Sinha,1991: Sensitivity of the earth's climate to height dependent changes in water vapour mixing ratio, *Nature*,**354**, pp 382–384.

Sinha, A., 1995: Relative influence of lapse rate and water vapour on the greenhouse effect, *J. Geophys. Res*, **100**, pp 5095–5103.

Sinha, A., M.R. Allen, 1995: Climate sensitivity and tropical moisture distribution, *J. Geophys. Res*, **99**, pp 3707–3716.

Slingo, J., 1997: The Indian Summer Monsoon and its Variability, UGAMP technical report No. 45.

Soden, B.J., F.P. Bretherton, 1993: Upper-tropospheric relative-humidity from the GOES 6.7 μm channel – method and climatology for July 1987, *J.Geophys. Res*, bf 98, pp 16669–16688.

Soden, B.J., F.P. Bretherton, 1994: Evaluation of water vapour distribution in General Circulation Models using satellite observations, *J.Geophys. Res*, **99**, pp 1187–1210.

Soden, B.J. and R. Fu, 1995: A satellite analysis of deep convection, upper tropospheric humidity and the greenhouse effect, *Journal of Climate*, **8**, pp 2333–2351.

Soden, B.J., 1997: Variations in the Tropical Greenhouse effect during El Niño, *Journal of Climate*, **10**, pp 1050–1055.

Spencer, R.W., W.D. Braswell, 1997: How dry is the tropical free troposphere? Implications for global warming theory, *Bull. Amer. Meteorol. Soc., 78*, 1097–1106.

Sperber, K.R., J.M. Slingo, P.M. Inness, W.K-M. Lau, 1996: PCMDI Report No. 36 on the Maintenance and Initiation of the Intraseasonal Oscillation in the NCEP/NCAR Reanalysis and the GLA and UKMO AMIP Simulations, Program for Climate Model Diagnosis and Intercomparison, University of California, Lawrence Livermore National Laboratory, Livermore, CA 94550.

Stephens, G.L., 1990: On the relationship between water vapour over the oceans and sea surface temperature, *Journal of Climate*, **3**, pp 634–645.

Stone, E.M., W.J. Randel, J.L. Stanford, W.G. Read, J.W. Waters, 1996: Baroclinic wave variations observed in MLS upper tropospheric water vapour, *Geophys. Res. Letts.*, **23** pp 2967–2970.

Sui, C-H., Lau K.-M., 1992: Multi-scale Phenomena in the Tropical Atmosphere over the Western Pacific, *Monthly Weather Review*, **120**, pp407–430.

Sun, D.Z., R.S. Lindzen, 1993: Distribution of tropical tropospheric water vapour, *J. Atmos. Sci.*, **50**, pp 1643–1660.

Swinbank, R., A. O'Neill, 1994: Quasi-biennial and semi-annual oscillations in equatorial wind fields constructed by data assimilation, *Geophys. Res. Letts.* , **21**, pp 2099-2102.

Taylor, F.W., C.D. Rodgers, J.G. Whitney, S.T. Werret, J.J. Barnett, et al, 1993: Remote sensing of atmospheric structure and composition by pressure modulayor radiometry from space: The ISAMS experiment on UARS, em J. Geophys Res., bf 98, pp 10799–10814.

Trenberth, K.E., 1997: The definition of El Niño, *Bull. Amer. Meteorol. Soc.*, **78**, 2771–2777.

Trepte, C.R., M.H. Hitchman, 1992: Tropical stratospheric circulation deduced from satellite aerosol data, em Nature, **35**, pp 626–628.

van Loon, H., R.L. Jenne, 1969: The half-yearly Oscillations in the Tropics of the Southern Hemisphere, *J. Atmos. Sci.*, **26**, pp 218–232.

van Loon, H., R.L. Jenne, 1970: On the half-yearly Oscillations in the Tropics, *Tellus*, **22**, pp 391–398.

Verbickas, S. 1998: Westerly wind bursts in the tropical Pacific, *Weather*, **53**, pp 282-284.

Vespirini, M. 1998: Humidity in the ECMWF model: Monitoring of operational analyses and forecasts using SSM/I observations, *Q.J.R. Meteorol. Soc.*, **124**, pp 1313–1327.

Vincent, D.G., 1994: The South Pacific Convergence Zone (SPCZ): A Review, *Monthly Weather Review*, **122**, pp 1949–1970.

Wang, B. 1988: Reply (to comments by Wang on "An air-sea interaction model of intraseasonal oscillations in the tropics", *J. Atmos. Sci.*, **44**, pp 3521–3525.

Waters, J.W., 1993: Microwave Limb Sounding, Atmospheric Remote Sensing by Microwave Radiometry, M.A. Janssen, Ed., Wiley, New York.

Weng, F., N.C. Grody, R. Ferraro, A. Basist, D. Forsyth, 1997: Cloud liquid water climatology from the Special Sensor Microwave/Imager, *Journal of Climate*, **10**, pp 1086–1098.

Wheeler, M., G.N. Kiladis, 1999: Convectively coupled equatorial waves: Analysis of clouds and temperature in the wavenumber-frequence domain, *J. Atmos. Sci.*, **56**, pp 374–399.

Wu, X., J.J. Bates, S.J. Khalsa, 1993: A climatology of the water vapour brightness temperatures from NOAA operational satellites, *Journal of Climate*, **6**, pp 1282–1300.

Yulaeva, E., J.R. Holton, J.M. Wallace, 1994: On the cause of the annual cycle in tropical lower-stratospheric temperatures, *J. Atmos. Sci.*, **51**, pp 169–174.

Zhang, C. 1996: Atmospheric Intraseasonal Variability at the Surface in the Tropical Western Pacific Ocean, *J. Atmos. Sci.*, **53**, pp 739-756.

Zhang, C., H.H. Hendon, 1997: Propagating and Standing Components of the Intraseasonal Oscillation in Tropical Convection, *J. Atmos. Sci.*, **54**, pp 741–752.

Zhu, B., B. Wang, 1993: The 30-60 day convection seesaw between the tropical Indian between the tropical Indian and western Pacific Oceans, *J. Atmos. Sci.*, **50**, 184–199.